Understanding the Earliest Stages of High-Mass Star Formation

by

Alana D. Rivera Ingraham

A thesis submitted in conformity with the requirements
for the degree of Doctor of Philosophy
Graduate Department of Astronomy and Astrophysics
University of Toronto

Abstract

Understanding the Earliest Stages of High-Mass Star Formation

Alana D. Rivera Ingraham

Doctor of Philosophy

Graduate Department of Astronomy and Astrophysics

University of Toronto

2012

High-mass star formation, contrary to its low-mass counterpart, remains poorly understood. This project aims to constrain the mechanisms driving the formation of OB stars and their precursors with the analysis of two main fields: Aquila, observed by the Balloon-borne Large-Aperture Submillimeter Telescope (BLAST), and the W3 Giant Molecular Cloud (GMC), provided by the *Herschel* Space Observatory and for which Canada has lead responsibility within the *Herschel* programme. The Aquila analysis, combining BLAST and interferometry data, presents a full characterization of the main high-mass star forming clumps in this field and their Ultracompact H II regions. We have found highly clustered environments, a range of evolutionary stages, and signatures of triggering within the parsec-scale clumps hosting OB stars. Our study of the W3 GMC comprises an analysis of the young stellar objects (YSO), the regions currently hosting on-going high-mass star formation, the environment, history, and compact source population. *Spitzer* data were used to identify, classify, and investigate the clustering properties of the YSO population. These complemented the *Herschel* datasets, with which we have produced column density and temperature maps, a full analysis of the probability density functions and mass distributions, and a catalog of reliable sources at $\sim 36''$ resolution. The clump sample was characterized and classified according to their stellar content, spectral energy distributions, the N_{H_2}/T maps, the L/M diagram, and various schemes presented in previous studies. Based on our environmental analysis and the unique in-

trinsic and stellar properties of the clumps hosting the clusters of high-mass stars in W3, we have proposed a new high-mass/cluster formation scenario based on external feedback from high-mass stars. This 'convergent constructive feedback' mechanism could not only explain the formation of clusters with an observed decreasing age (and increasing system/source mass) toward the innermost regions, but could also ensure the availability of material during cluster formation, explain the formation of rare Trapezium-like systems, and address various outstanding issues in high-mass star formation theory. New simulations and additional observations are now required in order to constrain the details and implications of this model.

Dedication

To my family, who I love with all my heart.

They have been by my side every step of the way.

They have given me the support and love that have kept me going each day.

Without them, I would have never gone so far.

Acknowledgements

The work presented in this thesis would not have been possible without the support of some very special people.

First and foremost, I would like to thank the most important people in my life: my family. They have encouraged me to pursue my dreams, no matter how difficult or how far. Day after day, year after year, they are always with me, and there are no words that can express my gratitude for everything they have done for me. This thesis is their work, as much as mine.

To my PhD supervisor, Dr. Peter G. Martin. For his patience, and all the years of guidance and support. He has opened the doors for me to the area of star formation and the amazing world of the *Herschel* Space Observatory. He is responsible for making this project, and all those exciting ones that are now to come, a reality. Thank you for taking me, and my research, to new heights.

To Dr. Marten van Kerkwijk and Dr. Howard Yee. For all their help, time, and the research we have carried out together. It is also because of them that this thesis, and my career, has come to fruition.

To Dr. Graziella Branduardi-Raymont, my first Astrophysics supervisor and good friend, whom I always remember with great affection. I cannot thank her enough for her continuous support. My success will always be her success.

To all my friends at University of Toronto, for making this wonderful journey with me. Special thanks to Marzieh Farhang, whom I can always count on, and Daniela Gonçalves, for keeping me sane, and for reminding me of those small things in life that keep you going each day.

This work could not have been carried out without the help of the University of Toronto, the Department of Astronomy and Astrophysics, and the Government of Ontario. Their financial support is the engine behind this work.

Contents

List of Tables

List of Figures

Chapter 1

Introduction

1.1 Background and Scientific Motivation: High-Mass vs. Low-Mass Star Formation

While the availability of nearby low-mass star forming regions has greatly favored the study of the earliest stages in the formation process of a low-mass star ($M< 8\,M_{\odot}$) and their low-mass clumps and cores (e.g., Andre et al., 2000), the early high mass stages remain, so far, poorly understood. Indeed, the investigation of the pre-stellar (prior to the onset of stellar activity) and protostellar (after the onset of stellar activity and during the assembly process of the star) stages in high-mass star formation has been severely hampered by 1) the paucity of high-mass stars ($M> 8\ M_{\odot}$; spectral type B3V or earlier), 2) the large distances involved (kpc), 3) their clustered birthplaces, 4) their short lifetimes, 5) high extinction, and 6) their disruptive effects on local/primordial environment.

OB stars are sources of UV photons, responsible for dissociating/ionizing molecules and atoms (H II regions), and of metals, which enrich the surrounding gas with heavier species. They also affect the local and global dynamical state of the interstellar medium (ISM) through ionization and radiation pressure, stellar winds, outflows and supernovae.

These stars are therefore fundamental in determining the state and evolution of the ISM, as well as the formation, maintenance, and dissipation of structures ranging from the largest, Galactic scales, to giant molecular clouds (GMCs), disks, and planetary systems.

However, the question as to whether high-mass star formation is simply a scaled-up version of low-mass star formation, or if it is the result of a completely different process, remains one of the main outstanding issues in star formation theory. Indeed, authors such as Yorke (1993) and Zinnecker & Yorke (2007) claim that a bimodality should arise from the shorter Kelvin-Helmholtz timescale for high-mass stars, their high L/M ratio, and the dramatic effects their strong radiation field have on their evolution compared to low-mass stars. The negative (lowering) effects of the radiation pressure and low temperature on the accretion rate have been defined as the major factors impeding the formation of a high-mass star via the same mechanisms and physics invoked to form a standard low-mass object. The immediate effects of high-mass star activity can be observed, for instance, with masers, shocks, 'hot spots', and the formation of hypercompact (HC), ultracompact (UC), and classical H II regions (e.g., Zinnecker & Yorke, 2007 and references therein). Furthermore, while low-mass stars are known to be able to form in isolation, most high-mass star formation is thought to occur in clusters embedded in their parent GMCs (Lada & Lada, 2003), making cluster studies crucial in order to understand and investigate the formation of high-mass stars. Unfortunately, because the properties of the star formation process are so highly dependent on the properties of the parent cloud and starless progenitors, the lack of suitable observational data has until now prevented a viable detailed study of the early stages in high-mass star formation. This remains a major impediment to creating a comprehensive theory aiming to describe the origin and early evolution of high-mass stars and stellar clusters in comparison to the low mass-case.

1.2 High-Mass Star Formation

1.2.1 Proposed Scenarios and Theoretical Models

The need for a complete and consistent picture of the overall process is evident from the lack of consensus and the various theories proposed to explain the formation of a high-mass protostar.

In order to form an OB protostar while overcoming the accretion problem, various studies have used the fact that OB stars are generally associated with rich stellar clusters. Bonnell et al. (1998) and Bonnell & Bate (2002) suggested a new mechanism based on collisions of intermediate-mass stars that have formed by accretion within the same parent core. In a later work by Bonnell & Bate (2005) it was suggested that mergers of high-mass binary systems might result in the formation of the most massive stars without the need to invoke unrealistically high stellar densities in the parent cluster.

The model of McKee & Tan (2003) relies on the key properties of supersonic turbulence and high pressure to form a high-mass star. In this scenario, a massive, long-lived, turbulent core forms a one high -mass star or a bound system (e.g., binary). Turbulence could support highly dense cores, which would result in the needed high accretion rates when collapsing. In this model, there is also a direct link between the mass of the parent core and that of the final star(s) born from such core, with the star having just as much material available as that already associated with it. This is in contrast with the 'competitive accretion' model presented by Bonnell et al. (1997), in which stars must compete with each other for material during the accretion process (i.e., they do not have an already assigned reservoir for accretion). Here, the most massive stars will be formed only in those locations were accretion is most favored, like in the central regions of a stellar cluster and the deepest regions of the gravitational potential well, therefore explaining those observations showing stellar clusters with primordial mass segregation.

Only recently, new scenarios have been proposed that combine characteristics of var-

ious of the above models, such as the 'clump-fed massive star formation' scenario from Wang et al. (2010). As its name indicates, this model relies on the material contained at clump (parsec) scales to feed the inner cores and the high-mass stars during the formation process. The properties of the turbulent gas in the clump will determine the accretion rate (through filaments, formed by turbulent compression an turbulence decay), with the most massive stars benefiting from being located in 'preferred' regions favorable for the accretion process (e.g., the center of the potential well).

1.2.2 Progenitors of High-Mass Stars and Clusters

Despite the lack of agreement as to the scale and mechanisms used to assemble an OB star, the general consensus is that high-mass star formation must comprise similar basic processes to the low-mass case: 1) the formation of a dusty molecular cloud which undergoes turbulent fragmentation into clumps and cores, 2) gravitational collapse of the cores, 3) accretion by the protostellar object, and 4) dissipation of the parent molecular cloud by star activity (Zinnecker & Yorke, 2007).

A key issue for distinguishing between the above theories lies on the properties on the parent structure and their local environment. Infrared analysis has proven to be particularly useful in this investigation, thanks to the emission from heated dust grains so common during the early embedded phases. The search for structures with high enough surface densities (e.g., Krumholz & McKee, 2008) and an availability of mass suitable to form stars with M$>8\,M_{\odot}$ led to the discovery of Infrared Dark Clouds (IRDCs: M$\sim 100-1000\,M_{\odot}$, n$\sim 10^4-10^6$ cm^{-3}; e.g., Simon et al., 2006), identified as ideal candidates for the elusive high-mass counterparts of the so-called Bok globules (e.g., Evans, 1999), known to be regions of isolated low-mass star formation. The 'pre-protostellar cores' within the globules have also been suggested to have massive counterparts within the IRDCs. These Cold Dense Molecular Cores (CDMCs: e.g., Zinnecker & Yorke, 2007), also called High Mass Starless Cores (HMSCs; e.g., Sridharan et al., 2005) or Pre-Proto-

cluster Cores (PPclCs; M$\sim 100-1000$ M$_\odot$, T$<$ 20 K, n$>$ 10^5 cm^{-3}; e.g., Evans et al., 2002), were soon identified as the possible starless progenitors of the Hot Dense Molecular Cores (e.g., Rathborne et al., 2006), hosting young compact stellar clusters and high-mass stars. However, despite the various surveys aiming to locate such massive starless precursors (e.g., Motte et al., 2007), so far only a very limited number of 'candidate' HMSCs have been observed. Their identification and characterization is a priority in the investigation of high-mass stars, and demands a detailed, self-consistent, and unbiased study of the pre-stellar population in regions with active OB star formation. This analysis can only be achieved through large-scale studies capable of detecting and characterizing those cold structures associated with the earliest stages of star formation, while at the same time providing a large enough sample to derive statistically significant results and conclusions.

1.3 The Potential of Submillimeter Studies: Instruments and Datasets

The study of the earliest stages of star formation is intrinsically connected to the ability to probe the cold and dense dusty regions within which stars are born. The short wavelength radiation from deeply embedded young stellar objects (YSOs) is absorbed by the dust and reaches the observer as re-processed far infrared (FIR) and submillimeter (submm) emission. The low optical depth at these longer wavelengths makes submm studies the best tool to investigate the coldest clumps and inner cores ($\sim 1-0.1$ pc; Williams et al., 2000) that produce new stars, especially the 'coldest' structures prior to the onset of stellar activity.

1.3.1 The Balloon-borne Large-Aperture Submillimeter Telescope

The 2-m Balloon-borne Large-Aperture Submillimeter Telescope (BLAST; Pascale et al., 2008), with two consecutive and successful science missions in 2005 and 2006, mapped the sky simultaneously with an effective resolution of ∼40, 50, and 60″ at 250, 350 and 500 μm, respectively.

BLAST studies of regions like Vulpecula (Chapin et al., 2008) and Vela (Netterfield et al., 2009) have provided robust samples of submm sources in a range of evolutionary stages. By fitting modified blackbody spectral energy distributions (SEDs) to the BLAST measurements, and with the aid of ancillary data at infrared (IR) wavelengths (e.g., the *Infrared Astronomical Satellite* (*IRAS*; Neugebauer et al., 1984), the Multiband Imaging Photometer for *Spitzer* (MIPS; Rieke et al., 2004), and the *Midcourse Space Experiment* (*MSX*; Egan et al., 2003)), these studies have been able to constrain dust temperatures, masses and bolometric luminosities for their respective samples. Their results aimed to characterize and investigate crucial properties of the submm population, including their star formation stage, the (core) mass function, and core lifetimes. Observing at the same long wavelengths as the *Herschel Space Observatory*[1][2] (hereafter *Herschel*), BLAST delivered valuable datasets that provided a first glimpse of the potential of the submm (and *Herschel*) for investigating the unknown early stages of evolution of a high-mass star.

[1] http://www.esa.int/SPECIALS/Herschel/index.html

[2] *Herschel* is an ESA space observatory with science instruments provided by European-led Principal Investigator consortia and with important participation from NASA

1.3.2 The *Herschel* Space Observatory: New Clues to the High-Mass Star Formation Process

The launch of *Herschel* in May 2009 marked the beginning of a new era in star formation studies. The Photoconductor Array Camera and Spectrometer (PACS; Poglitsch et al., 2010) and the Spectral and Photometric Imaging REceiver (SPIRE; Griffin et al., 2009) have delivered extensive data at unprecedented sensitivity and spatial resolution in the wavelength range between 70 μm (PACS: $\sim 5''$) and 500 μm (SPIRE: $\sim 36''$), suitable for detailed property, SED, and statistical studies.

The Guaranteed-Time Key Programme (GTKP) HOBYS (*Herschel* imaging survey of OB Young Stellar objects; Motte et al., 2010) is specifically designed to address the major outstanding issues in high-mass star formation. Using the simultaneous coverage of PACS and SPIRE, the programme is designed to observe all major regions of high-mass star formation at distances less than d$\sim$ 3 kpc in order to constrain the physical processes involved in the formation of an OB star, the early evolution prior to reaching the main-sequence stage, the effects of stellar feedback and triggering on star formation, and the nature of the elusive progenitors of high-mass stars and clusters.

While still preliminary, the evidence presented in recent studies of the first HOBYS fields suggest a dynamical process of high-mass/cluster formation, taking place in filamentary-like regions of high column density of the order of $N_{\mathrm{H_2}} \sim 10^{23}\,\mathrm{cm}^{-2}$ ('ridges'; Hill et al., 2011; Nguyen Luong et al., 2011a). These structures could be formed by convergence of flows, as proposed for W43 (Nguyen Luong et al., 2011b) and the DR 21 Ridge in Cygnus-X, the latter being one of the most prominent examples (Schneider et al., 2010; Hennemann et al. in preparation). The effects of this process in turbulent environments have been investigated extensively in previous studies (e.g., Klessen et al., 2004; Klessen et al., 2005; Heitsch et al., 2006). Other studies of high-mass star forming regions suggest enhanced accretion at the mergers of filaments in order to form clusters (Dale & Bonnell,

2011; Schneider et al., 2012). Questions remain as to whether such models can successfully explain the origin of other known high-mass systems in other regions of the sky. If more than one scenario is present, it is essential to identify the conditions common to all scenarios that might constitute the basic mechanisms for the formation of OB stars and their associated cluster.

1.4 The Project: Searching for Clues of the High-Mass Star Formation Process

1.4.1 Targets

As members of the BLAST and HOBYS Collaborations, the present work aims to constrain the unique properties of the earliest stages of high-mass star evolution using the datasets delivered by these two instruments of two regions with prominent OB activity:

1) The high-mass star forming region of Aquila, located at $\ell = 45°$,$b = 0°$, $6\,\mathrm{deg}^2$ of which was observed by BLAST during its 2005 flight (BLAST05).

Aquila is well known for its prominent high-mass star formation (e.g., Rathborne et al., 2004), and is dominated by two main molecular complexes. These are host to numerous UCHii regions (e.g., Wood & Churchwell, 1989; [WC89]), maser emission, and outflows from young and highly embedded OB stellar clusters. The stellar activity of the Galactic Ring Survey Molecular Cloud (GRSMC) 45.60+0.30, located in the Aquila field, has been extensively studied in the infrared and radio (e.g., Kraemer et al., 2003; Vig et al., 2006). However, although submm data have been used in past studies of this cloud (e.g., Vig et al., 2006), the overall population and properties of this entire region in Aquila are yet to be fully characterized at submm wavelengths.

2) The W3 GMC.

At a distance of 2 kpc (Hachisuka et al., 2006; Xu et al., 2006; Navarete et al., 2011),

W3 is a well-known high-mass star forming region in the Perseus Arm. With an estimated mass of $\sim 4 \times 10^5\,M_\odot$ (Moore et al., 2007; Polychroni et al., 2010) and a size of $\sim 1.5\,\mathrm{deg}^2$ this cloud is one of the most massive in the outer Galaxy.

Being one of the closest regions with ongoing high-mass formation, W3 is a prime candidate for OB studies (see Megeath et al., 2008 for a full review).

This cloud comprises a wealth of H II regions, clusters, and active star forming sites with clear signatures of both low-mass and high-mass star formation in various evolutionary stages (e.g., see Tieftrunk et al., 1997). The most active star forming sites are W3 Main, W3 (OH) and AFGL 333. All these regions are located in a prominent and dense structure, defined in the literature as the 'high-density layer' (HDL; e.g., Oey et al., 2005), which forms the western edge of the W4 bubble (powered by various O stars).

W3 Main contains the most prominent high-mass population of the entire GMC. The two brightest and most central infrared sources in this region, IRS5 and IRS4 (Wynn-Williams et al., 1972), are the youngest high-mass systems in the GMC, as indicated by the presence of numerous HCHII regions (Tieftrunk et al., 1997). IRS5 has been suggested to contain a proto-Trapezium system (Megeath et al., 2005; Rodón et al., 2008) powered by a cluster of OB stars (e.g., Claussen et al., 1994; van der Tak et al., 2005).

The W3 (OH) region is also comprised of two main regions: W3 (OH) itself, a young UCHII region rich in OH masers (Dreher & Welch, 1981), and a hot core with a younger massive proto-binary system, $\sim 6''$ east of W3 (OH) (Chen et al., 2006). The region associated with the binary has prominent H_2O emission and it is commonly referred in the literature as W3 (H_2O) (Little et al., 1977; Turner & Welch, 1984).

W3 (OH) and W3 Main are both located in the shell surrounding the cluster IC 1795. This 3-5 Myr old cluster is powered by various OB stars, the most massive of which has a spectral type O6.5V (Oey et al., 2005; BD $+61°411$). The location of W3 Main and W3 (OH), at the edges of the shell around this cluster, has been suggested as evidence for their formation having been induced by IC 1795, itself created by an earlier burst of

star formation in the W4 region (Oey et al., 2005). While a triggered origin by IC 1795 appears to be the case for W3 (OH), the characteristics of the cluster of low mass stars associated with W3 Main appear to suggest that this region might have actually formed in an earlier stage, prior to IC 1795 (Feigelson & Townsley, 2008).

KR 140 is a small H II region (5.7 pc in diameter at a distance of 2.3 ± 0.3 kpc; Kerton et al., 2008). Located west of the main star-forming activity in the W3 complex and ~ 40 pc SW of IRS5, this H II region is powered by a central and isolated O8.5 star (VES 735) about $\sim 1-2$ Myr old (Ballantyne et al., 2000). Contrary to W3 Main, KR 140 has been suggested to be the result of a rare case of spontaneous high-mass star formation (Ballantyne et al., 2000).

1.4.2 Thesis Structure and Analysis

Finding the common physical processes and primordial conditions leading to the formation of the most massive stars is key for constraining current theoretical models, determining the presence of a bimodality in star formation, and explaining the paucity of OB stars. If such bimodality is present and dependent on the pre-stellar/host conditions, only a detailed, multiwavelength analysis and characterization of the structures hosting OB stars will be able to discover it. In this work, this has been carried out using the BLAST datasets, delivered prior to the launch of *Herschel*, and the unique HOBYS data. The capability of these instruments allow for the investigation of the unique properties of high-mass star progenitors and the mechanisms acting from clump down to core scales (~ 0.1 pc).

The work presented in this thesis is structured as follows:

The first part of the project, included in Chapter 2, is focused on the BLAST datasets, with a general characterization of the submm clump population of the Aquila field. The analysis comprises an initial census and study of those structures that would be observed by *Herschel* as part of the Open-Time Key Programme Hi-GAL (the *Herschel* infrared

Galactic Plane Survey; Molinari et al., 2010). Like in previous BLAST studies, we provide estimates of physical parameters such as mass, dust temperature, and luminosity, focusing on the most prominent clumps in the field. This work therefore complements the analysis of the other BLAST05 Galactic plane star forming regions, including Vulpecula (Chapin et al., 2008) and Cygnus-X (Roy et al., 2011). Our study also makes use of the 4.8 GHz radio interferometry data from the Co-Ordinated Radio 'N' Infrared Survey for High-mass star formation (CORNISH; Purcell et al., 2008). In conjunction with BLAST, these data allow for a full characterization of the UCHii regions within the BLAST clumps. The results of the Aquila analysis presented in this thesis have been published in Rivera-Ingraham et al. (2010)[3], and are an example of the potential of multi-scale studies in the investigation of high-mass star formation.

As precursor of the SPIRE instrument, BLAST provided the ideal testbed for the methodology, codes and techniques required for the *Herschel* analysis that constitutes the second part of this thesis. This study includes a complete analysis of the W3 field, for which Canada has lead responsibility within the HOBYS Collaboration. Our analysis comprises separate studies of the YSO population, the youngest high-mass star forming regions, environment, and compact source populations.

The YSO analysis, presented in Chapter 3, is a follow-up of that initiated by Polychroni et al. (2010). It includes a full catalog, classification, and characterization of the clustering and spatial properties of the YSO population. This work, carried out using data from the *Spitzer Space Telescope* (Werner et al., 2004), has been published in Rivera-Ingraham et al. (2011)[4].

The 'dust' and structural analysis of W3 is based on the data delivered by *Herschel*. This study is subdivided as follows:

A first-look overview of the properties of the W3 GMC, included in Chapter 4, focusing

[3]Reproduced here by permission of the American Astronomical Society
[4]Reproduced here by permission of the American Astronomical Society

on the characterization of the regions currently hosting young high-mass stars. Results are used to constrain the processes that could lead to the formation of the progenitors of clusters of OB stars, and how these relate to the models proposed in similar studies of other HOBYS fields.

Additional evidence supporting the conclusions from the first-look analysis is presented in Chapter 5: a large-scale (environmental), independent analysis of each subregion of W3.

The final analysis is included in Chapter 6: a preliminary study of the compact source population. The use of multiwavelength data allows for a full characterization of the intrinsic parameters, including temperature and mass, through SED fitting, which was not possible in previous pioneering studies like that carried out by (Moore et al., 2007), who surveyed 2/3 of W3 at 850 μm using the Submillimetre Common-User Bolometer Array (SCUBA; Holland et al., 1999). Results are used to verify the unique properties of the clumps currently undergoing high-mass star formation. These are needed for constraining the unique mechanisms and conditions that could have led to their formation, which is the main goal of this thesis.

Chapter 2

BLAST: The High-Mass Star Forming Region in Aquila

2.1 Observations and Data Analysis

2.1.1 Submillimeter Data Products and Source Detection

BLAST observed Aquila during its first science flight in June 2005, mapping a total of 6 $\deg^2$ ($3^\circ \times 2^\circ$) at 250, 350, and 500 μm towards GRSMC 45.60+0.30. For the following analysis we note that the three BLAST maps were made such that the average of these maps is zero (Patanchon et al., 2008). During the reduction and mapmaking process, the SANEPIC (Signal and Noise Estimation Procedure) algorithm removed low-frequency noise (mainly sky signal). Large scale signals in the map were recovered, but the DC level was set to zero by application of a high-pass filter to the time-ordered data. The reduction process, as well as the subsequent procedures to correct the unexpected optical degradation that occurred during the flight (Truch et al., 2008), have been described in detail in Chapin et al. (2008) and Roy et al. (2010). The 250 and 350 μm maps were later convolved in order to produce BLAST maps with a common resolution of $60''$ for photometry analysis.

As can be seen in Figure 2.1, the final products still suffered from artifacts (ripples) surrounding the brightest objects and the map edges arising from the deconvolution process. These introduce false detections when running the Interactive Data Language (IDL[1]) routines designed to detect the main submm peaks in the field, and which we therefore have to eliminate manually after visual inspection. For source identification we used the IDL-implemented DAOPHOT 'FIND' routine and a S/N detection limit of 3 at 250 μm, the band with higher signal to noise ratio (S/N) for a typical star-forming clump. We kept a total of 66 sources between $\ell = 44°.6$ and $46°.8$ (to avoid map edges) which also had a match at 350 μm within $20''$ with a S/N> 3. We also kept six additional sources (identified with (*) in Table 2.1) with a lower S/N at 250 and 350 μm (combined S/N between $\sim 2 - 3.5$, visually prominent, and some with counterparts in the *IRAS* Point Source Catalog; PSC). Their lower S/N can be explained by their location in the local neighborhood of (clustered) bright sources, regions with difficult background estimation and significantly above average noise. This source catalog (Table 2.1) is robust to ~ 50 Jy at 350 μm (~ 140 Jy at 250 μm). For comparison, the cirrus noise ($3\,\sigma_{\rm cirrus}$) at 250, 350 and 500 μm is estimated to be ~ 20, 10, and 5 Jy for each map, respectively (Roy et al., 2010). In the present work we did not require completeness to faint flux densities, however, choosing to focus our analysis only on the most prominent submm peaks of our sample.

2.1.2 Distance Estimation

In order to investigate the velocities and distances towards the main clumps in the field we used the ^{13}CO molecular spectra from the BU-FCRAO Galactic Ring Survey (GRS; Jackson et al., 2006). The datasets cover the region between $18°< \ell < 55°.7$ with a velocity resolution of 0.2 km s^{-1}. The spatial resolution is $46''$ with an angular sampling of $22''$. Due to the distribution of the clumps throughout the field, this spectral analysis

[1]IDL is a product of ITT Visual Information Solutions, http://ittvis.com/

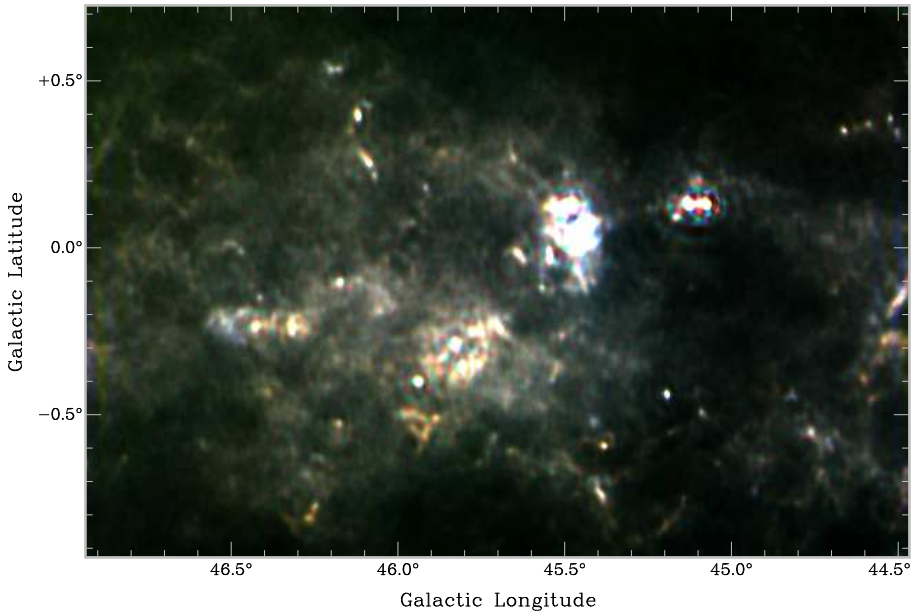

Figure 2.1 BLAST submm map in Aquila combining three wavebands at 250, 350 and 500 μm, with color coding blue, green and red, respectively.

is essential in order to estimate and justify the use of a suitable common distance to the most active regions in Aquila. A comparison of BLAST with the molecular emission is shown in Figure 2.2. To aid qualitative intercomparison, BLAST contours are presented in this and a number of later figures, from images in which an approximate DC level has been restored (300, 160, and 50 MJy sr^{-1} at 250, 350, 500 μm, respectively).

For the spectral analysis we first extracted and fitted the ^{13}CO spectra at the position of each submm peak. Molecular counterparts from the catalogs of Roman-Duval et al. (2009) and Rathborne et al. (2009) were assigned to each BLAST peak if the peak was located within the spatial Full Width at Half Maximum (FWHM) of the molecular clump. The velocity we obtained from the spectral fitting was then compared with the clump velocities in the catalog. This allowed us to distinguish the appropriate molecular counterpart to the BLAST clump in those cases where more than one molecular counterpart (but with different Local Standard of Rest (LSR) radial velocity) was found for a particular BLAST clump (e.g., Table 2.1). Our analysis and line fitting of the spectra is in good agreement with the significant dispersion of velocities (e.g., Figure 2.3) existing

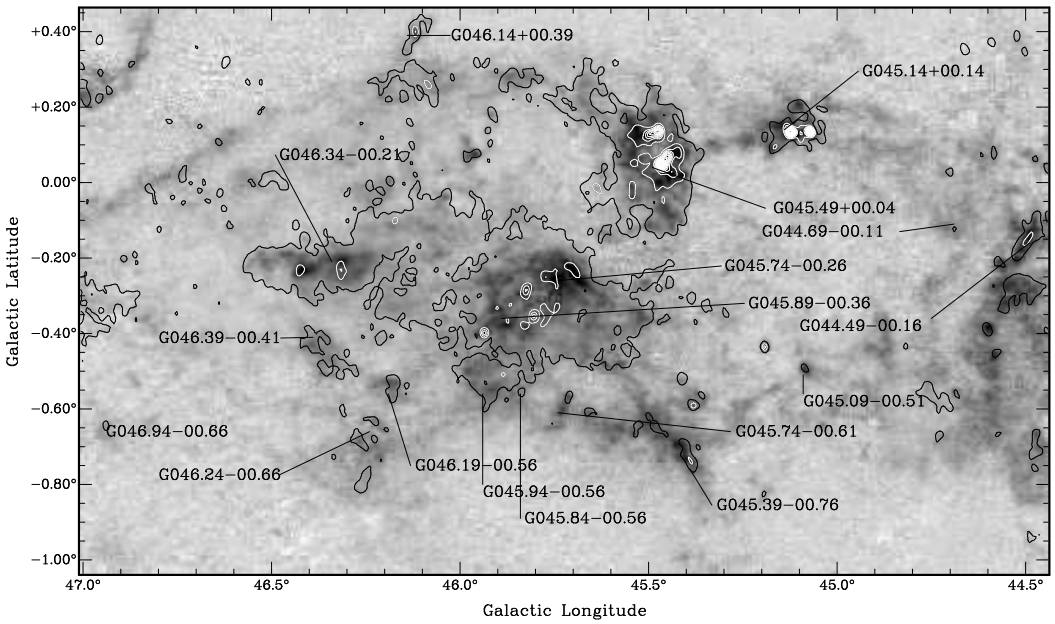

Figure 2.2 Greyscale: ^{13}CO molecular emission at $\sim 60 \pm 10\,\mathrm{km\ s^{-1}}$ with labels marking position and names (GRSMC) of clouds in this range from Rathborne et al. (2009). Contours are BLAST 500 μm surface densities. White: contours from 10 to 90% of map peak value of $2153\,\mathrm{MJy\,sr^{-1}}$ in 5% steps. Black: 5% contour level (see text).

in the recent cloud/clump catalogs of Rathborne et al. (2009) and Roman-Duval et al. (2009). The main activity of the field is located in the main broad high-velocity peak in Figure 2.3. The smaller peak at lower velocities could arise from clumps located either much closer or much farther away ($\sim$ 1 or $\sim$ 11 kpc; Roman-Duval et al., 2009) than the complexes forming the high-velocity peak (which cluster around the tangent point of ~ 6 kpc; e.g., Simon et al., 2001).

Using the Clemens (1985) rotation curve of the Milky Way, Roman-Duval et al. (2009) estimated distances to GRS molecular clouds (e.g., Rathborne et al., 2009) with the aid of H I self-absorption (HISA) and continuum absorption, both in data from the Very Large Array Galactic Plane Survey (VGPS; Stil et al., 2006). There are four clouds in their sample within the defined BLAST map limits (§ 2.1.1) with an assigned distance between $\sim 7 \pm 0.5$ kpc (LSR velocity within the second peak in Figure 2.3: v$\sim 60\,\mathrm{km\,s^{-1}}$): G045.49+00.04, G045.74−00.26, G045.89−00.36, and G045.39−00.76. However, one of

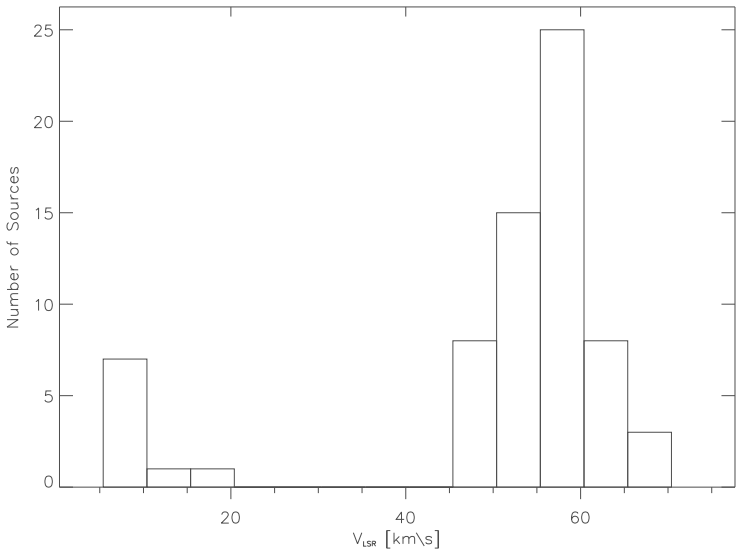

Figure 2.3 Histogram of ^{13}CO radial velocities of 68 BLAST detections with molecular clump counterpart (BLAST peak lying within spatial FWHM of clump) in catalogs of Roman-Duval et al. (2009) and Rathborne et al. (2009). The main stellar activity has velocities within the broad (high velocity) peak.

the major clouds in the BLAST field, G045.14+00.14 ($v_{LSR} \approx 60$ km s^{-1}), has instead been assigned its near distance of ~ 4.5 kpc.

Taking into account a maximum standard error of 10% for the distances (Roman-Duval et al., 2009), we estimate that a common distance of ~ 7 kpc would be a suitable approximation for the analysis of all the clouds with velocities of ~ 60 km s^{-1} and located in this distance range. Furthermore, this estimate is in good agreement with the distances derived by Pandian et al. (2009), who also resolved the kinematic distance ambiguities using H I self-absorption with data from the VGPS. These authors calculated, by means of methanol masers and a flat rotation curve, a range of distances for the clumps within G045.49+00.04 between 6.9 and 7.4 kpc, which again agrees well with the estimate from Roman-Duval et al. (2009). However, they assigned the far distance of 7.4 kpc to the clump in G045.14+00.14, which disagrees with Roman-Duval et al. (2009). This coincides with previous studies (e.g., Simon et al., 2001) that placed this cloud at the same

kinematic distance as its neighbor G045.49+00.04. In this work we adopt the far distance estimate of Pandian et al. (2009) for G045.14+00.14, and we restrict our main analysis to four clouds (G045.49+00.04, G045.74−00.26, G045.89−00.36, and G045.14+00.14), which comprise the most active complexes of the field. Our main BLAST detections corresponding to G045.39−00.76 are associated with a bubble (Churchwell et al., 2006), separate from the main clouds of the field, and we therefore omit these sources from the main analysis. A common distance of $\sim 7\,$kpc ($1^\circ\sim 0.1\,$kpc scale) is assumed in the present study (in contrast with those used by previous authors of ~ 6 and $\sim 8\,$kpc; e.g., Simon et al., 2001; Kraemer et al., 2003; Paron et al., 2009).

2.1.3 Ancillary Data

To create our SEDs we used the BLAST fluxes estimated using our own Gaussian fitting routine (§ 2.1.4). Whenever possible, we also included data from the *IRAS* Galaxy Atlas (IGA; Cao et al., 1997: HIRES; Aumann et al., 1990) at 60 and 100 μm and BOLOCAM (Galactic Plane Survey) data at 1.1 mm (Rosolowsky et al., 2010). *IRAS* flux densities were estimated individually using our Gaussian fitting routine, while for the convolved ($60''$) BOLOCAM images we used aperture photometry (single sources: an aperture centered on the BLAST source with $1'.8$ radius; an estimate for the background was obtained from an annulus formed by the source aperture and another aperture with radius 1.3 times larger than that of the source). The measured BOLOCAM fluxes were found to be within the error range of those provided by the GATOR service[2], and the latter values were therefore used to constrain the SEDs at longer wavelengths if a counterpart to the BLAST clump was found within $30''$ (we found 39 sources in Table 2.1 with BOLOCAM counterparts, including all those with measured SEDs, with the exception of A22). We note that *IRAS* was found to be saturated for the brightest clumps, for which we adopted the upper limits estimated by Kraemer et al. (2003). Most of our measured *IRAS* fluxes

[2]http://irsa.ipac.caltech.edu/applications/Gator/

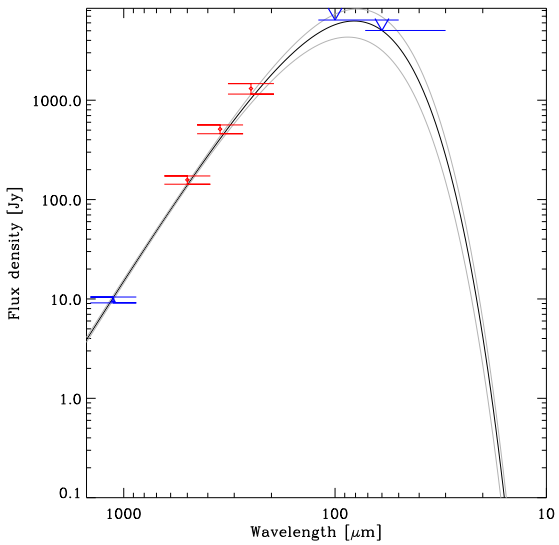

Figure 2.4 Spectral energy distribution of A16 (Table 2.1). Symbols are BLAST and ancillary data (*IRAS*; BOLOCAM). Upper and lower curves are the 1-sigma envelope of the dust emission model (Chapin et al., 2008).

were also found to be higher than those from the *IRAS* PSC. This effect, combined with the lower resolution of *IRAS* and the photometry of sometimes blended sources, imply that these values should also be generally considered upper limits in our fits.

To investigate the stellar content and the morphology of the emission at shorter wavelengths we used the InfraRed Array Camera (IRAC; Fazio et al., 2004) on *Spitzer*. Of the four available IRAC bands (3.6, 4.5, 5.8, and 8 μm), we focused on the longest wavelength in our morphology analysis. For our study of the stellar population we used data from the Galactic Legacy Infrared Midplane Survey Extraordinaire (GLIMPSE; Benjamin et al., 2003) through the online GATOR query system. The GLIMPSE I online datasets, covering about 220 deg^2 of the Galactic Plane ($\ell = 10°-65°$) in all four IRAC bands, include a highly reliable (GR) catalog and a more complete, but less reliable one (GC). Both were used in the present work.

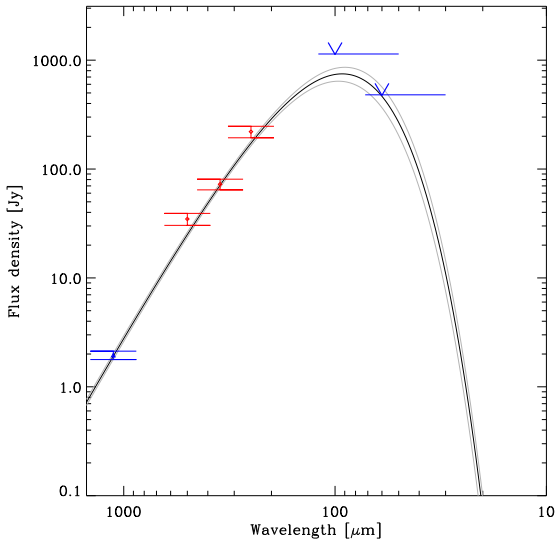

Figure 2.5 Same as Fig.2.4, but for A50 (Table 2.1).

2.1.4 Photometry: Spectral Energy Distributions and Parameter Estimation

Similar to other Galactic BLAST studies (e.g., Chapin et al., 2008), our SED analysis was carried out by estimating flux densities with our own IDL spatial Gaussian-fitting routine, and subsequently fitting them with a modified blackbody of the form:

$$S_\nu = A \left(\frac{\nu}{\nu_0} \right)^\beta B_\nu(T), \tag{2.1}$$

where β is the dust emissivity index, $(\nu/\nu_0)^\beta$ is the emissivity factor normalized at a fixed frequency ν_0, and $B_\nu(T)$ is the Planck function. The amplitude A can be expressed as:

$$A = \frac{M_c \kappa}{R D^2}, \tag{2.2}$$

where D is the distance to the source, M_c is the total clump mass, κ is the dust mass absorption coefficient, evaluated at $\nu_0 = c/250\,\mu$m, and R is the gas-to-dust ratio. A 2-D Gaussian is fitted to the three bands simultaneously with the amplitudes, centroid,

orientation angle, and major and minor FWHM as free parameters. The fit is carried out using a non-linear least-squares minimization IDL routine (based on MPFIT: Markwardt, 2009), which also allowed for simultaneous multiple Gaussian fitting in crowded regions of the field. The background was estimated by fitting a fourth-order polynomial to the regions around the clump.

Following Chapin et al. (2008), estimates and uncertainties for the dust temperatures, masses, and luminosities were obtained through a Monte Carlo analysis performed on our SED models, keeping the dust emissivities and R as fixed parameters ($\beta = 1.5$, $R = 100$, $\kappa = 10\,\mathrm{cm^2 g^{-1}}$). Examples of SEDs are shown in Figure 2.4 and Figure 2.5. A flux density consistency check between all convolved and deconvolved maps shows flux conservation to better than 5%.

The bolometric luminosities derived from the fits for each evolved clump were subsequently used to estimate equivalent single zero-age-main-sequence star (ZAMS) spectral types using the tables of Panagia (1973). This luminosity value was used as a general measure of the energy output of each submm detection. We note that the BLAST sources at a distance of $\sim 7\,\mathrm{kpc}$ are pc-sized, and therefore 'clump-like' objects (e.g., Bergin & Tafalla, 2007). We expect them to be powered by several embedded stars, with the luminosity dominated by that of the most massive source(s) within the clump. In addition, we also include the equivalent luminosity class V star spectral types from the more recent stellar calibration provided by Martins et al. (2005), which takes into account the effects of line-blanketing and winds in the non-LTE atmosphere models of O stars. For this case we used the calibration based on the observational T_{eff} scale; these authors note that the theoretical and observational scales are in good agreement for early type dwarfs and supergiants.

2.1.5 4.8 GHz Radio Interferometry Data and Analysis

For our radio analysis we used the CORNISH interferometry datasets, a 4.8 GHz survey carried out with the Very Large Array (VLA), and covering the northern GLIMPSE region with a resolution of $\sim 1''$. Our analysis of these data was carried out using the same procedure and Gaussian fitting codes used for the submm. The 4.8 GHz fluxes from our fitting were then used to estimate the total number of ionizing photons per unit time for each radio source (e.g., Panagia, 1973; Martins et al., 2005):

$$Q_0 = \int_{\nu_0}^{\infty} \frac{L_\nu}{h\nu} d\nu, \tag{2.3}$$

where ν_0 is the frequency at the Lyman edge.

These values were also used in conjunction with the tables from Panagia (1973) and Martins et al. (2005) to estimate the equivalent single-star radio spectral types for each detection. The positions and parameters derived using these data have been included in Tables 2.2, 2.3, and 2.4. The target S/N of our sample is > 3. As with the BLAST sources, we have also kept a few radio detections with lower S/N. These were identified and required by our Gaussian fitting routine, and are almost exclusively secondary peaks neighboring the brightest sources (clusters: A16-C24, A28-C15), where the S/N is greatly deteriorated (> 1.5). This effect has already been discussed in Purcell et al. (2008), and these sources will therefore require further examination as soon as additional/better data becomes available. Extra detections with low S/N have been identified (*) in Table 2.2. Nomenclature of radio sources is formed by the name of the BLAST clump, followed by that of the CORNISH detection (A#−C#).

Considering the uncertainties in our measurements and the above procedure for spectral type estimation, assuming optically thin emission, we estimate an uncertainty for these measurements of ~ 0.5 in spectral type (for a given calibration scale of the stellar parameters). This uncertainty is expected to be larger than any spectral type error that could arise when comparing our estimates (for a distance of ~ 7 kpc) and those obtained

by previous authors with a distance of ~ 6 kpc (Tables 2.3 and 2.4).

2.2 Discussion of Individual Sources

In the following sections we apply the results of our analysis to describe the main submm regions (G045.49+00.04, G045.74-00.26, G045.89-00.36, and G045.14+00.14), adopting the designations from Rathborne et al. (2009) (Fig. 2.2).

2.2.1 GRSMC G045.14+00.14

G45.12

GRSMC 45.122+0.132 (G45.12; IRAS 19111+1048; A16 in the present work), contains a cometary UCHiiR (WC89) classified as a massive young stellar object (MYSO) by Chan et al. (1996). It shows extended submm emission towards the north (upper left of Figure 2.6), observed in the mid-infrared (MIR) as a bright rimmed H II region. This structure is likely produced by the activity of the young massive population embedded in the innermost regions of the clump, as detected by Vig et al. (2006) using the Giant Metrewave Radio Telescope (GMRT) at 1200 and 610 MHz. The 19 embedded OB stars observed by these authors are located within and surrounding the peak of our BLAST clump, mainly within the H II region. Their brightest source agrees well with our submm peak ($\lesssim 5''$), and although it remained unresolved in their datasets, they suspected it to be a cluster responsible for the extended morphology in the radio. A possible cluster powering this region has also been suggested through [NeII] observations by Takahashi et al. (2000), and later by Zhu et al. (2008), who detected three additional peaks (G45.12N, G45.12SE and G45.12SW) nearby the main UCHiiR from WC89.

Our analysis of the 4.8 GHz CORNISH data confirms such suspicions, with the detection of 28 radio sources in a region ~ 0.8 pc in radius centered on (and including) the central brightest member (A16−C24; Table 2.3; Figure 2.7). These objects are believed

Table 2.1 Submm clumps in the BLAST Aquila map[a]

Column	Units	Description
1		Source number
2		BLAST Name: Source names include the prefix 'BLAST' as part of the standard BLAST nomenclature
3	°	Galactic longitude (ℓ)
4	°	Galactic latitude (b)
5		*IRAS*: Closest *IRAS* match (<30″) in the Point Source Catalog
6		IRDC: Closest IRDC (<30″) from Peretto & Fuller (2009)
7		Cloud: GRS name of clouds from Rathborne et al. (2009), which contain the molecular clump counterpart(s) to the BLAST source
8		Clump: Clump (Rathborne et al., 2009) with BLAST peak within FWHM
9	kpc	D: Distance from Roman-Duval et al. (2009)
10		Assoc: Cloud Association (Y) - BLAST clump is associated with cloud. Cloud has a molecular clump whose velocity FWHM contains the strongest molecular peak of spectrum measured at submm peak. Molecular clump also has peak velocity closest to that measured for BLAST source. (?) - Cloud membership unclear. Main molecular emission for BLAST source is within velocity FWHM of the molecular cloud/clump, but there is another cloud with a clump with peak velocity closer to that of the strongest line in BLAST spectrum. Contributions from many clouds are possible. A blank implies that the velocity of main BLAST molecular emission is not compatible with that assigned to the cloud/clump, despite the spatial agreement.

[a] Table lists the parameters for each source in the catalog for guidance regarding its form and content. It is shown in its entirety in the *Astrophysical Journal*.

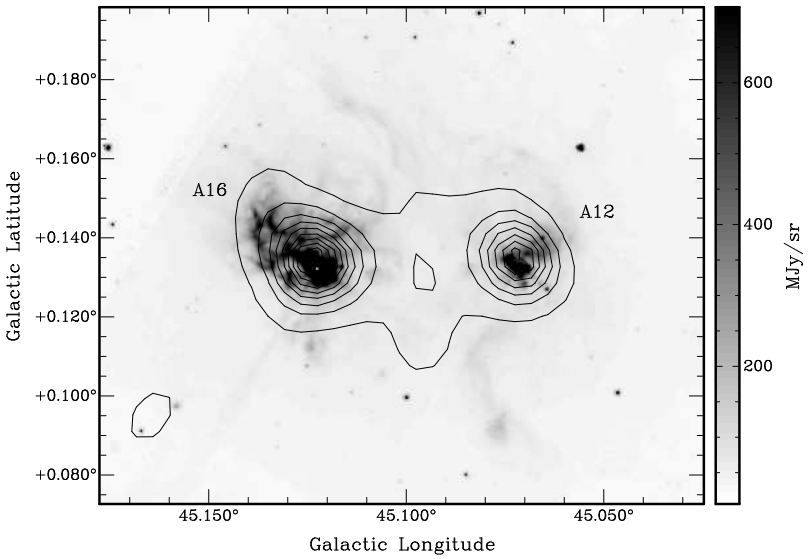

Figure 2.6 Greyscale IRAC 8 μm image of IRAS 19111+1048 (A16) and IRAS 19110+1045 (A12) with BLAST 500 μm contours superimposed. Contours are from 10 to 90% of map peak value 2153 MJy sr^{-1} in 10% steps.

Table 2.2 Coordinates of CORNISH sources in the BLAST Aquila field[a]

BLAST	CORNISH	RA (J2000) h m s	Dec (J2000) ° ′ ″
A12	A12−C0	19 13 19.063	+10 51 26.521
	A12−C1*	19 13 21.617	+10 50 56.756
	A12−C2	19 13 21.886	+10 50 49.704
	A12−C3	19 13 22.130	+10 50 52.163
	A12−C4	19 13 23.834	+10 51 42.624
...			

[a] Catalog is published in its entirety in the *Astrophysical Journal*.

* Detection S/N< 3.

Table 2.3 Spectral types and IR counterparts for the BLAST peaks A16 and A12 and the radio sources detected in the CORNISH data within $\sim 1'$ of the submm peaks[a]

Source	IR+submm[b] (ZAMS)	IR+submm[b] (Class V)	IR[c]	TFT1[d] (6 cm)	TFT2[d] (3.6 cm)
	$\log Q_0$[e] $[s^{-1}]$	4.8 GHz:ZAMS/Class V	IR[f]	3.6 cm[f]	GLIMPSE[g]
A16	O6−O5.5	O6−O4	O5	O6	O6
A16−C0	$46.86^{+0.01}_{-0.01}$	B0.5−B0/−			
A16−C1	$46.96^{+0.16}_{-0.26}$	B0.5−B0/−			
A16−C2	$46.97^{+0.01}_{-0.01}$	B0/−			
A16−C3	$47.36^{+0.00}_{-0.00}$	B0/−			
...					

[a] Table is published in its entirety in the *Astrophysical Journal*.

[b] ZAMS and Class V spectral types from Panagia (1973) and Martins et al. (2005) for $D = 7$ kpc. If the luminosity is not within the range of the calibration scale, no estimate (−) is provided.

[c] ZAMS spectral type derived by Kraemer et al. (2003) from the total source flux in the IR (*IRAS*) for $D = 6$ kpc.

[d] ZAMS spectral type of the counterpart of the brightest CORNISH source within BLAST clump in Testi et al. (1999) for $D = 7$ kpc.

[e] Total number of ionizing photons per unit time for a distance of 7 kpc and $T_e \sim 8000$ K, assuming optically thin emission.

[f] ZAMS spectral type derived by Kraemer et al. (2003) for $D = 6$ kpc. Values are given for sources lying closer than $5''$ to the CORNISH source.

[g] Closest IRAC GLIMPSE I Complete Catalog match within $\sim 5''$ of CORNISH peak.

to be forming the unresolved source observed by Vig et al. (2006, S14 in their sample). None have a radio ZAMS spectral type later than B0 (with the exception of A16−C18, which was not initially detected by our extraction routine).

We find that 22 of these radio sources lie within $\sim 0.5\,\mathrm{pc}$ of A16−C24. This object has a bolometric luminosity equivalent to an O6 ZAMS star, which is in good agreement with previous results for a distance of $\sim 6\,\mathrm{kpc}$ (e.g., Kraemer et al., 2003). The position of A16−C24 also agrees with the UCHiiR of WC89 and Testi et al. (1999). The two sources from the Two Micron All Sky Survey[3], detected by Vig et al. (2006) within their S14 source (IR4 and IR5), agree well with A16−C24 and A16−C26 and the two peaks (KJK1 and KJK2) detected by Kraemer et al. (2003). The G45.12SE peak from Zhu et al. (2008) traces the region of A16−C26; G45.12SW is formed by the conglomeration of radio sources towards A16−C13, and G45.12N is centered on the arc-shaped radio emission around A16−C21. The estimated spectral types of all radio sources within $\sim 1'$ of the BLAST coordinates have been included in Table 2.3 for an electron temperature similar to that estimated by Vig et al. (2006) ($\sim 8000\,\mathrm{K}$, for their source containing the cluster: S14).

Taking into account the $3\,\sigma$ positional error of our CORNISH source A16−C24 ($\sim 0.5''$) and that expected for the OH maser detection of Baart & Cohen (1985), ~ 10 milliarcsec, the separation of $\sim 3''$ between the two may be physically significant. Indeed, our projected separation of $\sim 0.1\,\mathrm{pc}$ positions the maser source at the edge of the UCHiiR, and agrees well with the displacement measured by Baart & Cohen (1985), of the order of $\sim 0.03\,\mathrm{pc}$ (with respect to the coordinates from Matthews et al., 1977). This distance, as pointed out by Baart & Cohen (1985), is well within the upper limit for the radius at which OH masers are produced in a shell-like front surrounding a high-mass young star. This suggests that these may be dense fragments of the expanding shell. The blueshift

[3]The Two Micron All Sky Survey (2MASS) is a joint project of the University of Massachusetts and the Infrared Processing and Analysis Center/California Institute of Technology, funded by the National Aeronautics and Space Administration and the National Science Foundation.

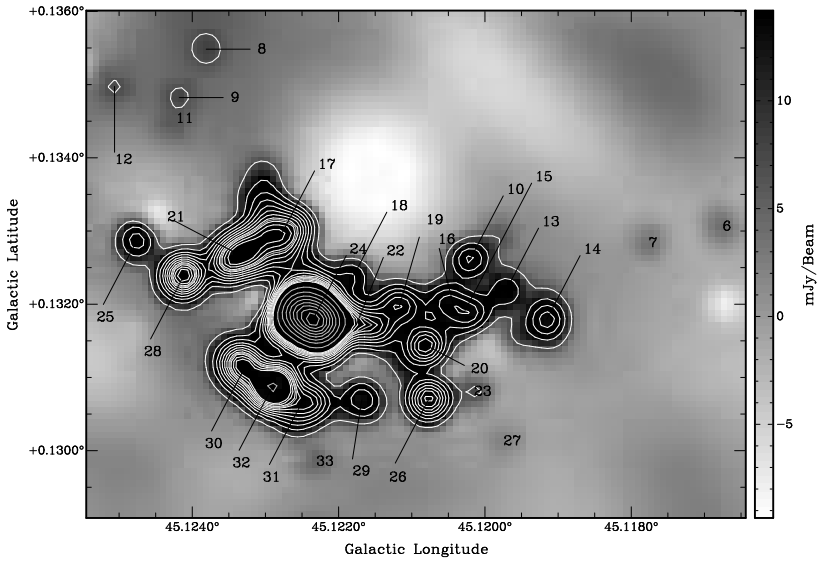

Figure 2.7 Greyscale CORNISH 4.8 GHz image of central cluster (S14 in Vig et al., 2006) in IRAS 19111+1048 (A16) with numbered emission peaks (Table 2.3). White contours are from 2.5% to 12.5% of map peak value 0.7 Jy beam^{-1} in 1% steps. Grey contours are from 15% to 85% in 10% steps.

for the maser clusters detected by these same authors ($\sim 6\,\mathrm{km\,s^{-1}}$) is also similar to that observed for the dense gas traced with ammonia by Hofner et al. (1999), whose absorption peak coordinates are also offset from our radio peak in the same direction as the maser source. This supports the real physical origin of the observed displacement.

Although further investigation is required, our analysis of the CORNISH data and the evidence in the MIR and submm suggest that A16−C24 may be the initial trigger and power source of G45.12. The massive outflow detected by Hunter et al. (1997) appears to follow the overall direction of the distribution of CORNISH sources well, which could indicate that A16−C24 has induced the formation of its lower mass companions. In addition, the distribution of CORNISH sources appears to have a slightly curved, bow-shock like morphology pointing towards the submm comma-like structure extending downwards in Figure 2.8. This structure also coincides with the strongest emission in ^{13}CO and CS. Considering its central position, A16−C24 appears as a suitable candidate for the main triggering/compressing source.

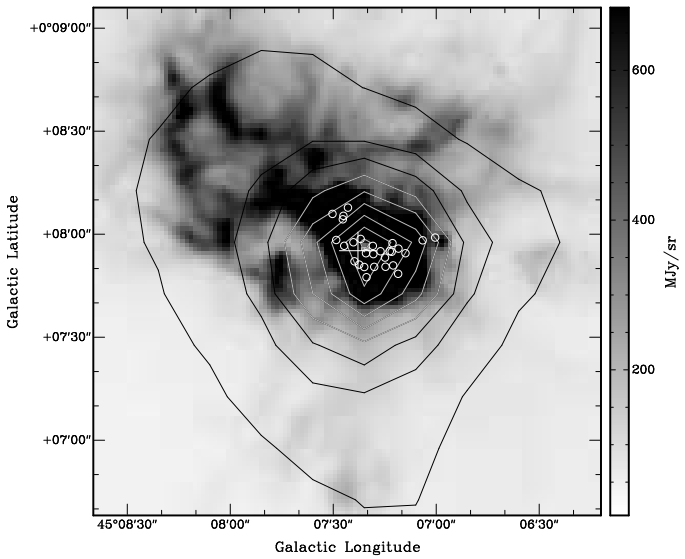

Figure 2.8 Greyscale IRAC 8 μm image of IRAS 19111+1048 (A16) with 250 μm BLAST contours overlaid. Cross marks the position of submm peak, and circles the positions of main CORNISH detections (central cluster). Contours are from 5% to 85% of the map peak value of 31500 MJy sr^{-1} in 10% steps.

G45.07

Just like its neighbor, IRAS 19110+1045 (A12; GRSMC 45.073+0.129 [G45.07]) also shows submm, IR, and radio structure signaling the presence of high-mass star formation, albeit significantly less pronounced than in G45.12. Only nine possible CORNISH detections are found within $\sim 1'$ of the BLAST position, with radio ZAMS/class V spectral types ranging between B0.5 and O9 for an electron temperature of 8000 K (Table 2.3). The lower number of stars and their later apparent radio spectral type is consistent with the more compact size of the resulting ionized region compared to G45.12.

Two CORNISH sources, A12−C2 and A12−C3 (Figure 2.9), match ($\lesssim 3''.5$) those detected by Vig et al. (2006) and the two embedded IR sources (KJK1, KJK3) from Kraemer et al. (2003). Despite the positional accuracy of our CORNISH measurements ($< 1''.5$ difference between our two coordinates and those given by Testi et al., 1999 and WC89), we find no indication of the third IR source (KJK2) detected by Kraemer et al.

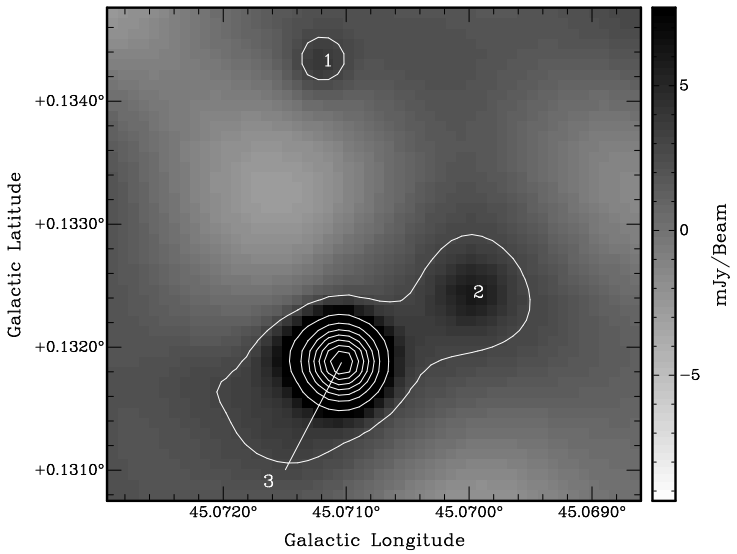

Figure 2.9 Greyscale CORNISH image of three central sources likely powering IRAS 19110+1045 (A12). Contours are from 2% to 9% of map peak value 0.7 Jy beam^{-1} in 1% steps.

(2003). This source is located $\sim 2''$ from A12−C3, and should have been identifiable at the resolution limit of the CORNISH data.

As with G45.12, G45.07 also contains a UCHiiR (spherical/unresolved UCHiiR; WC89) with a CO outflow (Hunter et al., 1997) and masers. Our brightest radio source lies at $< 1''.5$ from the coordinates given by WC89. The masers show a more significant displacement ($\sim 2''$), and appear to extend along the overall outflow direction. In addition to hydroxyl masers, G45.07 also shows several water maser sources (e.g., Hofner & Churchwell, 1996) and 6.7 GHz methanol emission (Pandian et al., 2007), with distances ranging between $\sim$ 1-3$''.5$ and $\sim 10''.5$ from our brightest CORNISH radio peak, respectively.

Most water masers align well with our radio source A12−C3 and the overall outflow direction. This, together with the clear separation from our radio peak, again supports the scenario where they are energized by the bipolar outflow (e.g., Hofner & Churchwell, 1996; De Buizer et al., 2005). The presence of these water masers also implies a less advanced evolutionary stage than that of its neighbor G45.12 (in agreement with previous

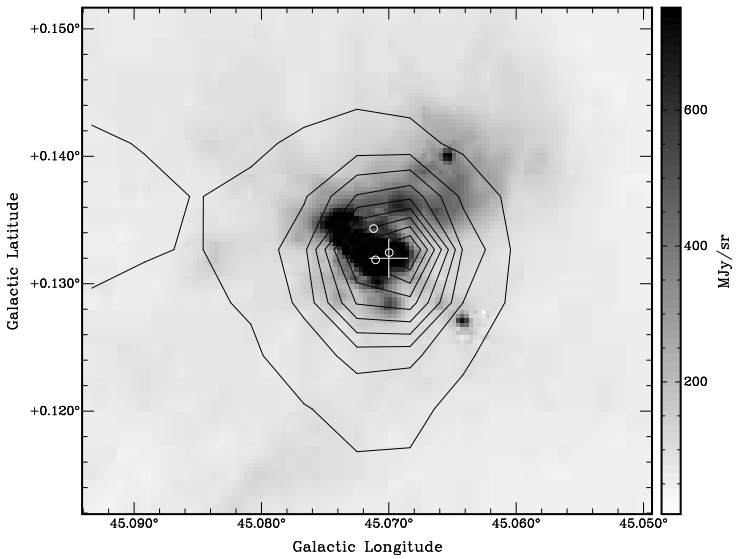

Figure 2.10 Greyscale IRAC 8 μm image of IRAS 19110+1045 (A12). Symbols and contours like Fig.2.8.

studies: e.g., Vig et al., 2006). This is supported by the simpler overall morphology, the lower stellar content, and the much earlier spectral type inferred from the IR/submm for A12−C3 and for the total clump with respect to those derived from the radio, suggesting a much more deeply embedded stage with significant radio optical depth.

While there appears to be extended MIR emission in the GLIMPSE images, consistent with the outflow orientation, there is also considerable emission in an almost orthogonal direction to its main axis (western upper right corner in Figure 2.10). The peak of the 21 cm radio continuum is displaced towards this region. The overall morphology appears to be similar to the extended H II in G45.12, albeit in a smaller scale, which could be due to its younger age and/or the lower stellar content in the innermost central region.

Submm Analysis

Our analysis of the SEDs yields total system masses for G45.12 and G45.07 of $\sim 3550\,M_\odot$ and $\sim 1400\,M_\odot$, respectively, for a distance of 7 kpc (Table 2.6). This differs from the estimates given by Hunter et al. (1997), who obtained (with temperature, dust emissivity index, and optical depth as free parameters) masses ~ 7 and ~ 4 times larger than our

Table 2.4 Spectral types and IR counterparts for the BLAST peaks A28, A29, A30, and A30a and the radio sources detected in the CORNISH data within $\sim 1'$ of the submm peaks[a]

Source	IR+submm (ZAMS)	IR+submm (Class V)	IR	TFT1 (6 cm)	TFT2 (3.6 cm)
	$\log Q_0$ $[s^{-1}]$	4.8 GHz:ZAMS/V	IR	3.6 cm	GLIMPSE
AA29	O6.5−O5.5	O7−O4.5			
A28			O5.5		O6.5[b]−O5.5[c]
Complex1	$49.25^{+0.00}_{-0.00}$	O5.5/O5			G045.4509+00.0570[d]
A28−C1	$47.35^{+0.04}_{-0.04}$	B0/−			
A28−C18	$46.79^{+0.15}_{-0.23}$	B0.5−B0/−			
...					

[a] Table is published in its entirety in the *Astrophysical Journal*.

[b] Compact source only, $\sim 6''$ in size, and therefore smaller than our aperture used for photometry.

[c] Compact source including the extended emission.

[d] The closest CORNISH counterpart to this source is C54 (Table 2.2).

estimated masses, respectively (when scaled to their distance of 8.3 kpc). Vig et al. (2006) obtained, through SED fitting and radiative transfer modeling (assuming a spherically symmetric homogeneous cloud of gas and dust and a distance of 6 kpc), masses of 5000 $M_\odot$ ($\sim$ 20 $M_\odot$ of dust, and a larger gas-to-dust ratio of 250) and 13,000 $M_\odot$ (for a dust mass of 30 $M_\odot$, and gas to dust ratio of 450) for G45.12 and G45.07, respectively. Scaling to the same distance, we obtain $M_{\rm d} \sim 26$ and $M_{\rm d} \sim 10.5\,M_\odot$. While our dust mass estimate for G45.12 is in good agreement with their estimate from the SCUBA maps, the mass for G45.07 is in better agreement with the mass these authors estimated from their 130 μm map (obtained with the TIFR 1-m balloon borne telescope; Ghosh et al., 1988), of $\sim 13\,M_\odot$.

We find temperatures for G45.12 and G45.07 of $\sim$ 40 K, and clump luminosities equivalent to an $\sim$O6 ZAMS spectral type star ($\sim$O5 Class V star). This is in good agreement with those estimated from the IR (e.g., Kraemer et al., 2003) for the brightest sources within the clumps. This suggests that A16−C24 and A12−C3 are the main sources responsible for the dust heating in G45.12 and G45.07, respectively. We note, however, that the significantly later spectral type derived from the radio for A12−C3 appears to suggest a much younger and highly embedded stage than A16−C24.

2.2.2 GRSMC G045.49+00.04

This cloud complex is dominated by the other two main submm peaks in the BLAST region, IRAS 19120+1103 (GRSMC 45.453+0.060; [G45.45]; a MYSO candidate in the Red MSX Survey (RMS); e.g., Mottram et al., 2010) and IRAS 19117+1107 (GRSMC 45.478+0.131; [G45.48]). Both sources show significant extended submm emission (Figure 2.11), and required additional Gaussians to model the emission local to the main submm peaks. At *IRAS* resolution the extended emission of both sources was not resolved, and so our BLAST flux densities were obtained with aperture photometry combining A28 with A29 (AA29; Figure 2.12, comprising G45.47+0.05 and G45.45) and A30 with A30a

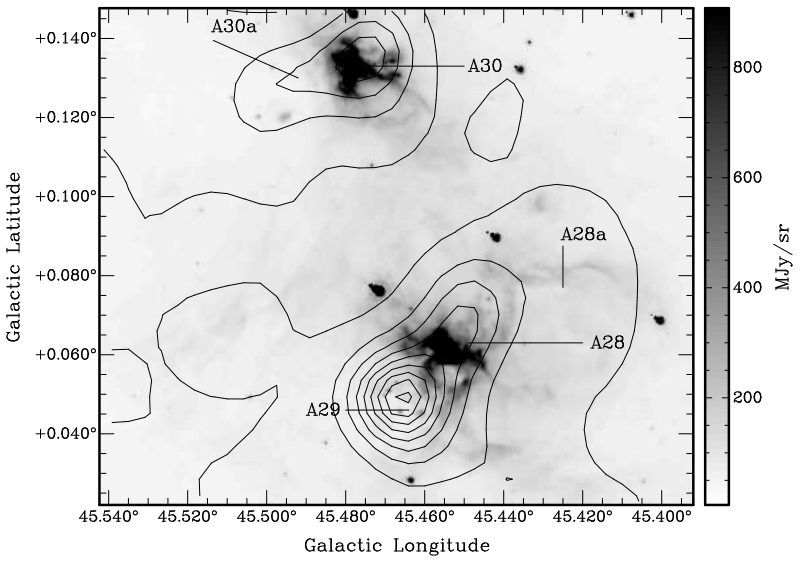

Figure 2.11 Greyscale IRAC 8 μm image of IRAS 19120+1103 and IRAS 19117+1107. Contours like Fig.2.6.

(AA30).

The presence of UCHIIRs was detected by WC89 and Testi et al. (1999) at 3.6 cm. Chan et al. (1996) classified AA29 as a MYSO. The activity and complexity of this region is particularly prominent in the IRAC images, as can be observed in Figures 2.11-2.13.

G45.47+0.05

A29 (G45.47+0.05) is the most prominent of all submm peaks in this complex, and yet lacks significant emission in the MIR (e.g., Figure 2.12; Figure 2.13). The submm peak is located in the neighborhood of 14 GR sources (five of which are associated with bright IR sources; Figure 2.12). All these sources are located within $\sim 30''$ of the BLAST peak. The appearance in the MIR may suggest that the submm emission is tracing a particularly dense part of the molecular clump. This material could be confining the expansion of the photodissociation region (PDR) as seen in IRAC, which also appears to be in a very young and embedded stage of star formation. Pillar-like structures seen in extinction and extending from A29 into G45.45 (Figure 2.12), and the main five IR detections embedded within the BLAST source (as suggested by their flux increasing

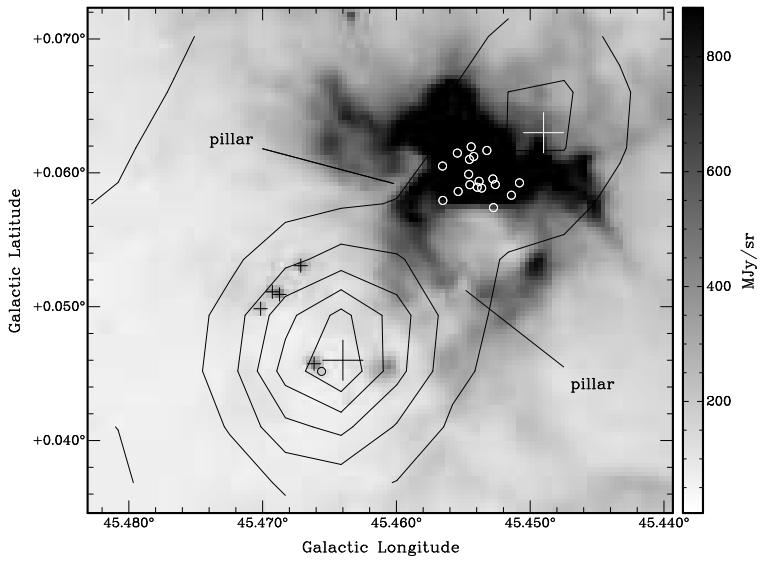

Figure 2.12 Greyscale IRAC 8 μm image of IRAS 19120+1103 (A28−A29) with 250 μm BLAST contours overlaid. Crosses mark the position of main GR sources. Contours are from 5% to 55% of the map peak value of 31500 MJy sr^{-1} in 10% steps. Other symbols like Fig.2.8.

with increasing wavelength) support this scenario.

The brightest CORNISH source in the neighborhood of the submm peak, A16−C0 (Figure 2.14), is a known UCHIIR (WC89, Testi et al., 1999 center agreement $< 1''$). The flux from our radio analysis is equivalent to an O9.5 radio ZAMS star at 7 kpc, which agrees with the spectral type we derived using the 6 cm flux from Urquhart et al. (2009). This source is also one of the most complex of the clump, and contains H_2O (e.g., Forster & Caswell, 1989), OH (e.g., Forster & Caswell, 1989; Argon et al., 2000) and methanol (e.g., Menten, 1991) masers. The most prominent OH sources are located closer ($< 0.5''$) to the radio peak than the methanol and H_2O masers ($\sim 1''$), and they all lie preferentially towards the northern (upper left direction; Figure 2.14) rim of the radio emission and towards the extended MIR region.

In the IRAC maps, the GR source (G045.4661+00.0457; G3 in Figure 2.14) is at the peak of the IR emission, at the opposite corner of the MIR elongation to the CORNISH source (at $\sim 3''$). Other GR sources are also present nearby the radio peak. Such

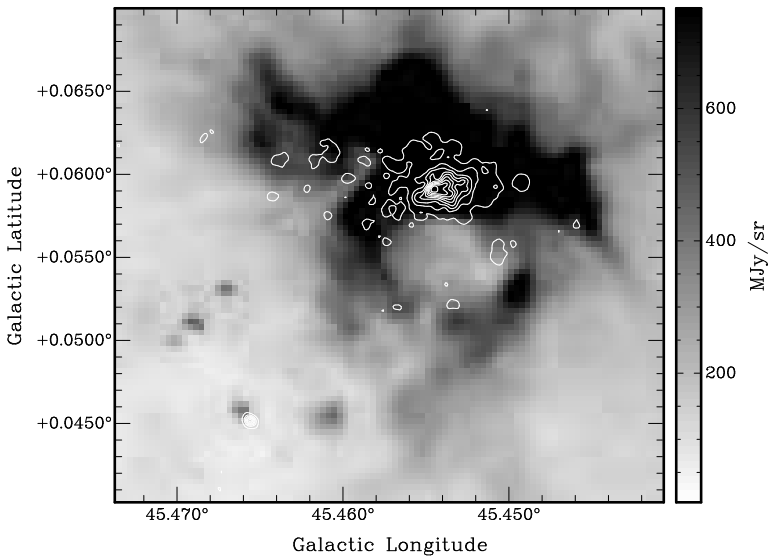

Figure 2.13 Greyscale IRAC 8 μm image of most central regions of A28 and A29 in Fig.2.12 with CORNISH contours. Contours are from 10% to 90% of map peak value of 0.07 Jy beam^{-1} in 10% steps.

astrometry differences between the radio and IR detections have been previously observed (De Buizer et al., 2005), which confirms this to be a true physical separation. The MIR elongation may be tracing the outflow morphology detected by Hunter et al. (1997) and the NH_3 emission (e.g., Hofner et al., 1999). Most maser sources are indeed located between the MIR peak (G3) and the radio peak, along the elongation, with a few OH masers located between the radio source and G2 (Figure 2.14). At the northern extreme edge of the elongation and closer to the main MIR peak there are more detections of methanol maser signatures (Kurtz et al., 2004), as well as SiO and NH_3 emission peaks ($\sim$10-15$''$ from the radio peak; Hofner et al., 1999). The presence of shocked gas along the northern MIR emission, the outflow, and the location of the UCHiiR opposite the main MIR peak may suggest the scenario where the outflow/jet originating at the UCHiiR interacts with its local environment, producing the observed structure in the MIR. An alternative interpretation claims this elongation may arise from accretion (De Buizer et al., 2005) or collapse (e.g., Cesaroni et al., 1992; Hofner et al., 1999) onto the UCHiiR. This could explain the emission and redshifted absorption observed in NH_3. More recent

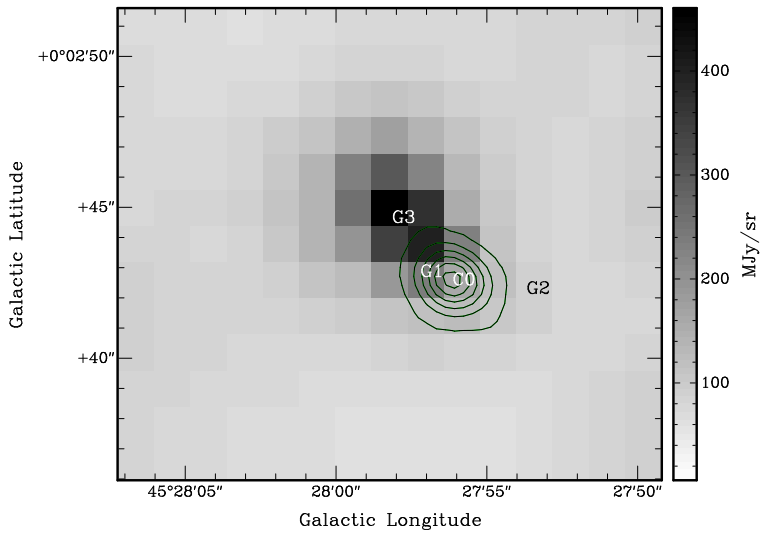

Figure 2.14 Greyscale IRAC 8 μm image of region around the main UCHIIR (A29−C0; C0 in the image) within A29 (Figure 2.12) with CORNISH contours superimposed. Contours are from 10% to 60% of map peak value of 0.07 Jy beam^{-1} in 10% steps. Figure shows closest IR counterparts retrieved from the GLIMPSE I complete catalog (GC), labeled as G1, G2 and G3.

studies have not confirmed the presence of infall signatures (e.g., Wilner et al., 1996; Klaassen & Wilson, 2007). Further analysis of the innermost regions is needed to solve this controversy.

The maser emission (especially methanol and H_2O) suggests that this source is one of the youngest in this complex. It has also been classified as an Extended Green Object (EGO) and a likely MYSO outflow candidate (Cyganowski et al., 2008). This supports the HCO analysis of Wilner et al. (1996), who suggested that this source is in the early stages of forming an OB star cluster.

G45.45

A28 is close to the most active region in the cloud as observed in the MIR (G45.45+0.06 [G45.45]), although from its position and extended morphology the submm emission may also be tracing the compressed and extended molecular gas. G45.45 (also a MYSO

candidate in the RMS Survey; e.g., Mottram et al., 2010) has been observed to lie in the border of a larger and fainter H II region $\sim 3'$ in size (G45L; Paron et al., 2009). Although this structure is also traced by the BLAST images, it has not been included in our photometry/radio analysis.

The IRAC images show a complex morphology, with the strongest emission in the MIR and 21 cm coincident with the main nebula-like radio structure observed in the CORNISH data (e.g., Figure 2.12; Figure 2.13). In Figure 2.13 the MIR emission appears to follow a horseshoe shape around a cavity-like structure (~ 1 pc in size at 7 kpc), within which no stars are detected in the IRAC images. Although this structure can be observed at 1.3 cm in the analysis of Mooney et al. (1995) at $\sim 12''$ resolution, the details and morphology of the dust in this region remain unresolved in our BLAST maps.

In the radio, the CORNISH data reveal a similarly complex substructure for G45.45 (Figure 2.15). There are 18 radio peaks detected within and surrounding the radio 'nebula', coincident with the brightest area in the GLIMPSE images. Within this extended radio emission, called 'The Orion nebula's younger brother' by Feldt et al. (1998), numerous emission peaks are noticeable. While we cannot easily distinguish or fit these peaks, we detect at least eight within an estimated size of 0.35×0.2 pc at 7 kpc (Figure 2.16). This supports previous studies that classify this source as a cluster of H II regions (e.g., Garay et al., 1993; Testi et al., 1999). Aperture photometry on the whole structure (including extended emission) yields a radio flux density comparable to that of an ∼O5.5 ZAMS spectral type (∼O5 class V) star, which is in agreement with previous estimates (e.g., Garay et al., 1993). Using the 6 cm flux from Urquhart et al. (2009) for a source major axis of $\sim 8''$, we obtain an estimate of ∼O6.5. This is comparable to the results we obtain using the flux estimates from Testi et al. (1999; Table 2.4).

Regarding the stellar content, Feldt et al. (1998) detected up to 14 near-infrared (NIR) sources (from *a*-*o*) possibly associated with this complex. They also detected additional MIR sources outside the main radio nebula (Figure 2.16). The roman numbers indicate

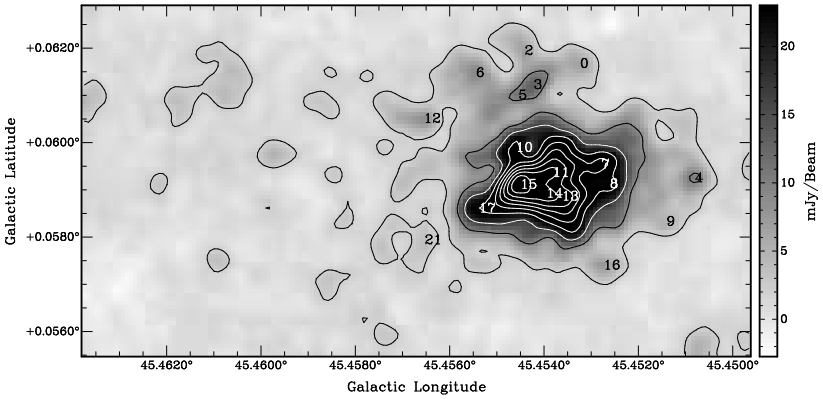

Figure 2.15 Detailed greyscale CORNISH image of central UCHiiR near A28 (part of IRAS 19120+1103; Fig.2.12; Fig.2.13), with numbered emission peaks (Table 2.2). Contours like Fig.2.13.

other point sources in their NIR images outside their VLA map. We confirm their observations that the majority of these objects lie on the sharp and distorted upper edge of the radio emission (Figure 2.16). This may support the scenario proposed by these authors where a central cluster of OB stars, deeply embedded within the radio complex, produces a front that has triggered further star formation. In their analysis, they claim that IR sources *l*, *m*, *n*, *o* (Figure 2.16) may be the source of the UCHiiR. Although these objects do lie close to two bright radio peaks within the cluster (A28−C13, A28−C11; Table 2.5), their source *b* is the closest to the brightest peak in the radio (A28−C15 in Figure 2.16). This CORNISH source lies at less than $\sim 1''$ from both the WC89 coordinates and source *b*.

At a resolution of $0''.4$, WC89 defined this source as a cometary UCHiiR. Indeed, two parallel extensions appear to emerge from the central source A28−C15. These structures form a tail-like morphology extending towards the right in Figure 2.16, within which A28−C13, A28−C14, and A28−C11 are detected. In total, we find that eight of these IR sources have CORNISH counterparts within $\sim 1''$. Sometimes one radio peak is found between several in the NIR (Table 2.5; Figure 2.16).

Blum & McGregor (2008) classified the main radio structure as a group of MYSOs

Table 2.5 4.8 GHz radio (CORNISH) sources with IR counterparts (Feldt et al., 1998) within 1″.

IR	Radio
b	A28−C15
d	A28−C10
f	A28−C11
l	A28−C11
m	A28−C11
n	A28−C11
o	A28−C13
MIR1	A28−C10

with late and early B stars surrounding the central source, probably similar to the central cluster powering G45.12 within A16. The offset between the NIR and radio peaks could be explained if the radio detections are dense clumps ionized by the surrounding high-mass stars (Feldt et al., 1998). Alternatively, we do not discard the possibility that the NIR stars may have been produced by the central and embedded star/cluster, whose expanding H II region could have triggered the formation of these sources by compression of the dense material traced in the submm. This last scenario is supported by the overall morphology in the CORNISH images; the observed emission supports A28−C15, the brightest radio source, as being responsible for the origin of *l*, *m*, *n*, *o*, rather than the latter sources being the actual 'ground zero' for the triggering mechanism (as suggested by Feldt et al., 1998). Further investigation at high resolution is required to corroborate the triggering hypothesis and to fully distinguish between the different cases.

The candidate counterpart to MIR1 (A28−C10) is clearly visible in the CORNISH data, albeit relatively weak compared to the most central sources. This weak emission is in contrast with the strong IR luminosity of this source. In combination with the nearby

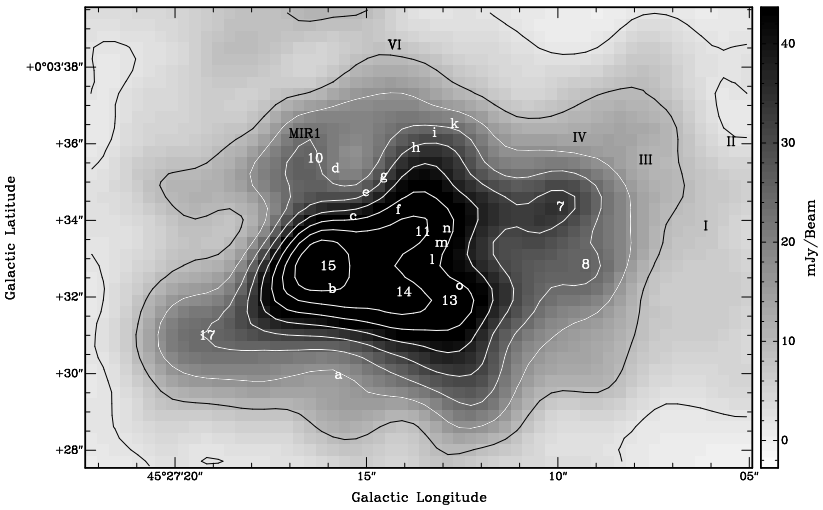

Figure 2.16 More detailed greyscale CORNISH image of innermost regions of the central UCHiiR in Fig.2.15 with numbered emission peaks (Table 2.2). Letters are NIR detections from Feldt et al. (1998) falling within VLA map (Table 2.5). Roman numbers are other NIR detections (Feldt et al., 1998). Contours like Fig.2.13.

OH maser (Argon et al., 2000), this may again suggest that at least some structures are actual stars still embedded within their natal cocoons (e.g., Kraemer et al., 2003).

The remaining possible radio detections within $\sim 1'$ and not lying within the main complex have been included in Table 2.4. Due to the complexity of the radio structures around this complex, we do not discard the presence of additional sources in this region (e.g., Figure 2.15).

G45.48

AA30 (G45.48; north of AA29 in Figure 2.11) also shows complex structure in the submm and IR. Our two submm peaks lie at opposite sides of the main emission visible in the IRAC images. As in previous cases, they may be tracing relatively cold, dense gas that is confining the expansion of the H II region.

WC89 classified this UCHiiR as irregular, but suggested that the elongated form could be due to an imaging artifact. Testi et al. (1999) identified no compact sources,

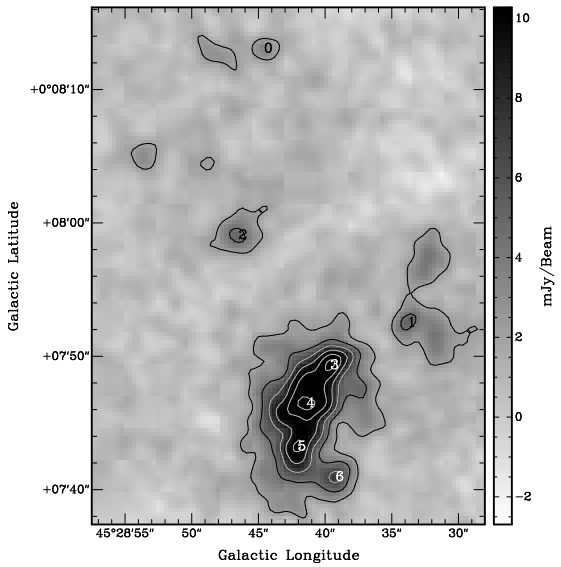

Figure 2.17 Greyscale CORNISH image of elongated (and brightest) radio emission in A30−A30a (IRAS 19117+1107; Complex 2 in Table 2.4); with numbered emission peaks (Table 2.2). Contours are from 10% to 25% of map peak value of 0.07 Jy beam^{-1} in 3% steps.

only extended emission. The elongation of this source, as well as several embedded peaks, are evident at 4.8 GHz (Figure 2.17), and the structure is identified in the MIR images as the equatorial ridge of the bipolar-like MIR structure (Figure 2.18).

Just like in G45.45, the MIR and main radio emission appear to wrap around a cavity-shaped structure, within which no IRAC sources are visible. The BLAST emission includes this 'cavity', but any such structure would be unresolved in our images. The adjacent radio/IR ridge could be compatible with illumination from the south, although the main source powering the region could in fact be located more towards the north, closer to source A30−C0 (Figure 2.18), the northern radio source detected by Garay et al. (1993), and the diffuse emission in the IR (KJK1) of Kraemer et al. (2003). Only one GC was found within $\sim 5''$ of A30−C0 (G045.4790+00.1365). KJK1 does appear to be coincident with an IRAC emission peak, even though there is no counterpart in the GLIMPSE I catalogs. The irregular radio structures, and the lack of a significant radio

counterpart for KJK1, could imply the presence of an embedded star/cluster around this position, which also coincides with an opacity peak and is estimated to be much colder than the southern counterpart (Kraemer et al., 2003).

The multi-peaked radio morphology of the elongated radio structure (coincident with the southernmost source detected by Garay et al., 1993 and the IR source KJK2 from Kraemer et al., 2003) clearly indicates the presence of embedded sources. Our Gaussian routine detects at least four main peaks in a filamentary structure about $\sim 0.2\,\mathrm{pc}$ in length (Figure 2.17). Aperture photometry on the entire filament yields a total radio flux equivalent to an O7.5 radio ZAMS (O8 class V) star. This is significantly later than the IR estimate (Table 2.4), perhaps an indication of self-absorption and a young embedded stage of evolution, despite our earlier spectral type estimate obtained using the 3.6 cm flux from Testi et al. (1999). This structure is also coincident with methanol masers (Menten, 1991), recognized as a signature of highly embedded stages of high-mass star formation. In addition, we observe (weaker) non-Gaussian, filamentary structures to the right of the main structure in Figure 2.17, also likely associated with methanol emission. A prominent cluster of methanol, OH and water masers has been detected about $\sim 15 - 20''$ southwest from A30−C0 and A30−C1. The presence of a GC/GR counterpart (G045.4725+00.1335) for this source and the lack of an equivalent CORNISH detection again argues in favor of the young stage of the stellar population in this region.

BLAST A35 and A36

Away from the main complex, A35 and A36 (Figure 2.19) also show some signatures of stellar activity, as suggested by their morphology.

Although our BLAST peaks generally overlap well with the emission observed in IRAC, *IRAS* 100 μm shows poor correlation. Only at 60 μm do we observe a reasonable match with A36, the only one of these two sources with a PSC *IRAS* match within $\sim 30''$. This IR source, IRAS 19124+1106, was estimated to be at a distance of 6.5 kpc, and has

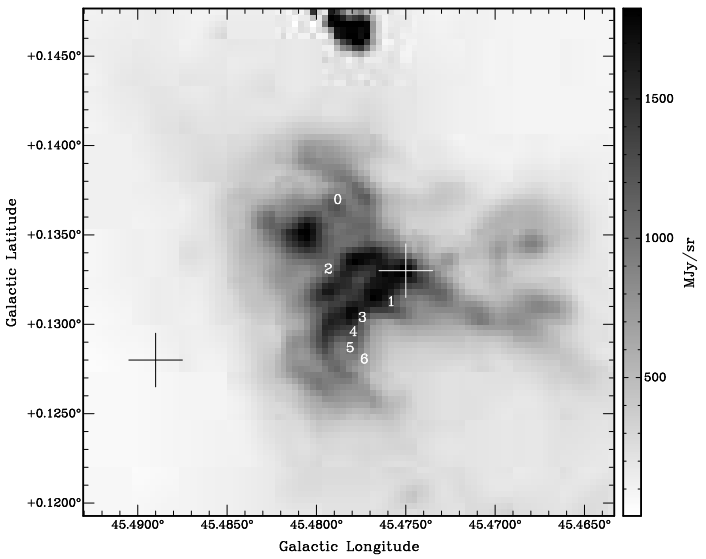

Figure 2.18 Greyscale IRAC 8 μm image of the H II region within IRAS 19117+1107. Numbers as in Fig.2.17. Crosses mark the position of submm peaks A30 and A30a.

been suggested to be one of the impact sites of the jets emanating from the microquasar and superluminal source GRS 1915+105 (Kaiser et al., 2004). The other impact site was identified as our BLAST source A19, a candidate MYSO from the RMS Survey (Mottram et al., 2010). GRS 1915+105 is believed to be a binary system consisting of an early-type K giant, accreting via a Roche lobe overflow onto a black hole (e.g., Greiner, 2001). The MIR structure of A36, if associated with this *IRAS* source, does not resemble what one would expect to see if caused by a jet originating at the position of GRS 1915+105. Furthermore, the new distance estimate for GRS 1915+105 of 11 kpc (Zdziarski et al., 2005) is now much larger than the kinematic distance to this IR/submm emission.

Our analysis of the CORNISH images reveals that, with the exception of some weak structures near the emission peak of A36 (likely tracing the ionized region as observed in the VGPS 21 cm maps), there are no major radio sources near these objects. This may suggest very early or very late/isolated low mass star forming activity.

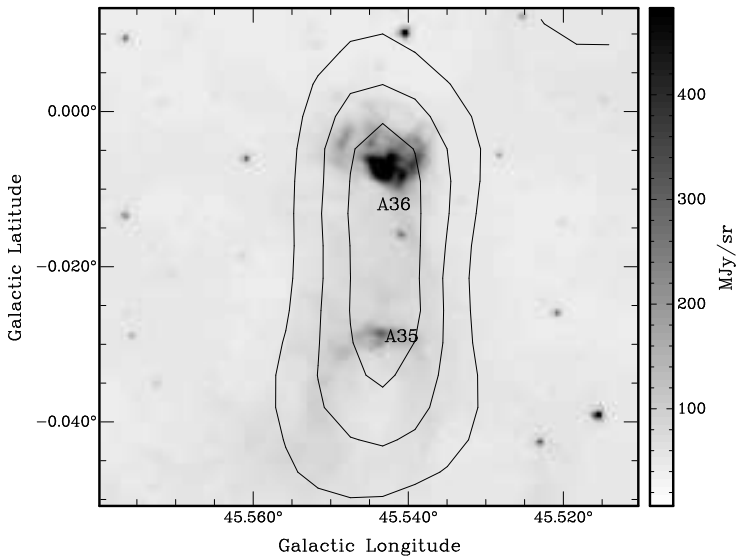

Figure 2.19 Greyscale IRAC 8 μm image showing cometary shape of A35+A36 with BLAST 500 μm contours superimposed. Contours are from 8% to 12% of map peak value of 2153 MJy sr^{-1} in 2% steps.

Submm Analysis

Estimated BLAST parameters for the main objects in this complex have been included in Table 2.6. The temperatures are warm, characteristic of active star forming clumps with ongoing stellar activity. The total mass of AA29 is $\sim$ 4800 $M_\odot$ for a temperature of $\sim$ 35 K, which contrasts with the mass estimate of 26000 $M_\odot$ obtained by Mooney et al. (1995) for a distance of 8.1 kpc and a much lower fixed dust temperature of 20 K. Scaling to this distance we obtain a total mass of $\sim$ 6300 $M_\odot$, and $\sim$ 34000 $M_\odot$ for a fixed temperature of 20 K and free β (best fit $\beta = 2.2$). This shows the importance of actually determining the temperature using the BLAST observations.

Our estimated IR+submm single-star spectral type for AA29 of $\sim$O5.5 is in excellent agreement with the radio spectral type of the radio nebula within G45.45 (Complex 1 in Table 2.4), the most luminous system within the BLAST emission formed by A28 and A29 (AA29).

The IR+submm spectral type of A30+A30a is in agreement with the IR spectral

type estimate of Complex 2 (the elongated radio emission; Table 2.4), but the CORNISH radio spectral type of this substructure is considerably later.

Although the radio flux estimates from Testi et al. (1999) at 3.6 cm and the uncertainties in the SED bolometric luminosities could be compatible with a relatively optically thin state for this source, the CORNISH measurements suggest a more embedded (and younger) stage for AA30 than for AA29. Just like the clumps within GRSMC G045.14+00.14, the BLAST sources in GRSMC G045.49+00.04 appear to be powered by the central OB young stellar clusters, which could also be responsible for the additional star formation detected within their parent clumps.

2.2.3 GRSMC G045.74−00.26 and GRSMC G045.89−00.36

This complex is dominated by three main (sub)mm sources (Figure 2.20) within an extended and largely filamentary molecular region.

BLAST A50

In the submm, A50 (IRAS 19145+1116) is largely structureless and symmetric, possibly with some weak emission surrounding the central peak. In the MIR, this H II region reveals a clumpy structure and numerous MIR peaks clustered within the main submm emission. There are seven GC sources found at less than $\sim 20''$ from our BLAST peak. Among the closest of these we find a string of three sources, G045.9352−00.4017 (the central one), G045.9362−00.4017 (the brightest), and G045.9344−00.4016, which constitute the most prominent structure in the GLIMPSE images.

Overall, the extended structure in the MIR and at 21 cm is rather circular, although emission arcs are visible within the region in the MIR. We detect only one weak 4.8 GHz source, found at less than $\sim 3''$ from the GLIMPSE source G045.9344-00.4016, with a flux corresponding to a B0.5−B0 ZAMS star. The IRAS clump was reported to satisfy the color criteria of WC89 for UCHIIRs (e.g., Bronfman et al., 1996), and was reported

by Codella et al. (1995) to be possibly associated with water masers. This would argue against the more evolved state of the system indicated by its 'disturbed' morphology, although from the coordinates provided by these authors we suspect that this maser emission could also be associated with a later generation of star formation within an older clump. The lack of a CORNISH or IR counterpart for this maser may also be indicating that the structure is due to a low mass star.

BLAST A46

While relatively structureless in the submm, the GLIMPSE images of A46 (IRAS 19141+1110) show a bow-shock cometary like structure, with the front oriented towards the south (lower right of Figure 2.20). Some possibly associated sources towards the south and southeast of the main structure are also detected. Despite the presence of numerous GC/GR sources, the bow-shock itself may be produced by a highly embedded source, closest to G045.8062-00.3518 (Figure 2.20).

Even though A46 also has *IRAS*, *MSX*, and IRAC counterparts, there appears to be negligible 21 cm emission and no NVSS (NRAO VLA Sky Survey), 4.8 GHz emission, H_2O or OH masers, or any other tracers that may be indicative of ongoing star formation. An exception is the methanol maser emission $\sim 25''$ eastwards (lower left) from the BLAST peak detected by Pandian et al. (2007). This is the $5_1 - 6_0$ A^+ line of methanol at 6.7 GHz, the strongest of Class II methanol masers, seen exclusively near high-mass stars. The authors suggest a very early stage of evolution, in which methanol activity has just turned on, before the onset of additional signs of star formation. Class II maser sources are radiatively pumped but are believed to be quenched by the formation of an UCHiiR, which is consistent with the absence of 4.8 GHz CORNISH sources and the 'young' age of the system (e.g., Minier et al., 2005; Ellingsen et al., 2007). This scenario would also be in agreement with Cyganowski et al. (2008), who classified this source as a 'possible' MYSO. The observed IRAC structures and methanol emission are all within

Table 2.6 Masses and temperatures of the main BLAST sources at $\sim 7\,\mathrm{kpc}$.

Source	T (K)	M_c ($10^2\,\mathrm{M}_\odot$)	L_bol ($10^3\,\mathrm{L}_\odot$)	Single-star Spectral Type
A12	42.5 ± 0.5	14.2 ± 1.0	282.8 ± 0.6	O6[a]/O5[b]
A16	39.9 ± 4.6	35.4 ± 8.0	340.9 ± 131.7	O6−O5.5/O6−O4
A22[c]	16.2 ± 4.6	65.7 ± 47.6	7.5 ± 6.6	<B0.5/−
A28−A29	36.7 ± 4.8	47.8 ± 10.3	262.3 ± 121.6	Combined due to *IRAS* unresolved (and saturated) emission O6.5−O5.5/O7−O4.5
A30−A30a	27.4 ± 5.8	33.4 ± 9.1	89.1 ± 67.2	Combined due to *IRAS* unresolved (and saturated) emission B0−O6.5/<O6.5
A35	33.9 ± 10.9	4.3 ± 1.5	62.0 ± 144.9	∼O8/∼O9
A36	41.6 ± 1.4	1.7 ± 0.3	30.1 ± 0.4	B0/−
A46	32.5 ± 1.6	4.5 ± 0.7	19.1 ± 2.7	B0.5−B0/−
A47	37.9 ± 2.5	7.9 ± 1.3	76.0 ± 14.7	O8−O7.5/O9−O8
A50	35.0 ± 2.0	6.9 ± 1.2	43.6 ± 6.6	O9.5−O8.5/<O9.5

[a] Spectral type from L_bol for a ZAMS star (Panagia, 1973).

[b] Spectral type from L_bol for a luminosity class V star (Martins et al., 2005).

[c] No PSC counterpart within $30''$. No BOLOCAM data available. Possibly associated (visually) with an *IRAS* source, but this source covers nearby BLAST sources as well and is therefore ignored in the fits. The rising SED in the submm and the lack of data at shorter wavelengths result in large error ranges.

the prominent BLAST submm emission, which also suggests the presence of local high density molecular material.

BLAST A47

A47 (IRAS 19139+1113) is a prominent MYSO (e.g., Chan et al., 1996) showing clear signatures of active star formation. A prominent carved structure (~ 2 pc in size at 7 kpc) is observed towards the north (Figure 2.20). This H II region is the most extended feature of this cloud, and is detectable in the IR, submm, millimeter (mm), and 21 cm images. The submm and radio peaks appear to trace a region of diffuse emission within this structure, close to three bright IRAC sources (G045.8263−00.2820, G045.8212−00.2846, and G045.8291−00.2858). The location of these IR objects, close to the center of curvature of some of the ionization fronts forming the edge of the ionized region in the molecular cloud, suggests that the combined contribution from these objects results in the sinusoidal boundary of the overall region.

We find three likely sources at 4.8 GHz within $\sim 1'$ of our BLAST source, all with GC counterparts within $\sim 5''$, and indicative of ongoing high-mass star formation. The extended morphology and the advanced state of stellar activity within the main H II would support the 'older' age suggested by the lack of maser emission (e.g., van der Walt et al., 1995; Szymczak et al., 2000).

Radio and Submm Analysis

From their measured fluxes, we estimate ZAMS spectral types for the radio peaks in these clumps of later than ∼B0 stars. Our SED fits show that, overall, none of the host clumps have an equivalent single-star ZAMS spectral type earlier than an ∼O8 star. In the case of A47, it is possible that additional sources are contributing to the total luminosity, in addition to those traced in the radio.

The detection of 4.8 GHz emission confirms previous studies that classified A47 and A50 as UCHIIRs from the WC89 color criteria (Bronfman et al., 1996). Although the radio peaks are not coincident with the brightest IRAC sources, they clearly indicate that high-mass stars are indeed being formed in this cloud, albeit at a lower level than

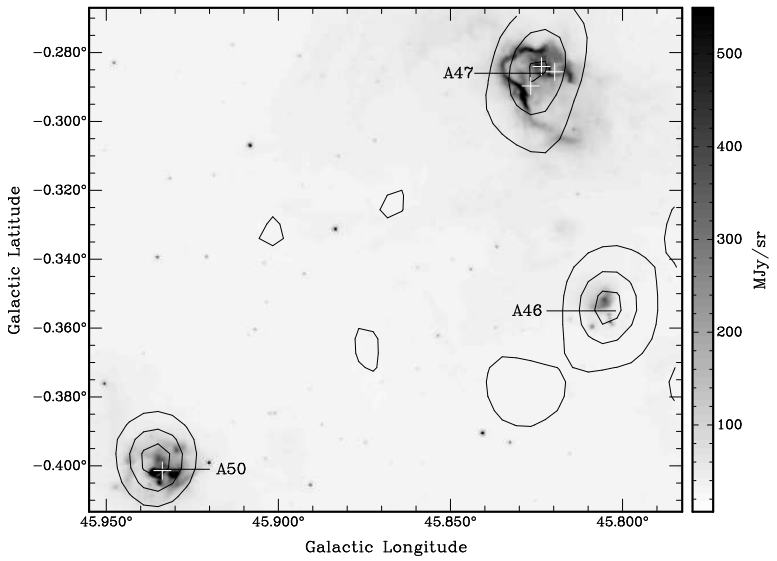

Figure 2.20 Greyscale IRAC 8 μm image of IRAS 19141+1110 (A46), IRAS 19139+1113 (A47), and IRAS 19145+1116 (A50), with BLAST 500 μm contours superimposed. Contours are from 10% to 20% of map peak value of 2153 MJy sr^{-1} in 5% steps. White crosses are CORNISH detections.

that observed in the two main clouds described above.

2.3 Aquila in Perspective: The Star Forming Activity in the BLAST 6 deg^2 Map

2.3.1 The Submm Population and Structural Properties of the Aquila Field

This region of Aquila consists principally of three main active complexes at ∼7 kpc (G045.49+00.04, G045.14+00.14, and the neighboring region of G045.74−00.26 and G045.89−00.36), as well as a quiescent cloud (GRSMC 45.60+0.30) at 1.8 kpc (e.g., Simon et al., 2001). There also exists (at various distances) additional dispersed (clump) star forming activity throughout the field, two cataloged (and two candidate) supernova remnants (Green, 2009), and a microquasar (GRS 1915+105).

In the present work we have used our BLAST submm data to identify and characterize the global parameters of the clumps at $\sim 7 \pm 0.5$ kpc, in which the molecular emission (and star formation activity) is the strongest. These clumps have been further characterized in the MIR and the radio with IRAC GLIMPSE and 21 cm continuum maps. The stellar content as well as the molecular structure have been investigated with CORNISH interferometry data and GRS ^{13}CO/CS emission.

At $\sim 60 \pm 10$ km s^{-1} the ^{13}CO maps reveal a dispersed and filamentary molecular structure covering the size of the BLAST map. Two of the main complexes are located at the central 'knots' of an overall heart-shaped like morphology (Figure 2.2). From the catalog of Rathborne et al. (2009) and Roman-Duval et al. (2009) only five clouds are at a distance of $\sim 7 \pm 0.7$ kpc (six including G045.14+00.14), but these contain the brightest objects in the field.

The submm emission follows the molecular emission well (Figure 2.2). Clumps with typical star forming characteristics ($T \sim 30 - 35$ K for $\beta = 1.5$) are associated mainly with the three main complexes. Outside of the central regions the star forming activity as traced in the submm is less organized, although still following the overall contours of the molecular emission. More 'isolated' clumps with *IRAS* counterparts (not all part of our final 7 kpc sample) show typical star-forming clump temperatures of ~ 30 K and disturbed environments, with their stellar content generally resolved, and in an apparently less embedded stage of evolution.

Relatively cold structures in Aquila (T< 20 K for $\beta = 1.5$ as measured in this analysis) have counterparts in major IRDC surveys. Simon et al. (2006) detected 20 IRDC candidates in absorption with *MSX*, and Peretto & Fuller (2009) found 79 candidates using *Spitzer* data. We have checked for IRDC matches within 30″ of our submm peaks in the entire field and found seven examples, all from the sample of Peretto & Fuller (2009). We note that several IRDCs, although not located within 30″ of our submm peaks, are frequently clustered in their immediate neighborhood; these may have not

been resolved in our data, or they may be confused by deconvolution structures. One prominent example of this is G045.49+00.04. Several IRDCs are observed in the local regions surrounding the brightest *IRAS* source formed by A28 and A29, especially towards A29. The intricate structures observed in the IRAC images, such as the pillar-like structures coincident with this BLAST source and the 'cavity', will require submm data with higher resolution and sensitivity in order to be properly characterized. We find a similar situation for the submm complex labeled in Figure 2.2 as G046.34−00.21, where the majority of the submm sources are identified as dark features in the IRAC maps. Many of these objects appear to be part of globular-like structures 'blown' by the stellar activity located to the northeast. The characteristics of these and similar sources outside the distance range chosen for the present work (which focuses on the most prominent and active clumps of the field) will be investigated in detail with the new *Herschel* data from Hi-Gal.

Although a more in depth study is required to confirm our results, the distribution and characteristics of the population within the main clumps suggest that triggering mechanisms (new star formation induced/initiated by external agents; e.g., Elmegreen, 1992) are likely taking place in the region. Our multiwavelength (MIR-radio) analysis is compatible with induced activity from the innermost region to the farthest (parsec) extent of the parent clump.

2.3.2 Evolution and High-Mass Star Formation in Aquila

Within G045.14+00.14, our analysis in the IR, submm, and radio, the molecular data, and the maser and stellar activity all support the scenario where A16 is in a more evolved stage of evolution than its neighbor A12. Figure 2.21 shows the measured bolometric luminosity for our BLAST sources relative to the combined total number of ionizing photons per unit time for all CORNISH sources possibly associated with each submm source. The apparent underionizing state of A12 suggests optically thick radio emission,

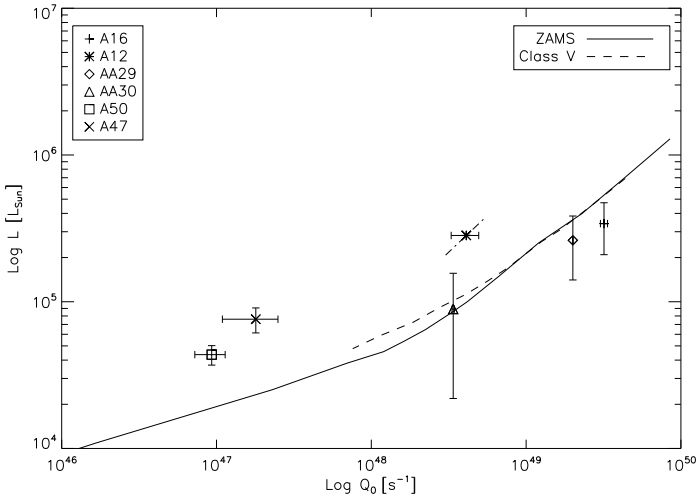

Figure 2.21 Comparison of L_{bol} (Table 2.6) and total Q_0 for BLAST sources with analyzed CORNISH sources (Tables 2.3 & 2.4). Results are compared with theoretical curves for ZAMS (Panagia, 1973) and Class V (Martins et al., 2005) stars. Example of expected effect of increasing (decreasing) the distance by 1 kpc shown by diagonal line of source A12.

and therefore a highly embedded stage of the central sources.

A28 likely contains the 'older' stellar activity of the observed clumps, while A29 and A30 appear to have characteristics of a relatively 'younger' population. The later spectral type obtained from the CORNISH data for the main complex in A30 (the filamentary structure) relative to its estimate from the IR would support the embedded stage of the main star forming activity in this region. Although our total luminosity measurement (and the radio estimates from Testi et al., 1999) are consistent with the theoretical curve in Figure 2.21, the large error range in luminosity for AA30 relative to the uncertainty in Q_0 could still support this conclusion.

Despite the apparent agreement of AA29 (A28+A29) with the theoretical models in Figure 2.21, the more compact radio emission of A29 and the weak MIR emission (compared to the prominent submm peak) would argue that A29 is the youngest active part of the entire cloud. Paron et al. (2009) suggested that G45.45 itself could have

been triggered by three possible O-type stars ionizing the extended H II region G45L. Although not analyzed in the present work, this is also a possibility for the original site ('first generation') of the activity within the BLAST clump.

A35 and A36 also have SED parameters consistent with on-going stellar activity, but lack obvious 4.8 GHz detections. Neither of these two sources show maser emission in the catalogs used in this work, and both have weaker ^{13}CO and CS antenna temperature. These sources may thus be in a relatively young and still embedded stage, or the star forming activity may be low and/or without significant high-mass star formation.

Of the three main submm peaks in the complex formed by G045.74−00.26 and G045.89−00.36, A50 has the strongest molecular emission. It is also possibly associated water masers, and has a relatively symmetric IR, submm and radio configuration. This source appears to have at least one possibly associated 4.8 GHz source, which would agree with previous studies that classified this source as an UCHiiR from the color criteria of WC89.

A46 shows the weakest molecular and radio emission, and no CORNISH counterparts or prominent signatures of star forming activity. However, the presence of methanol emission and the possible association with an EGO suggest that this clump is in a very early and deeply embedded stage of high-mass star formation.

A47 shows not only more extended emission at all wavelengths, but it also appears to contain a few associated CORNISH sources within the main H II region. The lack of any obvious maser emission, its morphology, the high dust temperatures, and weak molecular emission indicate that this clump has the most evolved stellar activity of the entire complex. The weak ^{13}CO and CS antenna temperatures for this source could also be explained by the more evolved stage of the system.

From the results in Figure 2.21, both A47 and A50 appear to be underionizing for their luminosity. This could be an indication that the total luminosity has significant contribution from several 'cooler' stars. However, the presence of water masers and CORNISH

detections may still suggest that unaccounted very optically thick radio emission, from a new embedded generation of star formation in these clumps, could also be a possibility.

2.4 Conclusion

By means of the submillimeter maps provided by BLAST at 250, 350, and 500 μm, together with IRAC imaging, 21 cm continuum emission, 4.8 GHz CORNISH radio interferometry data, and GRS FCRAO ^{13}CO/CS molecular datacubes, we have characterized the main clump population in the region of Aquila.

Our SED fitting of the most prominent star-forming sources at a distance of ~ 7 kpc has revealed clumps with temperatures ranging between $T \sim 35$ K and 40 K (for $\beta = 1.5$). Their total bolometric luminosities have equivalent single-star ZAMS spectral types earlier than ∼B0 stars.

The 4.8 GHz interferometry maps have been used to investigate the UCHIIRs within the submm clumps. The ZAMS spectral types estimated from the CORNISH data are overall in good agreement with previous results. The 'later' types obtained for some sources relative to their IR estimates support our BLAST and maser/outflow analysis, which suggest that highly embedded young OB stellar clusters are powering the most active clumps in the region.

On-going high-mass star formation is most prominent in G045.49+00.04 and G045.14+00.14 (containing our BLAST sources A12, A16, and A28, A29, A30, respectively). We confirm the presence of an OB stellar cluster deep within IRAS 19111+1048 (A16), containing a bright ∼O6 star surrounded by numerous late O and early B stars. This is in contrast with the scarcer maser and 4.8 GHz emission towards the complex formed by G045.74−00.26 and G045.89−00.36, in the field containing A46, A47, and A50. Despite the 'disturbed' environments observed in the MIR, the evolutionary stage of the three main clumps in this complex appear to range from quite evolved (with extended and bright rimmed

H II regions and a prominent IR stellar population), to the earliest stages of high-mass star formation detected so far in this field (A46, prior to the onset of significant maser emission and UCHIIRs). The parameters derived from these SEDs are typical of active clumps and are indeed suggestive of high-mass star formation, although at a lower level to that observed in the previous two clouds.

The enhanced datasets provided by *Herschel* (Hi-GAL) and SCUBA-2 at JCMT (JCMT Galactic Plane Survey; Moore et al., 2005) are crucial to fully characterize and complete the census of the clump population in this field, especially the fainter and the coldest structures. In addition, the higher resolution of these instruments will help to probe down to core scales and to investigate the dusty structures within the clumps, which appear to be channeling the stellar activity and shaping the ionized regions in the neighborhood of the embedded OB stellar clusters.

Chapter 3

The W3 GMC: Young Stellar Content

3.1 Photometry, Data Processing and Datasets

3.1.1 *Spitzer* IRAC and MIPS Infrared Observations

The main active regions of W3 were observed by *Spitzer* under two main Program Identification Number (PID) programs. The northern parts of the HDL comprising W3 Main and W3 (OH), shown in Figures 3.1 and 3.2, were first observed in 2004 under program P00127; AFGL 333 and the central/western region of W3 (including KR 140 and the active region to its north: 'KR 140-N') were subsequently observed in 2007 (program P30955). A preliminary analysis of the data obtained during the first observation has been presented in Ruch et al. (2007), while Polychroni et al. (2010) combined data from both programs for their analysis of the stellar population associated with SCUBA cores (Moore et al., 2007). For this work we also used data from both programs.

For the reduction process we downloaded the IRAC and MIPS 24 μm corrected Basic Calibrated Data (cBCD) from the *Spitzer* Archive. The IRAC cBCDs were produced with the S18.7.0 pipeline. P00127 and P30955 MIPS data were processed with the

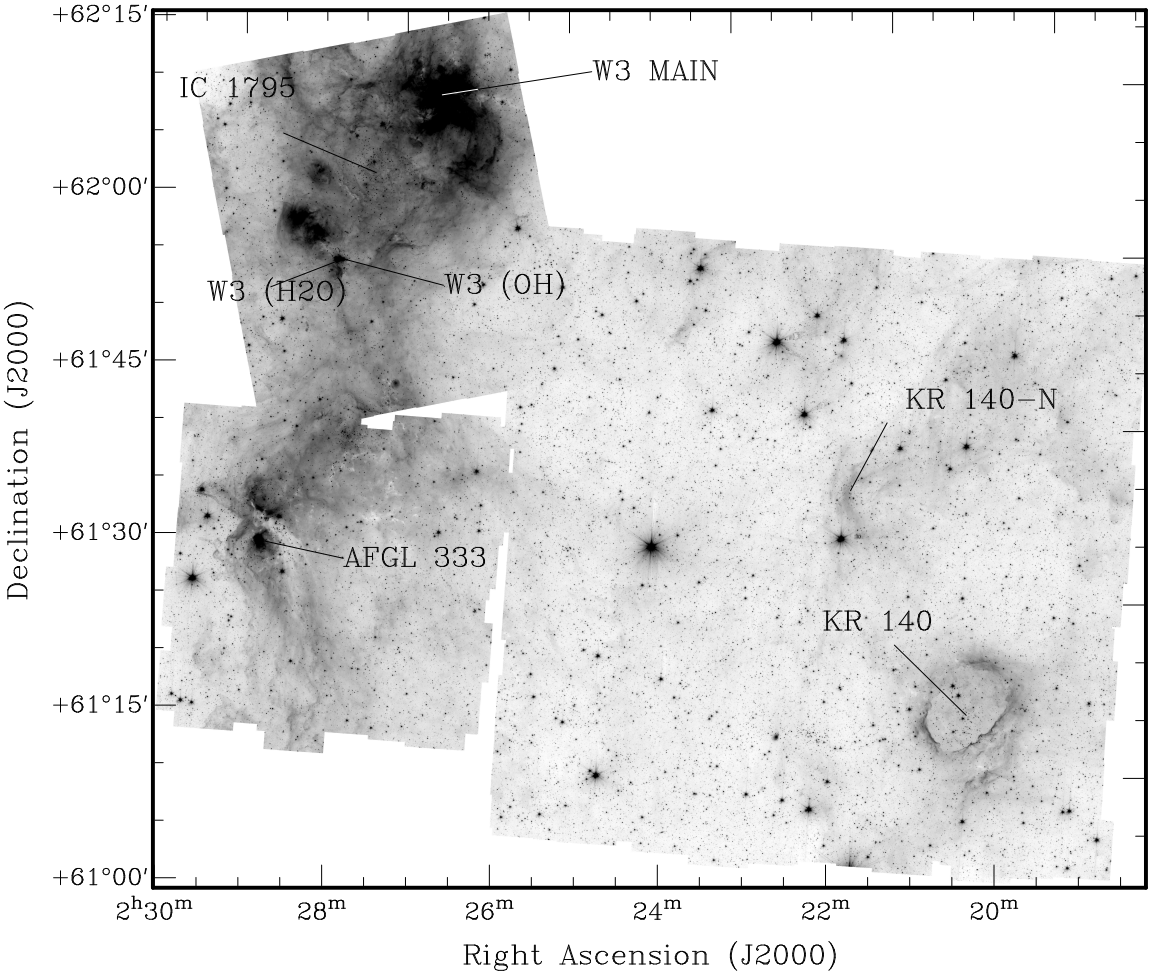

Figure 3.1 Greyscale *Spitzer* channel 1 mosaic, with labels marking the regions and key features in the W3 GMC.

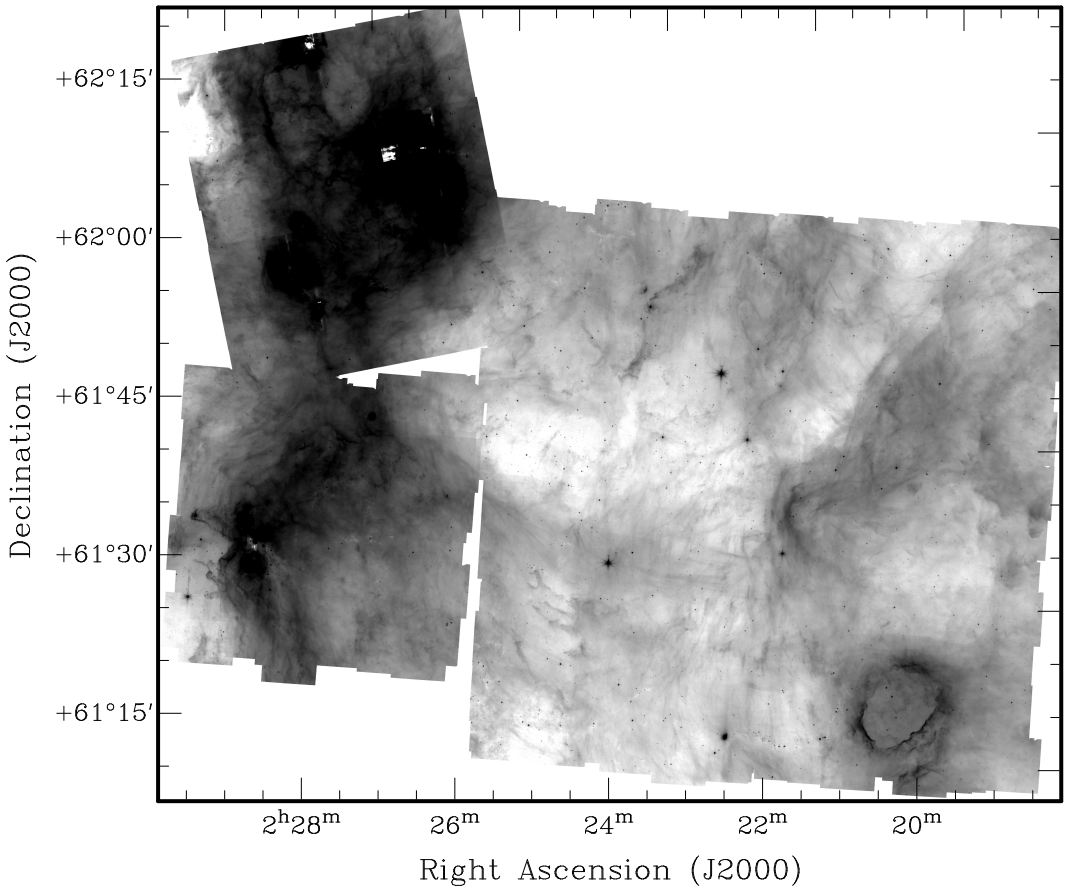

Figure 3.2 Greyscale *Spitzer* channel 4 mosaic of W3. Intensity scale has been chosen to highlight the weaker features surrounding the main star forming regions labeled in Fig.3.1 (at the expense of the latter). Details in this image include several Infrared Dark Clouds (IRDCs) and filaments (e.g., (α, δ)=($02^{\rm h}$ $26^{\rm m}$ $57^{\rm s}$, 61° $29'$ $45''$)).

S18.13.0 and S18.12.0 pipelines, respectively. These files already include all the pre-processing artifact mitigation corrections, including muxbleed, column pulldown/pullup and electronic banding. Tiles were reduced, background-matched, and mosaicked with the MOPEX[1] tool, which, with the exception of the MIPS observations from program P30955 (KR 140), produced maps of higher quality than the mosaicked pBCD data already provided by the Archive. The best available mosaics were chosen for our analysis. Photometry tests performed on both the pBCDs and our own reduced mosaics show no systematic differences in channels 3 and 4, and negligible (0.04 mag) differences in channel 1 and channel 2, which is much smaller than any of our expected photometric uncertainties.

3.1.2 *Spitzer* Source Extraction and Photometry

A preliminary list of sources was obtained using SExtractor (Bertin & Arnouts, 1996) and a mexican hat filter, which was observed to perform the best (with the highest detection rate of visually confirmed sources in the region) in the extremely crowded regions found in W3, especially W3 Main and W3 (OH). We note that this also introduced a significant number of artifacts and false detections which we eliminated through a series of cleaning steps, described below. SExtractor also produced noise and background maps, which we also checked visually to ensure optimal source extraction. This preliminary list was subsequently fed into the point source extraction package in MOPEX (APEX) for point response function (PRF) fitting, which provides a more accurate centroid calculation as well as additional statistics for each source resulting from the fitting (e.g., χ^2, signal-to-noise ratio (SNR), etc). When bandmerging the IRAC list with the 2MASS Point Source Catalog (through the GATOR interface in the NASA/IPAC Infrared Science Archive; IRSA [2]) we find the accuracy of our final PRF-fitted coordinates to be generally better

[1] http://ssc.spitzer.caltech.edu/dataanalysistools/tools/mopex/
[2] http://irsa.ipac.caltech.edu/applications/Gator/

than 0″.5, although in this work we allow for a more conservative matching radius of 2″ when bandmerging catalogs at different wavelengths and/or instruments. The internal background image used in APEX for photometry was produced choosing the option 'SExtractor background method' for consistency with the previous part of this analysis.

As recommended by the IRAC handbook we chose aperture photometry for our main photometric analysis, using in this case the most accurate centroids returned by APEX. The use of this technique also ensured consistency with the most recent *Spitzer* studies of this cloud (Polychroni et al., 2010).

Aperture corrections and zero points were obtained from the IRAC/MIPS Instrument Handbooks[3],[4]. Additional corrections (e.g., pixel phase and array correction) were applied when required. An aperture of 2 pixels (2″.4) with a sky annulus between 2 and 6 pixels (7″.3) for IRAC, and an aperture of 7″.0 with a sky annulus between $7 - 13''$ for MIPS, were found to yield results most closely agreeing with the magnitudes provided by Ruch et al. (2007), who used the version of DAOPHOT (Stetson, 1987) modified for GLIMPSE. Contrary to standard aperture photometry, the GLIMPSE technique is particularly useful for analysis in crowded fields and regions with variable background [5], and we therefore checked the accuracy of our results by comparing the photometry for those YSO candidates in our list with counterparts in the source list provided by these authors. The root mean square (rms) difference between the MIPS 24 μm photometry obtained in this work for the YSO list and that from Ruch et al. (2007) was found to be ~ 0.6 mag. Comparison of IRAC photometry yields an rms difference of < 0.2 mag in all four channels, which is consistent with the estimated 3σ errors and equivalent to the minimum signal-to-noise (S/N) required for our final catalog (S/N= 5; see below).

The same procedures applied to the IRAC long exposure mosaics were also performed on the short exposure images. While the final catalog is based on the long exposure maps,

[3]http://ssc.spitzer.caltech.edu/irac/iracinstrumenthandbook/
[4]http://ssc.spitzer.caltech.edu/mips/mipsinstrumenthandbook/
[5]see http://www.astro.wisc.edu/glimpse/photometry_v1.0.pdf; http://www.astro.wisc.edu/glimpse/

we used the short exposure mosaics to obtain replacement photometry for those sources with bad pixels within their apertures or observed/suspected to be affected by saturation in the long exposure mosaics.

3.2 Stellar Classification

3.2.1 General YSO Classification: Methodology and Techniques

Protostars and Optically Thick Disks

We aimed to provide the most reliable sample of YSOs in this GMC. For the main classification in our analysis we chose the 'revised', updated criteria in Appendix A of Gutermuth et al. (2009). The color and magnitude scheme developed by these authors includes a series of sequential steps (phases) to identify, clean, and classify the candidates: Phase 1) Removal of contaminants such as star-forming galaxies with strong polycyclic aromatic hydrocarbon (PAH) emission, active galactic nuclei (AGN), unresolved knots of shock emission, and PAH-emission-contaminated apertures. This step also includes the first separation of YSOs by means of the four IRAC bands. Phase 2) A search for additional YSOs based on 2MASS photometry[6]. Phase 3) Identification and re-classification of previously identified sources with suitable MIPS 24 μm photometry. When re-classifying photospheric sources into 'transition disk' objects (those with significant 24 μm emission; included within the Class II category) we required sources to have been classified as photospheric in both previous phases. To deredden the magnitudes we used the extinction maps and methodology described in Rowles & Froebrich (2009). The visual extinction map was transformed to a median A_H map using the extinction law from Mathis (1990). We changed extinction in the 2MASS bands to extinction in the IRAC channels using the numbers from Flaherty et al. (2007).

[6]One of the equations of Phase 2 (Gutermuth et al., 2008; Gutermuth et al., 2009) should read: $E_{[3.6]-[4.5]}/E_{H-K}=(E_{H-K}/E_{K-[4.5]})^{-1}$-$(E_{H-K}/E_{K-[3.6]})^{-1}$

The above classification was complemented and cross-checked with: i) the 'red source' classification scheme from Robitaille et al. (2008), which should include all Class 0/I and several Class II sources; and ii) the 'stage' phase from Robitaille et al. (2006) (Stage 0/I: $\dot{M}_{\rm env}/M_\star > 10^{-6}\,{\rm yr}^{-1}$; Stage II: $\dot{M}_{\rm env}/M_\star < 10^{-6}\,{\rm yr}^{-1}$ and $\rm M_{disk}/M_\star > 10^{-6}$; Stage III: $\dot{M}_{\rm env}/M_\star < 10^{-6}\,{\rm yr}^{-1}$ and $\rm M_{disk}/M_\star < 10^{-6}$). We used this last scheme to compare the above observational classification with an alternative method based on intrinsic physical properties (e.g., mass accretion rate, and disk mass). This last analysis was carried out by studying the position of each YSO in the color-color diagrams (CCDs) with respect to the limits marking the areas where most of the sources of one particular 'stage' are predicted to fall (Robitaille et al., 2006).

Pre-Main Sequence Population With Optically Thin Disks

Separation and classification of pre-main sequence stars (PMS) with optically-thin disks is a particularly complicated process due to their similarity (in infrared color) with more evolved reddened main sequence and giant stars (photospheric-dominated). These transition objects are however essential to fully understand the different stages in star formation. In an attempt to estimate the population of sources with weak infrared excess and other PMS stars that may have been missed with the above color classification, we first excluded those objects in our source list already classified as Class 0/I and II. We then used the 2MASS catalog and a process similar to that used in Kerton et al. (2008), who attempted to separate the YSO population guided by a sample of known low-mass T-Tauri and intermediate-mass Herbig Ae/Be (HAeBe) stars. In this work (see Section 3.3) we show that this method can only be applied successfully once the 'younger' YSOs have been identified using additional data (e.g., IRAC).

To investigate the possibility of missed candidates from the PMS population we first chose a sample of T-Tauri (Kenyon & Hartmann, 1995) and HAeBe stars with known distances (Finkenzeller & Mundt, 1984; The et al., 1994; Mendigutía et al., 2011 and

references therein). All sources where checked with SIMBAD[7], keeping variable, emission and pre-main sequence stars and rejecting those classified as double/multiple systems, low-mass stars and brown dwarfs. Infrared photometry was obtained by matching the sample with the 2MASS Point Source Catalog through the GATOR interface. Infrared photometric systems were converted to the 2MASS system using the transformations from Carpenter (2001). All magnitudes were shifted to a distance of 2 kpc for W3 with the inclusion of interstellar extinction by means of the A_V-distance relation from Indebetouw et al. (2005). Figures 3.3 and 3.4 show the CCD and color-magnitude diagram (CMD) for the T-Tauri and HAeBe samples shifted to the distance of W3. The CCD shows the T-Tauri locus from Meyer et al. (1997) and the main sequence and giant branch from Koornneef (1983) including interstellar reddening. Reddening vectors for an $A_V = 10$ have been included for an O6 V, M8 V, M2 V, and an M6 III star. The CMD shows solar metallicity isochrones (Marigo et al., 2008; Girardi et al., 2010) at $\log(t\,yr^{-1})$ =7, 8, and 9 for the same distance. The dashed-dotted line is the reddening vector for an ∼A0 star with $A_V = 10$ at d= 2 kpc, applied using the reddening law and the A_V/A_J conversion from Mathis (1990). The values used for extinction conversions between 2MASS bands are consistent with those from Indebetouw et al. (2005) up to one decimal place taking into account uncertainties, which is a negligible difference compared to the expected uncertainty in the transformation from optical to infrared extinction.

Figure 3.3 shows T-Tauri stars lying mainly above the T-Tauri locus. Many are within the reddening band formed by the reddening vectors (Mathis, 1990) of an O6 and ∼M2 main sequence stars (with a tail extending into the HAeBe region, to the right of the reddening band, and following the direction of the T-Tauri locus). The wide distribution implies variable amounts of extinctions toward these sources and variable disk emission. A large proportion of T-Tauri stars are indistinguishable from main sequence stars with just interstellar reddening or are consistent with weak-emission T-Tauri stars (Meyer

[7]http://simbad.u-strasbg.fr/simbad/

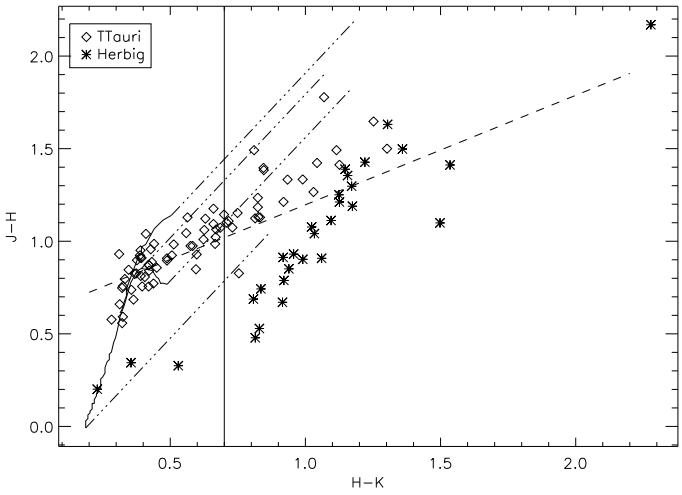

Figure 3.3 Color-Color Diagram showing the T-Tauri and HAeBe samples shifted to d= 2 kpc. Solid lines mark the main sequence and giant branch from Koornneef (1983), also shifted to a distance of 2 kpc. Dash-dotted lines are reddening vectors for an additional $A_V = 10$ for an O6 V, M8 V, M2 V, and M6 III star using the extinction law from Mathis (1990). Dashed line marks the locus of T-Tauri stars from Meyer et al. (1997) at the same distance. Vertical solid line marks the bluest [H-K] color accepted for PMS classification.

et al., 1997). The maximum A_V in the maps from Rowles & Froebrich (2009) is about $\sim 9.5 - 10$ in the region containing W3 Main/(OH), and ~ 7 for those comprising KR 140 and AFGL 333. Thus there will be considerable extinction of objects in the W3 field, and so color identification of this type of T-Tauri star without the aid of spectroscopic data will be severely contaminated.

In consequence, we chose a more conservative approach and selected our T-Tauri sample by requiring these PMS stars to be reddened enough to lie above the T-Tauri locus, with colors satisfying H-K$>$ 0.7 (similar to that used in Kerton et al. (2008) for KR 140). The above limits minimize the contamination from foreground or mildly reddened weak-emission T-Tauri stars (undistinguishable from main sequence), and early type stars. While the color cuts could still allow for non-negligible contamination from

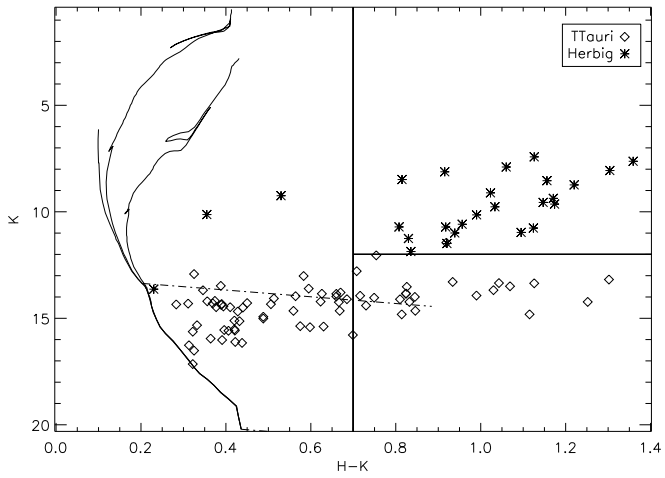

Figure 3.4 Color-Magnitude Diagram for the T-Tauri and HAeBe samples at d= 2 kpc. Solid lines are solar metallicity isochrones (Marigo et al., 2008; Girardi et al., 2010) $\log(\mathrm{t\,yr^{-1}})$=7, 8 and 9. Dashed-dotted line is the reddening vector for an ∼A0 star at this distance with $A_V = 10$. Horizontal solid line marks the magnitude limit separating T-Tauri and HAeBe candidates. Vertical solid line like in Fig.3.3.

late main sequence and giant stars with moderate reddening, the magnitude selection criterion below reduces this contamination to mainly that caused by highly extinguished ($A_V \geq 7$) stars of spectral type of ∼A or later (Figure 3.4).

HAeBe stars lie preferentially to the right of the reddening band. All suitable candidates should therefore be located in this region and satisfy the condition H-K> 0.7. This limit aims to minimize contamination from reddened early type stars and luminous T-Tauri stars. To separate candidates in regions of the CCD populated by both types of PMS (i.e., outside the reddening band) we used the information from the CMD (Figure 3.4), in which T-Tauri and HAeBe can be easily separated. All T-Tauri stars have K magnitudes $\gtrsim 12$. HAeBe stars tend to be brighter, approaching this limit only for 'late' stages reaching the main sequence, which we already discard with our imposed limit in the CCD to minimize contamination from reddened early type stars. The combined color plus magnitude condition minimizes contamination of the T-Tauri sample from reddened

Table 3.1 Selection Criteria for T-Tauri and HAeBe stars for d= 2 kpc

T-Tauri
$[H-K] \geq 0.7$
$[J-H] \geq 0.59([H-K]-0.187) + 0.72$
$[J-H] \leq 1.55([H-K]-0.39) + 0.85$
$K > 12$
HAeBe
$[H-K] \geq 0.7$
$[J-H] \leq 1.55([H-K]-0.187) - 0.008$
$K < 12$

giant stars. In addition, the color constraint imposed on HAeBe stars, which are mainly localized and 'isolated' outside the reddening band of typical stars, already minimizes the contamination from reddened main sequence and giant stars.

We note that this relatively simple scheme for PMS classification may only be applied *after* the Class 0/I and Class II populations have been identified using IRAC data, as there is considerable overlap in the CCD and CMD of T-Tauri candidates with *Spitzer* Class II/I/0 sources (see Section 3.3).

Our final PMS selection scheme has been summarized in (Table 3.1). The color and magnitude selection criteria were applied to all sources in our initial IRAC list satisfying i) the cleaning/reliability conditions in the *Spitzer* channels; ii) matched to a 2MASS source with quality flag better than 'D' in all 2MASS bands; and iii) classified as (mainly) photospheric or without a successful classification using the YSO scheme from Gutermuth et al. (2009) (i.e., no Class 0/I, Class II, or contaminant).

A search for additional PMS was also carried out by extending our analysis to 2MASS sources *in* the area covered by the *Spitzer* survey but without a suitable IRAC counterpart (i.e., satisfying our initial cleaning and reliability conditions) in the short wavelength

Spitzer channels. The lack of a detection in *Spitzer* minimizes the possibility of confusion with actual embedded protostars, which should have been previously identified with the color/magnitude criteria from Gutermuth et al. (2009).

3.2.2 The *Spitzer* Catalog

Here we present the final products and source lists derived from the analysis carried out in the previous section. Results and statistics from our YSO detection and classification procedures are shown in Tables 3.2 and 3.6. For the purpose of this work, we define as 'YSO' those Class 0/I and Class II candidates selected using the color/magnitude scheme from Gutermuth et al. (2009). The sample of PMS stars, that is those additional candidate young stellar objects selected using 2MASS photometry, will include stars with optically thick disks, e.g., classical T-Tauri stars and HAeBe stars (Class II) missed by the IRAC color/magnitude classification, and optically thin disks, e.g., weak-lined T Tauri stars (Class III sources). An analysis of this sample will be relevant to investigating the 'oldest' young stellar population in W3.

Statistics, Completeness & Reliability

The YSO search using the color and magnitude classification from Gutermuth et al. (2009) yielded a total of 616, 706 (two of which were also observed in neighboring AORs), and 246 YSOs in the regions surveyed in all four IRAC channels in each individual AOR: W3 Main/(OH), KR 140/KR 140-N, and AFGL 333 *Spitzer* regions, respectively (Fig. 3.5; Table 3.6). The full list of YSOs (Table 3.2) and 2MASS-based PMS candidates (Table 3.3) has been published in the *Astrophysical Journal*.

For the purpose of the present analysis we chose reliability over completeness, and so this sample requires S/N$\geq$ 5 for any IRAC/MIPS photometry used in any particular method. When using 2MASS photometry in Phase 2 of the color/magnitude classification scheme, those sources with the closest distance to our IRAC sources (within 2$''$) were

Table 3.2 YSOs in each subregion of W3: Sample list[a]

RA	Dec	Class	Class	Flag[b]	Flag
h m s (J2000)	° ′ ″ (J2000)	Catalog 1	Catalog 2[c]	Catalog 1	Catalog 2
2 17 24.53	61 40 06.24	classII*	nomatch	0	−1
2 17 26.66	61 41 32.64	classII*	nomatch	0	−1
2 17 27.26	61 38 12.12	classII*	nomatch	0	−1
2 17 37.06	61 44 10.32	classII*	nomatch	0	−1
2 17 51.86	61 34 42.60	classII*	nomatch	0	−1
...					

[a]Catalog is published in its entirety in the *Astrophysical Journal*.

A portion is shown here for guidance regarding its form and content.

[b] Reliability flag (see text):

1: Candidates satisfying cleaning/bandmerging requirements and with individual detections in each band.

0: Candidates satisfying cleaning/bandmerging requirements but with IRAC Channel 3 and 4, and MIPS 24 μm detection (centroid) and photometry based on a successful detection in Channels 1/2.

[c] Same as Catalog 1, but without MIPS 24 μm-based re-classification unless a successful detection was found in our original MIPS source list; i.e., MIPS centroid (and photometry) not based exclusively on an IRAC detection.

Table 3.3 2MASS-based sample of PMS in W3[a]

Name (2MASS)	RA h m s (J2000)	Dec ° ′ ″ (J2000)	Class Cat.1	Class Cat.2	Flag Cat.1	Flag Cat.2
02175736+6123496	2 17 57.36	61 23 49.56	ttauri	ttauri	0	0
02180709+6139314	2 18 07.08	61 39 31.32	ttauri	ttauri	0	0
02181518+6114317	2 18 15.19	61 14 31.56	ttauri	ttauri	0	0
02182760+6133131	2 18 27.60	61 33 12.96	ttauri	ttauri	0	0
02183106+6111390	2 18 31.06	61 11 39.12	ttauri	ttauri	1	1
...						

[a]Catalog is published in its entirety in the *Astrophysical Journal*.

A portion is shown here for guidance regarding its form and content.

Table 3.4 Galaxy Candidates[a]

RA h m s (J2000)	Dec ° ′ ″ (J2000)	Flag[b] Catalog 1	Flag Catalog 2
2 17 16.92	61 44 14.28	1	1
2 17 22.08	61 43 53.76	1	1
2 17 26.57	61 43 20.28	1	1
2 17 34.30	61 36 17.64	1	1
2 17 39.00	61 36 29.16	1	1
...			

[a]Catalog is published in its entirety in the *Astrophysical Journal*.

A portion is shown here for guidance regarding its form and content.

[b]Flag=1: Classified as galaxy in catalog.

Table 3.5 Photometry for YSOs in each subregion of W3[a]

3.6 μm	Error	4.5 μm	Error	5.8 μm	Error	8.0 μm	Error	24 μm	Error
11.869	0.006	11.836	0.008	11.777	0.028	11.886	0.094	8.342	0.093
12.831	0.011	12.823	0.012	12.871	0.062	12.446	0.161	8.542	0.101
13.207	0.012	13.191	0.016	13.206	0.071	13.247	0.133	8.499	0.154
12.714	0.010	12.686	0.012	12.744	0.046	12.794	0.138	8.618	0.072
11.823	0.007	11.757	0.008	11.680	0.028	11.673	0.054	9.009	0.104
...									

[a]Photometry (magnitudes) for sample in Table 3.2.

List is shown in its entirety in the *Astrophysical Journal*.

A portion is shown here for guidance regarding its form and content.

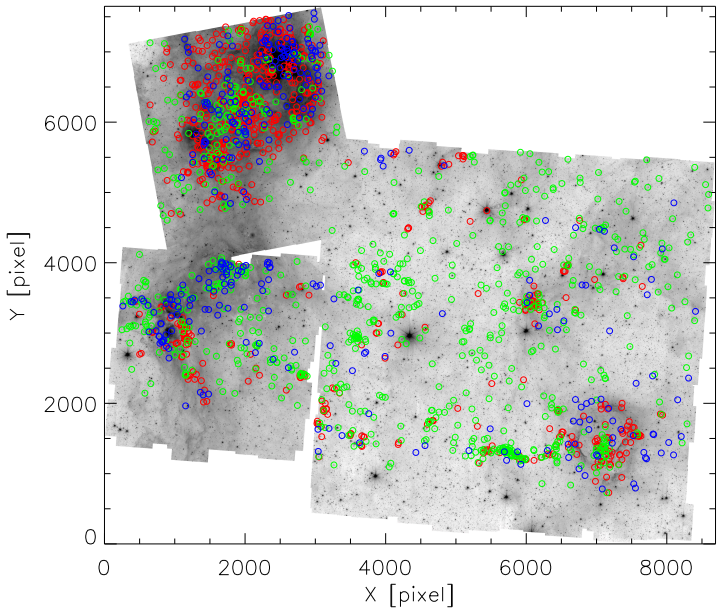

Figure 3.5 Greyscale *Spitzer* channel 1 mosaic with Class 0/I (red), Class II (green) and PMS (blue) candidates. Sample includes all sources (and all flags) from Catalog 1, as well as PMS candidates with no IRAC counterparts (see text).

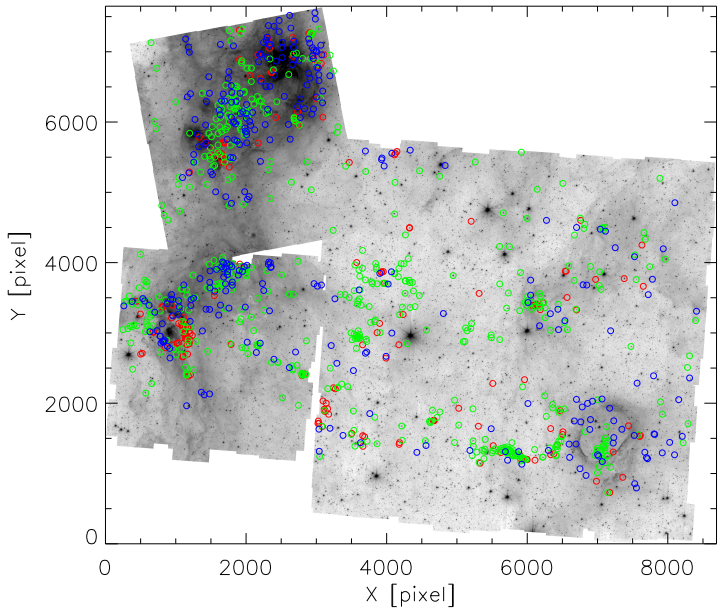

Figure 3.6 Same as Fig.3.5 but for Catalog 2, without PMS candidates with no IRAC counterpart.

chosen as suitable counterparts as long as they had a quality flag 'A', 'B', 'C' or 'D' in H and K-bands, and at least valid photometry ('D') in the J-band (if available).

In order to remove as many artifacts and false detections as possible, we first band-merged the IRAC channels using channel pairs. A candidate source could still be included in the initial list without suitable photometry in all four channels if it either appeared in channels 1 and 2, or channels 3 and 4. This was done as the first step to minimize the need for visual inspection of samples containing tens of thousands of sources, while at the same time attempting to minimize the loss of relatively 'cold' sources without a suitable detection at shorter wavelengths. In addition, we also imposed our own 'internal' cleaning conditions based on the properties provided by APEX and SExtractor for those sources already published as reliable detections in the catalog of Ruch et al. (2007) (e.g., successful PRF fitting, χ^2 of fitting, ellipticity and successful deblending). We note, however, that these internal cleaning parameters are physically meaningless

and were only used for 'relative' classification of sources within a particular sample, with the only purpose being to reject as many artifacts (e.g., PSF residuals and spikes around bright sources) and false detections as possible. Despite this procedure, these conditions were still conservative, and visual inspection and manual rejection were still required and performed in the last stages of the catalog production process. All sources successfully classified as YSO candidates and satisfying all the cleaning conditions and bandmerging requirements have an entry= 1 in the 'flag' column in the source catalog (Table 3.2). This defines the 'reliable' subset of the final list (Fig. 3.5).

In an attempt to improve the 'completeness' of the sample we also used the detections in IRAC channels 1 and 2 (with the best sensitivity) as a base for a new source list. Photometry was performed on fixed centroids at longer wavelengths (including MIPS), and all the cleaning/selection conditions and the Gutermuth classification scheme were again applied to each source. Those additional detections satisfying all the catalog requirements were included in the final catalog with a flag entry= 0. We note that in the scheme of Gutermuth et al. (2009), MIPS photometry was used mainly to reclassify as YSOs those sources initially rejected as galaxies, AGN, or fake excess sources in the first steps of the scheme.

Photometry derived from the MIPS 24 μm maps was generally less reliable. We therefore produced a Catalog 2 (Fig. 3.6) based on the same procedure as Catalog 1, but allowing for re-classification of IRAC/2MASS sources only if there was a successful MIPS counterpart in our original (independently obtained) MIPS source list (i.e., the standard fixed-centroid photometry is not used in MIPS phase 3). Catalog 2 is therefore more conservative, because although the SExtractor extraction was visually observed to detect all significant sources, a large fraction of these detections did not satisfy the cleaning conditions after performing APEX PRF fitting on the MIPS mosaics, on account of the variable and complicated background at longer wavelengths. Both catalogs (Catalog 1 and Catalog 2) yield very similar source lists for Class 0/I and Class II sources, differing

mainly on the number of Class 0/I* (highly embedded YSOs) and Class II* transition objects. Defined in this work as the (*) population, both the highly embedded and transition objects rely on MIPS photometry for identification and classification. A summary of the number of candidates found of each class in each field is given in Table 3.6. As expected, highly embedded and transition objects are particularly abundant in Catalog 1 due to the use of MIPS photometry based on IRAC centroids, with Class 0/I* sources forming up to $\sim 65\%$ of the population in W3 Main/(OH) ($\sim 5.5\%$ Class II*). In Catalog 2 these types of objects constitute less than $\sim 3.5\%$ of the YSOs in each field.

We created a sample resulting from bandmerging just channels 3 and 4 and ran it through the cleaning and classification procedures described above. This experiment produced no new sources. This shows that no significant sample of 'cold' sources (without detections in IRAC channels 1 and 2) should have been missed by the initial bandmerging-by-pairs procedure (within the limitations of this technique). We therefore conclude that the majority of sources potentially missed in our (flag = 1) analysis would have come from the samples in IRAC channel 1/channel 2 that do not have counterparts at longer wavelengths due to the diffuse emission and sensitivity loss (although we note that Catalogs 1 and 2 for flag = 1 are very similar; Table 3.6).

Unless mentioned otherwise, in the following sections we will use Catalog 1 (all flags) as the primary sample in our analysis. As we explain in Section 3.4, this source list is expected to be a more reliable indicator of the YSO properties. We find that the use (or omission) of the (*) population is mostly relevant in those highly populated regions with high extinction, mainly IC 1795 and KR 140. We cross-correlated our final YSO list with the list of infrared sources associated with the cluster IC 1795 presented in Roccatagliata et al. (2011), and we find 76 YSOs in our sample which are consistent with being cluster members. Of these, 30 YSOs belong to the (*) population in Catalog 1 (not classified as YSOs in Catalog 2), and yet all are also classified as YSOs (Class II) in Roccatagliata et al. (2011). When applying the color classification from Megeath et al. (2004) we find

that only 4 out of the 76 sources would not have been classified as YSOs, which supports our decision and the need to keep the (*) population in our analysis. Results based on Catalog 2 are only mentioned briefly when required.

We finally note that while the flag = 0 and IRAC short wavelength-based catalogs intend to improve the completeness of the final sample (and each source was visually inspected in channel 1), these detections are still tentative and should be treated with caution.

We compared Catalog 1 and Catalog 2 with the detections from Ruch et al. (2007) for W3 Main/(OH), the region analyzed in their study. These authors detected a total of 295 sources in the four IRAC channels, 21 ($\sim$ 7%) of which were classified as Class I sources, and 94 ($\sim$ 32%) as Class II. All 295 sources were in our initial catalog resulting from the SExtractor source detection process. Our analysis identifies a similar number of Class I and Class II candidates in this sample, with a total of 117 sources classified as YSOs in Catalog 1 (93 in Catalog 2). Of the remaining sources in their list not classified as YSOs in Catalog 1, 130 are stars, 0 galaxies, 3 shock/knots of emission or sources with PAH contaminated apertures, and 45 do not satisfy the cleaning and reliability conditions. Sources in their sample not classified as YSOs in Catalog 2 consist of 149 stars, 0 galaxies, 3 shock/contaminated aperture sources, and 50 sources not satisfying cleaning/reliability conditions. In all cases, the percentage of Class II sources is $\sim$ 3 times that of Class 0/I sources. Table 3.7 shows the results after applying our cleaning conditions and the Gutermuth scheme.

Table 3.6 includes the number of PMS stars found based on 2MASS color and magnitude information, with counterparts in the *Spitzer* images. We found 51 more T-Tauri stars and 2 HAeBe stars when searching for 2MASS sources (from the 2MASS PSC) without suitable IRAC counterparts (i.e., IRAC sources satisfying our initial cleaning conditions), but located in the common (4-channels) areas surveyed by *Spitzer*. Many of these sources are located in the bright, diffuse region surrounding W3 Main, (OH) and

Table 3.6 YSOs in the *Spitzer* Survey

W3 Main/(OH)				
	Catalog 1	Catalog 1	Catalog 2	Catalog 2
Flag	all[a]	1	all	1
Class 0/I	39	32	39	32
Class 0/I*	405	7	7	7
Class II	138	85	132	85
Class II*	34	3	3	3
HAeBe[b]	1	0	2	0
T-Tauri[b]	110	50	126	58
KR 140				
Class 0/I	88	80	84	78
Class 0/I*	130	3	3	3
Class II	271	252	271	252
Class II*	215	3	3	3
HAeBe	0	0	0	0
T-Tauri	94	56	96	57
AFGL 333				
Class 0/I	57	51	57	51
Class 0/I*	25	0	0	0
Class II	140	129	140	129
Class II*	24	2	2	2
HAeBe	0	0	0	0
T-Tauri	86	43	86	43

[a] Flag = 0 & Flag = 1 combined.

[b] With *Spitzer* counterparts.

Table 3.7 Breakdown of candidate YSOs with counterparts in the catalog of Ruch et al. (2007)

Class	Catalog 1	Catalog 1	Catalog 2	Catalog 2
Flag	all	1	all	1
Total YSO	117	77	93	77
Class0/I	21	20	21	20
Class0/I*	8	0	0	0
ClassII	72	57	72	57
ClassII*	16	0	0	0

Table 3.8 IRAC completeness limits for Catalog 1

AOR	Channel 1	Channel 2	Channel 3	Channel 4
	All/Flag= 1	All/Flag= 1	All/Flag= 1	All/Flag= 1
W3 Main/W3(OH)	14.1/12.4	12.9/11.8	12.7/10.6	11.3/10.3
KR 140	13.1/13.7	13.1/13.0	13.2/12.8	12.2/11.9
AFGL 333	12.9/12.8	12.1/11.8	11.9/11.6	10.4/10.9

AFGL 333 in the IRAC images, which did not allow for proper identification and extraction of candidate sources due to confusion. The imposed lower limit for the K magnitude of our HAeBe stars is within the 2MASS 10σ completeness limit for this band (14.3 mag). This sample is also complete in the H band (15.0 mag), and J band (15.9 mag). The faintest 2MASS magnitudes for the T-Tauri sample lie beyond the 2MASS completeness limits by $\sim$ 1 mag in K and H, and $\sim$ 2 mag in J band, and therefore our list will be incomplete at the faint end of the population.

The use of several steps of cleaning and reliability thresholds for our final sample, combined with different sensitivity limits in different regions for a given field, complicate the determination of a reliable completeness limit for our catalog. In order to provide an estimate of the magnitude at which a catalog is 100% complete, which due to our

cleaning and selection steps differs from a fainter limit at which some sources can be detected, we examined the number of detections as a function of magnitude for each field at each IRAC wavelength. Figure 3.7 shows the histograms for W3 Main and W3 (OH) for all YSOs in Catalog 1, the most complete sample derived in this work. Our estimates for 100% completeness, given by the 'turnover' points in the YSO distributions for each subregion of W3, are included in Table 3.8. The effects of strong, large scale emission in dense regions with high stellar activity is evident from the limits derived for the HDL.

Our choice of reliability over completeness excludes a large population of faint sources from our final list, and therefore the completeness limits for the different regions reveal a particularly conservative population for IRAC channels 1 and 2. The flag = 0 sample (using the short wavelength channels as a template for photometry at longer wavelengths) improves completeness at these channels significantly, although we note that our estimated completeness limits are still conservative compared to samples derived from similar *Spitzer* studies of W3 (Polychroni et al., 2010). Clearly, the completeness magnitudes quoted for our work are upper (faint) limits, especially for the long wavelength channels. The use of flag = 1 data or the sample from Catalog 2 would be more conservative (and therefore less complete). The latter candidate source list, while more reliable than Catalog 1, is expected to suffer a more severe loss of highly embedded sources. This is due particularly to the rejection of poorly fitted sources (failed PRF fitting) with APEX, and our strict requirement of suitable fitting and photometry in the MIPS band (with severe sensitivity loss and confusion due to strong diffuse emission).

With regard to Class types, Class II sources are generally weaker at the longer IRAC wavelengths than more embedded Class 0/I objects, and are therefore more likely to be missed because of lower sensitivity and bright PAH emission (e.g., Chavarría et al., 2008).

Despite our attempt to compensate for saturation in the IRAC sample by using the short exposure mosaics, some sources will still be missed in the brightest and most active regions such as W3 Main and W3 (OH) due to confusion and location within the bright

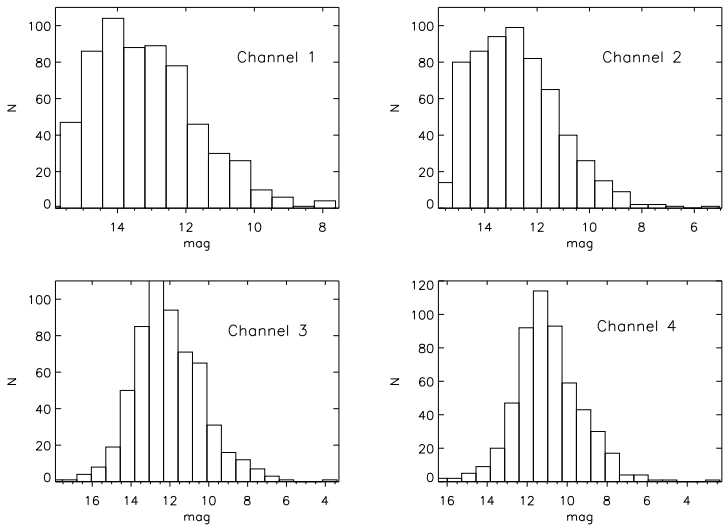

Figure 3.7 Number of YSO candidates as a function of magnitude and channel for the region comprising W3 Main and W3 (OH). Channels 1-4 are shown in order from left to right, top to bottom. Completeness limits for each region (Table 3.8) have been derived from the turnover points of the distributions.

infrared nebulosity. The catalogs would also exclude clearly extended sources and stellar groups.

Due to our attempt to provide a reliable sample for our PMS sources, we again note that weak-lined and low extinction T-Tauri and HAeBe stars have been excluded from our catalog in order to avoid major contamination from reddened main sequence stars. We cross-checked our final list of candidate T-Tauri and HAeBe stars with the SIMBAD database, and found no matches with the exception of a couple of sources, classified in the database as 'infrared sources' or 'star in cluster'. Ultimately, spectroscopic surveys of stellar candidates are the most reliable method to find and confirm PMS.

Contamination

The *Spitzer* based sample was subjected to strict cleaning conditions and cross-checked with other classification schemes to ensure the highest consistency and reliability of our

sample of YSO candidates. However, it is likely that some contamination from extraneous objects like galaxies/AGN, planetary nebulae (PNe) and AGB stars is present in the final sample.

A measure of the contamination by PNe and AGB stars was obtained by applying the conditions from Robitaille et al. (2008) to the reliable photometry derived from the previous YSO classification. For successful classification as PN, detections needed to satisfy at least two of the four color conditions to ensure reliability in their position in the CCDs. While the selection scheme still allows for mutual contamination of YSO/AGB stars in both samples, this technique can still provide a useful measure of the general contamination of our YSO sample. The PN contamination using this method is predicted to be $\leq 1.5\%$ for W3 Main/(OH), and $\leq 1\%$ and $\leq 2\%$ for KR 140 and AFGL 333, respectively. The contamination from AGB stars is expected to be $< 3.0\%$ and $< 0.5\%$ for W3 Main/(OH) and AFGL 333. No candidate AGB stars are found in KR 140 using this scheme.

In their analysis, Gutermuth et al. (2009) adapted their classification to work with the larger distances present in their survey of up to ~ 1 kpc. The use of this classification at the distance of W3 (~ 2 kpc) is expected to shift the proportion of classified YSOs toward the brightest sources, because of the loss of dimmer sources rejected through the magnitude limits imposed on the sample and a possible contamination of the galaxy sample with YSOs. To check this effect, we ran the codes on the YSO sample in W5 from the work of Koenig et al. (2008), applying the new classification conditions to the photometry provided by these authors. W5 belongs to a massive complex (neighboring W3 and W4) and is considered to be at the same distance as these GMCs. These authors found a significant proportion of YSOs being misclassified as non YSOs, which was evident, for instance, in the 'clustered' properties of the 'galaxies'.

Although the code used in the present work is a 'revised' version of that used by Koenig et al. (2008), we successfully classified $\sim 95.5\%$ of their sources as YSOs of the

same type (excluding the very few sources not satisfying the requirement of magnitude error < 0.2 mag). About two thirds of the 4.5% sources where we disagreed with the classification from Koenig et al. (2008) were classified as AGN, and 0% as PAH galaxies. Increasing the magnitude limits for AGN classification by 0.5 mag to account for the larger distance of W3 (e.g., Megeath et al., 2009), we find no differences in the percentage of sources classified as AGN. Although we cannot perform this test on their rejected (non-YSO) sample (as that data was not included in their publication), we expect this code to detect and recover successfully the main YSO population in W3, without the need for major additional modifications.

This is in agreement with the following analysis of the distribution of those sources classified as galaxies or AGNs. Using the 'Distance to Nearest Neighbor' technique (Clark & Evans, 1954) we measured the mean observed distance between galaxy candidates relative to the mean distance that would be expected for a random distribution for a population with the same characteristics. The ratio between these two quantities (R) would be equal to one for a perfectly random distribution. We obtain R= 0.94, 0.98, and 0.88, with significance levels of $\sim 25\%$, $\sim 37\%$ and $\sim 5\%$ for W3 Main/(OH), KR 140 and AFGL 333, respectively. This supports the random spatial distribution of our galaxy candidates and low YSO contamination based on the lack of significant clustering. Coordinates for the list of galaxy candidates are included in Table 3.4.

3.3 YSO Analysis: Observed and Intrinsic Properties

In this work we aim to produce a reliable list of YSO candidates, which will be used in the following sections to investigate the early stages of high-mass star formation in W3. An estimate of the mass of each of our YSO candidates in the different classes is a crucial component of our analysis. SEDs have been extensively used to estimate this

Table 3.9 General 2MASS Properties for 'Class 0/I' and 'Class II' Populations

Class	<[H-K]>	σ	<[J-H]>	σ	<K>	σ	#Obj.
0/I	1.5	0.6	2.0	0.8	13.6	1.1	68
II	0.9	0.4	1.4	0.5	13.6	1.1	412
		T-Test Stat.	Sig.[a]	F-Test Stat.	Sig.		
0/I vs. T-Tauri	[H-K]	11.5	8E-22	6.1	6E-13		
	[J-H]	10.0	3E-18	9.3	6E-18		
	[K]	-5.0	2E-6	1.3	0.3		
0/I vs. II	[H-K]	10.8	2E-24	2.3	5E-07		
	[J-H]	7.9	3E-14	2.6	1E-08		
	[K]	-0.8	0.4	1.1	0.6		
0/I vs. HAeBe	[H-K]	3.7	4E-04	2.8	4E-03		
	[J-H]	6.2	1E-08	3.1	2E-03		
	[K]	13.2	3E-23	2.2	0.01		
II vs. T-Tauri	[H-K]	5.5	6E-08	2.6	2E-06		
	[J-H]	7.1	5E-12	3.6	1E-09		
	[K]	-5.8	1E-8	1.2	0.5		
II vs. HAeBe	[H-K]	-2.2	0.03	1.2	0.6		
	[J-H]	4.5	1.0E-05	1.2	0.6		
	[K]	18.4	0.00	2.4	8E-04		

[a] Significance.

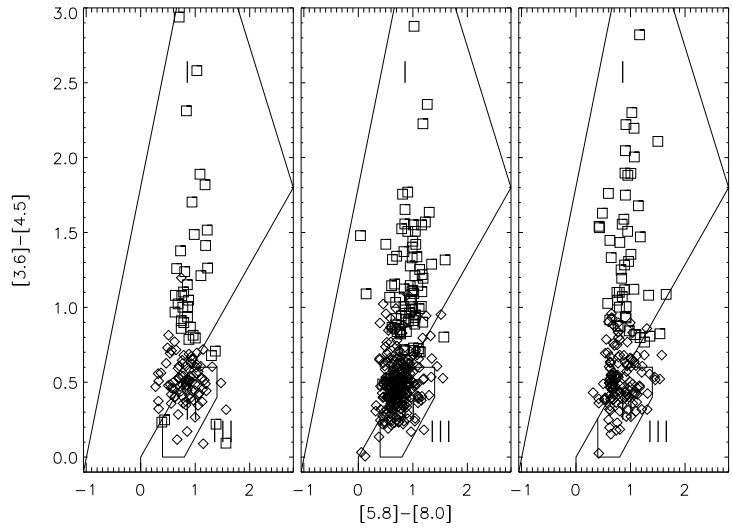

Figure 3.8 IRAC CCD of Class 0/I+(*) (squares) and Class II+(*) (diamonds) YSOs from Catalog 1 in W3 Main/(OH) (left), KR 140 (middle) and AFGL 333 (right). Black solid lines mark areas where the majority of Stage I, II and III sources from Robitaille et al. (2006) are found.

parameter (e.g., Robitaille et al., 2006). However, the highly embedded state of some of these sources demands proper modelling of the dust envelope and disk, which will be the focus of our future Herschel-based analysis.

Based on the classification scheme proposed by Gutermuth et al. (2009) we have produced a list of YSO candidates in the regions of W3 Main/(OH), KR 140, and AFGL 333, without any preliminary bias on selection according to clump/core association. This classification has been compared to and supplemented by alternative classification schemes, as described below.

We classified sources as 'red' according to the nomenclature from Robitaille et al. (2008), which should include all Class I, Flat, and a large number of Class II sources as defined by Lada (1987) and Greene et al. (1994). Only three sources in KR 140 classified as Class 0/I in Catalog 1 (and two in Catalog 2) were not initially classified as red sources. These sources showed a slight flattening of the SED at longer wavelengths

which is responsible for this misclassification, but all have been visually checked and their rising SEDs are consistent with embedded sources.

In this section we characterize the behavior of the *Spitzer* YSOs in the 2MASS and IRAC color-magnitude space. With this analysis we investigate the presence of possible identifying characteristics for the different classes, as well as near/mid-infrared properties that may help in the identification of low-mass and intermediate/high-mass YSOs in our sample (e.g., T-Tauri and HAeBe PMS stars) based on the information used in this work.

3.3.1 YSO Stages and the IRAC CCD

The 'stage' classification from Robitaille et al. (2006) is particularly useful when combined with the 'Class' scheme in order to avoid contradictions between observed (color, magnitude) and inferred (e.g., $\dot{M}_{\rm env}$; $M_{\rm disk}$) properties. Figure 3.8 shows our YSO sample from Catalog 1 (flag = 1) and the regions in the CCD that most sources of different stages are predicted to occupy (these and all the other figures in this analysis do not include error bars for clarity). We obtain a similar figure when using the candidate list from Catalog 2. While this scheme is useful to separate sources with and without circumstellar material, and a significant proportion of Stage I sources can be separated from the remaining population, some Stage I objects may however still exist in the regions occupied by Stage II (disk domain) and Stage III sources.

For all catalogs, we observed that more than $\sim 95\%$ of Class 0/I YSOs (flag = 1) and $\sim 90\%$ (flag = 0) are classified as Stage I sources. Flag = 1 Class II (including Class II*) YSOs are more evenly distributed ($\sim 50\%$) between Stage I and Stage II, although *none* of these sources is as red in [3.6]-[4.5] as Class 0/I (including Class 0/I*) candidates (Figure 3.8). We observe $< 1\%$ of Class II sources above [3.6]-[4.5]> 1, and none above 1.2. We consider this to be the limit separating the area exclusive to Class 0/I Stage I sources, and the area (bluer colors) where Class 0/I and Class II Stage I are mixed, perhaps indicative of a transition from envelope to optically thick disks.

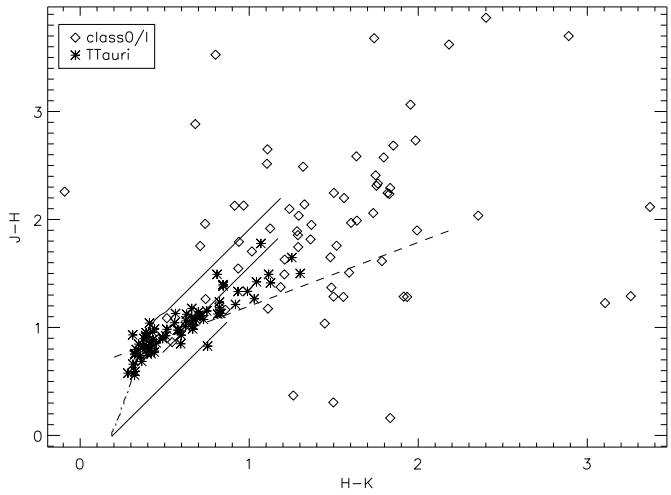

Figure 3.9 2MASS CCD showing Class 0/I IRAC sources with 2MASS counterparts. Lines and T-Tauri data as in Fig. 3.3.

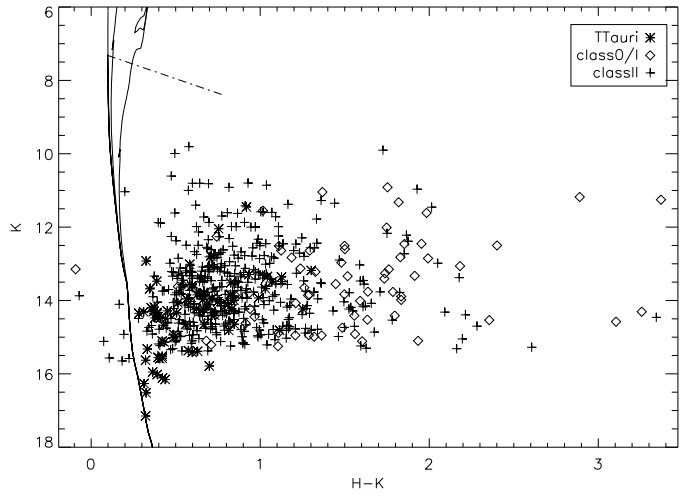

Figure 3.10 2MASS CMD showing Class 0/I and Class II IRAC sources with 2MASS counterparts. Lines and T-Tauri data as in Fig. 3.4.

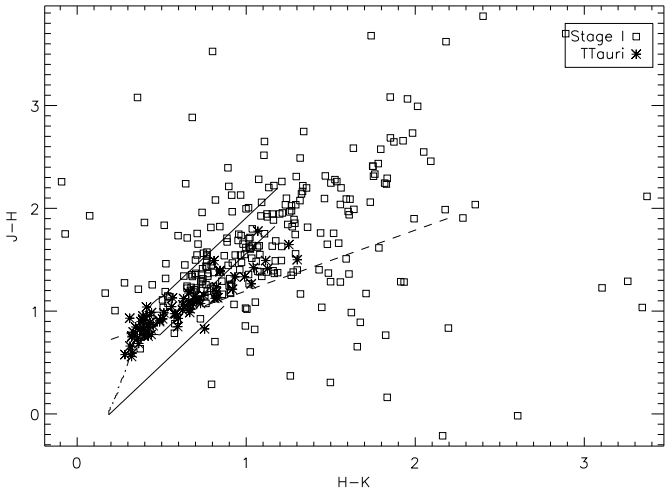

Figure 3.11 2MASS CCD showing Stage I IRAC sources with 2MASS counterparts. Lines and T-Tauri data as in Fig. 3.3.

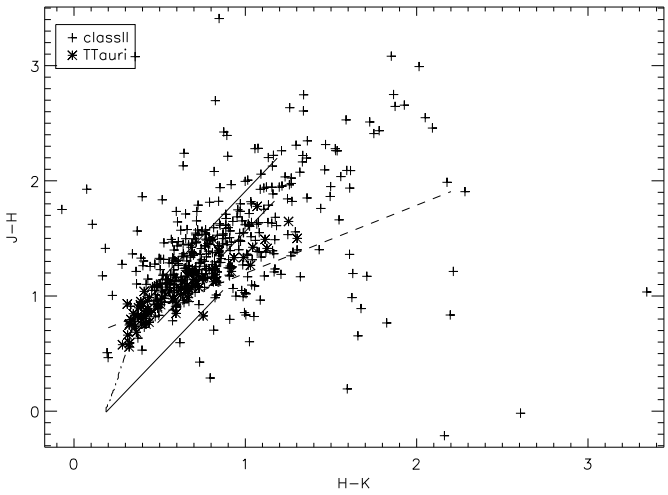

Figure 3.12 Same as Fig. 3.9, but for Class II sources.

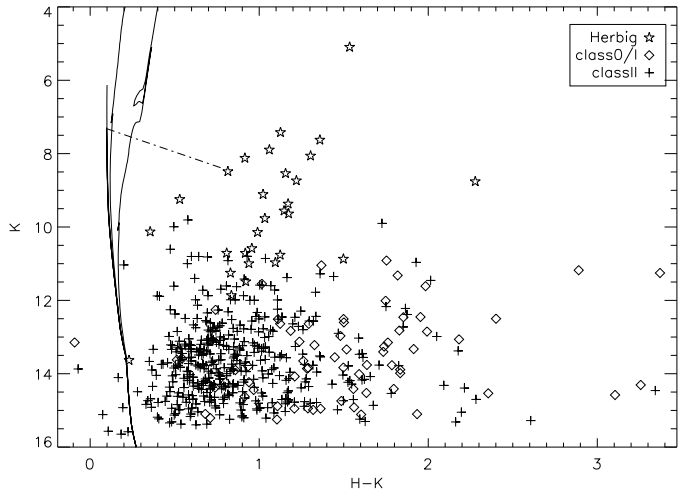

Figure 3.13 Same as Fig. 3.10, but with HAeBe stars.

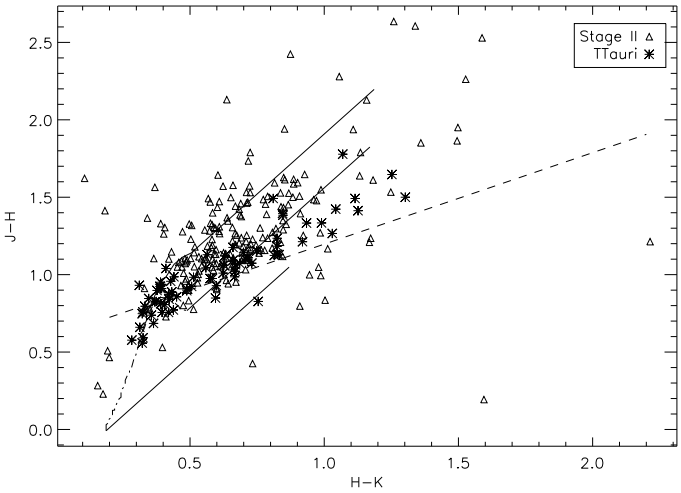

Figure 3.14 Same as Fig. 3.11, but for Stage II sources.

Very few sources lie in the Stage III area, which confirms the robustness of our sample and ability to separate embedded sources and optically thick disks from those consistent with photospheric colors and optically thin disks.

3.3.2 The 2MASS CCD and CMD

We next analyzed the behavior of the 'stage' vs 'class' classification in the 2MASS CCD and CMD for those IRAC sources (Catalog 1, quality flag = 1) with counterparts in the 2MASS PSC. As mentioned above, both Catalog 1 and 2 yield almost identical samples for Class 0/I and Class II sources, and therefore the conclusions below from this analysis are independent of the catalog used.

Analysis of observed (Class) properties

In Section 3.2 we established a scheme to separate the populations of T-Tauri and HAeBe stars based on magnitude and color information. HAeBe stars occupy a distinct region in the CCD, but K magnitude data is still essential to separate the two samples in the region near the T-Tauri locus populated by both types.

We carried out T-Test and F-Test analyses comparing the color and magnitude distributions of various classes. Results are reported in Table 3.9. Statistically, and as in previous cases, the Class 0/I, Class II and T-Tauri samples are indistinguishable in the 2MASS CMD diagram, and therefore selection of low-mass PMS stars is not possible in the infrared without prior knowledge of the protostar population. In color, the Class 0/I sample is intrinsically redder, with the main population of Class II sources lying more intermediate between Class 0/I (and closer) to the T-Tauri sample (Figures 3.9, 3.12, and 3.10). $\sim$ 90% of Class 0/I sources lie between 0.7 $\leq$[H-K]$<$ 2.5, compared to Class II sources, located within 0.4 $\leq$[H-K]$<$ 1.7. While both have similar maximum [H-K] value of $\sim$ 3.4, $\sim$ 80% and $\sim$ 50% of Class 0/I sources lie above [H-K]= 1.0 and 1.5 respectively, compared to $\sim$ 30% and $\sim$ 9% for the Class II population.

We find a completely different scenario when focusing on the intermediate mass HAeBe population. As shown in Figure 3.4, Herbig stars are not only redder, but brighter than T-Tauri stars, with both populations clearly separated in the CMD. Class 0/I candidates *are not* consistent with the colors *or* magnitudes of HAeBe stars (Class 0/I being redder and dimmer). Class II sources are consistent in color with Herbig stars (i.e., intermediate between T-Tauri and Class 0/I), but are again dimmer than typical HAeBe stars (Figure 3.13). While a spectroscopic analysis is still required to confirm our HAeBe candidates as such, we find that, contrary to T-Tauri stars, Herbig stars may still be selected without prior knowledge of the embedded population.

Comparative Analysis of Intrinsically Different Populations (Stages)

Using the 2MASS data we find that the populations in Stage I and Stage II (as defined in Robitaille et al., 2006), when treated as a whole, are indistinguishable with respect to observed K magnitude (e.g., Figs.3.15, 3.16, and 3.17). However, while Stage I sources are found in the color region occupied by Stage II, members of the former population consistently reach redder colors: $\sim$ 90% of Stage I sources have [H-K]$>$ 0.6, $\sim$ 85% have [H-K]$>$ 0.7, $\sim$ 55% have [H-K]$>$ 1.0, and $\sim$ 25% have [H-K]$>$ 1.5 (maximum [H-K]=$\sim$ 3.5). The corresponding statistics for Stage II are $\sim$ 65%, $\sim$ 40%, 10%, and 2% (maximum [H-K]= 2.2).

F-test significance levels between Stage I-Stage II and the T-Tauri population show both groups are statistically consistent with having been drawn from the same parent population in K magnitude as the T-Tauri sample (sig. levels: 0.41 and 0.58, respectively), with Stage II *also* consistent in color (sig. level: 0.39) with the PMS population (dominating in the reddening band of typical main-sequence and giant stars). Stage I sources show a larger scatter in the CCD (e.g., Figures 3.11, 3.14), and significance levels obtained from Student's t-test and F-test between the two populations agree with both having different parent distributions based on color information (Table 3.10).

Table 3.10 General 2MASS Properties: 'Stage I' vs 'Stage II' Population

Stage	<[H-K]>	σ	<[J-H]>	σ	<K>	σ	#Obj.
1	1.2	0.6	1.7	0.6	13.6	1.1	254
2	0.7	0.3	1.3	0.4	13.6	1.1	203
		T-Test Stat.	Sig.[a]	F-Test Stat.	Sig.		
	[H-K]	10.6	1E-23	4.1	4E-23		
	[J-H]	8.0	1E-14	2.9	5E-14		
	[K]	0.4	0.7	1.1	0.7		

[a] Significance.

We find no clear boundary in the CCD or CMD separating sources with intrinsic, physically different characteristics, which could easily be explained by different inclination angles. About 90% of Stage 0/I sources lie in the range 0.5 $\leq$[H-K]$<$ 2.0, $\sim$ 90% of Stage II between 0.4 $\leq$[H-K]$<$ 1.2, leaving the region in [H-K]$\geq$ 1.2 as the area dominated by (younger) sources with $\dot{M}_{\rm env}/M_{\star} > 10^{-6}\,{\rm yr}^{-1}$ (e.g., Figure 3.17).

3.4 Spatial Distribution and Clustering: Group Classification and Characterization

There is strong evidence that star formation in GMCs occurs primarily in clusters. The strong link between 'clustered star-formation' and high-mass star formation implies that in order to investigate the nature and processes involved in the formation of the most massive stars it is crucial to investigate the characteristics of young stellar clusters and their pre-stellar progenitors. This analysis, described below, was based on our YSO surface density maps (e.g., Chavarría et al., 2008) and on the so-called Minimum Spanning Tree Algorithm (MST).

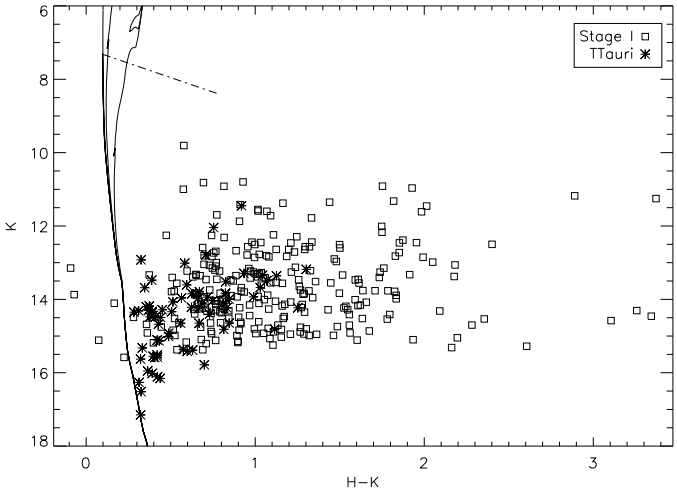

Figure 3.15 2MASS CMD showing Stage I IRAC sources with 2MASS counterparts. Lines and T-Tauri data as in Fig. 3.4.

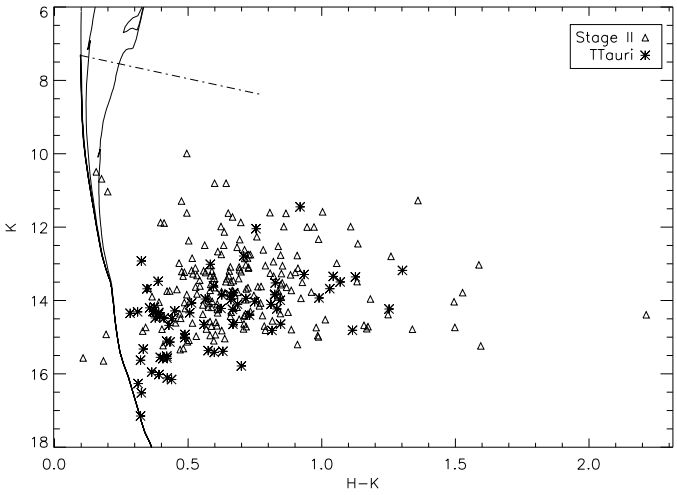

Figure 3.16 Same as Fig. 3.15, but for Stage II sources.

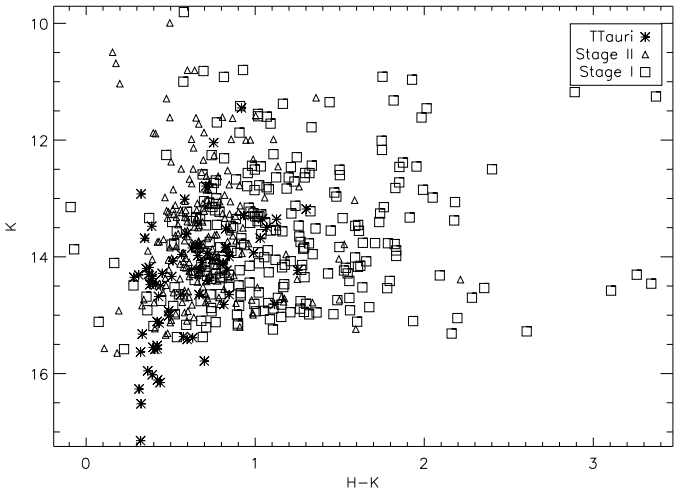

Figure 3.17 Same as Fig. 3.15, but for both Stage I and Stage II sources.

3.4.1 Minimum Spanning Tree Analysis

In order to identify and characterize regions of YSO clustering we first implemented the nearest-neighbor and MST techniques (Gower & Ross, 1969). In the MST algorithm there is an optimized break length, D_{break} (the branch length whose removal maximizes the number of groups, N_g, with members in each group separated by distances shorter than this length) for the specified N_{YSO}, the minimum number of YSOs for the group to be considered a 'cluster' (N_{YSO}). To facilitate comparison with previous analyses of adjacent regions at the same distance (e.g., W5; Koenig et al., 2008) we chose $N_{YSO} = 10$. We also obtained a new set of results for $N_{YSO} = 5$ to investigate the clustering properties at smaller scales. D_{break} was estimated from the peak of the distribution of the number of groups satisfying the YSO requirement (N_g) as a function of d_{break} (Battinelli, 1991); the minimum d_{break}, as well as the incremental step, were chosen to be 0.05 pc, similar to the resolution of MIPS 24 μm at 2 kpc.

D_{break} and N_g are expected to be affected by incompleteness and resolution (e.g., Bastian et al., 2007). Nevertheless, this technique is particularly useful when comparing the relative degree of clustering for different types of YSOs in different regions with

similar data, as in the case of the different subregions in W3. Since we cannot confirm physical associations in these groups, cluster membership cannot be determined without additional data. Therefore, for the following analysis we define the 'sub-branches' resulting for D_{break} as 'stellar groups', to avoid confusion from true clusters and associations. Global results for the *Spitzer* survey are presented in Table 3.11. When a range of break lengths is found to have the same maximum N_g we include the range. MST parameters for the entire YSO population (analyzed as a whole) and for each subregion (each AOR analyzed individually) are shown in Tables 3.11 and 3.12, respectively. Tables also include results for the YSO population as a whole and divided into classes. Each Class is also separated according to N_{YSO} in order to investigate a possible hierarchical structure within larger groups.

Using the group information provided by the MST algorithm and the technique from Battinelli (1991) we first explored whether there might be a characteristic scale in the entire *Spitzer* survey (Table 3.11).

Our list of YSO candidates (Class 0/I, Class II, Class 0/I* and Class II* candidates: 'All' class in Table 3.11) from Catalog 1 yields $D_{break} = 0.6$ for a minimum group membership of $N_{YSO} = 10$, resulting in 56% of the YSO population associated with a group. Flag = 1-only sources and Catalog 2 (both containing less than half the sources in Catalog 1) are more consistent with a larger length and grouped fraction of ~ 1.1 pc and 73.5%, respectively. It is clear that incompleteness will affect the optimal break length, as missing sources will affect the YSO grouping and result in spatially larger groups in order to satisfy the minimum group membership requirement. As shown in Table 3.12, this appears to be an issue mainly when considering the (*) population, which constitutes the most uncertain sample and the main difference between Catalog 1 and Catalog 2. Exclusion of this sample affects the Class 0/I candidate sample in particular, because when the highly embedded population is omitted the few remaining typical Class 0/I sources are more widely distributed, resulting in spatially larger groups for a given N_{YSO}.

Table 3.11 Identified Stellar Groups in W3

			All Survey					
			Flag= 0			Flag= 1		
Catalog	Class	N_{YSO}	D_{break}	N_g	% Assoc.	D_{break}	N_g	% Assoc.
1	All[a]	10	0.60	27	56%	1.2	13	76%
2	All	10	$0.60 - 1.2$	15	$40 - 78\%$	1.2	13	76%
1	Class0/I	10	$3.1 - 3.4$	6	$82 - 83\%$	$3.1 - 3.4$	6	$80 - 82\%$
1	ClassII	10	0.85	14	55%	0.85	14	56%
1	PMS	10	$0.70 - 1.2$	6	$30 - 61\%$			
1	Class0/I/II	10	$0.60 - 1.2$	15	$40 - 78\%$	0.80	13	54%
1	All	5	0.45	60	53%	0.55	33	54%
2	All	5	$0.55 - 0.60$	37	$55 - 60\%$	0.95	33	54%
1	Class0/I	5	$2.3 - 2.8$	10	$80 - 88\%$	$2.3 - 2.8$	10	$80 - 87\%$
1	ClassII	5	0.60	29	53%	0.60	24	51%
1	PMS	5	0.65	14	37%			
1	Class0/I/II	5	$0.55 - 0.60$	39	$57 - 62\%$	$0.55 - 0.65$	32	$54 - 63\%$

[a] Includes Class0/I, Class0/I*, ClassII, and ClassII*. Other classes exclude (*) candidates unless specifically mentioned.

Table 3.12 Identified Stellar Groups in Individual Subregions of W3[a]

W3 Main/(OH)						
	$N_{YSO} = 10$			$N_{YSO} = 5$		
Class	D_{break}	N_g	% Assoc.	D_{break}	N_g	% Assoc.
All[b]	0.45	11	48%	0.45	23	62%
Class0/I/II	0.75	5	63%	0.55	11	51%
Class0/I	$2.1 - 3.6$	2	$74 - 97\%$	2.0	4	77%
Class0/I+Class0/I*	$0.45 - 0.55$	6	$35 - 49\%$	0.55	22	72%
ClassII	$0.65 - 0.85$	2	$35 - 49\%$	0.55	8	44%
ClassII+ClassII*	$0.65 - 0.85$	2	$30 - 43\%$	0.55	9	40%
PMS	$0.75 - 1.2$	2	$38 - 85\%$	0.65	8	45%
...						

[a] Table is published in its entirety in the *Astrophysical Journal*.

[b] Class 0/I, Class 0/I*, Class II, and Class II*

The information from Catalog 1 (all flags) is therefore expected to be a more (statistically) significant indicator of the properties of the overall population, and so this is the primary catalog used in the following analysis. We also find that all the results derived for $N_{YSO} = 5$ are comparable with the results derived from Catalog 1 and $N_{YSO} = 10$, with a typical $D_{break} \sim 0.54\,pc$ containing 55% of the YSO population. This is in good agreement with the results from Koenig et al. (2008), who found optimal break lengths in the neighboring region of W5 (for a sample of the same characteristics) of 0.54 pc (YSO fraction: 44%).

3.4.2 Determination of Group Intrinsic Properties

Results above indicate that the global YSO population of W3 as a whole shows a tendency to group with a scale D_{break} comparable to or less than half a parsec. While larger than typical core sizes associated with the formation of individual stars ($\sim 0.1\,pc$; e.g., McKee & Ostriker, 2007; Motte et al., 2007), these scales are consistent with clump-like objects ($\sim 0.5\,pc$; e.g., Zinnecker & Yorke, 2007) considered to be the likely birth place of stellar clusters. This led Koenig et al. (2008) to conclude that these scales might well be typical of high-mass star forming regions. However, the relevance of this result and its underlying relation to the actual physical processes in star formation remains ambiguous.

It is important to quantify how representative this value is of the inter-YSO separations and how relevant this grouping is to the original birth configuration and conditions of the eventual stellar members. We examined the distribution of D_{near}, the distance of a YSO to its nearest neighbor, both for the entire sample (Table 3.13) and for members within a specific group (Table 3.14). Typically, D_{near} is considerably smaller than half a parsec, and therefore the optimal D_{break} is more indicative of 'inter-cluster' separation than YSO separation, and therefore more relevant for cluster formation than that of individual stars. We note that embedded clusters of high-mass stars like the one forming IRS5 (W3 Main) or the Trapezium in the Orion Nebula have *maximum* projected

stellar separations of the order of $0.02 - 0.05\,\mathrm{pc}$ (Megeath et al., 2005). These approach the resolution limits of IRAC and MIPS $24\,\mu\mathrm{m}$, respectively. Therefore, a given *Spitzer* 'YSO' may in fact contain more than one protostar. The clear link between high-mass stars and clusters, however, make the present study a required step for understanding the physics behind high-mass star formation and the differences with respect to that of low-mass stars.

With this goal in mind, we analyzed each subregion of W3 in more detail to investigate the underlying properties of the stellar groups found by the MST algorithm, as well as possible local differences on the intrinsic characteristics of the stellar population. Tables 3.13 and 3.14 include the parameters derived from the YSO candidate list in Catalog 1. The former includes, for each subregion, the total area surveyed, the extinction range, the total mass in the region derived from the extinction maps (e.g., Heiderman et al., 2010), the number of YSOs (Table 3.6), the total surface density, the YSO surface density (e.g., Chavarría et al., 2008), and the star formation efficiency (SFE) of the region assuming that the YSOs are solar-mass stars. The latter assumption is not expected to be accurate, especially considering the possibility of some *Spitzer* YSOs actually being more than one object. However, we used this parameter as a measure of the *relative* properties of the different stellar groups, just like when considering the 'ages' of the regions in W3 (Section 3.5). In both tables uncertainties for the mass and surface density have been derived from the statistical uncertainties in the extinction calculations. These uncertainties do not include effects such as variations in the extinction law or background fitting uncertainties during the creation of the maps. The final errors in these maps do not account for the larger differences observed with respect to other extinction estimates in the literature, and which depend on knowledge of the dust emissivity and temperature (Rowles & Froebrich, 2009). Changes in these last parameters can, by themselves, affect the estimated extinction values by a factor of ~ 2, and therefore the uncertainties derived from this work will be underestimated. We note that SFE is the amount of mass in

YSOs *at present* compared to the total mass, and therefore not necessarily the ultimate conversion efficiency.

Table 3.14 summarizes the average properties of the identified groups for $N_{YSO} = 10$ using the break length derived from the global analysis of the entire *Spitzer* survey ($D_{break} = 0.6\,pc$; Table 3.11). Several methods have been used to characterize the size and shape of identified groups, from circular to convex-hull techniques (e.g., Bastian et al., 2007; Gutermuth et al., 2009). To characterize the size and elongation of the group we chose to use an elliptical area. The center was defined as the average position of the YSOs within the group. The semimajor axis is the vector from the chosen center to the farthest YSO. The semiminor axis is the minimum size required to keep all the YSOs within the ellipse (Table 3.14). Parameters for individual groups have been included in Table 3.15.

3.5 W3 in Perspective: Stellar Content, Cluster Properties, and Star Formation Activity

W3 is believed to have signatures of both triggered (HDL; e.g., Oey et al., 2005) and isolated (KR 140; e.g., Kerton et al., 2008) high-mass star formation. The existence of different star formation processes in the same cloud makes W3 a prime location for further investigation. The identification and characterization of the embedded/young ($1-2\,Myr$) cluster population (including their relative age) can shed some light on cluster and high-mass star formation. With this goal in mind, in this section we use the spatial distribution of YSO classes, the properties of the identified groups, and the surface density/age maps to present a description of the star formation history and activity in W3.

We carried out the main analysis on W3 by working on each subregion individually, while using common group properties (e.g., N_{YSO} and D_{break}) for the entire survey. Clearly, the definition and properties of the populations that are 'clustered' or 'dis-

Table 3.13 Average Global Parameters in Subregions of W3[a]

Column	Units	Description
1		Region
2	pc	D_{Near} (Min-Max Range)
3	pc	D_{Near} (Mean)
4	pc^2	Area
5	mag	A_V (Min-Max Range)
6	mag	A_V (Mean)
7	$10^4\,M_\odot$	$Mass_{gas}$
8	$M_\odot\,pc^{-2}$	Σ_{gas}
9		n_{YSO}
10	pc^{-2}	Σ_{YSO} (Min-Max Range)
11	pc^{-2}	Σ_{YSO} (Mean)
12		SFE

[a] Table lists the parameters estimated for each subregion in W3 for guidance regarding its form and content. It is shown in its entirety in the *Astrophysical Journal*.

Table 3.14 Average Parameters of Groups in Subregions of W3[a]

Column	Units	Description
1		Data: Subregion
2	pc	D_{Near} (Min-Max Range)
3	pc	D_{Near} (Mean)
4	pc^2	Area
5	mag	A_V (Min-Max Range)
6	mag	A_V (Mean)
7	$10^2\,M_\odot$	$Mass_{gas}$
8	$M_\odot\,pc^{-2}$	Σ_{gas}
9		n_{YSO}
10	pc^{-2}	Σ_{YSO} (Min-Max Range)
11	pc^{-2}	Σ_{YSO} (Mean)
12		SFE
13	pc	a: Ellipse semi-major axis
14	pc	a/b

[a] Table lists the parameters estimated for each subregion in W3 for guidance regarding its form and content. It is shown in its entirety in the *Astrophysical Journal*.

Table 3.15 Individual Parameters of Groups in Subregions of W3[a]

Column	Units	Description
1	h m s	RA center
2	d m s	Dec center
3	pc^{-2}	Area
4	mag	Minimum A_V
5	mag	Maximum A_V
6	mag	Mean A_V
7	$M_\odot$	Gas Mass
8	$M_\odot$	Error Gas Mass
9	$M_\odot\,pc^{-2}$	Surface Density
10	$M_\odot\,pc^{-2}$	Error Surface Density
11	pc^{-2}	Minimum YSO Surface Density
12	pc^{-2}	Maximum YSO Surface Density
13	pc^{-2}	Mean YSO Surface Density
14	pc^{-2}	Error Mean YSO Surface Density
15		Star Formation Efficiency [SFE]
16	pc	Minimum Distance Neighboring YSOs
17	pc	Maximum Distance Neighboring YSOs
18	pc	Mean Distance Neighboring YSOs
19	pc	Error Mean Distance Neighboring YSOs
20	pc	Ellipse semi-major axis [a]
21		Axis Ratio [a/b]
22		Number of YSOs in Group
23		Group Designation in this work
24		Unique [catalog] Group Designation

[a] Table lists the parameters estimated for each group in W3 for guidance regarding its form and content. It is shown in its entirety in the *Astrophysical Journal*.

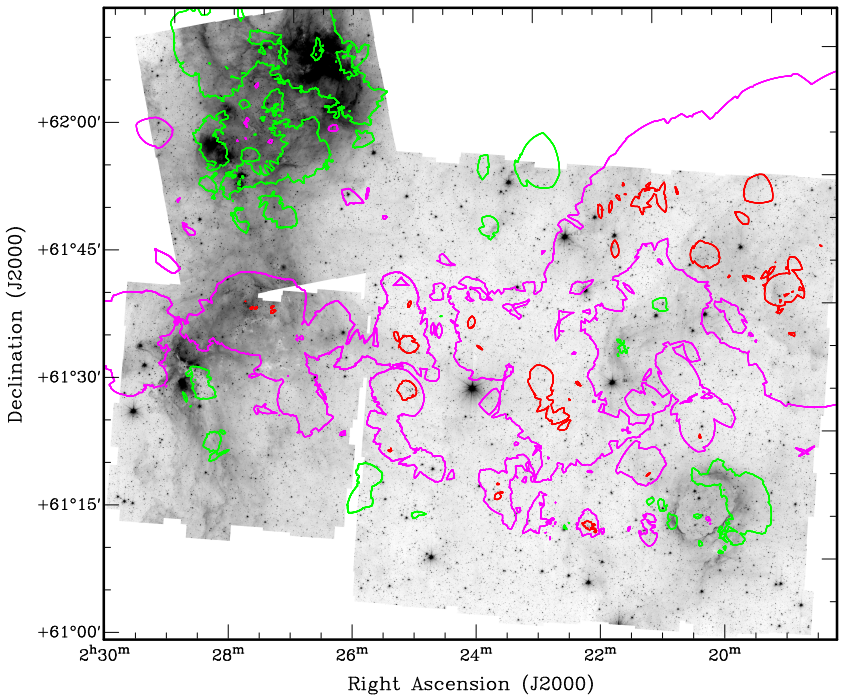

Figure 3.18 Greyscale *Spitzer* channel 1 image of W3 with a superposition of 'age' contours from the ratio of Class II/Class 0/I, including (*) population. Only specific contours are shown for clarity: relatively old, 3% of map peak value (red); intermediate, 0.5% (magenta); and relatively young, 0.05% (green).

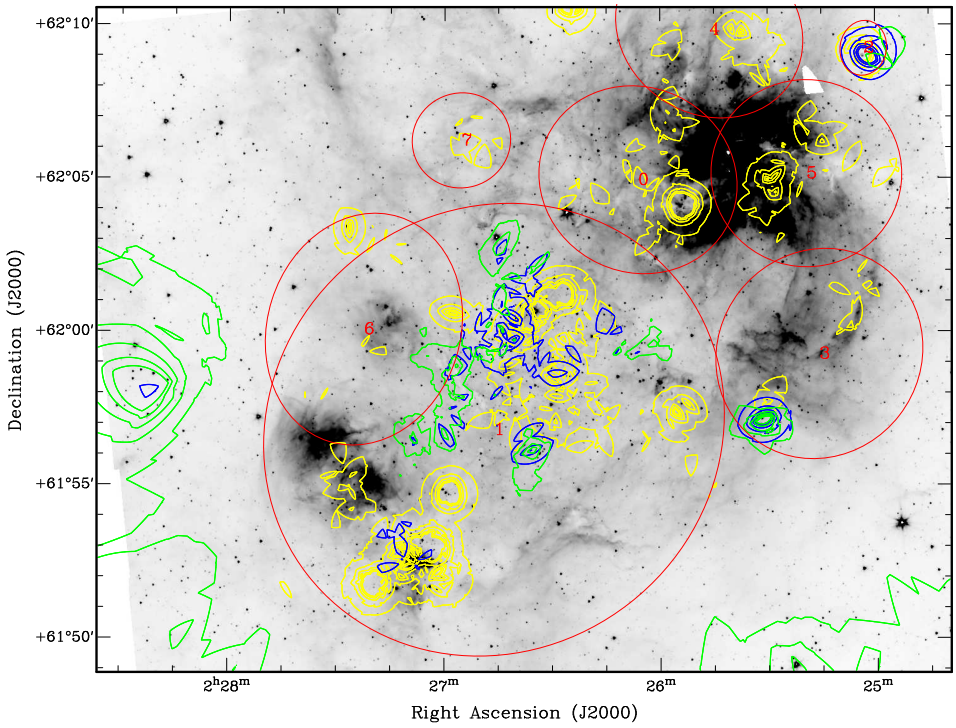

Figure 3.19 Greyscale *Spitzer* channel 1 image of W3 Main/(OH) with identified groups for $N_{YSO} = 10$ and $D_{break} = 0.6\,pc$ (red ellipses). Yellow contours are Class 0/I surface density contours between $1-5\%$ of peak value $\sim 560\,YSO\,pc^{-2}$ in 1% steps. Blue contours are Class II contours between $5-25\%$ of peak value $\sim 100\,YSO\,pc^{-2}$ in 5% steps. YSO contours have been chosen to span a common YSO range for both classes of $\sim 5-25\,YSO\,pc^{-2}$. Green contours are of the ratio of Class II/Class 0/I YSO surface density maps; these include transition and highly embedded candidates: (*) classification. These 'age' contours are for 0.5-2.5% of the peak value of ~ 300 in 0.5% steps, a range chosen to highlight the youngest regions.

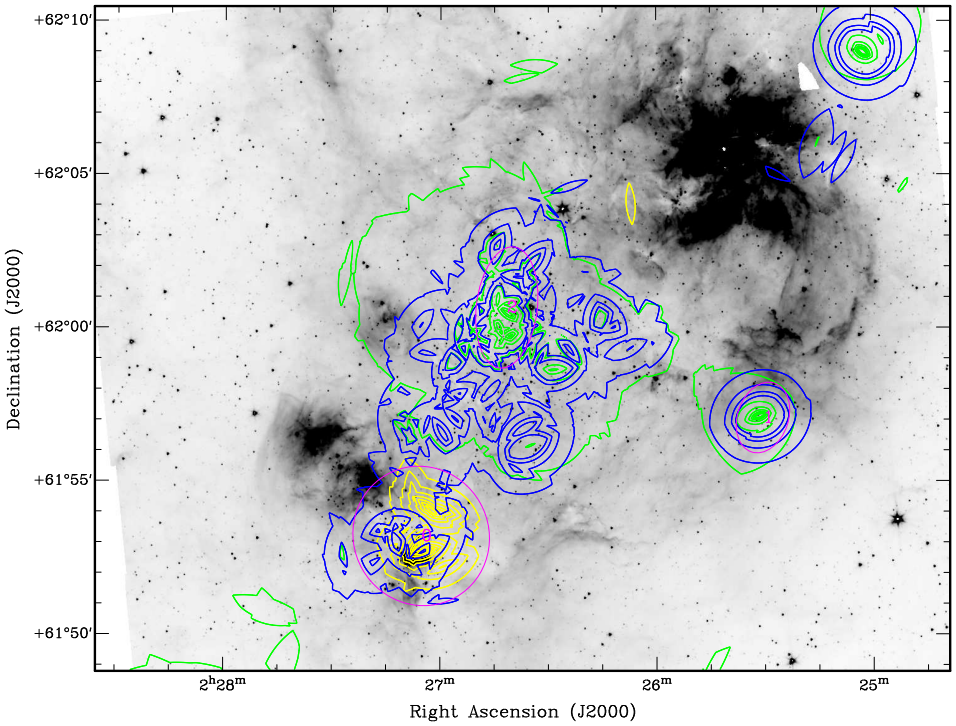

Figure 3.20 Like Fig. 3.19, but excluding the less reliable (*) population. Groups are marked as magenta ellipses. Class 0/I surface density contours (yellow) between $20-90\%$ of peak value $\sim 8\,\mathrm{YSO\,pc^{-2}}$ in 10% steps. Class II contours (blue) between $1.5-7\%$ of peak value $\sim 100\,\mathrm{YSO\,pc^{-2}}$ in $\sim 1.4\%$ steps. YSO contours have been chosen to span a common YSO range of $\sim 1.5-7\,\mathrm{YSO\,pc^{-2}}$. 'Age' contours (green) are between 1-31% of peak value of ~ 500 in 5% steps.

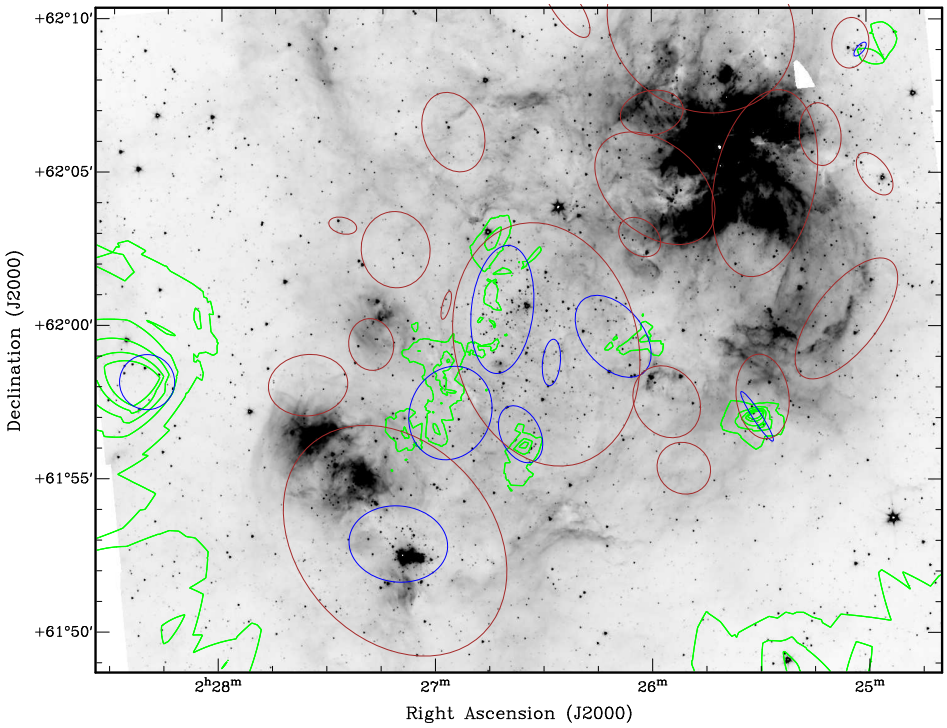

Figure 3.21 Like Fig. 3.19 but for $N_{YSO} = 5$ and $D_{break} = 0.55\,pc$, which is optimal in this region for both Class 0/I + Class 0/I* groups (brown ellipses), and Class II + Class II* groups (blue ellipses). Parameters are from Table 3.12. Figure shows the location of the highest concentrations of YSOs according to Class.

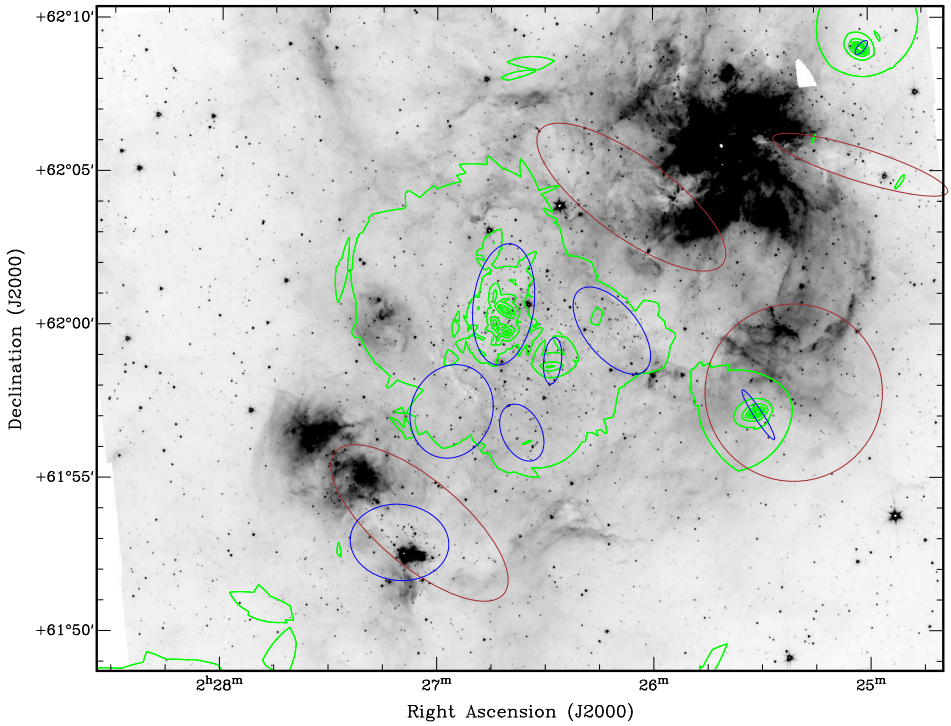

Figure 3.22 Like Fig. 3.21, but excluding the (*) population. Now $D_{break} = 1.95\,pc$, which is optimal for Class 0/I (brown ellipses), and $D_{break} = 0.55$, which is optimal for Class II (blue ellipses). Parameters are from Table 3.12.

tributed' (objects outside the 'cluster' boundaries, stars formed in isolation and members displaced from their original birthplaces) depend on the fundamental definition of 'cluster' and the chosen boundary (see e.g., Bressert et al., 2010 for a compilation of recent cluster identification techniques). The application of a common definition and technique throughout an entire cloud like W3 (same distance/resolution) can, however, be used to determine the *relative* properties of each subregion, avoiding major systematic effects arising from distance dependent factors or an assumed definition. For W3, this approach is used to investigate the possibility of intrinsic differences between stellar groups in different environments and with different stellar activity (e.g., HDL vs. KR 140), and so illuminate possible intrinsic differences between the clustered and distributed populations (e.g., Allen et al., 2007). Unless mentioned otherwise, the following analysis will be based on the YSO sample from Catalog 1 and groups with $N_{YSO} = 10$ and $D_{break} = 0.6\,pc$ ('red' groups).

We made use of the YSO density distribution maps and carried out an individual analysis of the identified groups in each subfield in W3 (W3 Main/(OH), AFGL 333, and KR 140). 'Age' maps were also created from the ratio of the YSO surface density images, for example the ratio of Class II to Class 0/I candidates. Peaks in this map represent the 'oldest' of those regions *containing YSOs*, whereas a low value in a region populated by YSOs indicates a relatively young region. The maps used in this work are best suited for the analysis of regions known to contain YSO groups, because the low map values in inactive or unpopulated regions depend on YSOs rather distant from the pixel in question. Figure 3.18 shows the age map for the entire W3 cloud. The 'oldest' star forming regions (peaks) are located in the KR 140 field, although we note that many of these old regions are not always associated with identified groups (see below).

Finally, it is important to distinguish between the actual 'age' of the system (from the start of star formation activity) and 'apparent age'. In an undisturbed system initiated by a short-lived burst of star formation, our ratio method yields reliable ages. High den-

sity, central regions would contain the oldest population and shorter free-fall timescales ($t_{ff} \alpha \rho^{-1/2}$). Such an idealized system would show a relatively ordered distribution of its population, and the age estimate would be an acceptable upper limit. On the other hand, our age estimates for triggered regions are expected to be biased toward younger ages, because there is strong evidence (e.g., IC 1795; see below) for star formation being an on-going process lasting for at least a few Myr, rather than being the result of an isolated burst of star formation. Thus, on average, the YSO groups in W3 Main/ (OH) might only appear to be the youngest using the simple age map contours (Fig. 3.18).

3.5.1 Star Formation in the HDL: W3 Main/(OH) and AFGL 333

AFGL 333 and W3 Main/(OH) are located in the eastern HDL neighboring W4 (Fig. 3.1). The HDL is the most dense structure and essentially all the major activity of the GMC is found within its boundaries. In both fields we have identified signatures indicative of several modes of star formation contributing to the overall structure and young stellar population.

The W3 Main/(OH) Field

The cluster IC 1795 is located at the center of an eroded shell-like structure containing the W3 Main and W3 (OH) complexes. Both show the most active high-mass star formation, including deeply embedded clusters, H II regions, and a trapezium-like system rivaling that in the Orion nebula (e.g., Megeath et al., 2005).

Figure 3.19 shows the W3 Main/(OH) field with the identified groups, the contours representing the surface density distributions for YSOs calculated on a grid identical to that of the *Spitzer* images, and including highly embedded and transition stage candidates (Class 0/I* and Class II*: (*) sample). This figure also includes 'age' contours, obtained from the ratio of the surface density maps: [Class II+Class II*]/[Class 0/I+Class 0/I*].

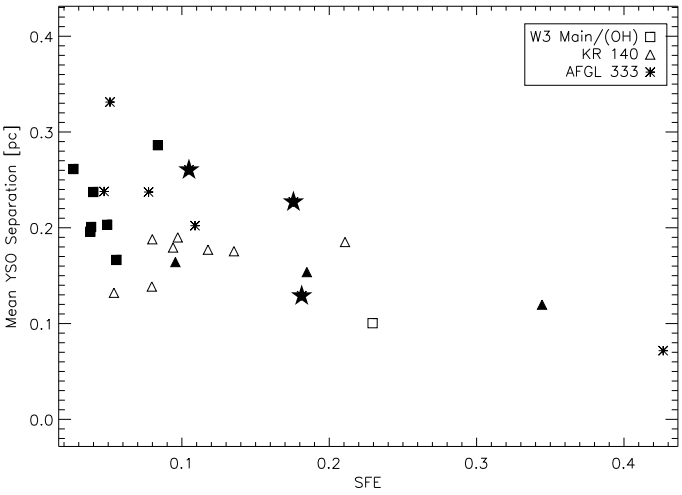

Figure 3.23 Inter-YSO separations as a function of SFE for W3 Main/(OH), KR 140, and AFGL 333. YSOs (including highly embedded and transition candidates) are associated in groups with $N_{YSO} = 10$ and $D_{break} = 0.6\,pc$. Filled symbols mark those groups with the youngest ages (Class II/Class 0/I < 1).

Figure 3.20 shows the groups found for the same N_{YSO} and break length as Figure 3.19, but excluding the less reliable (*) population. For convenience these will be specifically referred to as 'magenta' groups, to distinguish them from the 'red' groups in Figure 3.19. Reduction of the number of candidate YSOs yielded smaller and fewer groups, as expected. In addition, the omission of highly embedded sources, combined with the confusion in the regions of strong IR emission, highly affected the numbers of YSOs detected in the innermost and most active regions, especially around W3 Main. We find two magenta groups within red Group 1, coincident with IC 1795. The oldest (magenta Group 2; Fig. 3.20) coincides with the oldest part of IC 1795. Magenta Group 0 coincides with a high extinction region and contains numerous H II regions and known clusters, including the well known maser sources W3 (OH) and W3 (H_2O). Although with $N_m < 25$, the characteristics of these two groups are consistent with those of mid-rich triggered groups in Figure 3.19 (see below) linked to high-mass star formation,

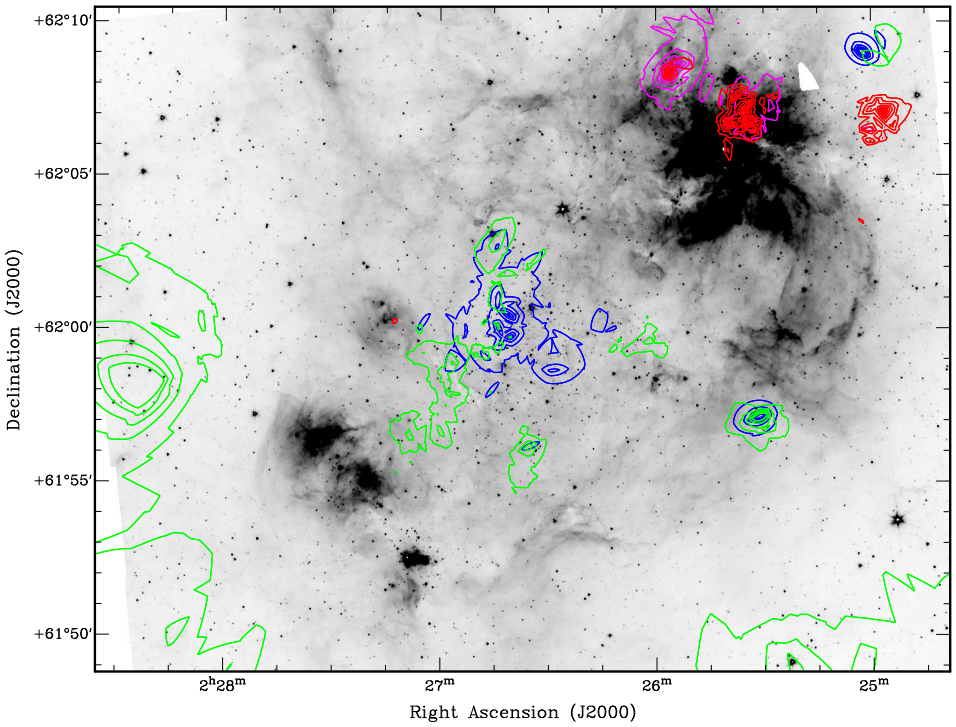

Figure 3.24 Same as Fig. 3.19 with various 'age' contours superimposed. Blue contours are Class II/Class 0/I surface density contours between 5-30% of peak value of ~ 500 in 5% steps, excluding the (*) population. Red and magenta contours are for PMS/[Class 0/I+Class II] between 3-10% of peak value of ~ 80 in 1% steps (red), and 10-60% in 10% steps (magenta), with and without the (*) population, respectively. Green contours like Fig. 3.19.

with surface densities greater than $70\,M_{\odot}\,pc^{-2}$, $A_{V-mean} > 5.0$, and mean inter-YSO separations $D < 0.25\,pc$.

In Figures 3.21 and 3.22 we show the groups identified for each particular Class (with and without the (*) population) with the relaxed requirement of $N_{YSO} = 5$. The identified groups more closely trace particular structures observed in extinction (e.g., filaments), as well as smaller separate concentrations of Class 0/I and Class II candidates.

We suggest that, overall, clustered formation in compact clumps/cores can be distinguished from the star formation process associated with young groups that have low surface density and extinction and that are found in triggered regions (e.g., Groups 6 and 7; Fig. 3.19). Figure 3.23 shows the inter-YSO separations as a function of SFE. Groups in 'induced' regions with the largest separations have been less efficient in forming young stars, which could be due to formation in a turbulent environment. This could be indicative of the 'distributed' star formation mode taking over in those regions that lack the conditions, like high column density and low turbulence, required to form high-mass stars and their (richer) parent clusters. Indeed, a SIMBAD search reveals no H II regions or clusters associated with any of these triggered groups, which also lack localized and significant radio continuum emission in the Canadian Galactic Plane Survey (CGPS; Taylor et al., 2003) maps. Rich groups ($25 \leq N_m < 50$) such as Group 0 and Group 5 have average inter-YSO separations $< 0.25\,pc$ and the highest surface densities, and both contain within their perimeters a large proportion of the major high-mass star activity of the W3 GMC. This supports the classical view that one can have clustered star formation caused by triggering when at *early stages* high surface densities without disruptive turbulence are present, to ensure that a gravitationally (unstable) bound system is formed.

The privileged location of IC 1795 (Group 1; Fig. 3.19), in the most central and dense parts of the HDL, was likely key in the formation of its rich population. Although it depends on the pre-existence of the HDL, its location, morphology and population characteristics are compatible with isolated/quiescent formation, and not necessarily the

product of a triggering event as suggested in previous studies. A similar (quiescent) origin is also suggested for some individual isolated groups in the outer boundaries of the field, characterized by a relatively poor and yet closely spaced (contrary to the poor groups associated with triggered regions discussed above) old population in a relatively compact configuration (e.g., Group 2 in Fig. 3.19). Group 1 is the next 'oldest' system after Group 2, and it is the most massive and richest group, with the smallest separation distances down to 0.02 pc.

W3 Main and (OH) (Fig. 3.1) show the highest extinction and both are likely to have (at least part) of their stellar population induced by IC 1795, in agreement with the conclusions from Oey et al. (2005) and Polychroni et al. (2010). A triggered scenario is supported by i) an elongated 'older' Class II dominated region within Group 1 extending in the directions of W3 Main and W3 (OH) (see Fig. 3.19); ii) the cavity and shell like structure around IC 1795 hosting both systems; and iii) a tendency of Class II candidates to be located toward the most central regions, with younger groups of YSOs following the shell around Group 1 (in increasing age: Groups 4, 7, 0, 5, 3, 6; Fig. 3.19). Using the ratio of Class II/Class 0/I as a relative measurement of age, Group 6, the oldest after Group 2 and Group 1, happens to be also the nearest to IC 1795, while younger groups have larger distances.

Secondary bursts of star formation, as well as a non-negligible star formation duration, are needed to reconcile the characteristics of the YSO population in IC 1795 with the age estimated by Oey et al. (2005) ($3-5$ Myr) using optical photometry and spectral analysis. We find a highly distributed population of Class II and Class 0/I sources in the vicinity of IC 1795. Star formation is estimated to occur in 1-2 dynamical crossing times (Elmegreen, 2000), but larger age spreads are possible if multiple events occur within a certain system. Figures 3.21 and 3.22 show the groups obtained when separating the YSOs according to Class with a minimum group membership requirement of $N_{YSO} = 5$. The 'class subgroups' observed within Group 1 and the triggered population could be indicative of

such additional star formation events. This combined activity likely reinforced the effects of the central cluster when forming the cavity and dense surrounding shell hosting the most massive stars in W3.

Contrary to the suggestion of Oey et al. (2005), some of the stellar activity in W3 Main might also have originally initiated in quiescent mode. Figure 3.24 shows an 'older' (low and intermediate mass) PMS population toward the outer edge of this region, shown by the magenta/red contours. On the other hand there are young groups at the inner edge of W3 Main, closer to IC 1795. By calibrating the Class II/Class 0/I ratio of Group 1 to the age of IC 1795 we obtain an average age for these young groups of $\sim 1.5-2.5$ Myr. In this calculation we assumed the onset of star formation occurred in a single event, and so a larger proportion of Class II sources implies a more evolved population. We ignored effects such as secondary bursts of star formation in the region, and assumed that for groups with similar initial stellar characteristics there is a direct relation between the class ratio and the actual age of the system. A non-negligible period of star formation and internal triggering would mean that it would be more appropriate to consider our age estimates as lower limits. This age estimate for the young groups is however comparable to the estimated age for the oldest (diffuse) H II regions and the PMS population known to dominate in this region ($\sim 10^6$ yrs; Feigelson & Townsley, 2008). Therefore, triggering (either indirectly by IC 1795, and/or by this pre-existing PMS population) could have been responsible for the observed young proto-OB population in the central regions of W3 Main, a secondary burst of high-mass star formation in a region with an already highly enhanced surface density. Such a scenario would nicely link IC 1795 to one of the possible models suggested by Feigelson & Townsley (2008) to explain the origin of W3 Main (option 4 in their list), and could explain the anomalous age distribution (a central young cluster surrounded by an older population) described by these authors.

The AFGL 333 Field

W3 Main and W3 (OH) dominate both in high-mass stars and in star formation activity. The other HDL field, containing AFGL 333, is characterized by a young stellar population in its most part associated with high extinction regions and filamentary structures, that have remained undetected in the 2MASS-based extinction maps. There are also clear similarities and some differences relative to W3 Main/(OH).

Figures 3.25 and 3.26 show the identified YSO groups (with and without the (*) population) for the AFGL 333 field, including YSO surface density contours and age contours. Figures 3.27 and 3.28 show the groups identified for $N_{YSO} = 5$ and different classes (each with their corresponding D_{break}). The oldest and youngest groups are clearly separated, with the youngest (brown ellipses) localized in the central regions, and the oldest (blue ellipses) toward the outer parts of AFGL 333 (northern parts and triggered regions neighboring W4).

Group 4 (Fig. 3.25) is the oldest and most massive group in the field, with the largest area, surface density, and highest extinction of $\sim A_{V-peak} \sim 7.5$). From our analysis we conclude that its population formed first, clearing a region and eroding a cavity-like structure much like IC 1795 (sizes $\sim 6-7\,pc$) but in YSOs less populated. Within this cavity, the YSO population shows a more compact configuration in the eastern side of the group, and a more widely separated population toward the western side, where some high extinction filamentary structures are identifiable. There is also a population of PMS candidates toward the edge of this cavity, on the western side of Group 4 (opposite W4). Just as with IC 1795, the properties of this group (its location in the middle of the HDL and the geometrically 'ordered' population, already eroding the surrounding material) are compatible with it being produced by quiescent formation, rather than having a triggered origin by the Perseus superbubble.

A significant difference relative to W3 Main/(OH) is the abundance of filaments with and without stellar activity. Groups in this field are all relatively poor, with only two

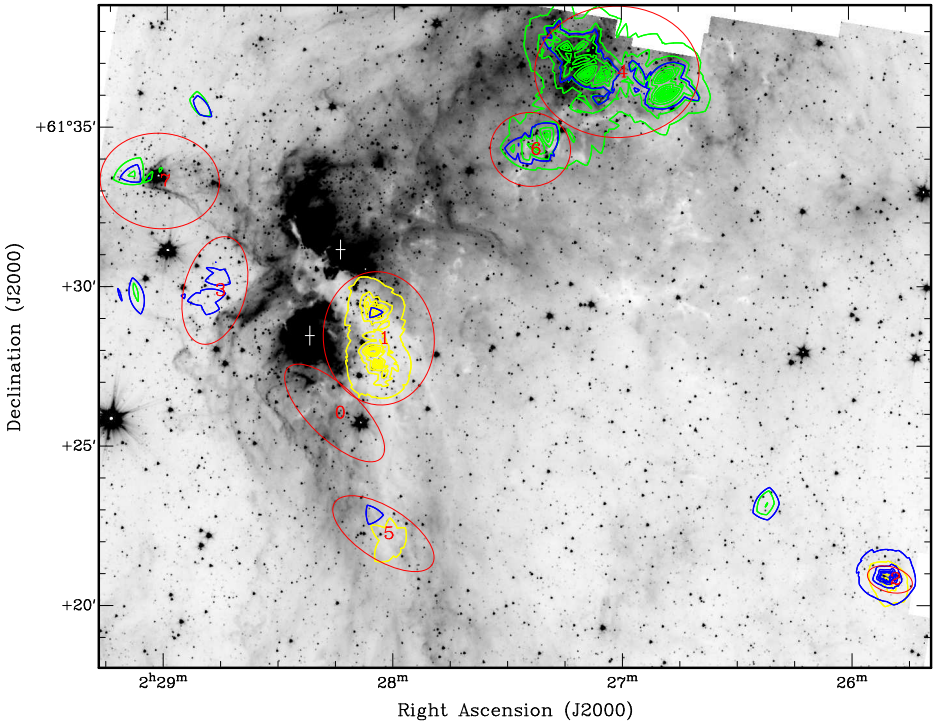

Figure 3.25 Greyscale *Spitzer* channel 1 image of AFGL 333 with identified groups for $N_{YSO} = 10$ and $D_{break} = 0.6\,pc$ (red ellipses). Yellow contours are Class 0/I surface density contours between $5 - 65\%$ of peak value $\sim 120\,YSO\,pc^{-2}$ in 10% steps. Blue contours are Class II contours between $3.5 - 43.5\%$ of peak value $\sim 170\,YSO\,pc^{-2}$ in 10% steps. Crosses are IRAS 02245+6115 (bottom) and IRAS 02244+6117 (top). YSO contours have been chosen to span a common YSO range for both classes of $\sim 6 - 75\,YSO\,pc^{-2}$. Green contours are of the ratio of Class II/Class 0/I YSO surface density maps; these include transition and highly embedded candidates: (*) classification. These 'age' contours are for 10-90% of peak value of ~ 300 in 10% steps. Groups like Group 1 are relatively young, while those like Group 4 are older.

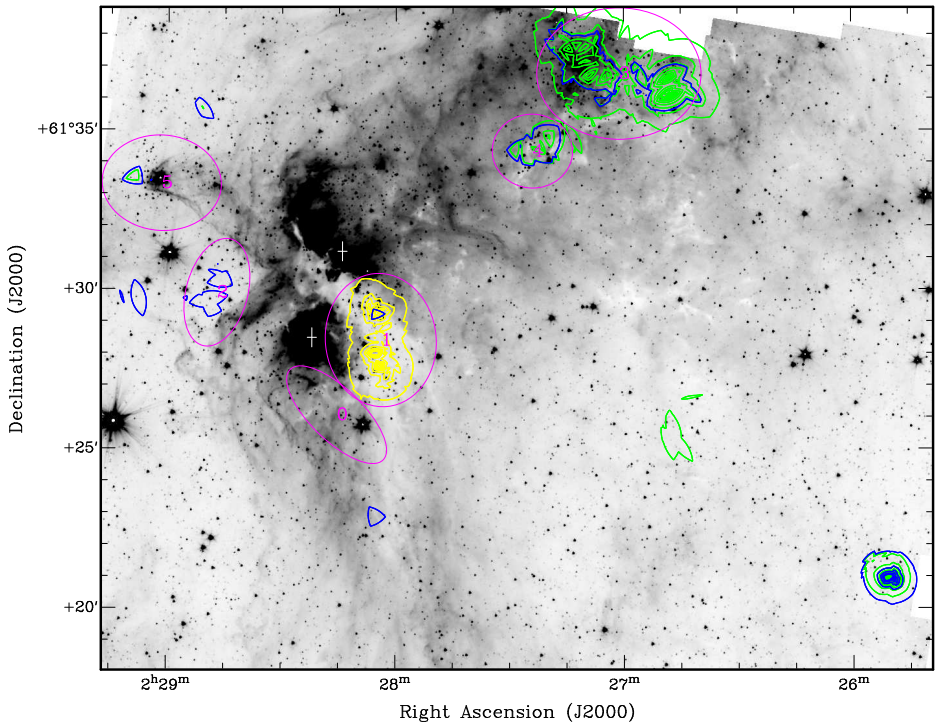

Figure 3.26 Like Fig. 3.25, but excluding the less reliable (*) population. Groups are marked as magenta ellipses. 'Age' contours between 5-80% of peak value of $\sim$ 1000 in 5% steps.

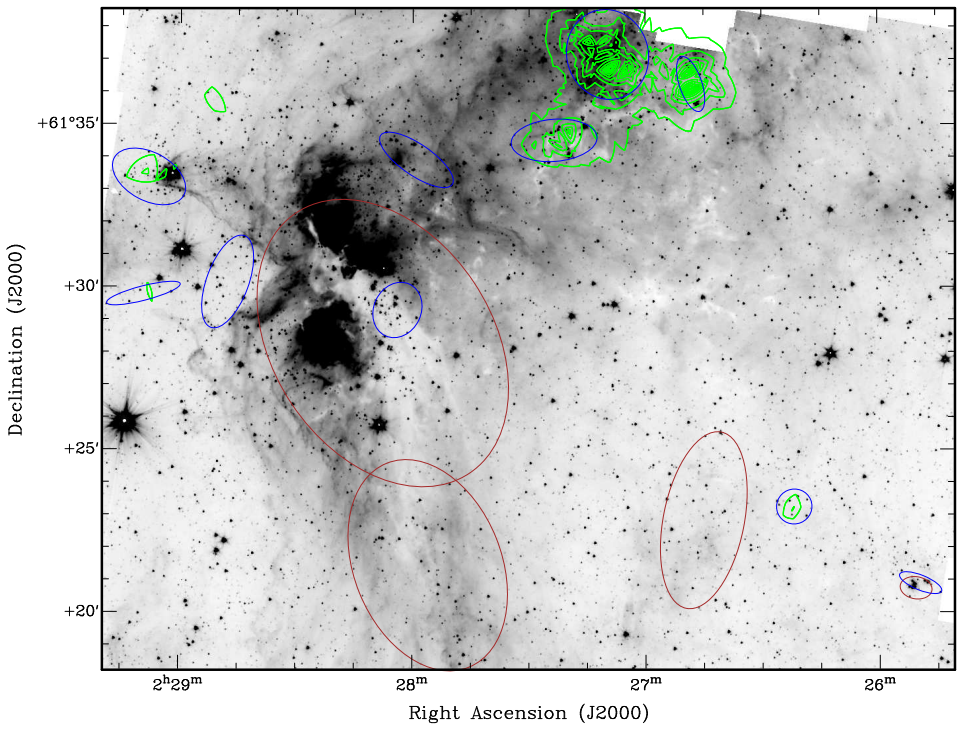

Figure 3.27 Like Fig. 3.25 but for $N_{YSO} = 5$, $D_{break} = 1.25$ pc, and Class 0/I + Class 0/I* (brown ellipses), and $N_{YSO} = 5$, $D_{break} = 0.55$, and Class II + Class II* (blue ellipses). Parameters are from Table 3.12.

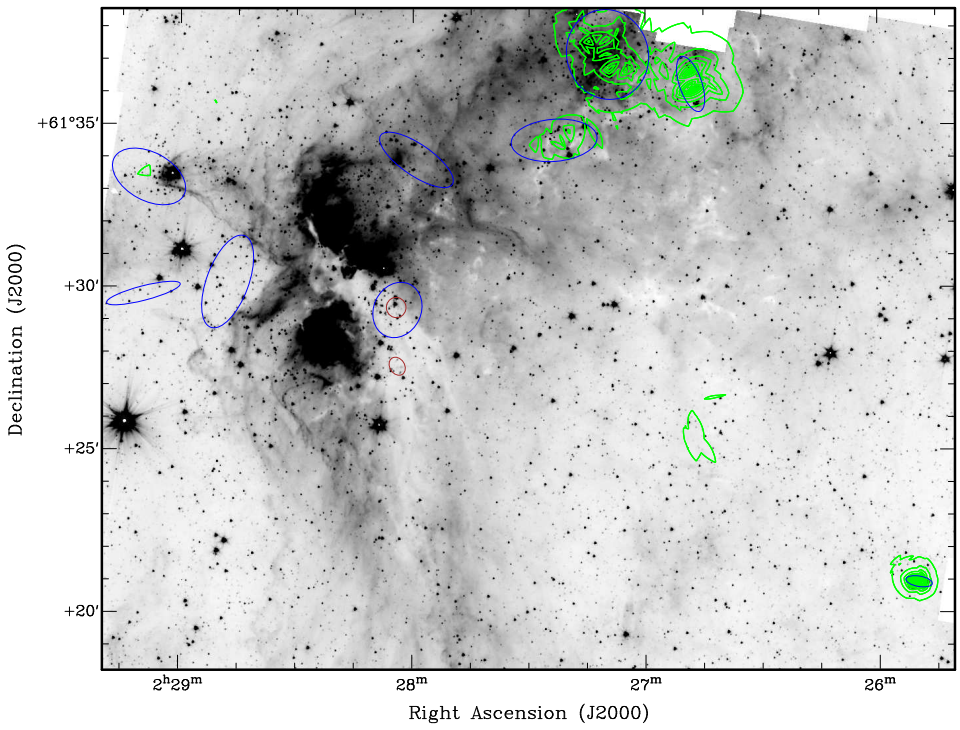

Figure 3.28 Like Fig. 3.26 but for $N_{YSO} = 5$, $D_{break} = 0.15\,pc$, and Class 0/I (brown ellipses), and $N_{YSO} = 5$, $D_{break} = 0.55$, and Class II (blue ellipses). Parameters are from Table 3.12.

groups (red Groups 1 and 4) with N> 25 members (Fig. 3.25) and with the YSO population mainly localized to these filamentary structures. The morphology of such filaments, seen well in *Spitzer* channel 4 (Fig. 3.2), suggests a turbulent origin, a suggestion supported by their remarkable similarity and continuity with nearby (non-extinction) structures. A good example is Group 6 (Fig. 3.25), associated with a filamentary structure within the cavity caused by the stellar population in Group 4, and containing a relatively old YSO population (but still younger than the latter). Its associated population, while slightly offset from that filament either due to displacement since formation or clearing of the immediate surroundings, clearly traces the overall shape of the high extinction, indicating a birth association. While the filament in Group 6 is easily traced, only dispersed 'remnants' of high extinction structures are visible at the western side of Group 4. This supports the 'older' evolutionary stage for the latter, where the apparently dissociated population may be due to the dispersal of their common parental filaments.

A triggered origin is clearly identified for Groups 7 and 3 ($N_m < 25$), both in the outer boundary of the HDL and associated within structures carved by the activity in W4. The pillar associated with Group 7 coincides with a known cluster (IRAS-02252+6120; Bica et al., 2003), containing both a Class II population, located toward the outer edges of the pillar, and Class 0/I sources, mainly in the innermost regions. Such a configuration has previously been observed in other pillar-like structures (e.g., Choudhury et al., 2010) and suggested to be the result of radiative driven implosion (RDI) triggered star formation, in which an ionization/shock front driven by an expanding H II region causes a neighboring overdensity to collapse, triggering the formation of stars.

Group 1 is the youngest and the richest group in Figure 3.25. It is located in the innermost regions of AFGL 333 and it is associated with the most dense and prominent filament in this field. If filaments are formed (or induced to collapse) by turbulence and compression by nearby star activity, then Group 1 might have been induced by the activity at opposite sides associated with IRAS 02245+6115 and IRAS 02244+6117,

bottom and top crosses in Figure 3.25, respectively. The latter contains bright infrared sources (BIRS; Elmegreen, 1980), and the former hosts a known cluster and high-mass star activity (Bica et al., 2003). These form the brightest regions in the MIR in AFGL 333 and both contain a population of PMS in their outermost parts. Thus two active older regions sandwich the central young stellar population of Group 1.

Group 5 (Fig. 3.25), while associated with the same high extinction structure as Group 1, is however relatively member-poor. Its location away from the influence of the main (infrared-bright) star forming activity in AFGL 333 may explain the low membership, in contrast with the richness of Group 1.

High extinction structures border Group 0 as well (especially noticeable in IRAC channel 4; Fig. 3.2). The associated filaments are located within an evacuated region, much like those in Group 6. However, as mentioned above, triggering in such regions of low surface density will likely result in isolated star formation (instead of clustered).

The results from the above analysis remain unchanged when the (*) population is excluded, except for the omission of red Groups 2 and 5 (Fig. 3.26).

We note that the features seen in extinction in the MIR are better tracers of high column density material than the 2MASS-based extinction map, the latter missing some major high extinction areas (e.g., Group 1, Group 7; Fig. 3.25). Thus the mass (and surface density) estimates for associated groups are lower limits. Indeed, Group 1 has the largest number of associated YSOs, and it is expected to have a large surface density comparable to or greater than groups of similar membership, $> 80\,\mathrm{M}_{\odot}\,\mathrm{pc}^{-2}$. The extinction structure associated with this group is the brightest in the AFGL 333 field in the $850\,\mu$m SCUBA map, which is an excellent tracer of column density. We find a similar situation in the KR 140 field (below). For small structures and filaments prominent in the submillimeter maps, including KR 140-N, north of the KR 140 H II region near the center of the field, information is lost in the 2MASS-based extinction maps.

Modes and Sequential Star Formation

It has been argued that the presence of high-mass star forming sites along the interface between W3 and W4 is evidence that the main activity in the HDL is triggered by the expansion of the W4 H II region (e.g., Carpenter et al., 2000 and references therein). This is supported by the estimated ages of the structures (e.g., Oey et al., 2005). We agree that the HDL structure itself was created by W4, with conditions (e.g., turbulence, surface density) favorable for star/cluster formation. However, whether the formation and ultimate collapse of clumps and cores in W3 were directly triggered is less clear. Based on the above evidence it seems also plausible to us that formation of the HDL was followed in sequence by a more quiescent evolution governed by local conditions.

Local triggering does play a major role in enhancing (high-mass) star/cluster formation: i) internal triggering within evacuated regions (inner shells) generates secondary bursts of star formation and a distributed population either by forming or collapsing pre-existing small overdensities (clumps and filaments; IC 1795, AFGL-Group 4, AFGL-Group 0); ii) compression of high density regions generates major bursts of star formation, including high-mass stars and highly embedded clusters (e.g., inner part of W3-Main, W3 (OH), AFGL-Group 1, AFGL-Group 7).

Overall, the star formation activity and processes in the AFGL 333 and W3 Main/(OH) fields operate similarly, albeit less vigorously in the former. Environmental physical differences between the two regions, such as column density distribution, are investigated in the following chapters.

3.5.2 Star Formation in the Central and Western Region: KR 140-N and KR 140 H II Region

The W3 molecular cloud is, overall, in an advanced state of evolution. Channel 4 *Spitzer* images reveal a highly turbulent and dynamic environment with a variety of structures

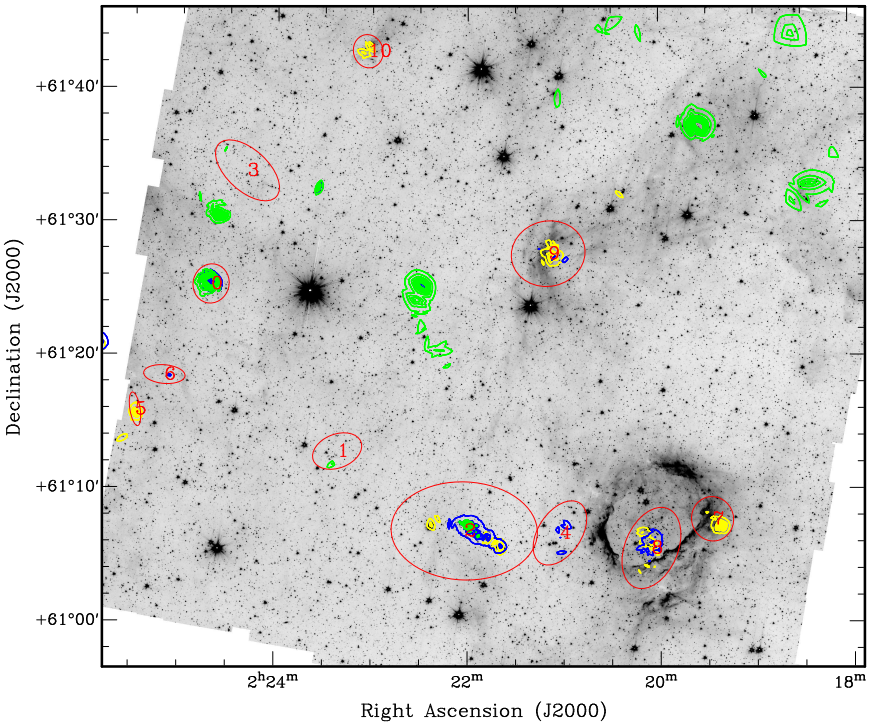

Figure 3.29 Greyscale *Spitzer* channel 1 image of the KR 140 field with identified groups for $N_{YSO} = 10$ and $D_{break} = 0.6\,pc$ (red ellipses). Yellow contours are Class 0/I surface density contours between $10 - 90\%$ of peak value $\sim 100\,YSO\,pc^{-2}$ in 10% steps. Blue contours are Class II contours between $4.0 - 34.0\%$ of peak value $\sim 250\,YSO\,pc^{-2}$ in 10% steps. YSO contours have been chosen to span a common YSO range for both classes of $\sim 10 - 90\,YSO\,pc^{-2}$. Green contours are of the ratio of Class II/Class 0/I YSO surface density maps; these include transition and highly embedded candidates: (*) classification. These 'age' contours are for 4-20% of peak value of ~ 680 in 2% steps.

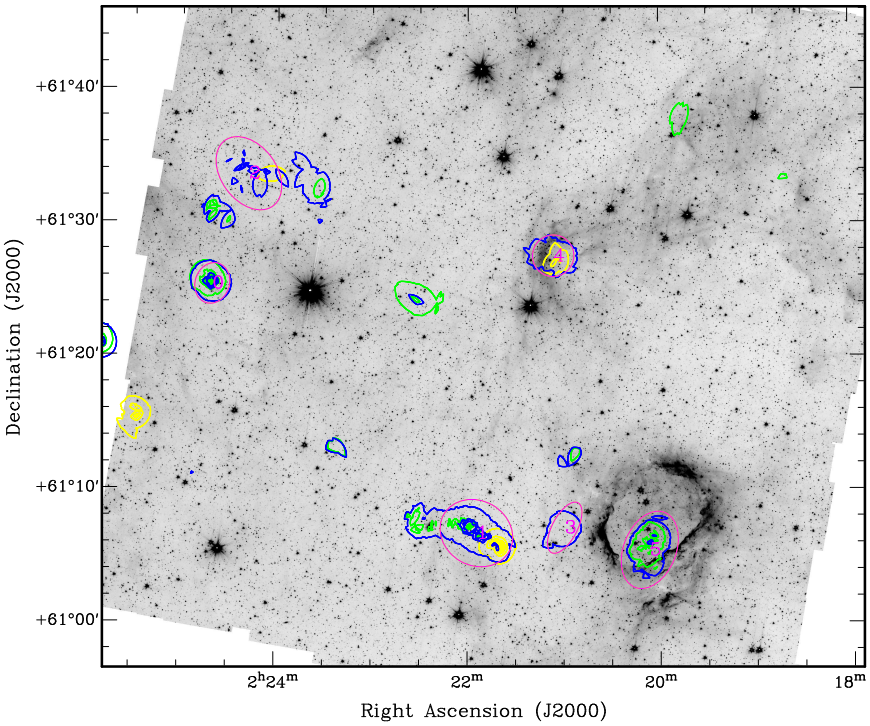

Figure 3.30 Like Fig. 3.29, but excluding the less reliable (*) population. Groups are marked as magenta ellipses. Class 0/I surface density contours between $5-95\%$ of peak value $\sim 50\,\mathrm{YSO\,pc^{-2}}$ in 10% steps. Class II contours between $1.5-30.5\%$ of peak value $\sim 175\,\mathrm{YSO\,pc^{-2}}$ in 10% steps. YSO contours have been chosen to span a common YSO range for both classes of $\sim 2.5-50\,\mathrm{YSO\,pc^{-2}}$. Age contours are for 2-52% of peak value of ~ 1000 in 5% steps.

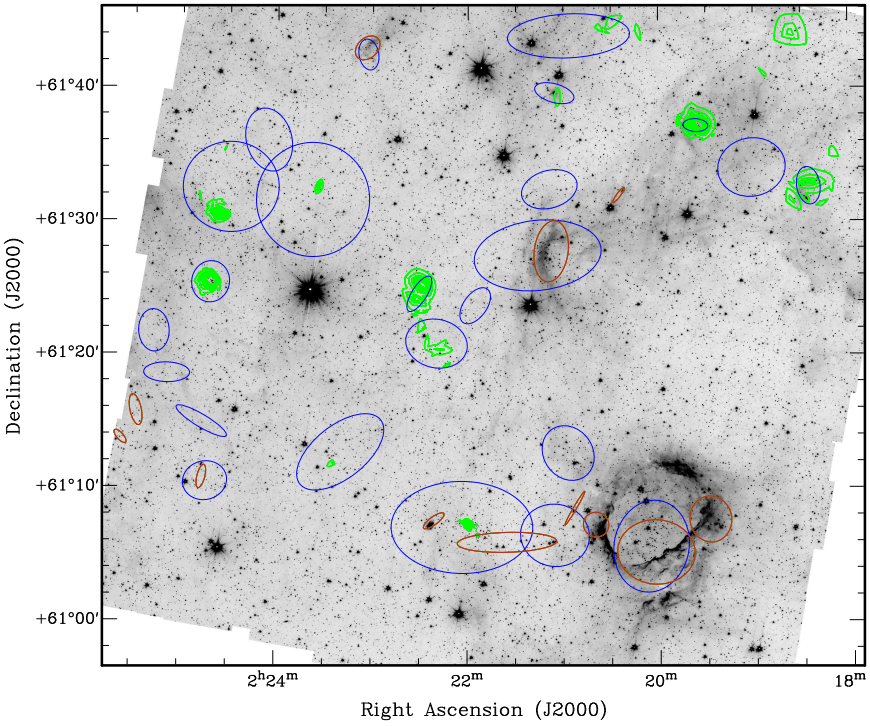

Figure 3.31 Like Fig. 3.29 but for $N_{YSO} = 5$, $D_{break} = 0.75$ pc, and Class 0/I + Class 0/I* (brown ellipses), and $N_{YSO} = 5$, $D_{break} = 0.95$, and Class II + Class II* (blue ellipses). Parameters are from Table 3.12.

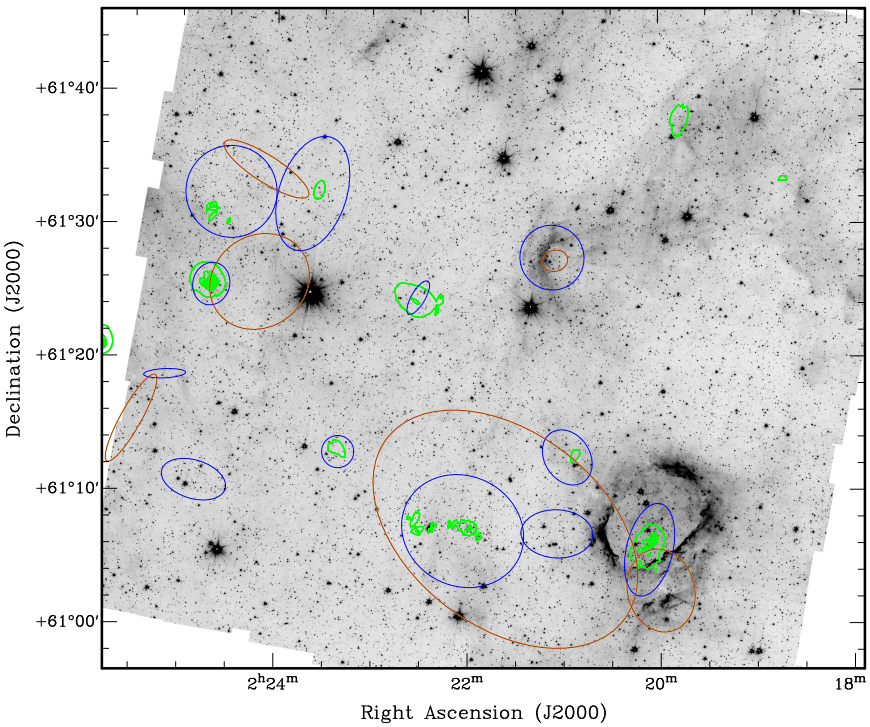

Figure 3.32 Like Fig. 3.30 but for $N_{YSO} = 5$, $D_{break} = 2.25$ pc, and Class 0/I (brown ellipses), and $N_{YSO} = 5$, $D_{break} = 1.05$, and Class II (blue ellipses). Parameters are from Table 3.12.

such as bright rims, pillars with varying orientation, cavities, and filaments (Fig. 3.2). In this third field, groups have a wide range of ages and properties and can be separated mainly into i) groups associated with filaments; ii) groups associated with the active star forming regions: KR 140-N and KR 140 (Fig.3.1).

Figures 3.29 and 3.30 show the YSO groups (with and without the (*) population) identified in the central and western regions of the W3 GMC. The figures also show YSO surface density contours and age contours. Figures 3.31 and 3.32 are like Figures 3.29 and 3.30, but for $N_{YSO} = 5$ and separating YSOs according to class. These figures show a tendency for Class II sources to be more widely distributed. While this effect could be enhanced by motion away from their birthsites, when Class II sources are found systematically located preferentially on one particular side of the parent structure, like in the case of Group 2 (Fig. 3.29), a propagating triggering disturbance seems more likely

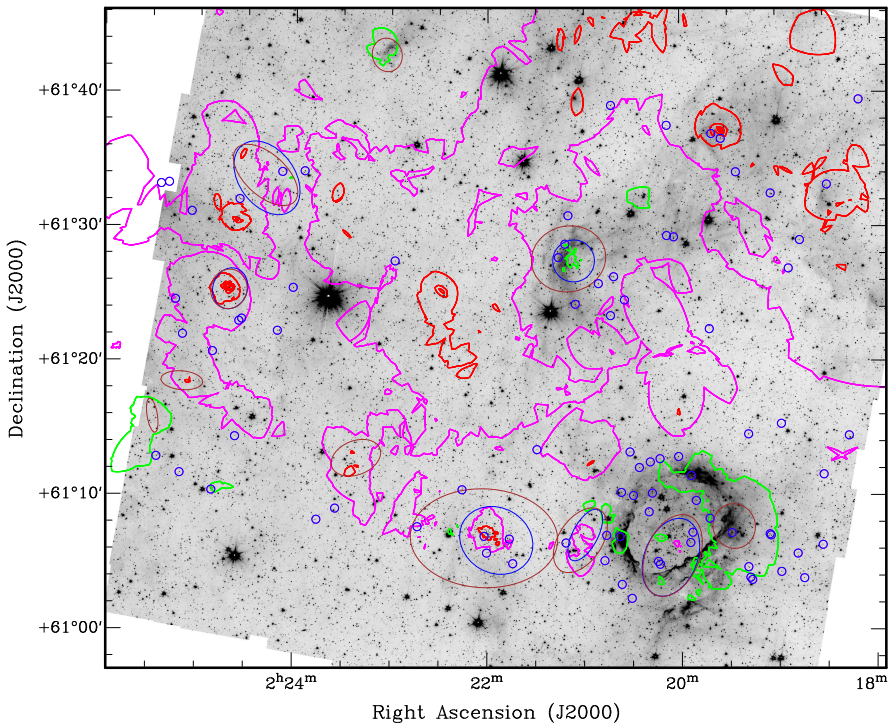

Figure 3.33 Greyscale *Spitzer* channel 1 image of the KR 140 field. Contours like Fig.3.18, but with red contours between $3-33\%$ in 10% steps (red). Small blue circles are 2MASS-based PMS candidates. Brown and blue ellipses like in Figs. 3.29 and 3.30, respectively.

responsible for the observed distribution.

The Class 0/I population is well localized, almost exclusively in the high extinction filaments and bright rims. The Class II population is found distributed throughout the entire cloud, following the infrared (PAH) emission structures (channel 4) and within the central 'cavity' that separates the HDL and the western region comprising KR 140-N and KR 140. Independent star forming events likely produced the observed distributed population. Star formation events throughout the cloud also triggered secondary bursts of star formation resulting in the eroded and turbulent environment observed at longer wavelengths. An almost square lower column density region is noticeable in the extinction maps, but we find no evidence of any major event that could have caused an evacuation. An age sequence could be inferred for the star forming regions associated with the HDL. However, the structures and groups found in the central and western regions of the W3 GMC (Fig. 3.29) appear more characteristic of sequential or even isolated events, perhaps more typical of the normal evolution and aging of a cloud without a neighbor like W4, and/or perhaps related to the original formation of the GMC.

Groups in the central region of the W3 cloud are member-poor ($N_m < 25$; Groups 6, 5, 1, 10, 3, and 0, in order of increasing membership; Fig. 3.29). Analysis of the environment of the filaments (Groups 6, 5, 1, 0, the latter also identified as magenta Group 0; Fig. 3.30) suggests their YSO population could have been triggered by external events. The fact that most run parallel to the HDL might indicate some interaction (pillars and elephant trunks in the region point toward the upper (and older) part of AFGL 333), but might, on the other hand, just reflect the high density there, based on their range of ages. Group 10, located in a bright rim of emission in the PAH band in the northern parts, does suggest a triggered formation. The orientation of other nearby pillar structures points to a triggering source located in the most northern parts of the cloud and outside the *Spitzer* surveyed area.

The age of the systems in the central regions of W3 range from the youngest (Group 5

or 10) to the oldest (Groups 0 and 3) in the GMC. Group 0 is also the filament with lowest extinction. Group 3 exists within a cavity-like structure in the neighborhood of weak emission pillar-remnants that point toward the location of Group 10. This, combined with the lack of association with an extinction structure and its low density is suggestive of an old triggered population that formed from material associated with the now low density pillar structures.

The richest groups ($N_m \geq 25$; Groups 4, 9, 8, and 2, in order of increasing membership; Fig. 3.29) are associated with KR 140-N, KR 140 (e.g., Kerton et al., 2001; Kerton et al., 2008), and the major filament east of this H II region.

The structure and YSO population of KR 140-N (Group 9) support a triggered origin from RDI. The innermost region of this structure contains a large population of Class 0/I sources, with Class II candidates extending in front and behind the shocked region. A similar YSO distribution was observed in pillars associated with embedded clusters triggered by W4 (e.g., Group 7 in the AFGL 333 field; Fig. 3.25) that were also suggested to have been produced by RDI. The cometary-like morphology also resembles that obtained by theoretical models of RDI of a cloud exposed to a high ionizing flux ($\Phi_{\rm LyC} = 3 \times 10^{11}\,{\rm cm^{-2}\,s^{-1}}$; Bisbas et al., 2011). A significant tail of 'blown' material extends toward the west, containing a largely distributed population of Class II and some Class 0/I sources, the latter generally associated with knots of bright PAH emission. Just as Group 7 in Figure 3.25 is triggered by W4, the presence of Class II sources 'ahead' of the front for KR 140-N suggests triggering by a source 'external' to this structure and to the east. The location of the rim, at the edge of an evacuated region, also suggests an external (albeit so far unidentified) influence.

The (low density) YSO population of Group 7 likely associated with the shell of KR 140 is the youngest, indicating active star formation triggered by the ionizing star VES 735. We find a population of Class II and PMS sources extending toward the north of the H II region (Fig. 3.33) that are likely to have originated because of the activity in the

latter. Group 8, a rich ($N_m > 50$) group projected on the H II region, contains a mixed population of Class 0/I and II sources (ratio ~ 1) indicative of an extended period of star formation. This group, together with Group 2, are not only the richest in the field, but are also associated with the highest surface densities ($> 60-70\,M_\odot\,pc^{-2}$) and extinctions ($A_{V-peak} \sim 5.5$). This extinction is in agreement with that estimated for the exciting O star of KR 140, VES 735, by Kerton et al. (1999) from spectroscopy ($A_V \sim 5.4$) and optical photometry ($A_V \sim 5.7 \pm 0.2$), confirming the reliability of the extinction map at least within the resolution-related limitations.

The filaments associated with Groups 2 and 4 are the most prominent of the region. Our analysis indicates that Group 2 is in a relatively highly evolved stage and was not triggered by KR 140, in agreement with previous analysis (Kerton et al., 2008). Contrary to the population of Group 4, Class II sources in Group 2 are displaced from the filament toward the north, with a string of Class 0/I still deeply embedded in the innermost regions of the filament. The east-west orientation and arc-like shape of this structure, as well as the distribution of the Class II population and the material traced in the MIR, suggest a possible trigger located in the direction of KR 140-N. Group 4 is younger, with characteristics and orientation that suggest a link to the activity in KR 140, at least in the northernmost parts.

All member-rich groups are also identified even after excluding the (*) sample (Fig. 3.30). When reducing the membership requirement to $N_{YSO} > 5$ we again reach similar conclusions (Figs. 3.31 and 3.32).

Overall, Class 0/I candidates are confined to the innermost regions of the filaments (high ellipticity groups), and therefore trace these structures with high accuracy. We also detect a distribution of mainly Class II groups around the 'cavity-like' region bounded by Group 10 (Fig. 3.29), KR 140-N, and Group 3. While such a configuration is reminiscent of a triggered origin, the distributed Class II population might actually be the result of percolating low level spontaneous star formation. A string of such Class II groups is

observed crossing the entire field, extending from the easternmost regions to KR 140, and incorporating the filaments identified with Groups 2 and 4 (Fig. 3.31), suggesting that the filaments in the southern central and western parts of W3 are the peak overdensities in a region of overall enhanced extinction.

VES 735 might have formed as part of a growing loose association of high-mass stars. Kerton et al. (2001) indicate that the nearby sources IRAS 02171+6058 and IRAS 02174+6052 have luminosities consistent with lower mass embedded B stars. We find a Class 0/I YSO matching IRAS 02171+6058 and no significant radio continuum emission, which supports their hypothesis of an embedded B-type star. We do not detect a *Spitzer* counterpart for the other source. A more detailed analysis is required to investigate this possible association for VES 735, including the numerous bright infrared stars (BIRS) in this region.

In Figure 3.33 we plot the 'age' contours deduced from the ratio of Class II/Class 0/I with (*) sources. Peaks in the red contours indicate the oldest age, while green represents the youngest. The distribution of ages throughout the field is evident. Group 7, associated with the shell, is the youngest. The age of VES 735 is estimated to be $\sim 2\,\mathrm{Myr}$, consistent with an H II region of $\sim 1 - 2\,\mathrm{Myr}$ (Kerton et al., 1999; Ballantyne et al., 2000), and so this age can be considered an upper limit for the YSO population associated with this group. Group 7 is followed in age by Group 5, and those associated with the other active (infrared-bright) star forming sites: Group 10, Group 9 (KR 140-N), and Group 8 (KR 140). Excluding the (*) sources we find the youngest group to be that associated with the filament closest to KR 140 (Group 4 in Fig. 3.29), followed by the population in KR 140-N (Group 9), the filament associated with Group 2, and Group 3 (central W3), with the *oldest* groups being Group 8, projected on KR 140, and Group 0.

The regions undergoing star formation (Class 0/I) in the central and western part of W3 are at very localized spots in the cloud. Neighboring groups have an age spread suggestive of individual star formation events and evolution. Filaments host some of

the oldest populations, while those with triggered morphology (Group 10, KR 140-N: Group 9) are younger, as expected if actually triggered by (and therefore dependent on) a *previous* event. Star formation events must also continue over at least a few Myr, as suggested by the Class II population distributed throughout the cloud surrounding the active star forming sites.

Figure 3.33 also shows the candidate PMS sources, which dominate near the KR 140 H II region. Finding the oldest population to be associated with KR 140 itself (and therefore independent of any previous star formation), would in principle support the 'spontaneous' origin of its high-mass exciting star. This issue is revisited during the analysis of the Herschel datasets.

3.6 Conclusion

By means of *Spitzer* and 2MASS data we have identified and analyzed the young stellar population in the W3 GMC. These were classified according to the standard 'class' nomenclature for YSOs, and compared to other classification schemes based on intrinsic stellar properties, such as envelope accretion rate and disk mass. We find distinct regions in the CCD separating the intrinsically (and observationally) young population from the disk-dominated sample, with an intermediate region likely containing edge-on optically thick disks and weaker envelope candidates.

Observationally, the low-mass PMS population cannot be identified unambiguously without first identifying the protostellar Class 0/I and Class II sources. Intermediate mass stars could in principle be identified *without* the need for any previous protostar classification, although it is likely that some HAeBe sources would then be missed through misclassification as Class II and T-Tauri objects.

The YSO population was divided into spatial groups according to the minimum spanning tree algorithm. We also created YSO surface density maps and 'age' maps. These

data were used to investigate the characteristics and history of the star formation in W3.

The distinctive HDL is no doubt influenced by the expansion of W4. The high density conditions there favored the formation of particularly rich bursts of star formation. The HDL contains the main star formation activity of W3 and has signatures of both spontaneous and triggered star formation from both external (e.g., W4) and internal events. Whether W4 was just key to creating the initial favorable *conditions* for (high-mass) star and cluster formation, the very high surface density regions, clumps and cores which then collapse at a later stage, or whether it also *triggered* the star formation in such clumps and cores is a more subtle question.

Our finding of a relatively older population in the western side of W3 Main and AFGL 333, opposite to shells formed by compression by IC 1795 and W4, respectively, suggest star formation could have started first in quiescent mode throughout the GMC, including these structures as well as the cluster IC 1795 itself. Subsequently, triggering mechanisms by the intense activity (e.g., IC 1795) were responsible for compressing an already dense environment, greatly enhancing and/or inducing major bursts of high-mass star and cluster formation (e.g., W3 Main, W3 (OH)).

The evolved state of W3 is also evident in the central and western parts of this cloud, an overall highly turbulent and eroded environment. This is believed to have been produced by numerous individual star formation events that were responsible for triggering secondary episodes of star forming activity. The central regions between AFGL 333 and KR 140 are particularly rich in filaments, seen in extinction in the MIR, whose formation and star forming activity appear to be associated with this highly turbulent environment. Recent star formation is confined mainly to these very localized regions.

The overlapping spatial distributions of the YSO class populations in the most active areas of W3 indicate on-going periods of star formation in regions of high-mass star and cluster formation, as opposed to a single, major short-lived event.

Based on number of YSO types (in groups) and ratios of class surface densities (in

regions) as relative measurements of age, we find that the region comprising W3 Main and W3 (OH) is the youngest, followed by the central/west region of W3 and AFGL 333. However, in AFGL 333 confusion does not allow us to detect groups in the currently most active areas, and therefore the age is representative of the YSO population associated with filaments. We cannot determine if the activity in AFGL 333 did start first or if the activity all across the HDL started at similar times triggered by W4, but of all the ages derived for the groups associated with isolated filaments we find those in this region to be the oldest. Indeed, the characteristics of the YSO population and individual group ages suggest that the activity immediately west of AFGL 333 could have induced some secondary triggered events in filamentary structures in the central regions of the cloud.

On-going stellar activity in W3 Main, IC 1795, and KR 140 results in younger apparent ages for their associated groups. Nevertheless, the KR 140 region appears to contain the oldest population in the western part of W3. This age is less than that of IC 1795, and the absence of a suitable nearby triggering mechanism supports the spontaneous origin for VES 735 and stars in this possible association. We find that the age of KR 140-N must be intrinsically young. This structure shows not only a morphology consistent with triggering by RDI, but also a well defined distribution of Class II sources surrounding the Class 0/I population, similar to that associated with pillar structures.

The age of IC 1795 has been estimated to be around $\sim 3-5\,\mathrm{Myr}$. Even when considering a supersonic velocity (for typical velocity in the ionized medium) of c$\sim 10\,\mathrm{km}^{-1}$, IRS5 would require $\sim 2.5\,\mathrm{Myr}$, and $\sim 3\,\mathrm{Myr}$ for interaction with KR 140-N. If IRS5 itself were actually triggered by IC 1795, then this makes the former an even more unlikely candidate for triggering activity in the western regions. If a source of triggering is indeed located in the HDL, then at least the western side of these structures must have been undergoing star formation activity well before the onset of the present major activity in the HDL. This is supported by findings of a relatively older population in the western side of these structures.

Results presented above reveal that despite having considered a range of relatively evolved stages of pre-stellar evolution, the W3 GMC is still a prime target for investigating different modes of star formation. We classified as a *grouped* population those YSOs not part of a previously cataloged cluster, but belonging to a group identified though the MST analysis.

Primordial/quiescent grouped formation is identified by old, relatively isolated systems with the closest inter-YSO separations and compact configurations (not necessarily circular if parental material is filamentary), whose richness depends on the primordial surface density of the clump/core. An example is Group 2 in Figure 3.19. *Triggering* may be a more efficient mechanism for creating high surface density structures favorable to high multiplicity and/or for inducing the collapse of such structures (e.g., by overcoming internal pressure and turbulent support). All current major clustered high-mass star activity in W3 is believed to have been 'triggered' to some extent. *Quiescent clustered formation* might nevertheless have occurred initially to produce IC 1795, whose preferential location in the HDL resulted in a rich population that subsequently triggered secondary bursts of star formation within an already overdense region. The outcome for the GMC would also depend ultimately on the physics, effectiveness, and limitations of the processes creating the precursors of groups and clusters in the parental cloud (e.g., filaments, clumps, and cores).

Triggered formation has occurred throughout W3. In some cases, unstable structures with enough surface density and low turbulence are created (collect/collapse model). Elsewhere there is collapse induced (RDI) in the neighborhood of the triggering source. Examples for triggered *grouped* formation are Group 7 in Figure 3.29, a YSO population associated with a shell of material compressed by the expanding KR 140 H II region, and Group 9 associated with a cometary like structure in KR 140-N. *Clustered* triggered formation can be observed in pillar structures such as Group 7 facing W4 (Fig. 3.25). The present data cannot confirm whether pre-existing cold seeds had formed in the cloud

prior to the triggering mechanisms, and this issue will be revisited with the available Herschel data.

Regardless of the detailed sequence of processes, our work indicates that triggering is the main mechanism associated with those structures dense enough to host the current main cluster and high-mass star formation activity (i.e., W3 Main). Clusters formed within such structures are the richest. IRS5 in particular, unresolved in our data, has been suggested to be a Trapezium-like system of proto OB stars within an envelope $< 0.02\,\mathrm{pc}$ in size; its protostellar density, of $\sim 0.5 - 5 \times 10^6\,\mathrm{pc}^{-3}$, makes it one of the most dense clusters known (Megeath et al., 2005; Rodón et al., 2008). This system is itself embedded in a massive cluster of low-mass and PMS stars (Megeath et al., 1996; Feigelson & Townsley, 2008) within the region of highest extinction in the entire W3 GMC ($\mathrm{A_V} = 9.6 \pm 0.3$).

We classified as *distributed* those YSO candidates not in groups and not presently associated with extinction structures in the infrared. Some of the distributed population has an origin associated with high extinction structures (e.g., filaments, pillars) cleared by the stellar activity (e.g., Fig. 3.25, western part of Group 4). A filament can follow a highly irregular and curved morphology, likely linked to large scale turbulence in the environment, and the YSOs born in the filament will looked highly distributed after the disappearance of their parent structure (e.g., Group 6, Fig. 3.25). The fact that the Class II population of Group 4 is surrounded by possible 'remnants' of parent structures suggests lifetimes for the filaments and clumps of the order of a few Myr. Whether the star formation processes within filaments differ from those in clustered formation needs to be determined. Note that a population of filamentary origin can be confused with that truly originated in isolation. The latter can be observed in the 'tail' of KR 140-N and in highly turbulent, low surface density regions in the vicinity of active star formation. An example can be found in the western side of W3, where 'knots' of infrared emission trace isolated overdensities (clumps, cores), more relevant for the formation of individual

objects.

Chapter 4

The W3 GMC: High-Mass Star Forming Structures

4.1 Data Processing and *Herschel* Images

W3 was observed by *Herschel* in March 2011. Continuum data were obtained in parallel mode at 70 μm and 160 μm with PACS (Poglitsch et al., 2010), and 250 μm, 350 μm, and 500 μm with SPIRE (Griffin et al., 2010). Datasets were reduced from level 0 to level 1 using HIPE v7, and the final maps were produced with v10.0 of the Scanamorphos[1] software package (Roussel, 2012). A check with 2MASS and *Spitzer* data indicates that the pointing accuracy is better than $2''$. Maps were transformed to MJy/sr and offsets were determined using *Planck* and *IRAS* data (Bernard et al., 2010).

Stokes I CGPS continuum images at 1420 MHz were used to investigate the location and distribution of the ionized regions.

A small saturated area was detected in W3 (OH) at 70, 250, and 350 μm ($\sim 2^{\rm h}\,27^{\rm m}\,4^{\rm s}$ $+61^\circ\,52'\,24''$). Other small (a few pixels) regions were also saturated in W3 Main at 70 μm ($2^{\rm h}\,25^{\rm m}\,40^{\rm s}.5$ $+62^\circ\,05'\,50''$) and 250 μm ($2^{\rm h}\,25^{\rm m}\,40^{\rm s}.5$ $+62^\circ\,05'\,50''$; $2^{\rm h}\,25^{\rm m}\,30^{\rm s}.5$ $+62^\circ\,06'$).

[1] http://www2.iap.fr/users/roussel/herschel/index.html

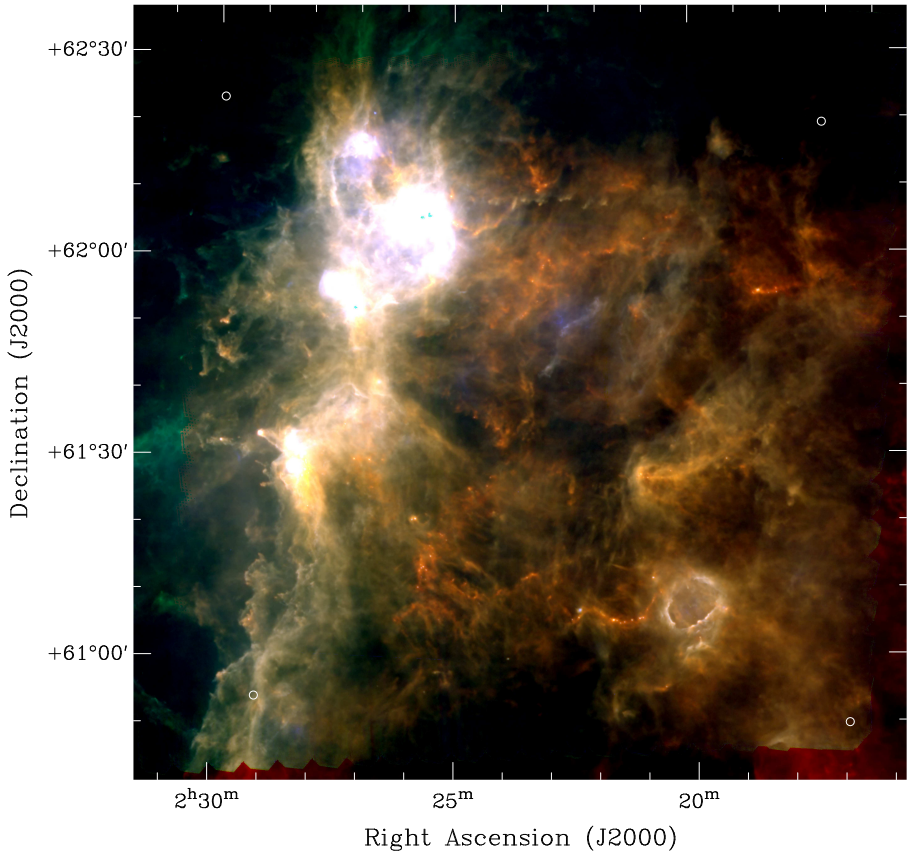

Figure 4.1 Three color (log-scale) image of the W3 GMC using *Herschel* HOBYS data at 70 μm (blue), 160 μm (green) and 250 μm (red). White circles mark the corners of the common science region (see text).

These regions are being re-observed with *Herschel* using the 'bright' mode, although we note that this saturation does not affect the conclusions of this work. Our analysis focuses on the common science region, $\sim 1.5^\circ$ in extent in RA and Dec, comprising the area scanned in two roughly orthogonal directions by PACS and SPIRE according to the telescope focal plane orientation of the date of observation. This region excludes the more unreliable 'turn-around' data, which is obtained during those periods in which the telescope slows down after each scan leg.

A three-color image of W3 is shown in Figure 4.1. Given the large dynamic range in brightness, this composite has been made using logarithmic representations of the emission to reveal complex detail. The five individual continuum images are presented in Appendix A.

4.2 Data Analysis and Structural Maps

In deriving column density and dust temperature maps, the PACS and SPIRE maps were convolved to the resolution at 500 μm ($\sim$36″; $\sim$0.35 pc at a distance of 2 kpc) and projected onto a common 9.5″ pix^{-1} grid ($\sim$ 1/4 FWHM at 500 μm resolution). Only those pixels with valid photometry in at least three *Herschel* bands $\geq$ 160 μm were considered (70 μm data were not used in creating the maps).

The intensities at each pixel were fitted with an optically thin modified blackbody function of the form

$$I_\nu = \tau_{\nu_0} \left(\frac{\nu}{\nu_0} \right)^\beta B_\nu(T) = \sigma_\nu B_\nu(T) N_{\rm H}, \tag{4.1}$$

where τ_{ν_0} is the optical depth evaluated at $\nu_0 = 1200$ GHz (250 μm), $B_\nu(T)$ is the Planck function, T is the dust temperature, σ_ν is the opacity of the medium, and $N_{\rm H}$ is the total H column density. We assumed a fixed dust emissivity index of $\beta = 2$ and adopted the same opacity standard as in other HOBYS studies (Motte et al., 2010), 0.10 cm^2 gm^{-1} at 1 THz, or equivalently $\sigma_0 = 3.3 \times 10^{-25}$ cm^2 H^{-1} using 1.4 as the mean atomic weight

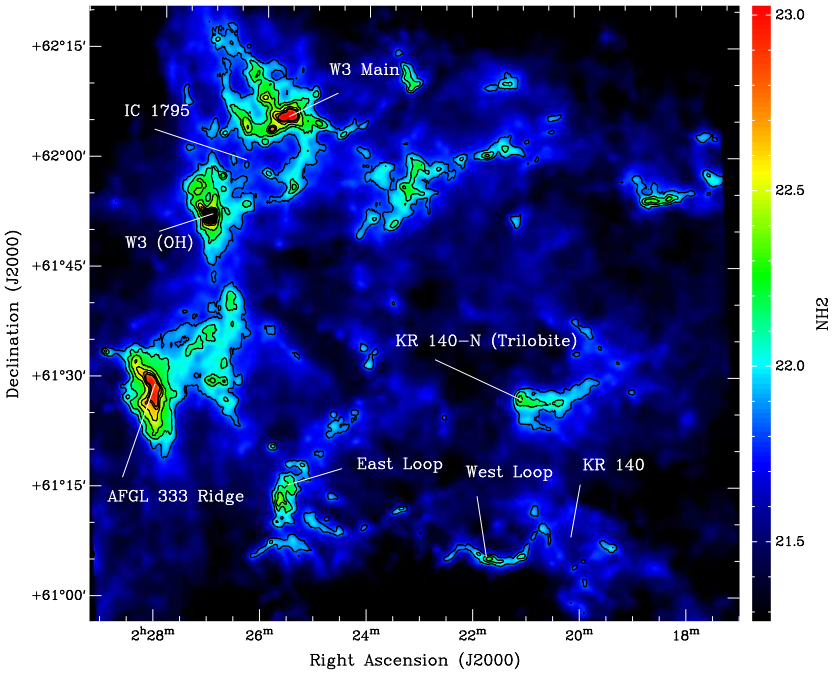

Figure 4.2 Column density map of the W3 GMC (log [cm^{-2}]) after correction for dust emission associated with foreground/background atomic and molecular material, as described in Appendix B (uncorrected version in Fig. B.1, left). A variety of filaments, pillars and structures are found throughout the GMC. Labels mark prominent features in W3. Contours are $N_{\mathrm{H_2}} \approx [7, 10, 20, 35, 50, 65] \times 10^{21}\,\mathrm{cm}^{-2}$.

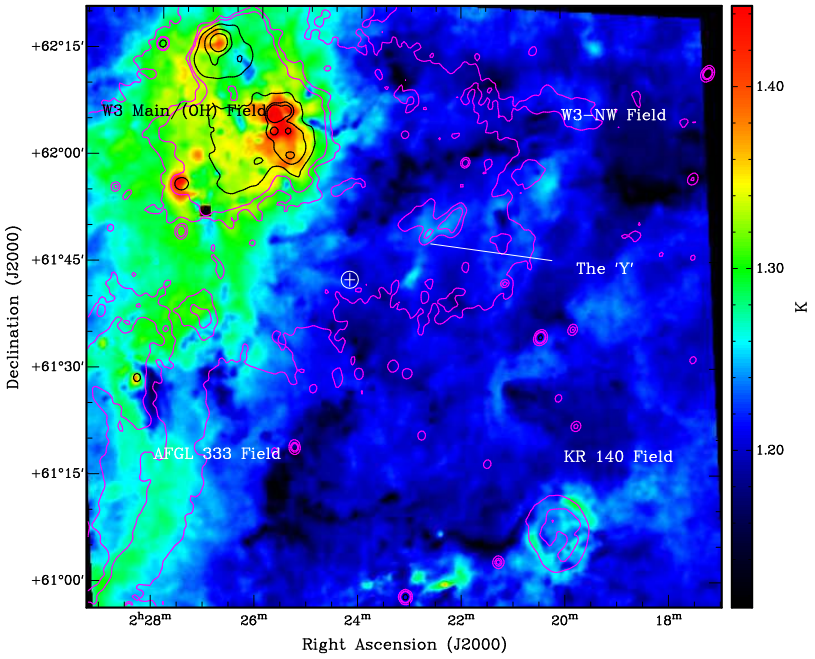

Figure 4.3 Dust temperature map of the W3 GMC (log [K]) after correction for dust emission associated with foreground/background atomic and molecular material, as described in Appendix B (uncorrected version in Fig. B.1, right). Contours are of Stokes I continuum at 1420 MHz: $T_b = 8, 12, 15\,K$ (magenta), and $T_b = 30, 100$, and $240\,K$ (black). Colors for contours have been chosen for better contrast in cold and warm regions. White circle with cross marks the intersection of the four fields in W3. From left to right and top to bottom: W3 Main/(OH) field, W3-NW, AFGL 333, KR 140 fields. Figure includes labels for the four fields and the location of the 'Y'-shaped hot structure (see text).

per H nucleon. Calibration errors of 15% and 20% were assumed for SPIRE and PACS 160 μm, respectively (Griffin et al., 2010; Poglitsch et al., 2010). More importantly, we note that intrinsic uncertainties in the adopted dust model parameters might alter the derived dust column densities systematically by a factor of ~ 2, and that there might be systematic differences in opacity across the field or with column density (Martin et al., 2012).

Our goal is to assess the column densities and temperature within the W3 GMC itself. The *Herschel* intensities I_ν, however, contain contributions from dust in the foreground and background, each with its own σ_ν, T, and $N_{\rm H}$; the right hand side of Equation [4.1] is summed over all components. The process of subtraction is described in Appendix B. While a challenging exercise, educated subtraction is definitely advantageous and necessary, without which results would provide a much less accurate representation of the true local conditions in the GMC. Subtracting the foreground and background is most important for accurate characterization of regions where the column density in the GMC is relatively low; it has little effect on the regions of highest column density.

The final corrected column density map is shown in Figure 4.2 in the metric $N_{\rm H_2}$ (preferred over $N_{\rm H}$), assuming the hydrogen to be largely in molecular form. The accompanying temperature map is shown in Figure 4.3. Both figures label the most prominent features of the W3 GMC. Unless mentioned otherwise, we used these corrected maps as the default images for our analysis.

For purposes of comparison and discussion, we separate the GMC into four different fields, labeled according to their physical location with respect to the center of the field or a major feature present in the field. The fields are: W3 Main/(OH), W3-NW, AFGL 333, and KR 140 fields (see Fig. 4.3). The W3 Main/(OH) and AFGL 333 fields together comprise what we define as the 'eastern' (or HDL) fields in W3, while the other two are the 'western' ('quiescent' and 'diffuse') ones.

4.3 The Column Density and Dust Temperature Maps

4.3.1 Global Overview

The most prominent thermal emission features in W3 are shown in unprecedented detail by the *Herschel* data.

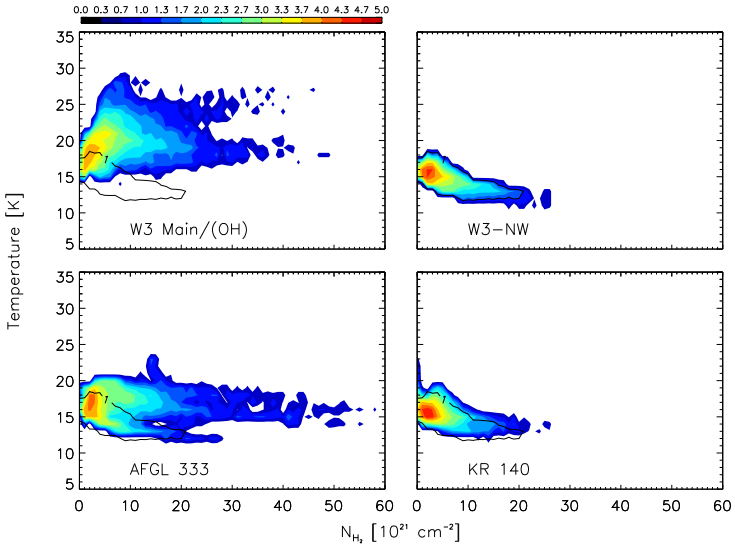

Figure 4.4 Two-dimensional histogram of dust temperature and column density in each W3 field. Color bar indicates number of pixels (log units). Black contour marks the distribution of the W3-NW field as a reference for distribution in the other fields.

Figure 4.4 presents the relationship between column density and dust temperature for the four fields, in the form of a two-dimensional histogram. The W3 Main/(OH) field shows a 'high-temperature' tail not observed in the cooler and more diffuse western fields (W3-NW and KR 140). The AFGL 333 field shows a similar high-temperature tail, associated with material at the boundary of W4 and with peak temperatures between W3 Main/(OH) and the western fields, as well as low-temperature material (not present in the W3 Main/(OH)) associated with the structures of the East Loop (Fig. 4.2).

When taking into account the material at all temperatures, we find that the four field have comparable mass. The masses, areas and surface densities (Σ) for each of the four

Table 4.1 Global Parameters for the W3 Fields

Field	Mass[a]	Mass[b]	Area	Σ[c]	Σ[d]
	[$10^4\,M_\odot$]	[$10^4\,M_\odot$]	[deg^2]	[$M_\odot$/pc^2]	[$M_\odot$/pc^2]
Main/(OH)	7.2	6.0	0.43	137	114
AFGL 333	8.4	6.5	0.50	138	107
KR 140	9.8	6.1	0.74	108	68
NW	6.7	5.0	0.53	104	79

[a] Mass from un-corrected (original) maps.

[b] Mass corrected for foreground/background material.

[c] Surface density from un-corrected (original) maps.

[d] Surface density corrected for foreground/background material.

fields are shown in Table 4.1, where the mass and area used to estimate Σ is the sum of the contributions from all valid pixels. This also includes high column density material above the limits used in Figure 4.4, which belong mainly to the W3 Main/(OH) field.

The total (all fields) uncorrected mass of the W3 GMC is found to be $\sim 3.2\times10^5\,M_\odot$, or $\sim 2.4\times10^5\,M_\odot$ when removing the contribution from foreground/background material ($\sim 1.3\times10^5 M_\odot$ and $\sim 1.1\times10^5 M_\odot$ for the HDL (W3 Main/(OH)+ AFGL 333 fields) and the western fields (W3-NW + KR 140 fields), respectively). Our estimate for the corrected total mass of the cloud is about half that estimated by Polychroni et al. (2010) from molecular data, but the uncorrected estimate is similar to that derived by Moore et al. (2007) from ^{13}CO of $\sim 3.8\times10^5\,M_\odot$ for a constant excitation temperature of $\sim 30\,K$.

4.3.2 Stellar Influence and Cloud Structure

The ionizing and eroding activity of the O stars powering W4 is clearly observed along the eastern edge of our mapped field. The ionization front can be traced in the radio continuum, as shown with Stokes I continuum contours in Figure 4.3. Diffuse radio emission

is observed to be most prominent in the HDL, with the strongest peaks coincident with W3 Main, and decreasing progressively toward the west, into the colder western fields.

Various elongated structures and protuberances emerging parallel from the same high column density region (HDL) are observed to extend more than 10 pc in projection along the boundary with W4, pointing towards the east and the O cluster (see Fig. 4.1). The most prominent of these features (defined as 'pillars' in this work), is located just northeast of AFGL 333 and has signatures of ongoing star formation (see Chapter 3). The location of this structure (P1), as well as other pillar-regions in W3, are marked in Figure 4.6, which shows that several of these are part of the coldest structures in the W3 GMC.

Interaction with W4 cannot, however, account for the level of complexity and diversity of features west of the HDL. Although the detail of such structures is not captured in the (lower resolution) column density maps, the original single-band *Herschel* images (see Appendix A) show for the first time a multitude of pillar-like structures, similar to those bordering W4, albeit here they are pointing south/south-east and are located in the area west of W3 Main (P2). Other groups of south-oriented pillars are identified in more central regions (P3: $\sim 2^{\rm h}\,24^{\rm m}\,00^{\rm s}$ $+61^\circ\,32'$; P4: $\sim 2^{\rm h}\,22^{\rm m}\,30^{\rm s}$ $+61^\circ\,24'$), again suggestive of stellar influence in the area. These can be clearly observed in Figure 4.1, while Figure 4.5 shows that the pillars are also prominent features in both the temperature and column density maps.

Contrary to the HDL, stellar influence in the western fields is very localized, as shown in Figure 4.3. Examples of these 'hot' spots are the KR 140 H II region, a 'Y' shape structure (Fig. 4.3) at $\sim 2^{\rm h}\,22^{\rm m}\,37^{\rm s}$ $+61^\circ\,49'\,41''$, and a bow-shock like 'high' temperature feature wrapping around the eastern side of KR 140-N (Trilobite). Being the YSO displacement associated with this structure also in this direction (as observed in Chapter 3) this supports a possible case of RDI.

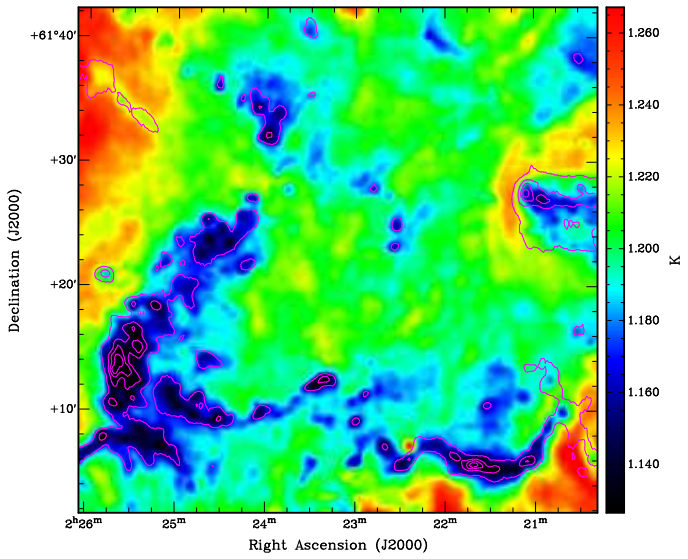

Figure 4.5 Temperature map (log [K]) of the East Loop, West Loop, and the eastern part of the Trilobite. Contours are $N_{\rm H_2} \approx [5.6, 12, 17, 23] \times 10^{21}\,{\rm cm}^{-2}$. Rows of pillars are observed north of the East Loop near $\sim 2^{\rm h}\,24^{\rm m}$ $+61^\circ\,32'$and $\sim 2^{\rm h}\,22^{\rm m}\,30^{\rm s}$ $+61^\circ\,24'$).

4.4 Clues to the Elusive High-Mass Star Formation Process: The Case of W3 Main

The W3 GMC offers a unique opportunity to characterize rare high-column density structures with ongoing high-mass star formation, and how their properties, origin, and evolution might be linked to the onset of high-mass activity.

4.4.1 Identification of High-Column Density Structures

Figure 4.7 and Figure 4.8 show up close the temperature of the most dense regions in the cloud: W3 Main + W3 (OH), and what we define as the 'AFGL 333 Ridge' (Fig. 4.2), in the innermost regions of the AFGL 333 field, respectively. The AFGL 333 Ridge is the only filamentary-shaped structure in the GMC reaching peak column densities of $\sim 10^{23}\,{\rm cm}^{-2}$, and therefore similar to those filaments defined as 'ridges' in previous HOBYS papers (e.g., Hill et al., 2011).

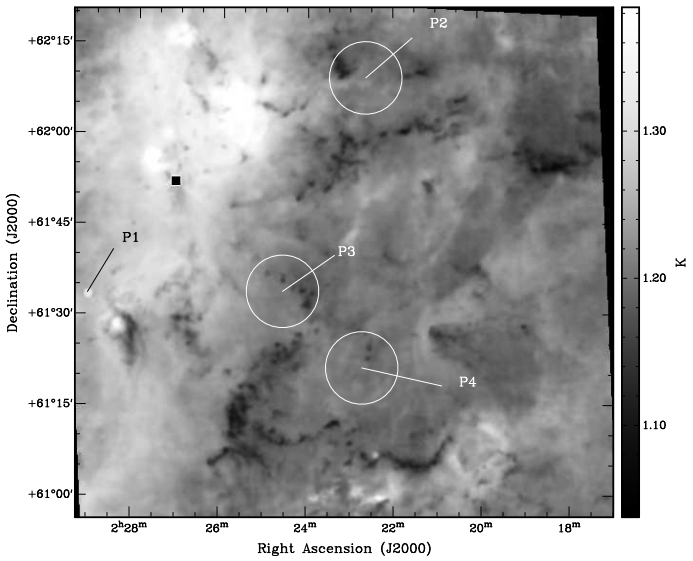

Figure 4.6 Same as Fig. 4.3, but with intensity range modified to highlight the coldest structures. Circles mark the location of pillar-like structures.

Krumholz & McKee (2008) predicted a star formation threshold for high-mass stars of $\Sigma = 0.7\,\mathrm{g\,cm^{-2}}$ for a star with $M \sim 10\,\mathrm{M_\odot}$. This surface density corresponds to $N_{\mathrm{H_2}} \sim 1.5 \times 10^{23}\,\mathrm{cm^{-2}}$ in our maps, which we will refer to as a 'MSFT'.

Only two structures in the W3 GMC, the W3 East and W3 West clumps (FWHM$\sim$ 0.44 pc), in W3 Main, reach column densities of this order, as shown in Figure 4.9. The highest value is in W3 West, $N_{\mathrm{H_2}} \sim 3 \times 10^{23}\,\mathrm{cm^{-2}}$. Despite the multiband saturation, we can get an estimate of the column density peak for W3 (OH) using the 500 μm data alone via Equation 4.1; being far from the peak of the SED, such an estimate is least sensitive to the temperature. The peak brightness is comparable to that of W3 West, and so the column density should be comparable too; i.e. $N_{\mathrm{H_2}} \sim (3 \pm 1) \times 10^{23}\,\mathrm{cm^{-2}}$. This value is somewhat higher than, though compatible with, the value $N_{\mathrm{H_2}} \sim 2.2 \times 10^{23}\,\mathrm{cm^{-2}}$ that we find for W3 East, and it is therefore in accordance with the ranking of column density strength found by Tieftrunk et al. (1998b) based on molecular $C^{18}O$ data, with W3 West $\sim$ 1.4 times higher than W3 East, and similar column densities for W3 East and W3 (OH). Column densities of this order are consistent with the findings reported by White et al. (1983), Richardson et al. (1989), and the presence of a strong, highly

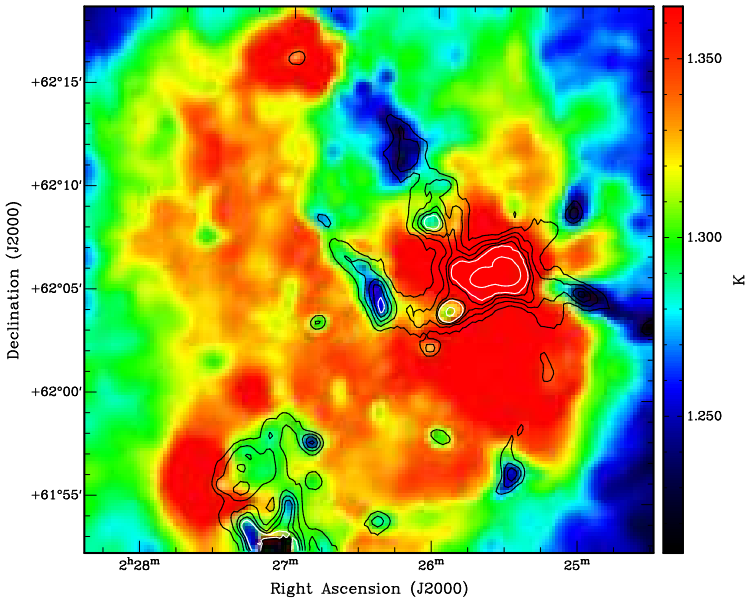

Figure 4.7 Temperature map (log [K]) of the structural details around W3 Main, W3 (OH), and W3 North. Black contours are $N_{\rm H_2} \approx [12, 17, 23, 29] \times 10^{21}\,{\rm cm}^{-2}$. White contours are $N_{\rm H_2} \approx [35, 82] \times 10^{21}\,{\rm cm}^{-2}$.

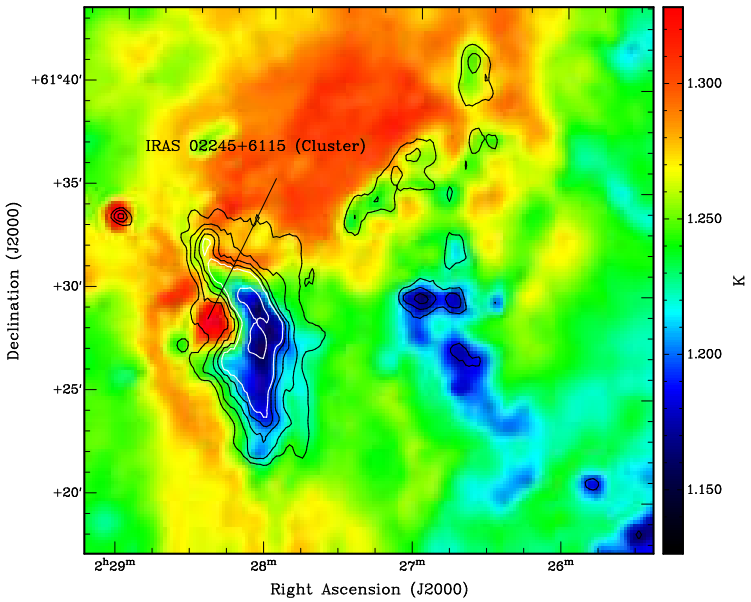

Figure 4.8 Same as Fig. 4.7, but for the central regions of the AFGL 333 field.

variable water maser in the W3 (OH) region (Little et al., 1977).

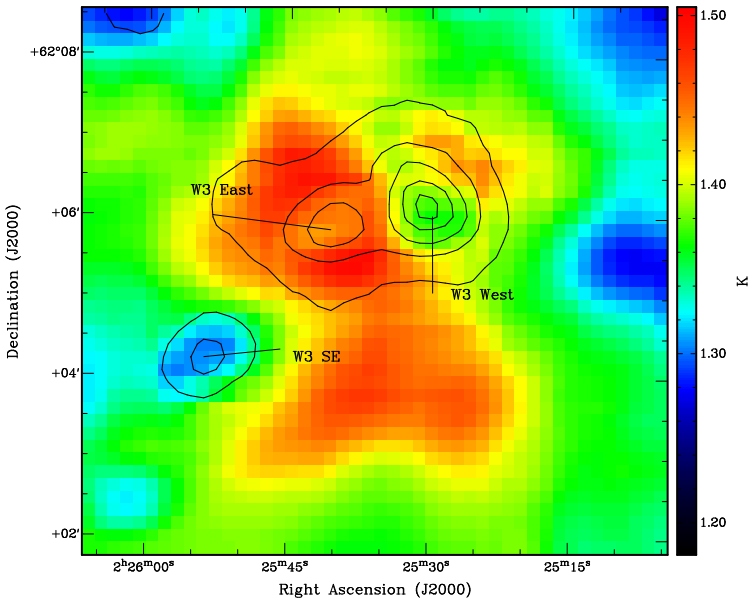

Figure 4.9 Same as Fig. 4.7, but focusing on the W3 Main region. Contours are $N_{\mathrm{H_2}} \approx [3.5, 8.2, 15, 22, 28] \times 10^{22}\,\mathrm{cm}^{-2}$.

W3 East, W3 West, and W3 (OH) are the only clumps with confirmed ongoing (clustered) high-mass star formation in the W3 GMC, as shown by the presence of masers, HCHii, or UCHii regions. While the MSFT value is used in this work just as a point of reference when comparing column density estimates, if such a threshold holds in practice, then this implies that $\sim 0.7\%$ of the mass of W3 (mass of valid pixels at and above the MSFT) is at present possibly associated with high-mass star formation, with a total combined mass between W3 East and W3 West of $\sim 1600\,\mathrm{M}_\odot$ for $N_{\mathrm{H_2}} \geq$MSFT.

4.4.2 Masses and Luminosities

To measure the luminosity and mass associated with the W3 Main peaks we need to measure their flux densities. First we examined the measurements derived by running the multi-scale, multi-wavelength source extraction software *getsources* (Men'shchikov et al., 2012; v.1.120316) on the original *Herschel* images. Given the changes in resolution with waveband, the apparent size of such extended sources is expected to change. For

Table 4.2 The high extinction structures in W3 Main: parameters from SED fitting[a]

Name	RA	Dec	Mass	L	T	<FWHM>[b]
W3	[h m s]	[°,′,″]	[$10^3\,M_\odot$]	[$10^4 L_\odot$]	[K]	[pc]
Convolved (500 μm) *getsources* flux densities						
West[c]	02 25 29.93	62 06 12.89	1.6 ± 0.5	4.1 ± 2.2	25.1 ± 3.5	0.46
[d]			1.0 ± 0.2	7.4 ± 0.7	30.3 ± 1.0	0.46
East	02 25 40.31	62 05 51.96	0.9 ± 0.3	8.2 ± 4.4	30.9 ± 4.2	0.46
			0.6 ± 0.1	14.6 ± 0.2	36.5 ± 1.5	0.46
Convolved (500 μm) + SCUBA 850 μm[e]						
West	02 25 29.9	62 06 09	1.9 ± 0.4	6.2 ± 2.8	25.9 ± 2.7	0.45
			1.44 ± 0.25	10.0 ± 1.8	29.9 ± 1.6	0.45
East	02 25 40.6	62 05 53	1.6 ± 0.5	8.1 ± 5.0	27.6 ± 4.2	0.43
			1.1 ± 0.2	14.5 ± 3.2	33.5 ± 2.1	0.43

[a] Using *getsources* extractions and parameters.

[b] Geometric mean FWHM of elliptical aperture at 500 μm.

[c] Excluding uncertain bands: 70 μm and 250 μm.

[d] Excluding just 250 μm.

[e] Manual aperture photometry; excluding 250 μm.

Sizes and coordinates are those derived from extractions in N_{H_2} map (Table 4.3).

Table 4.3 The high extinction structures in W3 Main: parameters from the $N_{\mathrm{H_2}}$ and T maps

Name	RA	Dec	Peak $N_{\mathrm{H_2}}{}^a$	Peak T^a	Mass	<FWHM>^{b}
	[h m s]	[°,′ ″]	[10^{23} cm^{-2}]	[K]	[10^3 M$_\odot$]	[pc]
W3 West	02 25 29.9	62 06 09	2.8 ± 0.8	23.4 ± 3.0	1.67 ± 0.03	0.45
W3 East	02 25 40.6	62 05 53	1.9 ± 0.6	27.2 ± 4.4	1.03 ± 0.03	0.43

[a] Measured at the coordinate center.

[b] Geometric mean FWHM of elliptical footprint.

both W3 East and W3 West, however, we found the deconvolved FWHM at 160 μm to be larger than those found at some of the SPIRE bands. This behavior can occur, for instance, if extended hot dust (traced better by PACS) surrounds the column density structure, whose emission dominates at the SPIRE bands. The origin of this problem has also been investigated in other HOBYS studies (e.g., Minier et al. 2012; submitted). This situation, however, precludes application of the flux density scaling recipe (Motte et al., 2010; Nguyen Luong et al., 2011a) used to correct for the different resolutions prior to SED fitting. Therefore, to ensure a consistent measurement, we extracted sources with *getsources* on the images after convolution to a common resolution corresponding to the 500 μm image.

Table 4.2 shows the parameters derived from fitting a modified blackbody, analogous to Equation 4.1, to the SEDs of the sources extracted at the positions of W3 East and W3 West. We used $\beta = 2$ and found the temperature T, the luminosity L, and, with the above opacity and gas-to-dust ratio R= 100, the total mass of each source. The SED fit depends on which bands are used, ideally all five *Herschel* bands for hot sources. As mentioned in Section 4.1, a few pixels in the original maps are saturated at the peak of W3 East at both 70 μm and 250 μm and for W3 West at 250 μm only. Nevertheless, a lower limit to the flux density at 70 μm is still estimated by *getsources*, and being

more uncertain it has less weight in the overall SED fit. The different entries in Table 4.2 show the sensitivity of the solution to band inclusion. Due to the SED peak being well constrained by PACS data, exclusion of the 250 μm data from the fits does not affect the final results significantly. Inclusion of 70 μm data results in a larger T and correspondingly lower mass; L is also higher.

The parameters listed in Table 4.2 have been verified by an independent analysis using manual (IDL) aperture photometry on the *Herschel* and SCUBA 850 μm maps (SCUBA Legacy Survey; Di Francesco et al., 2008), all convolved to the resolution of SPIRE 500 μm. The common apertures used were those estimated and used by *getsources* for the column density maps. The 250 μm band with the most severe saturation was again excluded from the fit. The SCUBA data were not important in changing the fit, lying close to the SED that would be obtained excluding it, and suggesting the assumption that $\beta = 2$ was reasonable. The resulting parameters are also included in Table 4.2.

Our analysis therefore confirms that the masses of W3 West and W3 East are of the order $\sim 10^3\,\mathrm{M}_\odot$. These are in agreement with previous estimates (e.g., Campbell et al., 1995; Megeath et al., 2008 and references therein), and the masses obtained by running *getsources* directly on the column density maps, as shown in Table 4.3. The centroids estimated by *getsources* from the convolved maps and used in Table 4.2 are 3.8″ and 2.2″ from the column density peaks (Table 4.3) for W3 West and W3 East, respectively.

W3 (OH) is the only other structure in this field with recent high-mass star formation. Neglecting the likely presence of non-linearity effects for those pixels in the 70 μm and 350 μm maps with a measurable signal in the neighborhood of the hard saturation (i.e., blank pixels), and excluding the 250 μm *getsources* measurement from the SED fitting, we obtain $T \sim 28.1 \pm 0.8\,\mathrm{K}$, $M \sim (1.0 \pm 0.2) \times 10^3\,\mathrm{M}_\odot$, and $L \sim (4.9 \pm 0.4) \times 10^4\,\mathrm{L}_\odot$ for a <FWHM> (500 μm) $\sim 45''$ (parameters comparable to those of the W3 Main sources). This mass estimate is lower than, but comparable, to the virial mass of the entire system obtained via NH_3 of $\sim 1300\,\mathrm{M}_\odot$ (Tieftrunk et al., 1998b). Compared to our estimates

for W3 East, W3 (OH) is therefore less luminous for a similar mass because of the lower temperature, or less luminous for the same temperature because of a lower mass. Based on the 500 μm estimate of column density and size, W3 (OH) could be as massive as W3 West for the same temperature, but less massive and luminous if warmer.

We conclude that the use of *Herschel* data not only confirms the massive nature of W3 East and W3 West, but also indicates that:

i) The clumps currently hosting the on-going high-mass star formation of W3 (W3 East, W3 West, and from our preliminary estimates, also W3 (OH)) are the most massive of the entire GMC. Only one source from the column density source catalog, located in the AFGL 333 Ridge, has a mass of this order (comparable to that of W3 East). It has, however, a lower peak column density and a deconvolved mean FWHM twice that of W3 East and West. Similarly, detections from the convolved multiband catalog (associated with the AFGL 333 Ridge) and with masses also of order $10^3\,M_\odot$, also show a mean FWHM (500 μm) $\sim$ twice that of W3 East and W3 West.

ii) W3 East and W3 West are the most luminous clumps in the GMC. Other than W3 (OH), only one detection has a reliable luminosity measurement that approaches that of W3 West. This source has $L \sim (2.6 \pm 0.5) \times 10^4\,L_\odot$ (including 70 μm data), $M \sim 100\,M_\odot$, and is associated with a column density peak east of the evolved compact H II region W3 A, which is itself NE of IRS5 in W3 Main. This structure could be tracing part of the 'shell' associated with W3 A (Tieftrunk et al., 1997), and only the massive star IRS2c is located within its FWHM. Indeed, the SED luminosity of this source is equivalent to a star of spectral type $\sim$B1V, which coincides with that estimated for IRS2c by Bik et al. (2012).

4.4.3 Stellar Content and Phenomena in a *Herschel* Context

The identification of properties *exclusive* to W3 East and W3 West (structural and stellar content) might reveal clues about their origin and the general process of high-mass star

and cluster formation. Therefore, here we attempt to find some of such properties by comparing *Herschel*-derived results with characteristics of the stellar population.

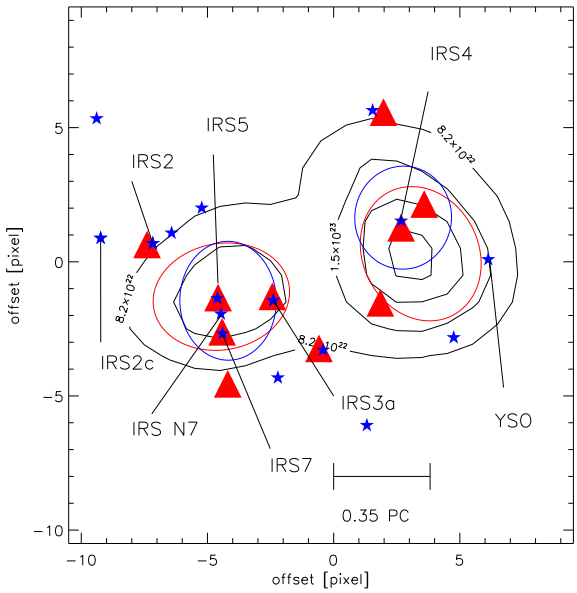

Figure 4.10 Distribution of H II regions (triangles; Tieftrunk et al., 1997) and OB stars (blue stars; Bik et al., 2012) in W3 Main. Contours are the same as in Fig. 4.9 (excluding the first contour). Ellipses are the FHWM ellipses provided by *getsources* during source extraction on the original *Herschel* maps (blue) and on the column density map (red). Axis units are in pixels (9.5″) offset from position RA/Dec:$2^{\rm h}\,25^{\rm m}\,35^{\rm s}.26$ $+62^\circ\,06'\,01''$. Labels mark the location of high-mass stars mentioned in the text.

Both clumps are unique in the W3 GMC due to their large population of young high-mass stars (e.g., Tieftrunk et al., 1997). These stars are present not only within the clumps, but also surrounding their outer boundaries. This can be observed in Figure 4.10, which shows the location of the OB population with respect to the *Herschel* detections. The spectral types of these stars were analyzed in detail by Bik et al. (2012). The figure also compares the FWHM ellipses derived by *getsources* when used on the unconvolved *Herschel* maps (blue ellipses), and the column density map (red ellipses). While there is a reasonably good agreement for W3 East, there is a clear discrepancy for W3 West.

Here *getsources* selects the warm bright (IRS4) region, offset $\sim 14''$ from the column density peak. Our choice to use *getsources* on the convolved maps, however, results in a better agreement with the column density measurement (Table 4.2), and therefore a more accurate representation of the properties of the 'clump' as a whole.

W3 East

W3 East is the most active of the two clumps in terms of the associated (external and internal) stellar population.

The YSO and proto-Trapezium system IRS5 is located at the column density peak . In addition to IRS3a, also located within the FWHM (boundary) at $d \sim 0.1$ pc is IRS7, a late O/early B star associated with an UCHii region and, closer still to the peak, IRS N7 (Fig., 4.10), also a YSO, albeit older than IRS5 (Bik et al., 2012). Using the technique presented in Chapter 2 we estimate that the luminosity of the W3 East clump is equivalent to a single-star main-sequence spectral type of ∼O7–O6.5 ($L \sim [1.5 \pm 0.2] \times 10^5\,\mathrm{L}_\odot$). The use of the ZAMS table in Panagia (1973) would decrease this estimate by ~ 0.5 (becoming an 'earlier' type star). Bik et al. (2012) provided no spectral type estimate for IRS5, but our value is compatible with that of IRS3a, the earliest (reported) star within the FWHM of W3 East, with an estimated spectral type of O5–O7.

Despite the significant population of high-mass stars within its boundaries, W3 East is externally heated. The highest dust temperatures of the entire GMC (~ 30 K) are located *outside* the NE and SW boundary of the $N_{\mathrm{H_2}}$ clump (Fig. 4.9), coincident with many late O/early B stars $\lesssim 0.5$ pc from the peak (Fig. 4.10). These outer stars range in spectral type from early B to O6.5 (IRS2) (Bik et al., 2012).

W3 West

Despite having more mass and higher column density than W3 East, W3 West is relatively more quiescent. There is no indication of internal high-mass star phenomena coincident

with the *Herschel* N_{H_2} peak; high-mass star formation appears to have not yet progressed or been initiated in the innermost regions. Corroborating this, there is an NH_3 peak at the position of the column density peak (Tieftrunk et al., 1998b), and this peak is offset from any PACS (hot) infrared source or any H II region. This differs from W3 East, whose column density peak lacks significant NH_3 emission, and was therefore suggested to be in a more advanced state of evolution in which it has already influenced its parental cloud locally (Tieftrunk et al., 1998b).

Only IRS4 is found within the boundaries of this clump, ~ 0.1 pc from the N_{H_2} peak (Fig. 4.10). It is a B0.5–O8 star predicted to be as young as IRS5, based on the presence of HCHII regions (Bik et al., 2012). This is in excellent agreement with the single-star main-sequence spectral type O8.5 derived from the *Herschel* luminosity of $L \sim (7 \pm 1) \times 10^4\,L_\odot$ (the wide range spanning the band inclusion uncertainty, $L \sim$(4 – 12) $\times 10^4\,L_\odot$, would yield a range of B0.5–O7.5). The *Herschel* measurement is therefore consistent with IRS4 being the main source powering this clump, and with the more quiescent nature of the region coincident with the column density peak.

The other members of the young population of W3 West lie close to or beyond the boundary of the column density structure (Fig. 4.10). The strongest column density gradients around W3 West are located toward the southern and SW boundaries, where a YSO and other high-mass stars are located. The presence of YSOs in a region of particularly steep gradients could suggest that these have been influenced by the diffuse H II regions at the south.

A very interesting point noted in previous studies of both W3 East and W3 West (e.g., Tieftrunk et al., 1997; Bik et al., 2012) is a progressive *decrease* in age of the stellar population from the outskirts toward the peak of the density structure, from the farthest diffuse H II regions, to the more centrally located evolved compact, and HCHII regions. The lower dust temperature, higher mass, and higher peak column density estimated by *Herschel*, combined with the presence of a high-mass star population toward the

boundary, the presence of ammonia (Tieftrunk et al., 1998b), and lack of internal high-mass star indicators in W3 West, imply that this clump is indeed in an earlier evolutionary stage than W3 East, and therefore a prime candidate for further studies.

4.4.4 W3 East and W3 West In Perspective: High Column Density Structures Lacking High-Mass Star Formation Indicators

In addition to W3 (OH), *Herschel* identifies only two other structures in the W3 GMC with column densities of the order $N_{\rm H_2} \sim 10^{23}\,{\rm cm}^{-2}$: W3 SE (Fig. 4.9), in the W3 Main region, and the AFGL 333 Ridge.

W3 SE is the coolest of the three clumps in W3 Main. It is located $\sim 1.3\,{\rm pc}$ from IRS5, with the closest high-mass star indicator being a diffuse H II region $< 1\,{\rm pc}$ to the southwest.

Also located in the HDL, the AFGL 333 Ridge, despite being at the boundary with W4, shows evidence of a more locally triggered origin. For example, it has i) an elongated morphology on the east curved around an embedded cluster IRAS 02245+6115 ($\sim 1.3\,{\rm pc}$ from the strongest column density peak in the Ridge and containing a compact H II region powered by a B0.5-type star; e.g., Hughes & Viner, 1982); ii) steep column density and temperature gradients associated with this structure that are oriented toward the cluster; iii) a distribution of YSOs that follow the curvature of the structure and is abundant in the boundary between the Ridge and the cluster (Chapter 3); and iv) an overall much younger population compared to all the other YSO groups in the rest of the field (Chapter 3). Indeed, the AFGL 333 Ridge contains $\sim 70\%$ of the Class 0/I population in the AFGL 333 field (excluding the population in the East Loop, due to its environmental conditions being more consistent with the western fields than the HDL; see Chapter 5), while only $\sim 5\%$ of the Class II population is found within this structure.

W3 SE and the AFGL 333 Ridge are both forming stars (Chapter 3), and both appear to have the potential to form high-mass stars. They also have a possible 'trigger', i.e. a high-mass star, in their local neighborhood that could aid in the process. However, they do not reach the column densities, masses, and degree of stellar activity (internal and external to the clumps) characterizing W3 East and W3 West.

4.5 Discussion: Formation of Clusters with High-Mass Stars and 'Trapezium-like' Systems by a 'Convergent Constructive Feedback' Process

The evidence presented in recent *Herschel* HOBYS studies suggest that an active process aiding in the supply of material, beyond that required to form a low-mass star, is likely a critical feature of the high-mass star/cluster formation (e.g., convergence of flows, junctions of filaments). In addition to those scenarios aiming to describe the origin of the parsec-scale progenitors of massive clusters, there currently exist various models describing the origin of the individual cluster members by invoking processes acting at sub-parsec scales, such as small-scale convergence of flows (Csengeri et al., 2011) and turbulent cores (McKee & Tan, 2003).

In order to explain the physical properties inferred by *Herschel* in this work for W3 East and W3 West, which we confirm to be unique in the entire W3 GMC, in the context of their (also unique) geometry, stellar population characteristics, and star formation history, we propose an scenario for the formation of a massive clump (suitable for hosting a cluster of high-mass stars) as well as the individual high-mass stellar members.

Local stellar feedback results in much faster and more efficient star formation than in the quiescent mode at the interaction boundaries (e.g., Elmegreen & Lada, 1977), between the 'triggering' stars and a dense environment. We have observed this effect

between W4 and the HDL, near AFGL 333 (e.g., Chapters 3 and 5). Enhanced star formation in triggered regions has also been reported in previous studies (e.g., Thompson et al., 2012; Koenig et al., 2012). Here we argue that high-mass stars ('triggers') can not only collectively influence the creation of new high-mass stars, but also the new, massive structures that would be hosting this new population of high-mass stars. The 'positive' effects of stellar feedback by high-mass stars have been extensively studied in other HOBYS fields (e.g., Minier et al. 2012; submitted).

In addition to the efficiency of triggering as a star formation process, our model suggests that the *configuration* of the high-mass triggers is a key factor in the formation of the most compact and massive systems (i.e., Trapezium-like systems), like those in W3 Main. When acting on a dense region with enough mass, different populations of high-mass stars with the right configuration can lead to a 'convergent' process, creating/enhancing a central massive structure, moving and confining the material, and ensuring the availability of mass during the early disruptive stages of high-mass star formation. The central column density would continue to grow as new high-mass stars form by sub-parsec triggering at the 'boundaries' of the high column density region, where triggering is most effective, in a sequential process which we describe as *'convergent constructive feedback'*.

Our proposed scenario, while based on the principles of classical triggered star formation, is, like previous *Herschel* HOBYS results, also based on a 'convergent' process. The present scenario can, however, also explain the unique stellar distribution and characteristics of W3 East and W3 West in conjunction with the *Herschel*-based properties, and could also be invoked to address other outstanding issues in high-mass star formation, as discussed below.

4.5.1 Elaboration

Low and high-mass star formation induced by external OB stars is a well-known and readily observed phenomenon (e.g., White et al., 1999; Tothill et al., 2002; Minier et al.,

2009).

The progress of triggering is, however, dependent on the environmental conditions. A high-mass star in a dense environment (e.g., a shell or ridge) can influence local material or induce further compression only at smaller (sub-parsec) scales, as the disruptive effects of newly formed high-mass stars are not efficient in relatively dense regions (Dale & Bonnell, 2011) and are therefore of more limited range. Nevertheless, this further compression could propagate the triggering process and the formation of new high-mass stars on the relevant small scales, starting at the boundaries and progressing toward the more dense (inner regions) of the compressed structure. This process would explain, for instance, the presence of molecular cores and condensations in the perimeter of the ionized regions (e.g., Tieftrunk et al., 1995; Tieftrunk et al., 1998a) in W3 Main (W3 East). In such dense environment, the progressive formation of high-mass stars can, in addition, result in the formation of even higher column densities, rather than disruption by the mechanical and radiative output of the high-mass stars. A particular case could then arise, where a particularly massive and dense structure forms *between* separate high-mass star populations, due to their combined effect in compressing and *confining* the material.

W3 West exemplifies this possibility, as it is a prominent quiescent column density peak with infrared sources at its periphery, with a clear anticorrelation between molecular and ionized gas (e.g., Tieftrunk et al., 1998b). A similar confining arrangement is also observed for W3 East, but there higher resolution studies have shown an even smaller central core containing IRS5, within our *Herschel* clump, surrounded by the other H II regions (e.g., Tieftrunk et al., 1995). Observations therefore suggest that W3 East contains an already active version of what is occurring in W3 West. Furthermore, Tieftrunk et al. (1998b) suggested that the lack of ammonia associated with W3 East was due to NH_3 being 'thinned out' or destroyed by ongoing activity *without* dispersal, which also supports the 'confinement' aspect of the process. In contrast, an ammonia peak is still present in W3 West. The combined evidence supports a similar process for both clumps,

but with W3 West at an earlier stage.

The compression of convergent feedback might also be able to explain the 'pinched' morphology of the magnetic fields (e.g., Roberts et al., 1993; Greaves et al., 1994; Tieftrunk et al., 1995), where compression leads to an enhancement of the component of the observed magnetic field parallel to the compressed structure (e.g., Peretto et al., 2012).

In alternative models of high-mass cluster formation (e.g., Peters et al., 2010), the central, most massive star forms first, followed by the formation of secondary high-mass stars in the accretion flow. The stellar companions would limit the accretion onto the central high-mass star, leading to 'fragmentation-induced starvation'. A key consequence of the convergent constructive feedback process is, however, that stars would form progressively closer to the central regions, each generation 'aiding' in the formation of new high-mass stars, and resulting in a systematic *decrease* in age toward the innermost regions of the clump. This behavior is indeed observed in the high-mass stellar population in W3 Main (e.g., Tieftrunk et al., 1997), as well as an enhanced concentration of young Class 0 stars at the boundaries of the H II regions within the W3 East clump (Ojha et al., 2009) suggestive of induced star formation. A sequential process of high-mass star formation in W3 Main was already suggested in previous studies (e.g., Tieftrunk et al., 1997; Feigelson & Townsley, 2008: option 4 in their analysis).

While (low/intermediate-mass) star formation likely has taken place in the dense region prior to the present triggering, accounting for the large cluster of low mass stars in the region (Feigelson & Townsley, 2008), the rate and efficiency will likely be enhanced at later stages. The effects of sub-parsec triggering acting within the high column density structure being formed, together with the amount of mass and limited range of the triggering, could sustain lasting periods of star formation in the most central regions, therefore emphasizing the differential age effect.

4.5.2 Implications

Above we have attempted to established a link between all the properties that make W3 East and W3 West unique with respect to all other sources in this GMC: the unique (external) high-mass population, their (internal) population, the temperature distribution, column density, and their intrinsic (SED) characteristics. Current theoretical models, however, face several challenges when trying to address even the most basic processes of the high-mass star formation process, such as: 1) the low core accretion rate m^* (and therefore the long formation times) due to initially low temperatures (e.g., $m^* \propto T^{3/2}$; for isothermal core collapse; Shu, 1977); 2) the suppression of accretion due to radiation pressure and ionization by the forming high-mass star (Zinnecker & Yorke, 2007); 3) formation in clustered environments; and 4) primordial mass segregation with anomalous age distributions (e.g., young central massive systems surrounded by a cluster of older low-mass stars).

The convergent constructive feedback could also provide a useful framework for addressing some of these problems.

First, given the age spreads in W3 observed by Bik et al. (2012), a progressive formation of the central column density clump and cluster members must have occurred over a 2-3 Myr period. Therefore, there is no need to form such structures fast enough to prevent major internal fragmentation or to invoke long and unrealistic 'starless' lifetimes. The 'older' halo cluster of low-mass stars surrounding the high-mass star population in W3 Main (e.g., Megeath et al., 1996; Feigelson & Townsley, 2008) that formed throughout the region might already have initiated or enhanced the process of compression in the center, as well as contributed to the formation of the first population of high-mass stars.

Second, the simultaneous, small-scale (sub-parsec) triggering by high-mass stars could provide more turbulent and warmer environments. These changes could inhibit fragmentation by increasing the minimum Jean's mass, leading to the formation of new massive

cores (e.g., Zinnecker et al., 1993; Peters et al., 2010) and an increase in the characteristic stellar mass toward the more central regions, as observed for the IRS5 clump for the high and low-mass population (Megeath et al., 1996; Ojha et al., 2009). The combination of high efficiency of triggering and higher temperatures could then be key to the formation of rich clusters of high-mass stars. Consequently, the final morphology of the cluster would resemble that of a more evolved cluster after mass segregation. Indeed, from their timescale analysis of W3 Main, Ojha et al. (2009) suggested that the apparent mass segregation must be not dynamical in origin.

Third, when a high-mass star forms close to the central (and most dense) regions of the clump, the limited range of the stellar influence (Dale & Bonnell, 2011) and the efficiency of triggering could then lead to the most compact and richest systems, by forming new overdensities, inducing the collapse of preexisting ones, or by direct interaction between the effects of the embedded high-mass stars such as outflows and shocks (Phillips et al., 1988). In W3 East, this could account for the high star formation efficiency and multiplicity observed in the innermost regions of the clump, local to the IRS5 system (Megeath et al., 2005; Rodón et al., 2008). The sub-parsec convergence of flows scenario from Csengeri et al. (2011) would also benefit from the confined environment created by the convergent constructive feedback, minimizing the disruptive effects.

Fourth, in a scenario with multiple and simultaneous triggering by various high-mass stars, as in W3 Main, the resulting central structure could reach rare, high column densities suitable for the formation of central Trapezium-like systems.

Fifth, the continuing confinement and influence by the high-mass stars at the outer boundaries of clumps could aid the accretion required to produce very massive protostars in the central region, sustaining the feeding process by counteracting or minimizing mass loss due to the stellar outflows, winds, and radiative energy of the newly formed (and more embedded) high-mass stars. How the actual feeding (accretion) mechanism at in-clump scales proceeds (e.g., in filaments) is, however, beyond the scope (and resolution

capabilities) of this work.

4.5.3 Applications: W3 (OH) and Other High-Column Density Regions

W3 (OH) has an asymmetric cluster spreading *along* the direction perpendicular to the direction of IC 1795, evidence of direct triggering by IC 1795 itself (e.g., Oey et al., 2005; Feigelson & Townsley, 2008). This evidence is also supported by the 'string' of stellar clusters extending north of W3 (OH) in the same direction. There is, however, also evidence of influence by W4, as observed in the various nebulosities and stars extending from W4 toward the W3 (OH) 'ridge'/shell (Tieftrunk et al., 1998b), and in the dynamics of this structure and the associated stellar population (e.g., Thronson et al., 1985).

The location of W3 (OH) at the interaction point between the effects of two high-mass populations is therefore more reminiscent of large (parsec) scale convergence of flows, albeit in this case directly powered by high-mass stars rather than large-scale cloud turbulence. Indeed, very large-scale feedback (e.g., over tens of parsecs) might by itself be capable of enhancing and inducing the collapse of pre-existing structures (e.g., Peretto et al., 2012).

Based on the derived *Herschel* properties it appears that clumps with similar properties are produced in both, W3 (OH) and W3 Main. Contrary to the latter, however, W3 (OH) has not benefited from the combined effect of favorable environmental conditions, the efficiency of sub-parsec triggering by (boundary) high-mass stars, and the associated positive effects. This lack of local high-mass stars might explain why, for similar clump mass, the W3 (OH) system is overall less active, or why there are two massive clumps with significant high-mass star activity in W3 Main, compared to just one in the 'shell/ridge' containing W3 (OH).

On the other hand, W3 SE and the AFGL 333 Ridge have only relatively weak and/or *localized* (one-sided and of scale $< 1\,\mathrm{pc}$) high-mass star feedback, driven by isolated late

O/early B stars that likely originated from larger-scale stellar feedback from IC 1795 and W4, respectively. Although small-scale (sub-parsec) triggering might have led to the formation of these high column density structures, the collective effects of compression, confinement, and stellar feedback have not (yet) been sufficient to form high-mass stars within them.

In addition to those examples in the W3 GMC, 'convergent constructive feedback' could also be responsible for the observed morphology and high-mass star formation in other regions, like the S255-S257 complex (Minier et al., 2007).

The feasibility of this and the other proposed scenarios dealing with the origin and evolution of high-mass stars and clusters will be better constrained with the release of new evidence from other HOBYS fields, currently under investigation.

4.6 Conclusion: Toward Unifying High-Mass Star Formation Theories

This work is the first analysis of the W3 GMC using the *Herschel* data delivered as part of the Guaranteed Time Key Programme HOBYS.

The data was reduced, corrected for contributions from background/foreground material, and used to produce and analyze the column density and dust temperature maps. The software *getsources* was used to extract a preliminary catalog of compact sources from the *Herschel* maps (convolved to the 500 μm resolution) and the column density maps. In particular, the multiband datasets were used to carry out a detailed study of the intrinsic (SED) properties of the clumps currently hosting on-going high-mass star formation, suitable for comparison with the results (and high-mass star formation models) recently obtained from other HOBYS fields.

Our results indicate that the clumps hosting on-going high-mass star formation are unique in terms of luminosity, temperature, mass, and column density, with W3 East

and W3 West being the most massive, and the highest column density structures of the entire GMC.

Being W3 East and W3 West, in addition to W3 (OH), the only clumps currently forming clusters of high-mass stars in this field, we have used the properties *exclusive* to these clumps as a base to create an scenario capable of linking their 'extreme' *Herschel*-based properties with the well-known characteristics of their high-mass stellar content, which is also unique in the W3 GMC.

While numerical models and simulations are required to test the feasibility of different scenarios, we conclude that the observational evidence in W3 points toward a very basic prerequisite for high-mass star formation: an active assembly of material for the formation of the most massive cores/clumps. In particular, and in agreement with the conclusions from other HOBYS studies, we agree that 'convergence' appears to be a common mechanism for achieving this goal. The movement of material would guarantee a build-up of mass and maintainance of the feeding process, ensuring access of material to the massive protostars during their earliest stages despite their disruptive power. A dynamical formation of massive precursors has also been suggested in previous studies based on a statistical analysis of core populations (Motte et al., 2007).

A major difference between the model proposed in this work and the convergence of flows scenario, is that here we use stellar feedback, the efficiency of triggering in star formation, and the associated displacement, compression, and confinement of material, to ensure the availability of mass during cluster formation. In this process of 'convergent constructive feedback', the sub-parsec influence from different populations of high-mass stars can lead to the creation/enhancement of a massive clump in the most central regions (suitable for the most massive, e.g., Trapezium-like, systems), as well as sequential star formation events initiated at the boundaries of the high-column density structure. This scenario could explain not only the non-dynamical cases of mass segregation, but also those clusters with stellar age decreasing towards the innermost regions of the cluster.

The power, configuration, scale of the triggering process, and the environmental conditions, are all likely important in determining the final richness, geometry, timing (e.g., inner young regions versus an outer older population), and the initial mass function (IMF) of the formed cluster. Overall, the low probability of satisfying all the prerequisites and conditions for the formation of the most massive clusters could explain the relatively small numbers of systems like those in Orion, W3 IRS5, and the massive clumps in DR 21.

Chapter 5

The W3 GMC: Environment, History, and Evolution

5.1 Maps and Data Processing

This study makes use of the column density and dust temperature maps created from the *Herschel* intensity maps, as described in Chapter 4. Unless mentioned otherwise, this works uses the ISM-corrected maps as default for our analysis.

Information about the YSO population was obtained from the *Spitzer* analysis in Chapter 3. We refer to this analysis and the studies of Ruch et al. (2007) and Polychroni et al. (2010) for a description of these datasets.

5.2 Methodology: Identification and Characterization of Star-Forming Structures

The observed differences between neighboring regions in W3 make it necessary to quantify how in-cloud local conditions affect the star formation process. To this end we have carried out an individual analysis of each of the four fields (described in Chapter 4) and

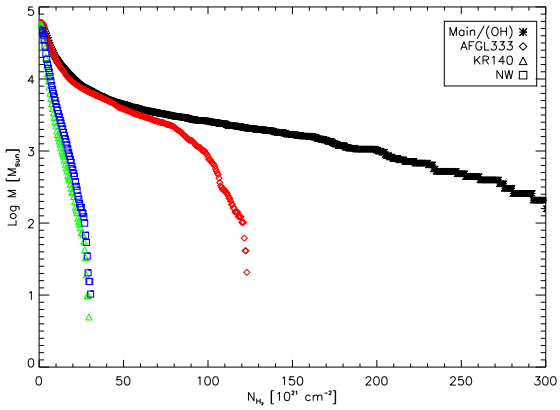

Figure 5.1 Mass distributions for the entire W3 GMC (black) and each of the four fields: W3 Main/(OH) (black), AFGL 333 (red), KR 140 (green), and W3 NW (blue).

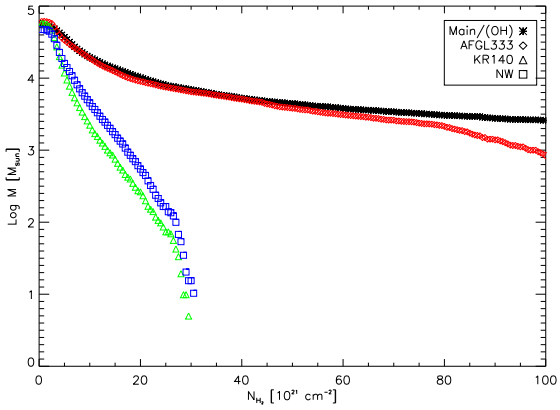

Figure 5.2 Same as Fig. 5.1, but for $A_{\rm V} < 100^{m}$.

their regions with the highest potential for recent and future star formation.

In order to characterize the density structures we created mass distributions and probability density functions (PDFs) of the column density maps, for the entire cloud and for each individual field. We note, however, that while PDFs have been extensively used as analytical tools for describing the distribution of mass in a given cloud or region, the cumulative form of the mass distributions (total mass above any given magnitude; e.g., Froebrich & Rowles, 2010) allows for a more straightforward analysis of the column den-

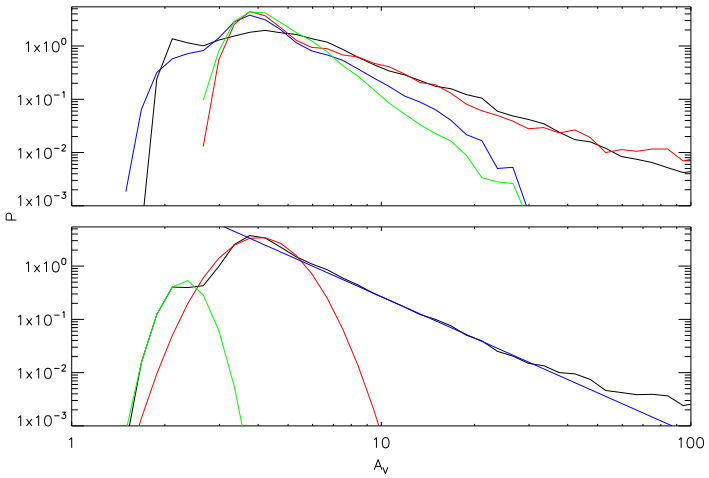

Figure 5.3 Top: Probability Density Functions (PDF) for each field in W3 without correcting for the background/foreground emission: Colors like Fig. 5.1. Bottom: Global PDF for the entire W3 GMC with two fitted lognormal distributions (green and red), and a power-law tail (blue).

sities theorized to be associated with high-mass star formation (A_V[1]$> 160^m$; Krumholz & McKee, 2008; defined here as 'massive star formation threshold' (MSFT); see Chapter 4 for the dust parameters and assumptions used in this work). In the PDF, column densities of this order are characterized by poor statistics and a complex (power-law) tail, with prominent substructure such as breaks and peaks, which result in a poor and unreliable fit. As an example, magnitude bins in the PDF of the W3 Main/(OH) field with $A_V \geq 100^m$ have $N \leq 15$ pixels per bin ($< N > \sim 8$); and yet the mass above this extinction limit comprises $\sim 4.5\%$ ($\sim 3.5\%$ without correcting for the ISM) of the mass of the field. This implies that material suitable for high-mass star formation is accounted for by only $< 0.2\%$ of the total number of valid pixels. This calculation excludes pixels not in the common science region, zero-valued, with observed dust temperatures T <40 K, or saturated (i.e., $\sim 25\%$ of the pixels in this field). The temperature limit was

[1] $N_{H_2} = 9.4 \times 10^{20}\,\mathrm{cm}^{-2} A_V/\mathrm{mag}$; Bohlin et al. (1978)

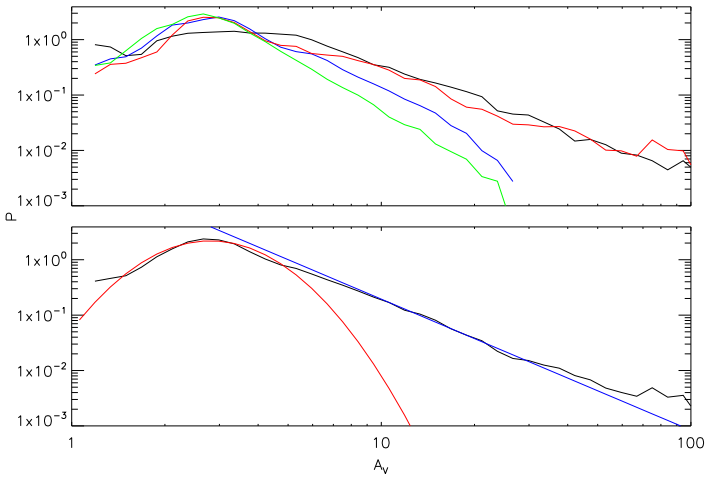

Figure 5.4 Same as fig. 5.3, but for the ISM-corrected maps.

chosen as pixels above this limit were exclusively associated with the saturated regions in W3 (OH). Dust temperatures of this order are consistent with those estimated toward known UCHii regions (e.g. Chapter 2).

Figure 5.1 shows the mass distributions for each field and the W3 GMC, plotted as a function of mass contained above a given magnitude. Figure 5.2 shows the extinction range $A_{\rm V} < 100^m$ in more detail. The un-corrected and ISM-corrected mass distributions can be compared in Figures 5.3 and 5.4, respectively, which show the global PDF of W3 and its decomposition into contributions from each of the four fields. Following the technique used in previous studies (e.g., Schneider et al., 2012 and references therein), each peak was fitted with a lognormal distribution. When fitting the main peak of the PDF we used data with extinctions in the range $1.5 \leq A_{\rm V} \leq 6^m$. When more than two peaks were present in the PDFs we fitted them with separate lognormal distributions, although as observed in Figure 5.4 this was not necessary after correcting for the ISM contribution. All fits were carried out using a non-linear least-squares minimization IDL routine based on MPFIT (Markwardt, 2009).

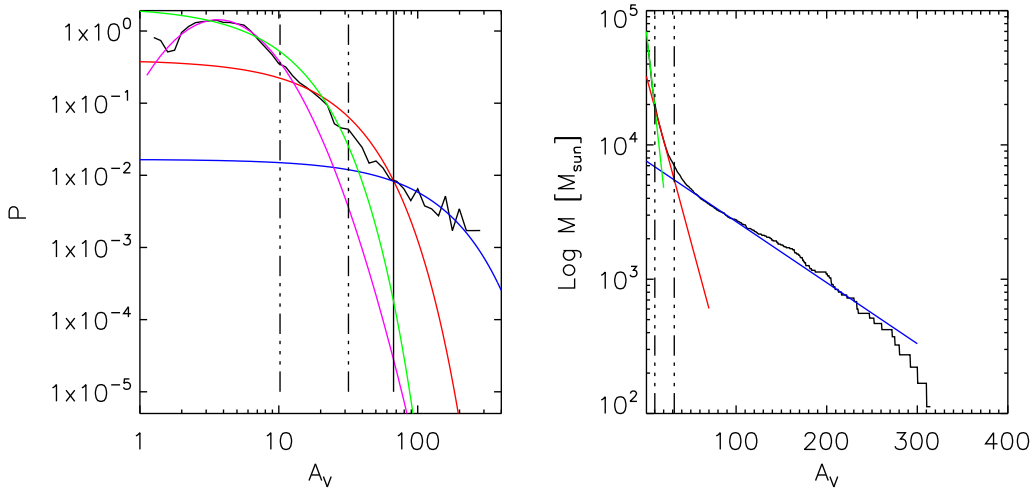

Figure 5.5 Right: Mass distribution of the W3 Main/(OH) field. Solid green, red, and blue lines are the best linear fits to the data. Vertical lines mark the breaks in the distribution ($A_{\rm V,SF}$ and $A_{\rm V}$(HTB)). Left: PDF of the same field. Vertical and colored lines are those of the mass distribution. Solid vertical line is the $A_{\rm V}$(HB).

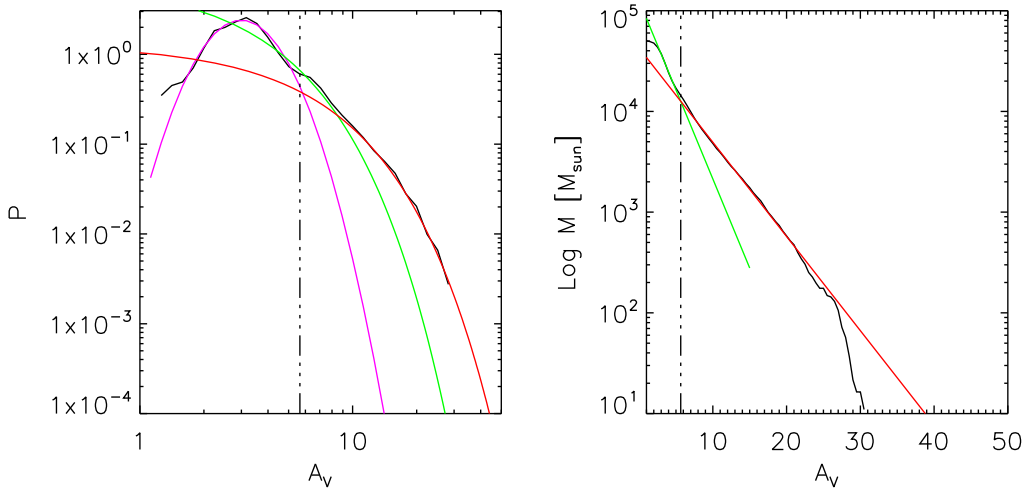

Figure 5.6 Same as Fig. 5.5, but for the W3-NW field.

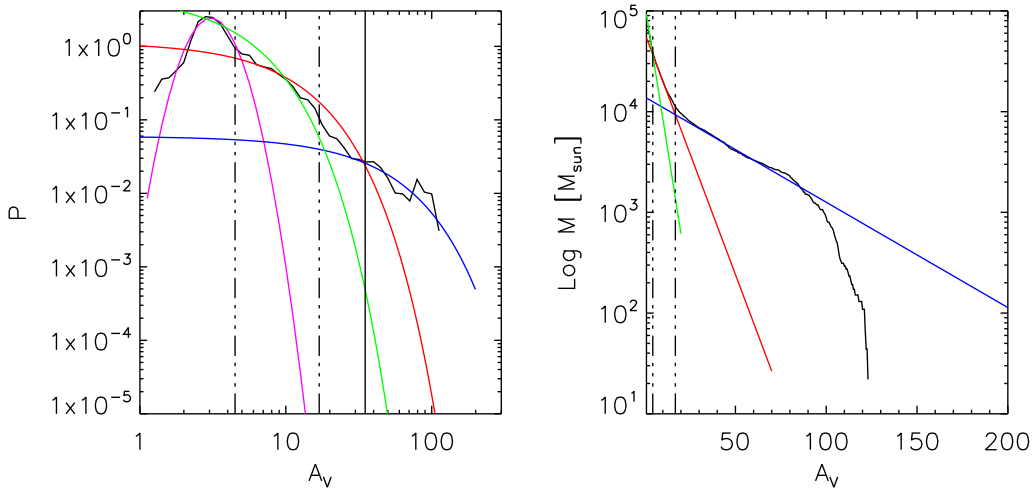

Figure 5.7 Same as Fig. 5.5, but for the AFGL 333 field.

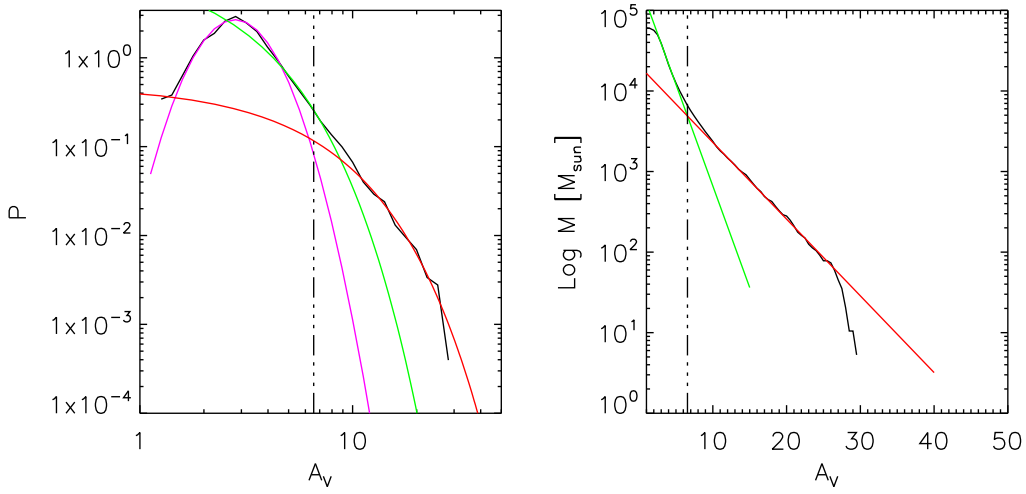

Figure 5.8 Same as Fig. 5.5, but for the KR 140 field.

5.3 Understanding the Probability Density Functions

5.3.1 PDFs vs. Mass Distributions

The magnitude at which a break occurs in the low extinction range of the mass distributions has been suggested to separate the turbulent environment from the gravity dominated structures ($A_{\rm V,SF}$; Froebrich & Rowles, 2010). This break is defined as the point where linear fits to adjacent regions of the mass distribution cross (e.g., Fig. 5.5). The 'sharper' the transition (quick transition and small region of curvature) of the function the better the constraint on the break.

Similarly, the 'break' at which the PDF deviates from a lognormal distribution into a power-law has also been commonly interpreted as the point separating the turbulent medium from the regime where star formation dominates (e.g., Ballesteros-Paredes et al., 2011 and references therein). Being PDFs and mass related distributions representations of the same data, any 'physical' or 'real' break should be identifiable when using any of the two methods. In this work we used the mass distributions as the primary approach for deriving the breaks, as these were observed to be much easier to fit with a linear function than the 'power-law' tail of the PDFs, especially in the high column density regime. The derived values, as well as the parameters for our best linear fits, have been included in Table 5.1.

In order to check for consistency with features observed in the PDFs, we transferred our best linear fits to the mass distributions (log(M) vs $A_{\rm V}$) to the PDFs (linear binning) using the following expression:

$$P(PDF)_{AV1}^{AV2} = \frac{10^{Y_{AV2}} - 10^{Y_{AV1}}}{N_{tot} < A_V > M_{const} Bin}, \tag{5.1}$$

where $\rm Y_{A_V}$ is the best-fit Log[M] (in $\rm M_\odot$) at $A_{\rm V}$, derived using the parameters from our best linear fit (Table 5.1); $N_{\rm tot}$ is the total number of valid pixels in the field; $< A_{\rm V} >$ is the mean extinction of the magnitude bin defined by $A_{\rm V}1$ and $A_{\rm V}2$; 'bin' is the bin size used in the PDF; and $M_{\rm const} = 0.18$, a constant comprising all the transformation

Table 5.1 Breaks and parameters for the best linear fits to the mass distributions

Field	Break[a] (mag)	Slope/Intercept (1)	Slope/Intercept (2)	Slope/Intercept (3)
Main/(OH)	10.0-31.5	-0.061/+4.900	-0.025/+4.533	-0.005/+3.884
AFGL 333	4.5-17.0	-0.115/+5.082	-0.048/+4.783	-0.011/+4.147
KR 140	6.5	-0.2524/+5.3458	-0.0953/+4.3148	
W3 NW	5.5	-0.1772/+5.1026	-0.0935/+4.6297	

[a] Breaks in the mass distributions ($\sigma > 0.5$ mag) rounded to nearest 0.5.

Fields in the HDL show two breaks. The first break is the $A_{\mathrm{V-SF}}$.

parameters used to derive masses from extinction measurements at the distance of W3. This equation was transformed to the logarithmic binning of the PDFs and normalized accordingly. The final result can be observed in Figures 5.5-5.8.

The figures show that the 'first' breaks derived from the mass distributions are coincident with the breaks in the PDFs, while the overall shape of the functions can account for visual changes (bumps) in the tail of the PDFs. We note than an anomalously 'broad' curve/transition region between the first and second power law lines in the mass distribution of the KR 140 field (not observed in any of the other fields) results in a higher degree of uncertainty when determining its $A_{\mathrm{V-SF}}$ (first break). However, we note that the point in the PDF where the data deviates from a lognormal distribution is consistent with the point where the first slope in the mass distribution (green line; Fig. 5.8; right diagram) deviates from the data (start of transition region). A higher degree of uncertainty for KR 140 is expected, however, as this field is also the one with the most severe ISM (molecular) contamination.

In the two fields of the HDL the mass distributions have also revealed the presence of a second 'break' (defined in this work as A_{V}(HTB), for 'High extinction Transition Break'). This marks the transition point between the power-law tail of the PDF and a

'flatter' regime, fitted in the mass distributions with a third linear function (blue slope; Figs. 5.5 and 5.7). As with the mass break in the KR 140 field, this second transition was found to have considerable breadth for both HDL fields. The 'break' at which this flat regime starts to dominate in the PDF ($A_{\rm V}$(HB)) is marked by the point where the mass distribution is properly described by the third linear function in Table 5.1, also coincident with the point where the two power law lines (blue and red) derived from the mass distributions intersect in the PDF. These points are $A_{\rm V}$(HB)$\sim 35^m$ and 65^m for AFGL 333 and W3 Main/(OH), respectively. The presence and nature of this possible break, while uncertain due to the poor statistics at these high extinctions, is important due to its possible link with high column density material, including that associated with high-mass star forming regions.

5.3.2 Interpretation: Comparative Analysis and Clues About Cloud Structure

Overall, the morphologies of the mass distributions of the two western fields are consistent with having been drawn from the same parent distribution, with a Kolmogorov-Smirnov (KS) test probability of P$>$ 0.6. The two mass distributions of the two HDL fields are also consistent with each other for $A_{\rm V} \lesssim 50^m$ ($P = 0.95$), but diverge by more than $1-3\sigma$ for $A_{\rm V} > 40-50^m$. These diverge from those of the western fields for extinctions higher than $A_{\rm V} \sim 3-5^m$.

When analyzing the structures in the PDFs for the ISM-uncorrected maps we observe that all fields in W3 have a peak at $A_{\rm V} \approx 4^m$ ($\approx 4.5^m$ for W3 Main/(OH); Fig. 5.3). Only the two northern fields (W3 Main/OH) and W3-NW) show another peak at $A_{\rm V} \approx 2.2^m$, which we find to be due to low extinction diffuse material *external* to the W3 GMC (i.e., below average internal environmental conditions in the GMC). Indeed, removal of foreground/background material eliminates most of the component associated with this first peak (e.g., Fig. 5.4), although a 'remnant' of a peak is still observed for the W3

Table 5.2 Characteristics of On-going and Potential Star Forming Structures

M ($10^3 M_\odot$)	%[a]	$< T >$ (K)	Area (pc^2)	%
W3 Main/(OH)				
20.4 ± 0.21	34.2	21.2	45.8	8.7
5.0 ± 0.04	8.4	18.4	12.3	2.3
AFGL333				
38.4 ± 0.09	58.9	17.1	183.9	30.1
24.0 ± 0.08	36.8	15.8	109.7	17.9
KR140				
6.6 ± 0.03	10.8	15.3	34.33	3.8
5.4 ± 0.03	8.8	14.9	26.8	3.0
W3-NW				
14.3 ± 0.04	28.4	14.9	80.0	12.4
13.8 ± 0.04	28.3	14.8	76.3	11.9

[a] % of total field.

[d] $N_{H_2} \geq A_{V-SF}$ (Table 5.1).

[e] $N_{H_2} \geq A_{V-SF}$ and $T \leq T_{env}$.

Main/(OH) field. This is expected, as our correction does not remove the contributions from the ISM in the velocity range (similar distance) of W3 itself. This emphasizes the need for a careful selection of the area chosen for analysis, and which should preferably contain material exclusive to the cloud. Correcting for the ISM contribution broadens and shifts the main peak of the PDFs to lower extinctions, ranging from $A_V \approx 2.5^m$ for the KR 140 field to $A_V \approx 3.5^m$ for W3 Main/(OH).

Based on the similar regions in the mass distributions and the common peak in the PDFs, we conclude that material with extinction $A_V \sim 3^m$ comprises the *common plateau*

in W3 (GMC environment), on which the 'star-forming' structures are observed. A peak at $A_{\rm V} \sim 2-3^m$ was also observed for the regions in the Rosette cloud (Schneider et al., 2012) with the exception of their most central field, which contained only the highest column density material of the cloud (and is therefore not representative of the average cloud characteristics). As expected, this value is also considerable lower than the critical extinction for core formation of $A_{\rm V} \sim 8^m$ estimated by (André et al., 2010), which rely on a 'filamentary' environment.

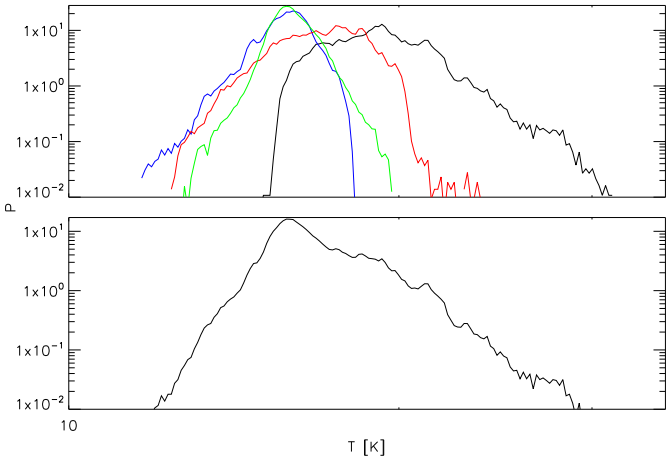

Figure 5.9 Same as fig. 5.4, but for the ISM-corrected temperature maps.

In order to identify the major potential star forming sites, distinguishable from the environmental conditions of the GMC, we required these structures to have $N_{\rm H_2}$ above the $A_{\rm V-SF}$ in each field. More than 90% of the Class 0/I YSO population is contained above this limit except in the KR 140 field, where $\sim 30\%$ is below the $A_{\rm V-SF}$ ($< A_{\rm V-YSO} > \approx 4.5^m$). Considering the intricate structure observed in the IRAC maps for this field (Chapter 3) it is plausible that isolated (and unresolved) column density knots can form in turbulent environments and result in isolated low mass star formation out of the major structures selected from the convolved *Herschel* maps. Class II sources are commonly found in regions below $A_{\rm V-SF}$, with $\sim 30\% - 60\%$ of the population in each field located out of the major high column density regions.

Excluding W3 Main/(OH), the only field with confirmed on-going high-mass star formation (e.g., HCHII regions), the transition to gravitationally bound star-forming structures based on the derived breaks ($A_{\rm SF} \approx 4.5 - 6.5^m \pm 0.5$) is consistent with the estimates derived by Froebrich & Rowles (2010) for clouds such as Orion, Auriga, or Perseus ($A_{\rm V} \approx 6^m \pm 1.5$).

Figure 5.9 shows the temperature PDFs for the entire cloud and for the individual fields. The peak of the PDFs ($T \approx 19.3$, 17.5, 15.8, 16.0 K for W3 Main/(OH), AFGL 333, KR 140, and W3 NW, respectively) are equal to the mean temperature of the material below $A_{\rm V-SF}$ in each field, and are therefore defined in this work as 'environmental temperatures' ($T_{\rm env}$). We observe that more than half of the Class 0/I population not associated with material above $A_{\rm V-SF}$ in the HDL fields are also associated with temperatures above these 'environmental' temperatures, which suggests that stellar feedback is likely a key factor in dispersing the local neighborhood of the YSOs. Indeed, in regions of very high local feedback such as W3 Main/(OH), about $\sim 90\%$ of Class II sources with $A_{\rm V} \leq A_{\rm V-SF}$ also have $T > T_{\rm env}$.

The amount of mass associated with the main structures suitable for star formation is shown in Table 5.2. In this table we exclude those pixels not in common science region, zero-valued, with observed dust temperatures T <40 K, or saturated. Figures 5.10-5.12 show the major regions in each field satisfying both $T \leq T_{\rm env}$ and $A_{\rm V} \geq A_{\rm V-SF}$. Clearly, this selection will depend on the size of the regions chosen for background estimation. However, and as observed in these figures, material above the environmental temperatures with high column densities exist that are currently forming stars. This is particularly prominent in the local neighborhood of high-mass stars, like in KR 140 and W3 Main, which implies that, depending on the radiation field, temperature selection might not always be appropriate when selecting the youngest structures in a particular region.

A second break in the PDF similar to those found for the HDL fields was also observed by (Schneider et al., 2012) for the Rosette field containing the highest column

densities (reaching $A_V \sim 70^m$ in their maps). In this work we find a comparable break for the AFGL 333 field, which reaches extinctions of the order of $A_V \sim 100^m$. The W3 Main/(OH) field reaches extinctions of $A_V \sim 300^m$, with a second break that doubles that of Rosette and AFGL 333. In the following sections we suggest that these high column density breaks are related to stellar feedback/triggering by high-mass stars on already relatively dense structures, and are therefore suitable signposts of 'sub-regions' with the potential for high-mass star formation.

5.4 Discussion: Low and High-Mass Star Formation in W3

The W3 GMC offers a unique opportunity to investigate star formation under different environmental conditions. The presence of material at and above the MSFT and the different characteristics of the HDL and the western fields allow for a direct comparison between high density structures with high stellar feedback, and star formation in more diffuse and quiescent regions (e.g., see Chapter 3). In the following sections, and to complement the analysis of the cluster forming clumps (Chapter 4), we carry out a comparative, independent analysis of the environments in W3 in order to further constrain those characteristics exclusive to the high-mass star formation process.

5.4.1 Identifying Characteristics of the HDL and the Western Fields

Mass and Structural Properties

As expected, the fields in the HDL show the largest percentages of mass above their respective A_{V-SF}: $\sim 35\%$ of the total mass in the W3 Main/(OH) field is selected, $\sim 8.5\%$ with temperatures below our chosen environmental limit. The AFGL 333 field

reaches higher values, with $\sim$ 60% and 35% of its mass, respectively. In total, the HDL comprises up to $\sim$ 75% and 60% of the potential dense/gravitationally bound, and cold/dense/gravitationally bound, star forming material in W3. They contain up to $\sim$ 3 times more mass suitable for star formation than the neighboring western fields.

The W3-NW and KR140 fields comprise the coldest and more diffuse regions with very localized star formation (Chapter 4), and although high-mass stars are present and intermediate mass objects might be forming (Kerton et al., 2008), there is however no reported on-going or recent high-mass star formation.

Assuming that 1/3 of the mass with $A_{\rm V} > A_{\rm V-SF}$ is transformed into stars (Alves et al., 2007), Froebrich & Rowles (2010) estimated a maximum total mass fraction involved in star formation of in any of the clouds in their sample of $\sim$ 10% (Corona Australis). Using the same approach and assumptions as these authors (but at a resolution of $\sim 0.35\,$pc, and selecting the regions associated with star formation based on the *local* properties in each field) our derived $A_{\rm V-SF}$ for the different fields yield a total mass fraction involved in star formation ($\rm Mass_{SF}$; defined as 'MSF' in Froebrich & Rowles, 2010) in the W3 GMC of 11% ($\sim$ 6.5% when taking into account only 'cold' ($T \leq T_{\rm env}$) material; Table 5.2). This is comparable to that of Corona Australis, despite W3 being at least 240 times more massive than this cloud. The mass of the W3 GMC is comparable to that of Cepheus, and yet this cloud only shows a $\rm Mass_{SF}$ of just 0.26% (Froebrich & Rowles, 2010). Compared to Cepheus, W3 therefore appears to have an anomalous proportion of mass involved in star formation relative to the total mass of the cloud.

The western fields show a $Mass_{\rm SF} \sim 6\%$ (with respect to their total mass $M_{tot} \sim 1.1 \times 10^5\,{\rm M}_\odot$), which is comparable to that of Orion A. The HDL by itself would have $\sim$ 15% (cold: 7.5%) of its mass involved in star formation. This suggests that, despite its already significant ongoing star activity, W3 still has a very high potential to form new stars in the next $10^6\,$yrs (Froebrich & Rowles, 2010). A possible explanation is that processes such as stellar feedback by already ongoing stellar activity can alter the

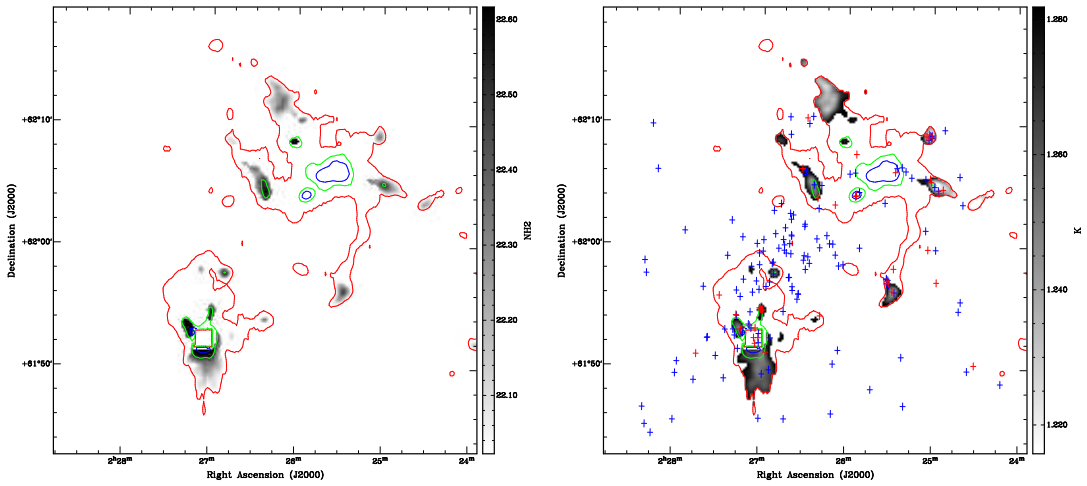

Figure 5.10 Left: Mask showing the column density structures in the W3 Main/(OH) field with the most potential for star formation (log units): $A_{\rm V} > A_{\rm V-SF}$ and $T < T_{\rm env}$. Structures too hot and/or not dense enough are masked (white). Red, green, and blue contours mark the $A_{\rm V-SF}$, $A_{\rm V}$(HTB), and $A_{\rm V}$(HB) limits, respectively (without temperature constraint). Right: Like Fig. 5.10(a), but using the dust temperature map. Red and blue crosses are Class 0/I and Class II candidates (Chapter 3).

local environment, enhancing/creating high column density structures suitable for hosting future star formation. The compressive effects of W4 could then also explain the anomalously high $\rm Mass_{SF}$ of the HDL.

Stellar Properties

Although we lack *Spitzer* coverage for most of W3 North and W3-NW, and suffer from incompleteness in bright, confused areas such as W3 Main, (OH) or AFGL 333 (Chapter 3), we also observe differences in the low mass YSO population.

For all Class 0/I and II candidates from Chapter 3 (Catalog 1; all flags) we measured the $N_{\rm H_2}$ and T of the pixel coincident with the YSO coordinates. These values, which due to the pixel size (0.1 pc) are representative of the (core scale) conditions hosting a given YSO, were observed to vary significantly from region to region, as observed in

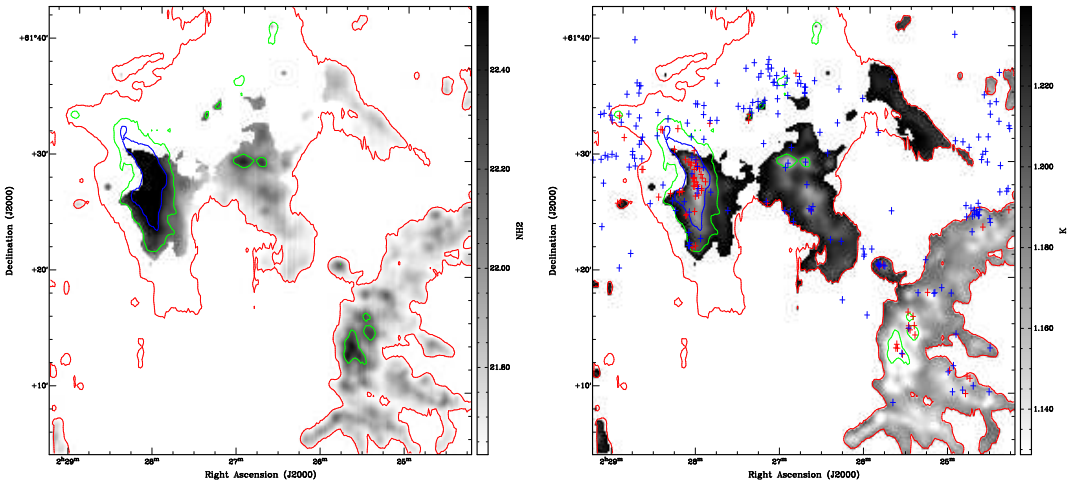

Figure 5.11 Like Fig. 5.10 but for the AFGL 333 field.

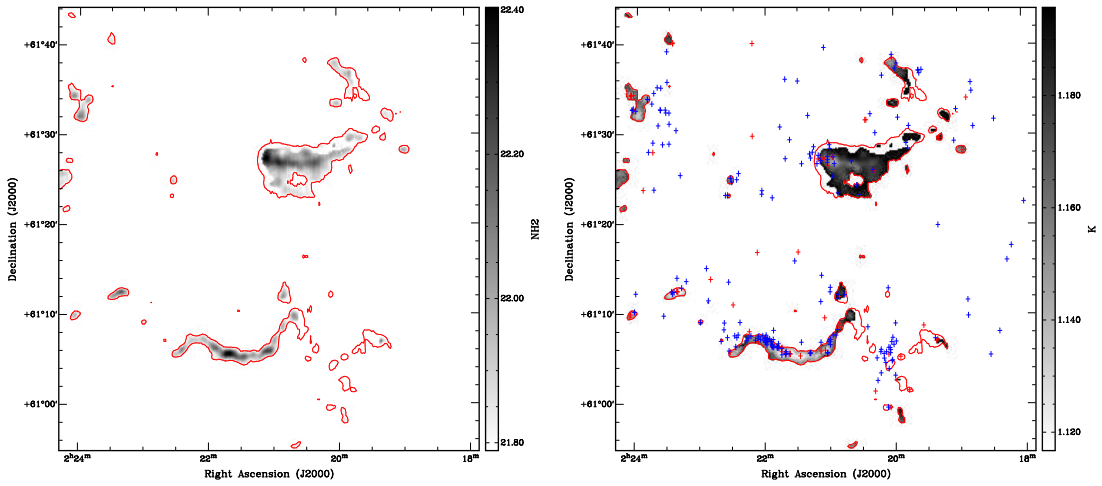

Figure 5.12 Like Fig. 5.10 but for the KR 140 field. Only one break (red contour) is found for this field.

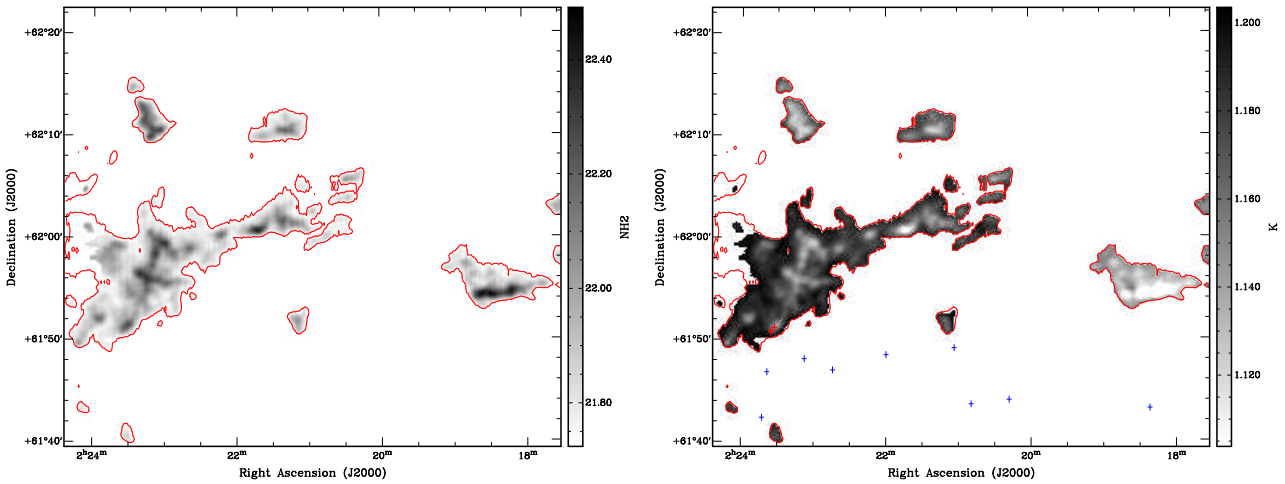

Figure 5.13 Like Fig. 5.12 but for the W3-NW field.

Figure 5.14. Our analysis yields a mean temperature of $\sim 17\,\mathrm{K}$ with a clear separation between the HDL ($T \sim 18.0\,\mathrm{K}$) and the western fields ($T \sim 15.5\,\mathrm{K}$). This YSO sample also yields a mean extinction of $A_\mathrm{V} \sim 15.0^m$, and a minimum value of $A_\mathrm{V} \sim 1.5^m$. This estimate is a strong lower limit, as YSOs might move away from their original birthsites, clear their surrounding environment, or have their local material disrupted by external feedback (e.g., IC 1795).

Separating the YSO sample according to class, the average dust temperatures for Class 0/I and Class II sources in the HDL (W3 Main/(OH) + AFGL 333) are $T_{0/I} \approx 16.5\,\mathrm{K}$ and $T_{II} \sim 18.5\,\mathrm{K}$, respectively. The mean extinction of Class 0/I sources is $A_{0/I} > 3.5 \times A_{II}$ ($A_{0/I} \approx 42^m$).

The equivalent temperature and extinction parameters for the YSOs in the western fields (W3-NW, East-Loop, and KR 140) are $T_{0/I} \sim 15\,\mathrm{K}$, $T_{II} \sim 15.5\,\mathrm{K}$, and $A_{0/I} \approx 1.5 \times A_{II}$ ($A_{0/I} \approx 11^m$). The mean extinction of Class 0/I and Class II candidates in the HDL is therefore found to be $A_{0/I-HDL} > 3.8 \times A_{0/I-West}$ and $A_{II-HDL} \approx 1.8 \times A_{II-West}$, respectively. YSOs in the HDL therefore form in a more dense and warmer environment. Assuming a total lifetime for the Class 0/I (+flat SED) and Class 0/I + Class II phases of ~ 0.9 and $\sim 2.9\,\mathrm{Myr}$ (Evans et al., 2009), then for coeval evolution

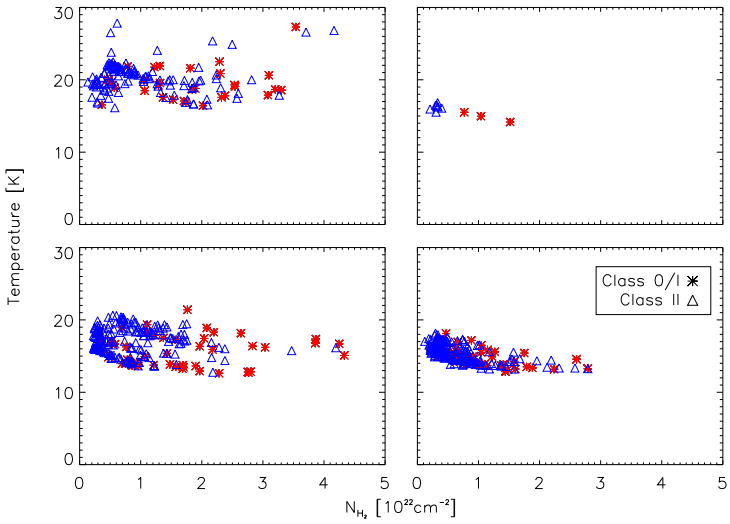

Figure 5.14 Column density/temperature diagrams for the Class 0/I and Class II YSOs in each W3 field (Chapter 3; Catalog 1, all flags).

(same age) Class II YSOs in the HDL could leave or have their environment disrupted (e.g., higher external activity) up to ~ 7 times faster than in the western fields, whose Class 0/I and Class II candidates co-exist in similar/nearby (cool) environments and comparable column densities. In a more conservative scenario in which Class II sources in the HDL are the oldest (2.9 Myr old) Class II population in W3 (while those in the western fields have just been formed; i.e., 0.9 Myr old), then Class II sources in the HDL still dissociate from their primordial material ~ 2 times faster than those in the western fields. These characteristics suggest an evolutionary distinction when describing the eastern and western fields in W3.

5.4.2 THE HDL: Star Formation and Evolution in Dense Fields

Stellar Feedback by High-Mass Stars and Influence on the Star-forming Structures: The First Break in the PDF/Mass Distribution

Despite the similar mass distributions of the two HDL fields (extending to column densities of the order of $N_{\rm H_2} \sim 10^{23}\,{\rm cm}^{-2}$), their PDFs are more sensitive than the cumulative version when investigating local changes at particular extinctions. In this case, these indicate that the AFGL 333 field has a higher percentage of mass than W3 Main/(OH) at $A_{\rm V} < 5^m$ and $A_{\rm V} \sim 40 - 100^m$, while the latter dominates mainly at intermediate and high extinction ranges: $A_{\rm V} \sim 5 - 40^m$ and $A_{\rm V} > 100^m$. The dominance of AFGL 333 at the lowest extinction ($A_{\rm V} < A_{\rm V-SF}$) can be explained by the multiple 'swept-up' and diffuse regions, like those neighboring W4. Figures 5.15-5.17 show some of these regions, characterized by low CO emission and 'cavity-like' morphologies in the CGPS CO map. This map was used in Chapter 4 to correct the *Herschel* images for foreground/background contamination, and was observed to follow the column density regions closely. The coincidence of low column density/low CO surrounded by high column density structures, many of these with pillars, suggest these could indeed have been produced by local (in-cloud) stellar activity, as suggested by the YSO distribution (with Class IIs displaced towards the inside of some of these 'cavities', as observed in the region defined in this work as CO-NE; Fig. 5.16).

The W3 Main/(OH) field has a higher surface density, and a $A_{\rm V-SF}$ (first break) twice that of the AFGL 333 field. This higher break selects the shell-like structures around IC 1795, which in Chapter 3 we argued showed indications of having stellar populations triggered by the central activity of the central cluster. This suggests that this break might be directly associated with the feedback effects produced by the central cluster and the (parsec-scale) feedback of its local high-mass star population. As the $A_{\rm V-SF}$ can be interpreted as the limit at which gravity (and star formation) start to dominate the large scale

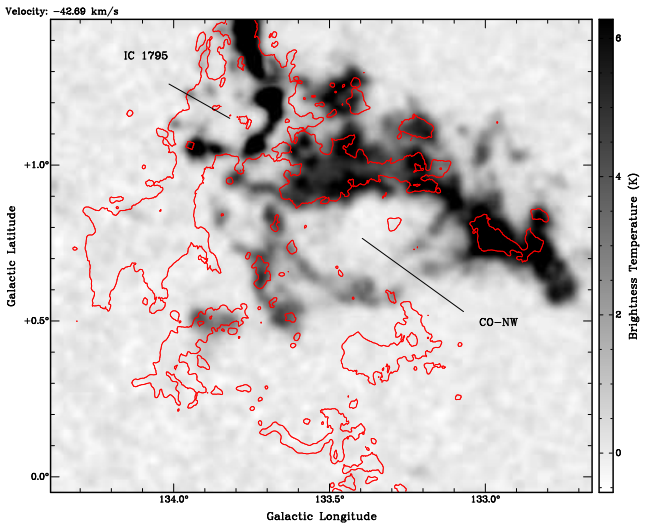

Figure 5.15 Molecular structures in the W3 region observed in the CGPS data at v≈ $-42.7\,\mathrm{km\,s^{-1}}$. Contour is for $A_\mathrm{V} = 5^m$.

properties of the cloud, this shows how stellar feedback/turbulence can shift this limit (in this case, to higher values) according to the magnitude of the feedback/compression effect.

The effectiveness of high-mass stars at creating high column density structures and possibly even the progenitors of new high-mass stars and clusters (as described below) could then explain why fields classified as 'massive star forming' regions have a higher $A_{\mathrm{V-SF}}$ than 'low-mass' star forming regions (e.g., Schneider et al., 2012). Stellar feedback would sweep and compress the material, altering the distribution of mass (and the corresponding $A_{\mathrm{V-SF}}$), ultimately producing the structures suitable for hosting the (currently) detectable new high-mass star formation. Stellar feedback as the driver distinguishing the structures in the HDL from those in the western fields is also supported by molecular observations (Polychroni et al., 2012). This process is also believed to be responsible for the creation of the 'isolated' high-mass star population in the HDL, such as that in the neighborhood of the AFGL 333 Ridge, the stars powering the diffuse H II regions in the western (inner) boundary of the shell around IC 1795, possibly even VES 735 in KR 140 (see below).

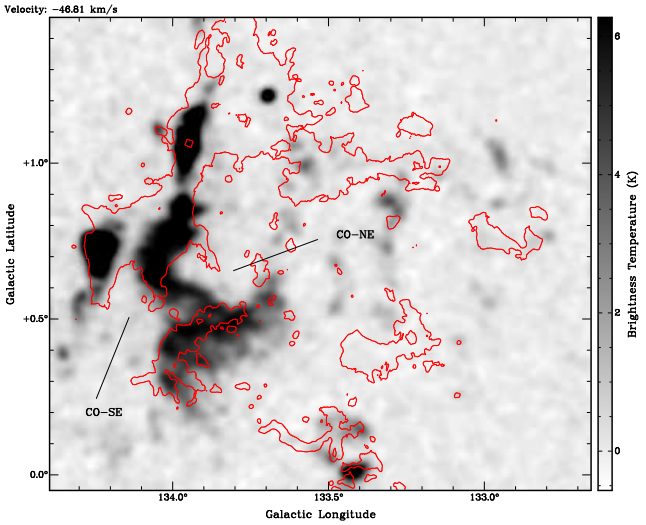

Figure 5.16 Like Fig. 5.15 but for v$\approx -46.8\,\mathrm{km\,s^{-1}}$.

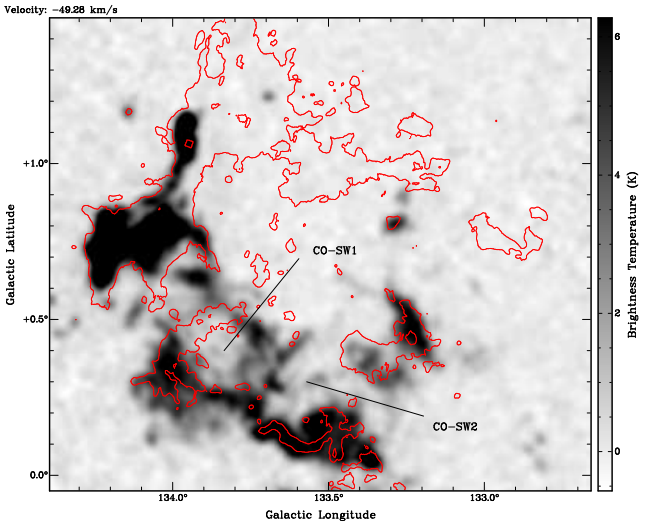

Figure 5.17 Like Fig. 5.15 but for v$\approx -49.3\,\mathrm{km\,s^{-1}}$.

An enhanced local star formation/feedback activity in the W3 Main/(OH) field is evident in the temperature maps. While both fields in the HDL are being influenced by the activity in W4, the mean dust temperature ($T_{\rm env}$) for the regions in AFGL 333 is lower than that of the W3 Main/(OH) field, despite the former being closer to the high-mass star activity in W4. This is still the case even when excluding the portion of the AFGL 333 field containing the Eastern Loop (RA$<2^{\rm h}\,27^{\rm m}$), which then yields an environmental ($A_{\rm V} < A_{\rm V-SF}$) temperature of $T_{\rm env} \sim 18.2 \pm 0.7\,{\rm K}$ for the eastern side of the AFGL 333 field (bordering W4). More than 90% of the AFGL 333 field is below the mean temperature of the W3 Main/(OH)) field of $T_{\rm env} \approx 19.3\,{\rm K}$. The W3 Main/(OH) field, however, contains much more active regions of star formation than the AFGL 333 field. This emphasizes the need, at least at the present spatial resolution, to tailor the identification of sites of future and recent star formation according to the local radiation field and external stellar activity , as these will dominate the local properties of the clumps in the region. The only structures with temperatures comparable to the environmental value of W3 Main/(OH) are the regions north and east of the AFGL 333 Ridge, with temperature peaks coincident with the pillar east of the AFGL 333 Ridge (YSO 'Group 7'; Chapter 3) and IRAS 02245+6115, an H II region associated with a cluster (Bica et al., 2003) powered by a B-type star (Hughes & Viner, 1982; Straižys & Kazlauskas, 2010). This implies that, excluding the isolated high-mass star formation in this region producing the temperature peak in the temperature histogram (Chapter 4), heating in the AFGL 333 field appears to be dominated by the influence of W4 (resulting in overall lower temperatures than an environment heated by more local high-mass stars). The Eastern Loop on the other hand shows $T_{\rm env} \sim 16.4\,{\rm K}$, and therefore consistent with the environmental temperatures derived previously for the western fields.

Stellar Feedback by High-Mass Stars and Star Formation

The effects of W4 on the AFGL 333 field are also observed in its YSO population. The main YSO groups (Chapter 3) are located at the boundary with W4 and the warmer regions. These range from Class II-dominated groups at $A_{\rm V} < A_{\rm V-SF}$ (no longer associated with the main column density structures, e.g., Group 3; Chapter 3) to the eastern boundaries of the 'cold' star forming sites (Fig; 5.11) and comprising filaments or remnants of filaments (e.g., Groups 6 and 4, respectively). Here YSOs are systematically displaced toward W4, leaving the cooler western side (at comparable column densities) with few YSO detections.

Indeed, excluding the material with $A_{\rm V} > 50^m$ (with different properties and origin, described below) we find that $\sim$ 70% of the current YSO population in HDL-part of the AFGL 333 field might have had a triggered origin by W4. For this calculation, we considered as part of the 'HDL' those regions warmer than the mean environmental temperature of the western fields ($T_{\rm env} \sim 16\,{\rm K}$ for $A_{\rm V} < A_{\rm V-SF}$). 'Triggered' regimes (under the influence of stellar feedback) are those with $T > 17.5\,{\rm K}$, the $T_{\rm env}$ of the AFGL 333 field and a temperature that selects the entire eastern boundary of the HDL with W4, as well as those YSOs at the boundary of W4 (and with a displacement suggestive of triggering) but still embedded in their parent structure (and therefore in a slightly colder medium than the mean environmental temperature). 'Shielded' (or quiescent) regions in the HDL were chosen to have a temperature range of $16 < T_{\rm d} < 17.5\,{\rm K}$.

Assuming that all Class II YSOs (with $A_{\rm V} > A_{\rm V-SF}$) have similar lifetimes, then the the star formation rate (SFR) in triggered regions could be at least $\sim$ 2 times higher than in quiescent regions not affected by stellar feedback. Taking into account those Class II sources already dissociated from the high density material, then this rate could be up to $\sim$ 3 times the 'quiescent' SFR, with triggering being at least $\sim 1.5-2$ times more efficient per unit solar mass (assuming solar mass YSOs and ignoring the change in mass of the material with $A_{\rm V} > A_{\rm V-SF}$ during the formation of the Class II candidates).

Based on the YSO classification, lifetimes, and structure in the IRAC images (Chapter 3), filament dispersal after YSO formation could also be as fast as ∼1-2 Myr in these triggered environments.

Overall, our results suggest that while W4 might be interacting with both fields, *at the present time the local stellar radiation field and parsec-scale feedback are the dominant mechanisms driving (and distinguishing) the evolution in each of the HDL fields.* The AFGL 333 field, which lacks significant local high-mass star activity, therefore differs from W3 Main/(OH). A *particularly enhanced local, parsec-scale stellar feedback* in the latter would then explain the more extreme environmental conditions (e.g., higher temperature), the higher (and on-going) stellar activity (Chapter 3), and the higher $A_{\rm V-SF}$.

If stellar feedback is indeed affecting the observed breaks, a higher $A_{\rm V-SF}$ or the presence of a second break could be interpreted as evidence for a cloud in a relatively evolved state of evolution. This would agree with both of these fields also having relatively enhanced power law tails in the PDF, characteristic of more evolved clouds (Ballesteros-Paredes et al., 2011). However, while these simulations do not include stellar feedback, this also implies that the shape of the PDF would also be greatly dependent on the magnitude and conditions of the stellar activity, and this will therefore be required in order to explain the observed PDF characteristics at later stages.

The Second Break in the Mass Distributions and Origin of High Column Density Structures

A second break in the mass distributions ($A_{\rm V}$(HB)) is a property unique to the HDL fields, with the break in the W3 Main/(OH) field being twice that of the AFGL 333 field. Column densities above the $A_{\rm V}$(HB) breaks are exclusively associated with the AFGL 333 Ridge and the two massive star forming regions: W3 (OH) and W3 Main. AFGL 333 and W3 Main/(OH) contain $\sim 4 \times 10^3\,{\rm M}_\odot$ and $\sim 4.5 \times 10^3\,{\rm M}_\odot$ above $A_{\rm V} \sim 50^m$, respectively, a lower limit in the case of the latter due to the lack of data in the saturated

area of W3 (OH). We note, however, that this mass might only translate to actual high-mass star formation under specific requirements. As mentioned in Chapter 4, all clumps above the MSFT and currently forming high-mass stars appear to have been formed by a 'convergent' effect by high-mass stars.

In Chapter 4 we described a possible scenario of high-mass star formation, based on the properties of W3 East and W3 West, by simultaneous stellar feedback by multiple high-mass stars. Here we confirm, using an independent approach, that structures above $A_{\rm V}$(HB) are indeed associated mainly with such high-mass star activity at less than d~ 1 pc. This suggests that, at least in W3, *the highest column densities are formed by the influence of local high-mass stars acting at sub-parsec scales in already compressed environments*. W3 East and W3 West represent the most extreme case, with multiple OB stars acting at sub-parsec scales.

A major difference between the massive star-forming W3 Main and the AFGL 333 Ridge for the material above $A_{\rm V} \sim 50^m$ is that the former has more of this mass more concentrated at the highest column densities ($A_{\rm V} > 100^m$), while AFGL 333 has more of its mass below this value (with maximum extinction reaching $A_{\rm V} \approx 120^m$). Additional small-scale compression in an already enhanced column density environment (in addition to the additional gravitational inflow of material from the local neighborhood this amount of mass might induce) could then lead to the formation of the most massive precursors suitable for clusters of high-mass stars, like the W3 Main clumps (Chapter 4).

The mass distribution and the lack of high-mass stars in the AFGL 333 Ridge, despite the presence of low/intermediate mass (Class 0/I) YSO activity, might be due to a less evolved (or prior) state of high-mass star formation than W3 Main (e.g., Sakai et al., 2007; Polychroni et al., 2012). However, it is also possible that the lower number of high-mass stars able to influence the region and their farther distance might have led to a smaller degree of compression than the W3 Main region.

Convergent feedback by high-mass stars might also be capable of producing an equally

massive clump even at larger (parsec) scales, like W3 (OH), produced by W4 and IC 1795 (Chapter 4). However this larger scale converging process might not be as efficient in producing massive clumps. This part of the shell around IC 1795 has the massive clump associated with W3 (OH) and a couple of small clusters. W3 Main shows two clumps above the MSFT surrounded by a richer cluster of low mass stars (Feigelson & Townsley, 2008). Similarly, a clump not benefiting from sub-parsec effects might not be as efficient in producing high-mass stars, consistent with what is observed in W3 (OH). Different scenarios might arise depending on whether the large scale triggering acts on one side, enhancing the column density of a structure wider than the fragmentation scale and therefore suitable for continuing star formation via the sub-parsec triggering process, or whether the high column density structure is formed and compressed directly by the convergent process (possibly leading to more filamentary-like structures and/or direct fragmentation and collapse).

The above results are in agreement with the conclusions from Chapter 3, which suggested that feedback is the main assembly mechanism producing structures dense enough to host the current (and future) major cluster and high-mass star formation activity in W3. This also suggests that a second break could act as an *efficient signpost for structures with enough mass at high extinctions suitable for potential high-mass star formation.*

5.4.3 The Western Fields: Star Formation in Typical Less Dense Fields

.

Despite the different percentage of their mass associated with star formation ($A_{\rm V} > A_{\rm V-SF}$): $\sim 30\%$ and $\sim 10\%$ for W3-NW and KR 140, respectively, these fields show similar maximum extinction of $A_{\rm V} \sim 30^{m}$, as well as similar (field) environmental conditions ($T_{\rm env} \sim 16\,{\rm K}$ for $A_{\rm V} < A_{\rm V-SF}$), differing from those of the HDL.

Although with similar $A_{\rm V-SF}$, the KR 140 field has a slightly lower surface density,

$\sim 70\,M_\odot/pc^2$ compared to $\sim 80\,M_\odot pc^{-2}$ for W3-NW, and a greater fraction of mass associated with lower column density environmental values. The 'star-forming' material (above the break) is exclusively related to filamentary and shell-like structures: West-Loop, the Trilobite, and the shell of the KR 140 H II (Fig. 5.12). *All* of these structures have morphologies consistent with some kind of local triggering: boundary of the SW Cavity, morphology consistent with Radiative-Driven Implosion (RDI) (Chapter 3), and the shell around the O-type VES 735, respectively. The YSO population is localized mainly to these structures, and like in the region of the HDL bordering W4, a large fraction is systematically displaced towards 'triggers', located at the inner boundaries of the 'cavities', shells, and ahead of the shocked regions (Fig. 5.12). The presence of stellar feedback can also be observed in the column density/temperature profiles of some of the structures. An example of this is the Trilobite. Figure 5.18 shows the north-source and east-west profiles of the main source in this structure detected by *getsources* when used on the *Herschel* maps, all convolved to the common resolution of the 500 μm band. We observe a more pronounced column density gradient towards the east and north-east directions, coincident with the direction toward which the YSOs are displaced, as well as an asymmetric temperature profile, with an increase in temperature toward the 'compressed' sides.

The W3-NW field contains up to twice the mass in the KR 140 field for $A_V > 10^m$, which combined with the possible identification of a cluster towards the central-southern parts of the western fields (M. Rahman, priv. comm.) might suggest that the initial SFE in the KR 140 field (and subsequent feedback) was more significant than in the W3-NW field (overall more dense and less 'shaped' by feedback processes). A higher degree of stellar activity is also supported by temperature distribution. The W3-NW field has, for instance, ~ 7.5 and $\sim 25\%$ of its mass at $T < 14$ and 15 K, respectively. The KR 140 field has ~ 7 and $\sim 1.5\%$ of its mass at those temperatures. At each extinction range the latter always shows a much smaller proportion of 'cold' material relative to

the mass contained in that extinction range compared to the W3-NW field, despite both having similar environmental values. Indeed, the KR 140 field has not only embedded clusters (e.g., Carpenter et al., 2000), but also various (late) B stars (e.g., Voroshilov et al., 1985). A period of enhanced activity (and feedback) in the KR 140 field could also explain the presence of the only (confirmed) O-star (VES 735) outside the HDL (according to SIMBAD).

The W3-NW field also has largely localized YSO formation (e.g., Figs. 5.13; 5.15), one region clearly noticeable as a bright 'Y-shaped' region in the *Herschel* PACS images (e.g., Chapter 4; RA/Dec: $\sim 2^{\rm h}\,22^{\rm m}\,36^{\rm s}$ $+61^{\circ}\,49'$).

The main difference between the two western fields and these and the HDL might therefore be the *magnitude* of the feedback, which is likely ultimately related to the primordial amount of mass and mean density in these fields. A more moderate initial burst of local star formation and feedback in the western fields (e.g., due to lower initial column densities) could explain the relatively homogeneous environmental dust temperature in the neighborhood of the filamentary-like regions and 'cavities' despite the systematic YSO displacement, the largely evolved (Class II dominated) population of these structures, the evolved high-mass star activity (KR 140 H II region), and the lack of an obvious second break in the mass distributions (requiring significant mass as well as compression).

5.5 The *Herschel* View of the Star Formation History and Evolution of the W3 GMC

In Chapter 3 we presented results regarding the evolution of W3 based on our *Spitzer* data, in particular: 1) not all the stellar content in W3 Main started triggered by IC 1795 (in agreement with previous studies), and 2) the star formation in the western fields is suggestive of a more isolated evolution with sporadic and localized bursts of star formation, probably more typical of the evolution of a cloud with mean 'star-forming'

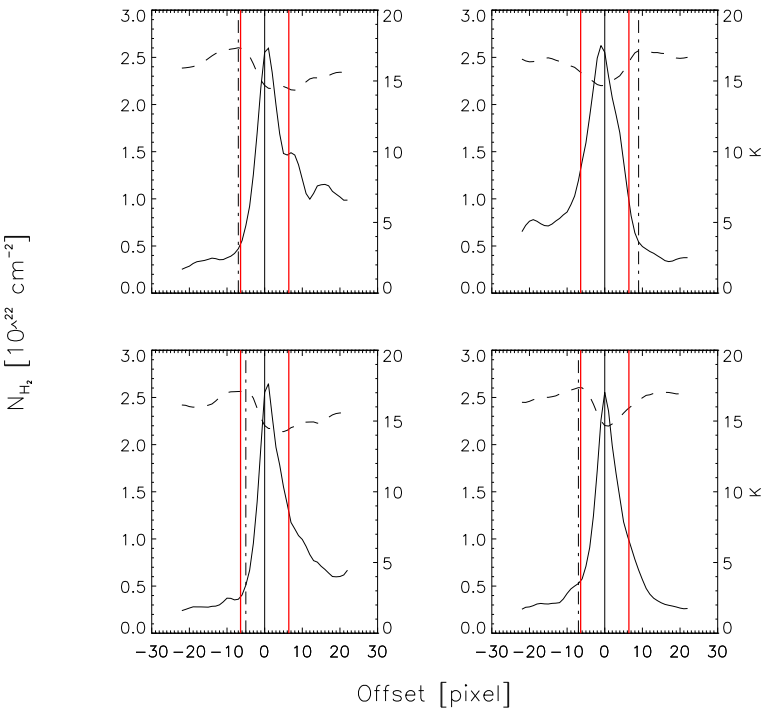

Figure 5.18 Temperature (dashed line; right scale) and column density (solid line; left scale) profile of the column density peak of the Trilobite in the East-West direction (top-left); South-North (top-right); NE-SW (bottom-left); SE-NW (bottom-right). Black vertical lines mark the coordinate from the *getsources* catalog (solid line) and temperature peak (dashed line). Red vertical lines mark the (mean) elliptical footprint in the 500 μm band as measured by *getsources* from the convolved *Herschel* maps. Profiles extend ~ 2 pc in each direction (~ 22 pixels) centered on position RA/Dec: $\sim 2^{\rm h}\,21^{\rm m}\,6.4^{\rm s}$ $+61^\circ\,27'\,38.7''$.

($A_{\rm V} > A_{\rm V-SF}$) column densities.

The age of VES 735 (exciting star of KR 140) has been estimated to be $\sim 2\,$Myr (Kerton et al., 1999). Evolved high-mass stars in W3 Main show a comparable age of $\sim 2-3$ (Bik et al., 2012). Assuming a timescale of 1 Myr between the formation of the first high-mass star in W3 Main and VES 735 then this implies that for a distance of $\sim 40\,$pc the triggering effects should have traveled at the unphysical speed of $\sim 40\,{\rm km\,s^{-1}}$. This implies *that star formation in the western fields, especially in the KR 140 field, must have been initiated at the same time as (if not before) than the HDL.* The eastern and western sides of the cloud, however, would share a common history of inter-arm material flowing into the spiral arm potential, which could then explain the similar ages on opposite sides of the cloud.

The initial level of star forming activity, which depends on the amount and column density of primordial material in a particular region, will influence the subsequent history of a GMC. Based on their similarities, both western fields likely started with a column density environment more typical of a GMC, unlike AFGL 333 and W3 Main/(OH), which benefited from the creation of the 'anomalous' HDL. This characterized the initial burst of star formation and in turn formed the structures currently forming stars. *The relatively low average column density of the primordial material limited the efficiency of the initial star formation in the western fields of the GMC. This, and the consequent lower magnitude of triggering events, sealed the fate of these regions and governed their evolution*, as follows. A lower initial SFE results in a lower efficiency for inducing star formation in secondary star forming events, and a lower probability and capability of compressing the already relatively low column density surrounding medium to produce column densities high enough for high-mass star formation. This might however still result in few, relatively isolated, high-mass stars (e.g., KR 140). The limited secondary star formation and 'low' environmental column densities never give rise to strong, local, small-scale type triggering required for the creation of the most massive systems observed

in the W3 Main/(OH) field (Trapezium-like systems).

The self-enhanced process in regions of star formation with greatly enhanced column densities, like the HDL, is different. In this case, an initially high SFE would result in more intense compression and triggering events. When acting in an already dense environment this would induce a more massive and richer stellar population in a relatively faster and more efficient way than in quiescent regions. The evidence presented in this work, together with the results of Carpenter et al. (2000), who found that embedded clusters in the W3 region are preferentially located in triggered regions, support the 'fireworks hypothesis' presented in Koenig et al. (2012).

The activity of W4 likely produced the embedded cluster and high-mass star activity in the eastern boundary of AFGL 333, that subsequently induced the formation of the AFGL 333 Ridge. Star formation in W3 Main started and progressed independently (Feigelson & Townsley, 2008; Chapter 3). This star formation was subsequently enhanced by the on-going low-mass activity and the local large-scale triggering effect from IC 1795 (age $\sim 3 - 5$ Myr; Oey et al., 2005; Roccatagliata et al., 2011), which also created the first generation of high-mass stars in the shell around this cluster. These, combined with the large clusters of low mass stars throughout this region, compressed the high column density material and formed new high-mass stars within the W3 Main region. This ultimately lead to the sub-parsec 'convergent constructive feedback' process described in Chapter 4, which produced the two massive clumps now forming the young Trapezium-like systems.

5.6 Conclusion

The W3 GMC offers a unique opportunity to investigate the formation process of low and high-mass stars in a variety of environments, from the HDL to the more diffuse western fields. In this work we have aimed to create a coherent picture of the evolution of this

GMC in order to constrain the processes that have led to the formation of the observed high-mass star population and the environments hosting the highest column density structures and clumps. This has been carried out by means of a comparative analysis of the fields in W3, relating the current star formation activity with the observed structures and the large scale properties derived from the *Herschel* column density and temperature maps.

The W3 Main/(OH) and AFGL 333 fields show a second break in the mass distributions, which we suggest is caused by small-scale 'triggering'/stellar feedback by high-mass stars in a massive and previously compressed environment. Being this process a possible mechanism to form clusters of high-mass stars (as described in Chapter 4), this break could therefore act as an effective means of locating possible high-mass star forming sites.

We suggest that differences in the primordial *local* conditions are ultimately responsible for the observed differences in the magnitude and scale of the initial stellar feedback, which subsequently determines the evolution, structural properties, and star formation history of each field. The W3 Main/(OH) field shows signatures of particularly enhanced local large scale triggering, which is likely why this is the only field with significant high-mass star formation. The western fields on the other hand show only moderate stellar feedback, which would be more typical of the standard evolution of a cloud that has not benefited by the conditions provided by W4 and the HDL.

A high initial surface density, mass, and column density could therefore allow for a higher initial SFE. The combination of high SFE in an already high density region, combined with the speed and efficiency of triggering as a star formation process, results in a self-enhancing process in which subsequent triggering events generate a richer population, a 'fireworks hypothesis' as suggested by Koenig et al. (2012), as well as more massive stars. This will ultimately lead to the formation of the most massive systems – clusters of high-mass stars and Trapezium-like systems –through processes like the 'convergent constructive feedback' mechanism (Chapter 4).

Chapter 6

The W3 GMC: Compact Source Population

6.1 Introduction

The production and analysis of a reliable catalog of compact sources in W3 is a key objective of the HOBYS Collaboration, and therefore essential for the creation of the *Herschel* Legacy in star formation. In addition to the *getsources* code used in this project, the reliability and accuracy of this and similar codes (e.g., CuTex; Molinari et al., 2011) are still being tested in preparation for the creation of a consistent set of catalogs for all HOBYS fields. While this implies that no completely definite study of compact sources can be produced for W3 until approval of the best (common) approach, in this chapter we present a general, preliminary view of the sample, suitable for comparison with the characteristics of the two, high-mass star forming clumps in W3 Main presented in Chapter 4.

6.2 The Catalog: Extraction and Selection

Following the technique used in Chapter 4, we used the multi-scale, multi-wavelength source extraction software *getsources* on the ISM-corrected, convolved *Herschel* maps to produce a preliminary bandmerged list of sources (with coordinates, flux, size, and reliability measurements).

While the *getsources* code and the map-making process are currently being refined, the choice of common resolution maps not only allows for a direct comparison with the structures in the column density and temperature maps, but also significantly reduces what we define here as 'false multiplicity' effects. SPIRE detections are frequently divided into various smaller components, which is expected (and required) when attempting to distribute the observed flux at longer wavelengths among all the detections from the high-resolution PACS maps, found within a given SPIRE aperture. This process is, however, not straightforward when working on a highly complex background and/or regions of high, diffuse emission, like those found in the HDL (e.g., W3 Main). This demands a careful and detailed analysis, currently being carried out by the *Herschel* Collaboration, as well as individual, one-by-one source inspection, in order to fully quantify the effects produced by false multiplicity on the final measurements and the completeness of the catalog.

Despite the loss of resolution, the convolved catalog used in the present work removes the multiplicity problem almost entirely. Furthermore, the use of a common resolution implies that no flux scaling of the SPIRE fluxes is required prior to SED fitting (as described in Chapter 4). As this is one of the most uncertain aspect of the *Herschel* analysis, our approach therefore effectively eliminates a major source of uncertainty in our final measurements. The present catalog and analysis, in addition to providing an overview of the general (clump) characteristics, will serve as a reference when investigating all these issues when preparing the W3 field for the official final release as part of the HOBYS *Herschel* Legacy Database.

A source in the common science region was classified as 'reliable' if the S/N as measured by *getsources* (Flux Peak/Error) is > 7 in at least two bands at $\lambda > 160\,\mu$m. These bands should not have been flagged by *getsources* as: i) substantially larger than the source characteristic size (i.e., AFWHM$> 2^{1/2}\times$scale, where 'scale' is the spatial scale used by *getsources* during image decomposition, and AFWHM is the major axis FWHM estimate). ii) Larger than the desired maximum size at that band (i.e., AFWHM$> 2^{1/2}\times$SRCMAXSIZE, where SRCMAXSIZE=129″, 158″, 170″, 170″, 170″ for 70 μm, 160 μm, 250 μm, 350 μm and 500 μm, respectively). iii) Low monochromatic significance (i.e., SIG-MONO< 3.5).

The chosen selection requirements yield a reliable sample of 26 detections (at the resolution of the SPIRE 500 μm band) out of the 314 originally extracted. While the S/N selection criteria was chosen to match that used in previous HOBYS studies (e.g., Nguyen Luong et al., 2011a), it clearly results in a very conservative sample when applied to the convolved maps. A more complete source list will be created with the criteria and techniques imposed by the *Herschel* HOBYS Collaboration, currently in preparation, for the creation of catalogs at PACS spatial resolution.

When used on the column density maps, *getsources* yields 64 detections with a S/N> 7 (145 with a S/N> 3) suitable for refining the 5-band convolved catalog when searching for the most reliable and prominent detections. Each source was also checked visually to ensure that no artifacts were included in the sample.

6.3 Source Characterization

6.3.1 Spectral Energy Distributions

Using the codes from Chapter 2 and the dust parameters used in Chapter 4 for the two major clumps in W3 Main, we obtained masses, luminosities, and temperature estimates for each source by fitting a modified blackbody to the SED, excluding from the fit those

bands with a S/N (integrated flux/error) < 3. The PACS 70 μm datum was included only for internally heated sources (see below). For W3 West and W3 East we used the parameters derived in Chapter 4 using the *getsources* fluxes and excluding the saturated bands, although the results presented in this work do not change when using the PACS 70 μm data due to saturation being more limited at this wavelength than at 250 μm. The SEDs of W3 East and W3 West (including PACS data) are shown here (Figs. 6.1 and 6.2) as examples.

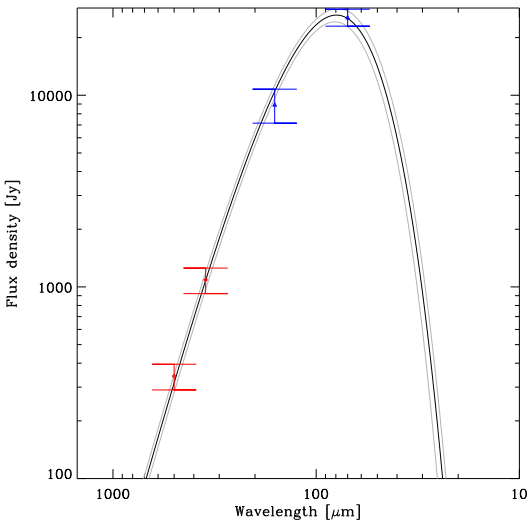

Figure 6.1 Spectral Energy Distribution of W3 East (containing IRS5), located in the W3 Main region. Upper and lower curves are the 1-sigma envelope of the dust emission model (Chapin et al., 2008). The image is saturated at 250 μm.

Figure 6.3 compares the masses derived from the column density maps, obtained using the elliptical apertures derived by *getsources* at 500 μm, with the masses derived from the SED fits. Differences are expected based on various factors such as the use of different (albeit similar) sizes at each band by *getsources*, the different photometry methods, and the assumption of a single temperature for the entire aperture in the SED fitting. Despite these issues, we find that the masses of $\sim 90\%$ and $\sim 95\%$ of the sample agree within a factor 2 and 3, respectively. We note, however, that although SED fitting

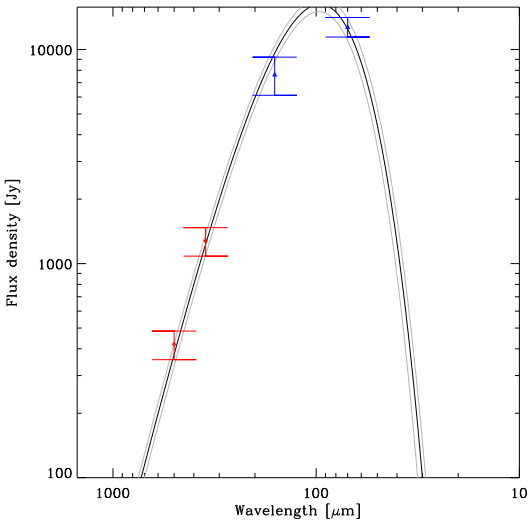

Figure 6.2 Same as Fig. 6.1 but for W3 West (containing IRS4).

(source and per pixel) assuming constant temperature throughout the integrated area is common for this kind of analysis, this is an unphysical approximation and temperature gradients will always be expected around any embedded source.

6.3.2 Properties of Compact Sources from SED fitting, *Spitzer*, and *Herschel* T/N_{H_2} Maps

In addition to the basic parameters derived from the SEDs, we used these measurements, in combination with the YSO sample from the *Spitzer* analysis (Chapter 3) and the temperature and N_{H_2} maps, to further characterize the intrinsic properties of the reliable sample.

Each detection was first characterized according to its properties in the column density and temperature maps: observed and background-corrected peak extinction, observed external background temperature (outside the mean FWHM of the source), and external background column density as determined by *getsources* during the extraction process on the column density maps.

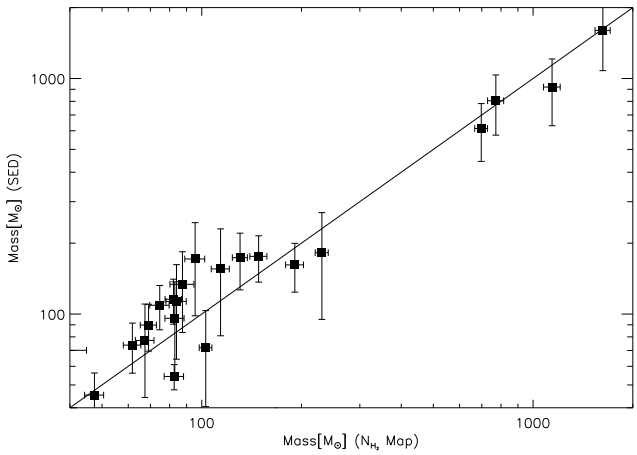

Figure 6.3 Comparison of mass estimates derived from the column density map with those obtained from SED fitting for the sources in the reliable catalog.

A source was classified as externally heated (or at environmental temperature) if the mean temperature within the FWHM in the temperature map is lower than the mean temperature in the region outside the FWHM (FWHM<R< 2×FWHM). This classification was checked and verified by direct inspection of the temperature and column density profiles.

We have also used the available data to carry out a preliminary classification based on evolutionary state. This is essential in order to identify properties and constrain intrinsic differences that might be key to the formation of stellar precursors leading to the onset of high-mass star formation.

A source was classified as 'starless' if it lacked a 70 μm detection above 3σ level (e.g., André et al., 2010; Könyves et al., 2010). We note that the lack of 24 μm data can lead to some classification errors, which have been estimated to be $\sim$ 3% (Könyves et al., 2010). While this 'starless' classification is a good approximation when assessing the presence of high-mass protostars, we note however that such clumps might still contain some low-mass YSOs in the *Spitzer* datasets that do not contribute significantly at PACS wavelengths. Although the IRAC coverage of W3 is incomplete and our study in Chapter

3 suffers from severe confusion in the brightest regions of W3 Main, W3 (OH), and AFGL 333, whenever possible we also estimated the number and type of YSOs within the FWHM of each reliable detection.

A 'pre-stellar' source is defined as one that is 'starless' as well as gravitationally bound (Andre et al., 2000). Due to the lack of molecular data we used the classical Jeans instability (Jeans, 1902) to determine whether the *Herschel* detection is gravitationally unstable. According to this criterion, an object with gas temperature (T) and mass (M) will be unstable against collapse if $M/M_J > 1$. Here M_J is the Jeans mass (e.g., McKee & Ostriker, 2007), given as:

$$M_J = \frac{(\pi\sigma)^2}{3G} R_J, \tag{6.1}$$

where R_J is the Jeans radius. The speed of sound σ is given as $\sigma = (kT/2.3m_p)^{1/2}$, where k is the Boltzmann's constant and m_p is the proton mass. For the purpose of this analysis, we used the SED temperature, SED mass, and mean (observed) FWHM.

For better comparison with previous studies we also classified the sample according to the scheme presented in Motte et al. (2007) for the Cygnus-X region: i) 'High Luminosity Infrared Sources' (HLIR) were classified as those having $L_{bol} > 10^3\,L_\odot$ (B3 star in the main-sequence). Using the results from Mottram et al. (2011) we estimate an equivalent MSX flux to that luminosity at $21\,\mu$m of 7.4 ± 0.5 Jy at the distance of W3. Those sources with M$> 40\,M_\odot$ were defined as 'massive' (MHLIR). ii) 'Massive Infrared-Quiet Protostellar Cores' (MIRQ) were assumed to have $MSX_{21} < 7.4 \pm 0.5$ Jy and M$> 40\,M_\odot$. We again note that this term was used in Cygnus-X to define objects with characteristic size of ~ 0.1 pc (maximum size of ~ 0.3 pc). At the resolution of SPIRE $500\,\mu$m (~ 0.35 pc) sources in our catalog would therefore be better described as 'clumps'. We did not impose further constraints for MIRQ candidates in terms of the presence of other signatures of stellar activity (e.g., masers), as this allows for the comparison of various degrees of stellar activity, together with luminosity, for sources of similar mass.

Table 6.1 Distribution of Stage 'E' and Stage 'A' Sources in W3

Field	Early	Late	Early[a]	Late[a]
Main/(OH)	0	5	0	4
AFGL 333	2	3	1	2
KR 140	5	2	5	2
W3-NW	7	2	5	1

[a] With a S/N> 3 N_{H_2} detection.

Our catalog was further classified according to the nomenclature presented in Roy et al. (2011), who separated their BLAST sample from the Cygnus-X region in the L/M diagram based on the dominant source of energy determining the temperature of the object. 'Early' stage sources ('E' for 'external' heating or 'earliest') where classified as those below the L/M= 1 line, while those in stage 'A' ('A' for 'accretion' powered) were found in the region in the L/M diagram between the early stage sources and the early ZAMS phase, where nuclear fusion becomes the main energy source (Molinari et al., 2008). The point where the accretion stage ends is marked in high-mass star evolutionary models by the appearance of radio emission in the form of H II regions. Table 6.1 shows the distribution of early/late detections for each field in W3.

While the ultimate goal of evolutionary studies is to investigate the origin and early stages of individual high-mass stars, the distance (and spatial resolution) of most high-mass star forming regions imply that the characteristics presented here will be more relevant for the study of those progenitors leading to the formation of clusters. The origin of massive precursors hosting several OB stars is, however, a crucial first step in the high-mass star formation scenario, and so the focus of our analysis here.

6.4 Formation and Evolutionary Studies with the L/M Diagram

6.4.1 Overview: Stage E vs. Stage A Sources

The L/M diagram is a powerful tool for investigating the evolutionary models during the embedded stages of star formation (Molinari et al., 2008). Here we focus on its analysis, in conjunction with the properties described above, in order to constrain the evolution of clumps suitable for forming high-mass stars and clusters, checking for consistency with our previous results as well as other classification/evolutionary schemes.

Figure 6.4 shows the L/M diagram for the reliable sources (with measurable SEDs) separated according to field (W3 Main/(OH), AFGL 333, W3-NW and KR 140) and deconvolved size at 500 μm resolution (0.3 pc limit). The same plot, but just for those sources with an associated column density detection with S/N$>$ 3, is shown in Figure 6.5. Both figures also include the $L/M = 1$ and ZAMS locii (Molinari et al., 2008).

The total mass contained in this conservative sample is found to comprise between $\sim 5\%$ (AFGL 333) and $\sim 14\%$ (W3 Main/(OH)) of the mass above the A_{v-SF} threshold for each field, which implies that the fraction of mass contained in cores and clumps comprises at least $\sim 2.5\%$ of the total mass of the GMC.

Two key properties stand out: i) all sources with M$>$ 200 $M_\odot$ are exclusively in the HDL; and ii) all sources in the W3 Main/(OH) field are Stage A sources (Table 6.1), while the detections in the western fields are mainly Stage E.

Visual inspection reveals that Stage A (accretion powered) sources are generally associated with clusters, high-mass stars, and regions under the effects of external feedback, including those regions bordering W4 (in the AFGL 333 field) and the Trilobite. Stage E sources are located in the AFGL 333 Ridge and those filamentary structures not associated with shells around high-mass stars, such as the West Loop and the pillars found

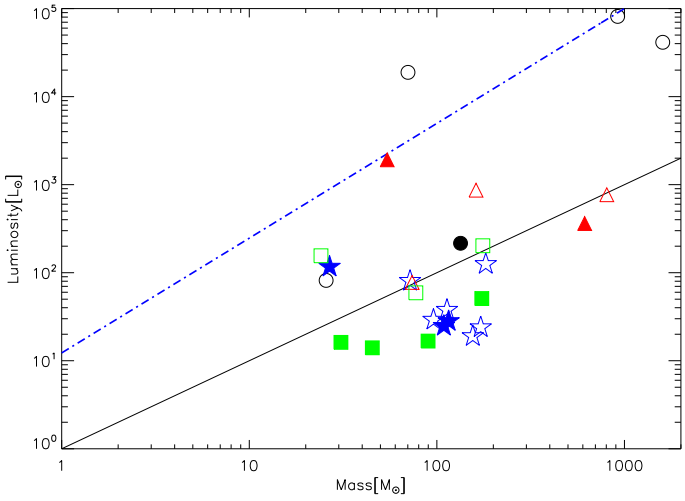

Figure 6.4 Mass Luminosity diagram for reliable sources in W3 Main/(OH) field (black circles), W3-NW (blue stars), AFGL 333 (red triangles), and KR 140 (green squares). Filled symbols are sources with deconvolved FWHM$<$ 0.3 pc. Dash-dot and solid lines mark the ZAMS (onset of nuclear burning) locus (Molinari et al., 2008) and the $L = M$ limit, respectively.

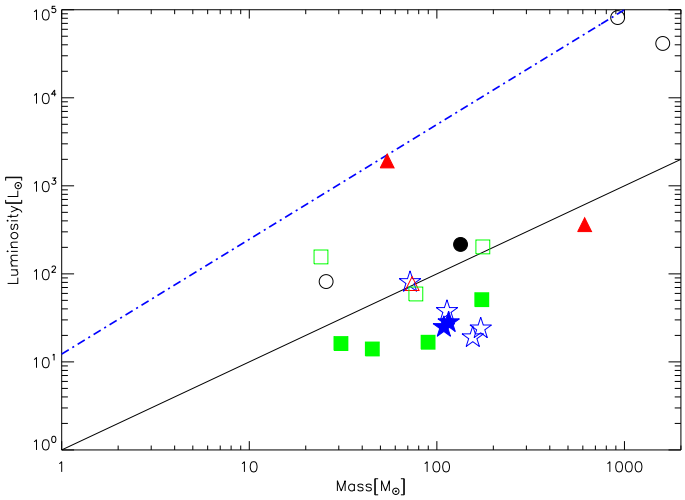

Figure 6.5 Like Fig. 6.4, but for those sources with an associated column density peak with S/N$>$ 3.

in the central regions of the W3 GMC (see Chapter 4).

All Stage E sources are found to be 'externally heated'. We also find, however, that $\sim 40\%$ of the Stage E sample contains YSOs. Some of these sources only have a Class 0/I population, while others are only associated with Class II objects. Although proper YSO identification is sometimes not possible in regions of bright diffuse emission (e.g., W3 Main; see Chapter 3), we observe that Stage A candidates with YSO detections tend to have similar YSO content, varying from just Class 0/I to just Class II. These results cannot therefore confirm that Stage E sources are truly in an 'earlier' evolutionary state than those classified as Stage A. Indeed, more than 50% of the Stage A sample is, in fact, externally heated. This is found even for those sources with major internal activity, such as W3 East and W3 West (as described in Chapter 4).

Our finding that different 'evolutionary' stages show distinctly different environmental conditions could be an indication of the dependence of the L/M diagram on the environment itself, such as the external radiation field and the opacity. This explanation could be consistent with our results from Chapter 5, which argued that a particularly high degree of external feedback-driven processes is what separates the evolution of W3 Main/(OH) relative to the other fields. Similarly, the boundary of AFGL 333 with W4 is also under the influence of the OB cluster in W4.

There are, however, alternative processes that could be contributing to the different environments of Stage E and Stage A clumps.

Assuming a similar age (and therefore no real evolutionary distinction in terms of time after the onset of star formation), a source might appear to be in Stage A if the core/clump envelope is cleared faster (e.g., by external feedback) compared to those in more quiescent regions. This result was already presented in Chapter 5 of this thesis. In addition, some Stage A sources in the HDL contain the most prominent stellar activity of the entire GMC (e.g., embedded clusters) despite the intense external radiation field which results in many of them being classified as 'externally heated'. We recall that higher external

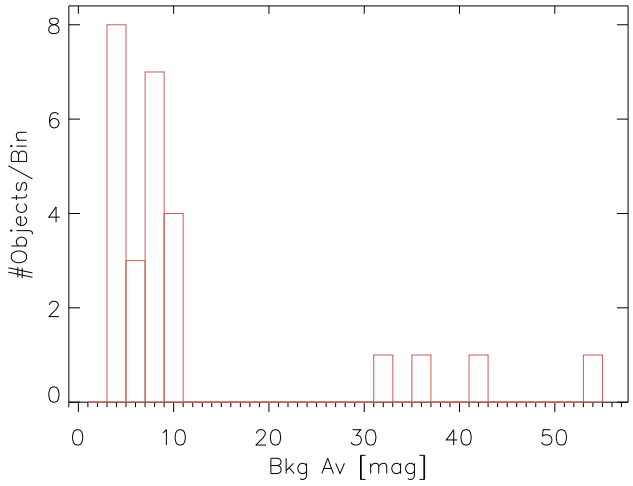

Figure 6.6 Histogram of background A_V for reliable sources.

feedback is predicted to be more efficient in star formation (Chapters 4 and 5), leading to a higher multiplicity (e.g., Koenig et al., 2012) and more disruptive internal activity. A faster clearing of the envelope by external and internal stellar influence could then lead to a faster decrease in mass with increasing luminosity than those clumps, also forming stars, although located in a more quiescent environment (therefore appearing, and remaining, as 'Stage E' for a longer time, even if they initiated star formation simultaneously with those presently classified as 'Stage A').

6.4.2 On Clusters and Filaments

The high-quality datasets provided by *Herschel* have provided strong evidence in favor of star formation occurring preferentially in filaments (e.g., Andre et al., 2000). Furthermore, the data also point toward a critical extinction for core formation, which in André et al. (2010) was defined to be $A_{V,crit} \sim 8^m$.

This value is comparable to a major peak in the histograms of background extinction for the entire reliable sample, shown in Figure 6.6, and for those reliable sources with a significant N_{H_2} counterpart, included in Figure 6.7.

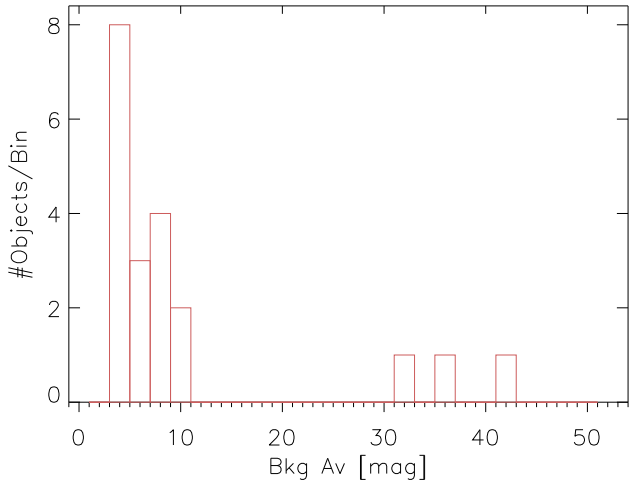

Figure 6.7 Same as Fig. 6.6, but for those sources with a significant (S/N> 3) N_{H_2} counterpart.

Both source lists show, however, the most prominent peak at low background extinction, with a value comparable to the characteristic in-cloud background of W3 as estimated in Chapter 5. This is due to the lower (convolved) resolution, which detects sources with sizes comparable to the FWHM of their host filament (e.g., East/West Loop), as well as isolated clumps with relatively diffuse background (e.g., pillars).

In order to identify those sources associated with filaments, we used the filament detection code integrated in *getsources*, which produces a SPIRE bandmerged map of all filamentary structures (including shells and pillars) in a given field. The result of this preliminary filament detection routine is shown in Figure 6.8.

The tendency of high-mass stars to form in clustered environments also makes cluster identification and characterization particularly important for the investigation of the earliest stages of OB stars. In order to identify the hosts of clusters in an early stage of evolution we correlated the list of reliable *getsources* detections with the list of known clusters in the W3 GMC from Carpenter et al. (2000) and Bica et al. (2003). Excluding the one associated with W3 (OH), for which there is no data in the column density and

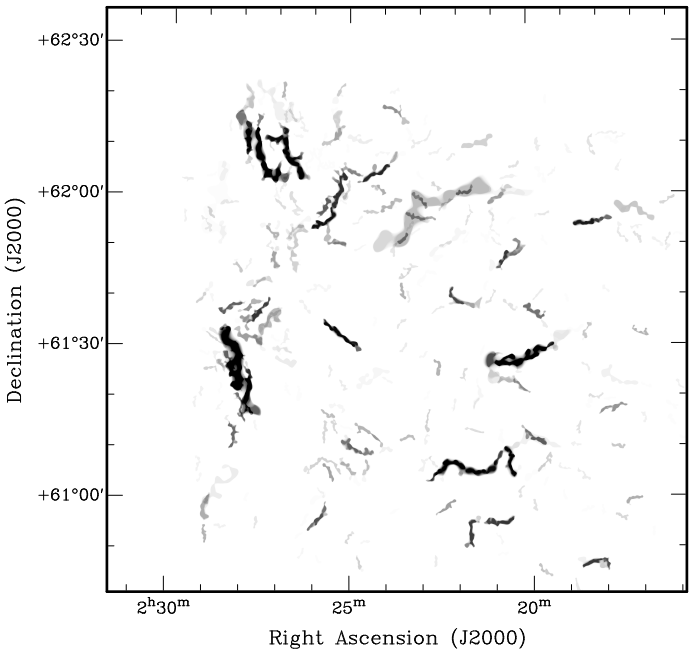

Figure 6.8 Filamentary structures extracted by *getsources* from the SPIRE (unconvolved) maps.

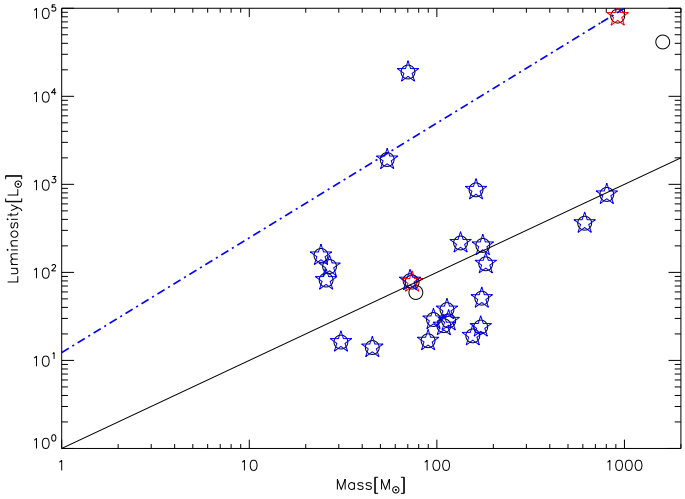

Figure 6.9 Like Fig. 6.4, but separating those sources associated with filamentary structures (blue), and clusters (red).

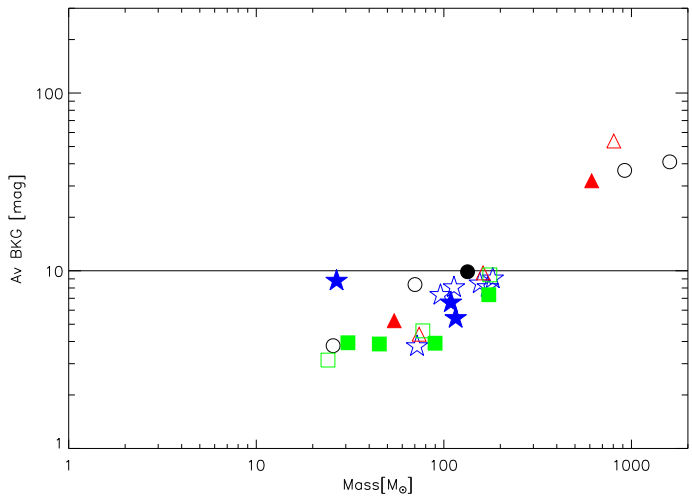

Figure 6.10 Background extinction as a function of source mass for the reliable sample. Colors and symbols as in Fig. 6.4. Solid black line is the $A_V = 10^m$ limit.

temperature maps, two reliable *Herschel* sources with SED measurements have a match in the cluster sample within $\sim 30''$. These can be observed in Figure 6.9, which shows the L/M diagram for all reliable sources, in this case separated into those associated with a filamentary structure in the *getsources* map or a cluster. We observe that, essentially, all detections are coincident with some type of 'filamentary' host, although this is not the case for the two clusters. We note, however, that a total of five sources (again excluding W3 (OH)) are identified as clusters when using the entire list from *getsources*, including the unreliable detections. The three *getsources* detections not in the reliable list but with a cluster match are found to be relatively evolved, above the ZAMS locus, with low clump masses ($\sim 3 - 35\,M_{odot}$), low observed peak extinction ($A_V \sim 5 - 15^m$), and relatively diffuse environments (peak extinction, background-corrected: $A_V < 1^m$). Two of these contain OB stars (the AFGL 333 cluster and W3 North), while the third is located in the West Loop.

The two younger clusters, not associated with a filamentary structure, are W3 East, a MHLIR source, and another cluster without high-mass activity, located between the

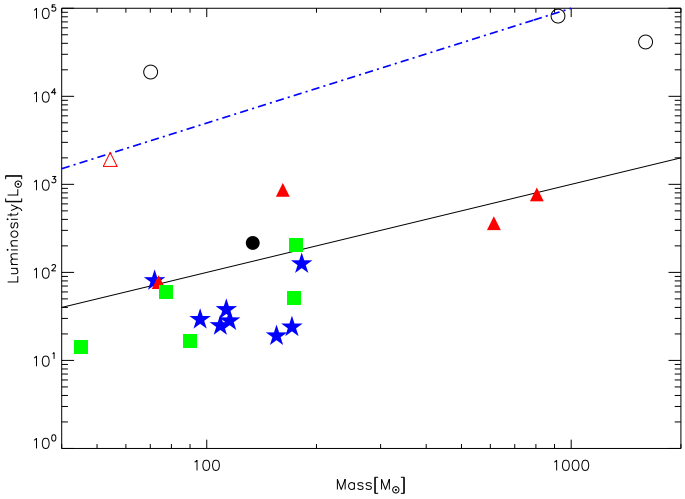

Figure 6.11 Like Fig. 6.4 but for sources with M> 40 $M_\odot$. Filled and open symbols are MIRQs and MHLIR sources, respectively.

HDL and the East Loop, and classified as a MIRQ object. Both clusters are dominated by external heating, have M> 75 $M_\odot$, peak extinction $A_V > 15^m$, and corrected peak extinction $A_V > 10^m$. Figures 6.7 and 6.6 also show a clear drop of sources at this particular extinction ($A_V \sim 10^m$). The plot of background extinction as a function of mass in Figure 6.10 indicates that the regime above this extinction is exclusive to the HDL fields, where all current high-mass star formation is located.

6.4.3 High Mass Progenitors

A link between high-mass star formation and column density has already been suggested in previous studies (e.g., Krumholz & McKee, 2008), so the presence of all current high-mass star formation in the HDL fields agrees with predictions. In an attempt to further characterize the process leading to high-mass star formation we examined in more detail those clumps which, together with W3 East and W3 West, show potential for producing high-mass stars. Figures 6.11 and 6.12 show the L/M diagrams of the MIRQ and MHLIR reliable sources with and without a significant N_{H_2} association.

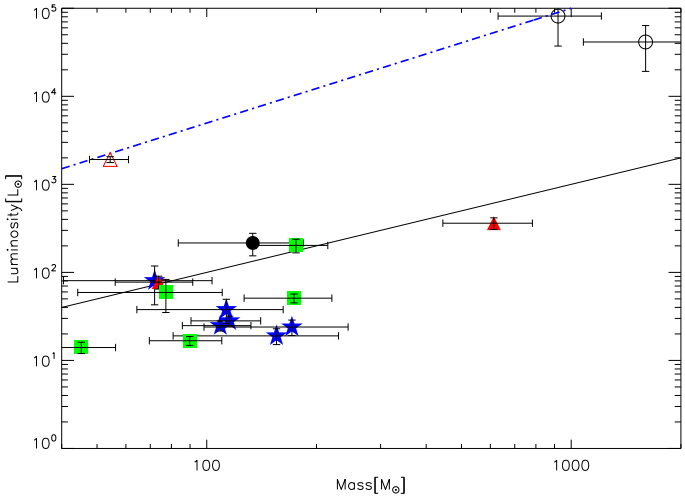

Figure 6.12 Same as Fig. 6.11, but for those sources with an associated column density peak with S/N> 3. Errors are shown here as examples of the uncertainties associated with the data.

These figures clearly show that, while MIRQ sources are common in all fields, MHLIR are present only in the HDL. Furthermore, similarly to Stage A sources, MHLIR candidates appear to be associated exclusively to those regions in the proximity of external stellar activity, and more particularly, 'high-mass' activity: the main pillar in the AFGL 333 field, next to the AFGL 333 Ridge (Chapter 4), W3 North, W3 (OH), and W3 Main. The uniqueness of the last two regions, the only ones hosting clusters of high-mass stars, has been discussed in Chapter 4. Despite having the potential for forming high-mass stars, with masses reaching $\sim 1000\,M_{\odot}$, the majority of the MIRQ detections do not appear to turn on high-mass activity. Half of the MIRQ population, however, already has YSOs, and most are unstable ($\sim 90\%$).

Figure 6.10 shows a clear trend where more massive sources are characterized by higher background extinction. Furthermore, the sample also shows an increase of peak (background-corrected) extinction, as shown in Figures 6.13 and 6.14 for the reliable sample and those reliable sources exclusively associated with a significant N_{H_2} detection, respectively.

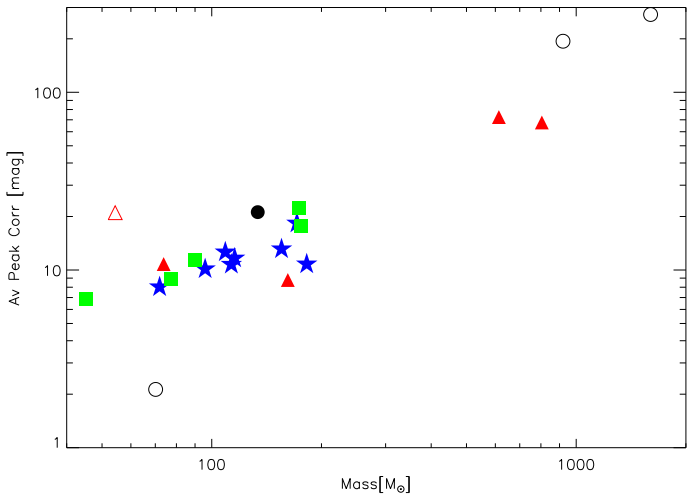

Figure 6.13 Background-corrected peak extinction (measured at central coordinates) as a function of source mass for the reliable sample. Colors and symbols as in Fig. 6.11.

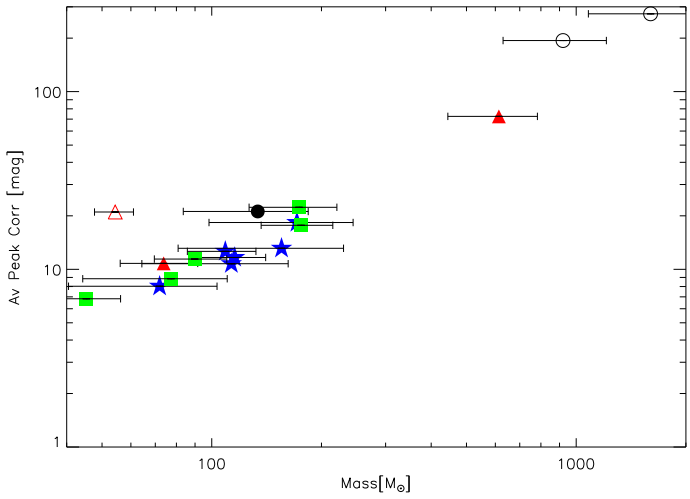

Figure 6.14 Like Fig. 6.13, but for those sources with an associated column density peak with S/N> 3. Errors are shown here as examples of the uncertainties associated with the data.

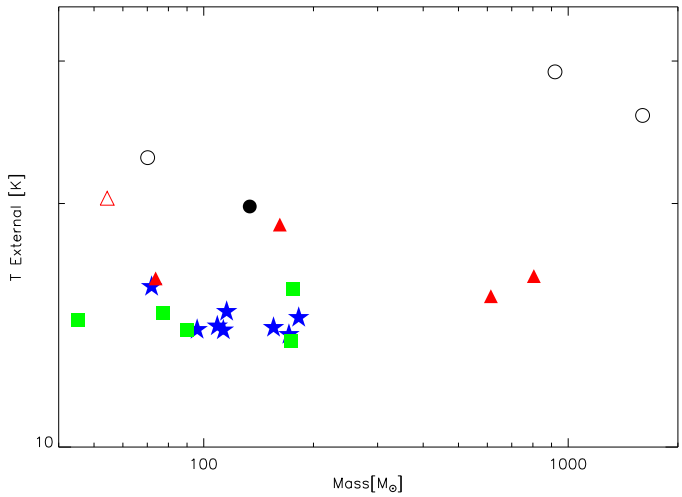

Figure 6.15 Environmental temperature as a function of source mass for the reliable sample. Colors and symbols as in Fig. 6.4. Filled symbols are MIRQs, and open symbols are MHLIR sources.

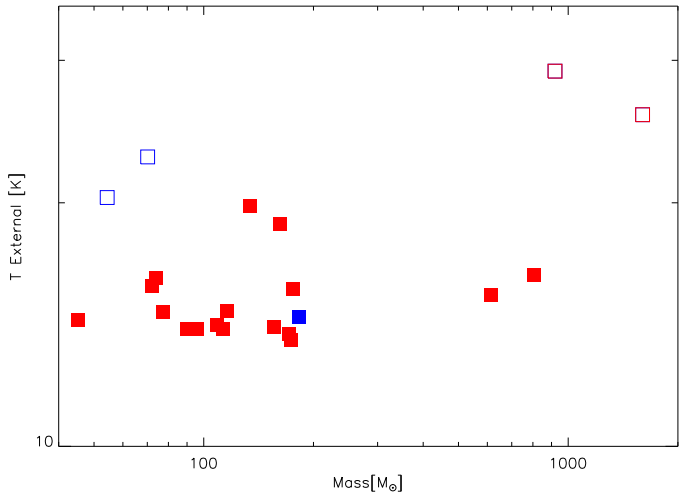

Figure 6.16 Like Fig. 6.15. Here colors are 'externally' (red) and 'internally' heated sources (blue) as derived from the temperature profiles.

Current evolutionary models of individual YSOs have predicted an increase in luminosity at constant mass from Stage E to the ZAMS stage (Molinari et al., 2008). Focusing on W3 East and W3 West as the 'target' clumps (the only ones with ongoing high-mass star formation, in addition to W3 (OH)), this implies that early stage (MIRQ) sources with similar mass (and therefore similar background extinction/environment, as observed in Fig. 6.10) would need to increase the central extinction as luminosity increases, therefore forming/enhancing the column density peak they are currently lacking compared to the MHLIR sources.

If mass is assembled as luminosity increases, then the increase of central column density and the necessary mass must also be accompanied by the formation of a dense enough environment, which is characteristic of the most massive sources (Fig. 6.10).

Both scenarios are compatible with the basics of the convergent constructive feedback process, i.e., external feedback by high-mass stars and the (positive) effects of the 'triggering' mechanism, as presented in Chapters 4 and 5. Indeed, Figure 6.15 indicates that all MHLIR sources have a higher external temperature/radiation field. While internal activity can contribute to raising the temperature of the clump and its local neighborhood, our analysis of the temperature profiles indicates, as mentioned above, that the most massive MHLIR objects are, in fact, externally heated. This can be observed in Figure 6.16, which shows the observed temperature of the reliable MHLIR and MIRQ sample as a function of mass. W3 East and W3 West are the most prominent examples (Chapter 4), and as mentioned earlier in this thesis, all sources with masses approaching the $\sim 1000\,M_{\odot}$ (with the potential to form clusters) are located at d$\sim 1\,$pc or less from high-mass stars.

6.5 Conclusion

By means of the *Herschel* catalog extracted with *getsources* from the convolved *Herschel* maps, we have a produced a preliminary list of reliable detections in the W3 GMC. Each source was characterized according to its SED, its location in the L/M diagram, and its properties in the column density and temperature maps. The sample was also classified according to various schemes used in past studies of high-mass star forming regions. Results indicate that, in order to form the most massive systems (clumps) suitable for hosting clusters of high-mass stars, one needs to assemble the mass and i) acquire the potential (high extinction environment), and ii) increase the central extinction. Massive sources without these conditions do exist in W3, and yet lack high-mass star activity.

The 'convergent constructive feedback' process (introduced in Chapter 4) can effectively accomplish both requirements by collecting and compressing the material via external feedback by high-mass stars. Stellar feedback can assemble the mass of the clump as star formation within the clump proceeds (with the 'triggering' stars also compressing and enhancing the background environment; e.g., a shell, ridge). The clump mass could also remain more or less constant during the pre-stellar and protostellar stages, but the central column density will be enhanced by the local external high-mass stars as star formation progresses, as described in the convergent constructive feedback scenario of W3 Main.

Chapter 7

Summary and Future Work

Herschel has for the first time delivered data of unprecedented spatial resolution and sensitivity at far infrared and submm wavelengths. In combination with BLAST, and as members of the Canada Team in the HOBYS Collaboration, *Herschel* data has been used in this thesis to constrain the mechanisms driving the poorly understood high-mass star formation process.

7.1 Overview: Techniques and Main Results

7.1.1 Aquila

Methods

In the first part of this thesis, and as members of the BLAST Collaboration, we have used BLAST data to carry out the first general submm analysis of the field towards GRSMC 45.46+0.05. The deconvolved 6 deg^2 ($3^\circ \times 2^\circ$) maps were used to characterize the clump population located at $\sim 7\,\mathrm{kpc}$. Interferometric CORNISH data at 4.8 GHz served to characterize the UCHII regions within the main clumps.

Results

The SEDs present an active population with temperatures of $T \sim$ 35-40 K and masses of $\sim 10^3\,M_\odot$ for a dust emissivity index $\beta = 1.5$. The clump evolutionary stages range from evolved sources, with extended H II regions and prominent IR stellar population, to massive young stellar objects, prior to the formation of an UCHIIR. The CORNISH data reveal the details of the stellar content and structure of the UCHIIRs. In most cases, the ionizing stars corresponding to the brightest radio detections are capable of accounting for the clump bolometric luminosity, in most cases powered by embedded OB stellar clusters.

7.1.2 The W3 GMC

Methods

As a precursor to SPIRE, the Aquila analysis refined the tools (codes) and methodology that were used in the *Herschel* analysis. The study of W3 was divided into a i) a YSO analysis, ii) an investigation of the high-mass star forming structures in W3, iii) the environment and large scale properties, and iv) a preliminary analysis of the compact source population.

The YSO population was identified and classified in the IRAC/MIPS color-magnitude space according to the 'Class' scheme and compared to other classifications based on intrinsic properties. Class 0/I and II candidates were also compared to low/intermediate-mass pre-main-sequence stars selected through their colors and magnitudes in 2MASS. The classification was used to produce age maps of the cloud, and the clustering and spatial distribution of the YSOs were characterized by means of the MST algorithm.

The HOBYS datasets were first used to analyze the structures in W3 currently forming high-mass stars, and therefore prime candidates for constraining the (unique) processes leading to the formation of clusters of OB stars. The data were used to produce temper-

ature and column density maps, which combined with a photometry analysis, served to identify and characterize (e.g., luminosity, mass, temperature) the high-mass star forming clumps relative to the properties of their associated stellar population.

The environmental component of the W3 study included a comparative analysis of the HDL and the western fields, their large scale properties, and the YSO information derived from the *Spitzer* maps. The mass distributions, PDFs, and the YSO population were used to characterize potential sites for current and future star formation, constraining the environmental conditions leading to the observed low/high-mass populations.

The compact source analysis was based on the catalogs produced by running the software *getsources* on the *Herschel* maps, convolved to the 500 μm spatial resolution. A 'reliable' catalog was produced, characterized (SEDs, column density/temperature maps), and classified according to schemes presented in recent studies of high-mass star forming regions.

Results

The *Spitzer* analysis has revealed signatures of clustered and distributed star formation in both triggered and quiescent environments. The central/western parts of the GMC are dominated by isolated bursts of star formation that triggered secondary star formation events. Star formation in the eastern high density layer also shows signs of quiescent and triggered stellar activity, as well as extended periods of star formation. While some degree of quiescent/spontaneous star formation is required to explain the observed YSO population in W3 Main, our findings support triggering as a key factor for inducing and enhancing some of the major star forming activity in this region and in the HDL.

Herschel indicates that, among the compact sources (<0.3 pc), and apart of W3 (OH), the most massive and luminous are the two clumps in W3 Main, defined as 'W3 East' (hosting IRS5) and 'W3 West' (IRS4). Both these sources, together with W3 (OH), are also the only ones hosting clusters of high-mass stars and on-going high-mass star

formation. The unique, massive nature of these sources, which are also identified as having the highest column densities of the entire GMC, is verified by an independent analysis of two separate catalogs: one extracted from the convolved *Herschel* maps, and another catalog of column density structures, produced by running *getsources* directly on the column density map.

Based on the unique *Herschel* properties of W3 East and W3 West, and the also unique characteristics of their high-mass stellar population, we suggest a 'convergent constructive feedback' mechanism to explain the formation of a cluster of high-mass stars with an observed decreasing age (and increasing system/source mass) toward the innermost regions. This process, which relies on feedback by local high-mass stars to ensure the availability of material during cluster formation, can not only address various outstanding issues in high-mass star formation theory, but it could also explain the formation of those environments suitable for the formation of the rare Trapezium-like systems.

Results from the environmental and compact source studies provide further evidence supporting the constructive convergent feedback scenario.

The environmental study indicates that local (in-cloud) stellar feedback, mainly by high-mass stars, is the key factor distinguishing the current state and evolution of the fields in W3. This agrees with the results from the *Spitzer* YSO analysis. Feedback by high-mass stars in an already compressed environment originates a second break at high extinction in the mass distributions/PDFs of the fields in the HDL. This high extinction material is observed to be associated with sub-parsec triggering by high-mass stars. We also estimate that the triggering process is more efficient in star formation, with a star formation rate $\sim 2-3$ times that of the quiescent mode. The association of high column density material with external feedback by high-mass stars, together with the efficiency of triggering, are the basics of the convergent constructive feedback process. Furthermore, this process can explain the needed combination of high column density,

mass, and environmental extinction with increase in luminosity observed in our compact source analysis.

When compared to alternative scenarios proposed for high-mass star formation in other HOBYS fields, we conclude that an active/dynamic process aiding in the accumulation, compression and confinement of material is a critical (basic) feature of the high-mass star/cluster formation, distinguishing it from classical low-mass star formation. The environmental conditions and availability of nearby triggers determine the form in which this process occurs, implying that high-mass star/cluster formation could occur due to a relatively wide range of scenarios: from large scale convergence of turbulent flows, to convergent constructive feedback in dense, highly clustered environments, as in W3 Main, or mergers of filaments in more quiescent and less dense regions.

7.2 Follow-up and Future Goals

As part of the objectives of the GTKP HOBYS, one of the main responsibilities of the Collaboration is the release of a robust catalog for all fields, produced and analyzed using self-consistent techniques and methodology. This is crucial for an effective comparison of all fields in order to identify and constrain the mechanisms driving the high-mass star formation process. The use of ancillary data from ground and other space-based observatories is also crucial to maximize the potential of *Herschel*. Here we list other issues that still need to be addressed for the W3 GMC, and which are applicable to other HOBYS fields.

7.2.1 Calibration of *Herschel* Data and Production of Final Catalogs

A common analytical approach when treating all *Herschel* data is indispensable for the creation of the *Herschel* Legacy Archive.

As a first step towards the development of this common analytical approach, the *Herschel* collaboration has already established common physical assumptions for dust modeling (e.g., dust opacity law), and developed a source extraction software capable of producing bandmerged catalogs with measured flux densities from all *Herschel* bands (e.g., *getsources*). In addition, derivation of physical parameters such as mass, luminosity, and temperature require accurate SED fitting. With the spatial resolution of *Herschel* decreasing by more than a factor of 6 from PACS (70 μm) to SPIRE (500 μm), this implies that the SPIRE flux densities provided by *getsources* must be scaled (lowered) to match that expected from a higher (PACS) resolution (as described in this work). Due to the use of the convolved maps, this work did not require scaling of the SPIRE fluxes. The spatial resolution of PACS is essential for the investigation of sources at 'core' sizes ($<$0.1 pc) up to d=3 kpc, and therefore scaling will be required for the production of the final catalogs of W3 and the other HOBYS fields. However, this process of 'scaling' to a higher resolution is still poorly constrained.

The current scaling method, while effective for sources in an idealized scenario (e.g., highly symmetric, isolated), needs significant modification depending on the evolutionary state of the source and its local environment. Furthermore, the current approach relies on a successful (and resolved) detection at 160 μm with a size smaller than that at SPIRE. In our analysis of the W3 GMC we observed that a large proportion of the detections in W3 do not satisfy this requirement. This also implies that there is currently no available technique to measure the coldest structures, which are also crucial for the investigation of the earliest stages, and those associated with more extreme environments, e.g., under the influence of a high-mass star. This is particularly important for W3, as our findings suggest that stellar feedback could be a key process when forming the precursors of high-mass stars and clusters.

This issue can be addressed with the use of long wavelength datasets with resolution comparable to that of PACS. The Submillimeter Common-User Bolometer Array 2

(SCUBA-2; Holland et al., 2006) can provide high resolution submm data at 450 μm and 850 μm, which would result in the production of full SEDs at the best resolution currently available, without the need of scaling. The creation of such scaling-independent SED models will provide robust parameters, as well as a direct characterization of the SED behavior, for each type of source and environment. This can then be used as a base to calibrate the scaling process of the SPIRE bands.

Development of a more suitable scaling technique is therefore crucial for the creation of the *Herschel* Legacy database, maximizing the potential of the *Herschel* datasets by exploiting the PACS capabilities.

7.2.2 Constraining Evolutionary Models, Cloud Statistics, and a Possible Bimodality in Star and Core Formation

The identification of possible differences in the primordial and intrinsic conditions of the parent structures is essential for determining whether there are distinct processes driving the formation and evolution of high-mass stars and clusters. Some hints of a possible bimodality in core/clump formation have already been presented in recent *Herschel* studies (e.g., Csengeri et al., 2011) and in the present work. Confirmation, however, requires accurate prior classification according to evolutionary state, for which near and mid-infrared data are essential. Based just on the information from the *Herschel* bands, the sample can only be tentatively characterized as starless/pre-stellar or protostellar based on the presence of PACS 70 μm(e.g. André et al., 2010). Before *Herschel*, alternative classifications have used narrower wavelength ranges in the near and mid-infrared (e.g., Class 0/I, II; e.g., Gutermuth et al., 2009). A first YSO classification scheme based on the full-sky WISE Survey (Wide-field Infrared Survey Explorer; Wright et al., 2010; Jarrett et al., 2011) has also been recently released (Koenig et al., 2012). However, the most accurate classification of the evolutionary state of a source can only be obtained from detailed SED modeling of the entire IR/submm spectrum, incorporating the warm

(stellar) as well as the cold (envelope) components.

The use of WISE, *Herschel* PACS, and SCUBA-2 datasets, all at comparable spatial resolution, will produce the most accurate SEDs that can be achieved using the full IR/submm spectral range, capable of effectively constraining the behavior at the crucial wavelengths required for evolutionary classification purposes.

Successful evolutionary classification and characterization is crucial, not only for investigating a possible bimodality in star formation, but also to address other outstanding issues:

1) Global (cloud scale) star and core formation characteristics: core formation efficiencies, lifetimes, star formation rates, and initial stellar/core mass functions.

2) The properties of the hosting core/clump relative to the standard (single-object) YSO classification. With a core or clump capable of hosting various stars in a range of evolutionary states, nomenclature based on the evolutionary state of one embedded star is not appropriate when describing the parental structure. A different description (classification) is required when analyzing the column density structures.

4) The effects of stellar feedback: a full evolutionary classification will allow for a more accurate quantification of the effects of triggering on the local environment and structures. This process, as shown in this thesis, is likely a major player in high-mass star formation.

7.2.3 Filaments, Disks, and Dynamics

In addition to the issues already presented, other major topics remain that need to be addressed when refining the current theoretical models of high-mass star formation.

Latest results from *Herschel* studies have revealed the importance of filaments and ridges in low and high-mass star formation (e.g., Hill et al., 2011). The identification and full characterization of these structures, their origin, and evolution, must be carried out in conjunction with the properties of the core/clump and stellar population. A full

filamentary analysis is achievable with current filament extractor and analysis codes, such as DisPerSE (Sousbie, 2011) and *getsources*.

Disk formation and evolution remains a major outstanding issue not only in high-mass star formation but also in planetary research. Standard evolutionary models and classification schemes (e.g., André et al., 2010) have yet to incorporate the complexity and diversity of disk properties (e.g., Cieza et al., 2011) and the links with the parent core. These studies are necessary in order to describe the conditions leading to the formation of planetary systems and the role of disks in the global star formation scenario.

Molecular data is indispensable to complement continuum datasets with chemical and dynamical information. In the case of the W3 GMC, full molecular datasets have already been obtained by collaborators in Europe (Polychroni et al., 2012) with HARP (Heterodyne Array Receiver Programme; Buckle et al., 2009). With evidence in support of a dynamical high-mass star formation process (e.g., convergence of flows; convergent constructive feedback), spectral line analysis is crucial to confirm and quantify the inflow/outflow of material and the stability conditions of the compact source population.

Ultimately, interferometers such as the Submillimeter Array (SMA), the IRAM PdB interferometer, or the Atacama Large Millimeter/submillimeter Array (ALMA; for those fields observable from the southern hemisphere) will be needed to probe the *Herschel* structures down to typical condensation/single-star scales (sub-arcsecond resolution already approaching the inner-disk domain). This is necessary for investigating the fragmentation process in core formation, discriminate between star formation scenarios such as monolithic collapse, competitive accretion, and mergers, and illuminate the role, evolutionary stages, and characteristics of disks in the star and planet formation process.

Appendix A

Herschel Images of W3

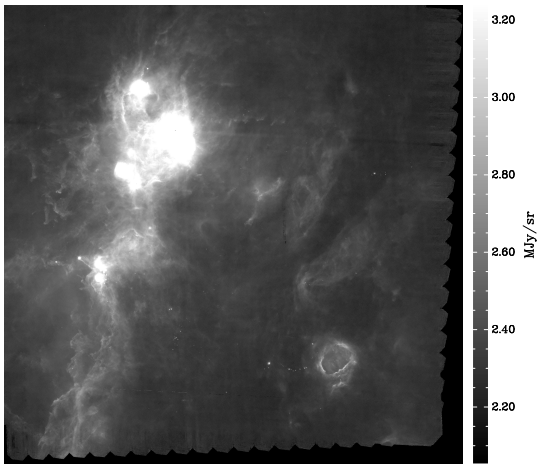

(a) PACS 70 μm

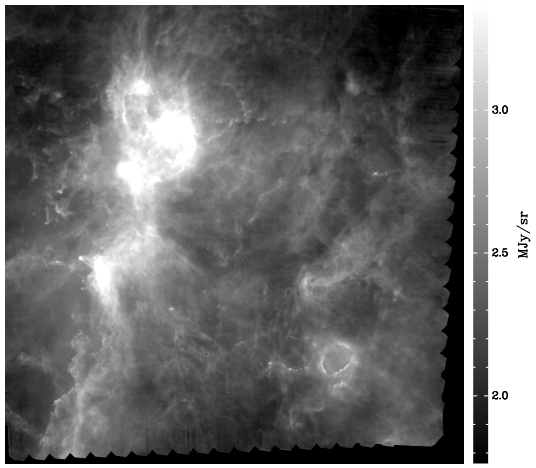

(b) PACS 160 μm

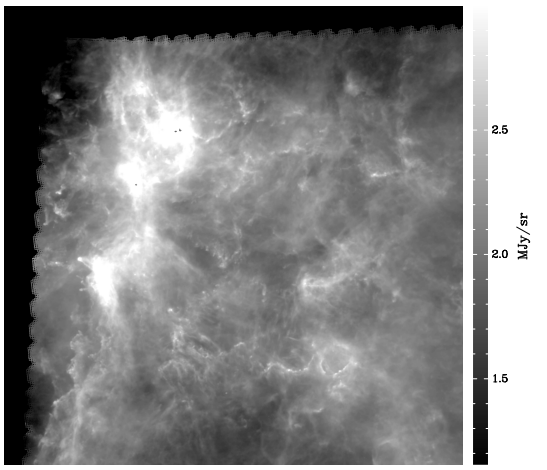

(c) SPIRE 250 μm

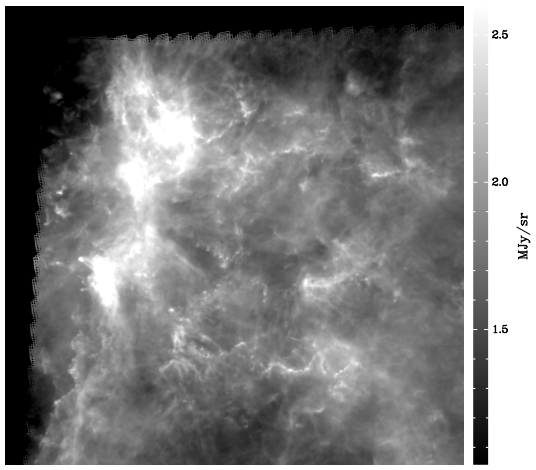

(d) SPIRE 350 μm

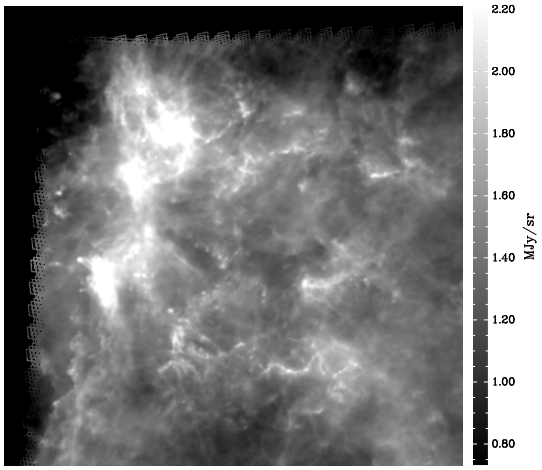

(e) SPIRE 500 μm

Figure A.1 *Herschel* monochromatic (log-scale) maps of the W3 GMC.

Appendix B

Contributions from Foreground/Background Gas

The uncorrected column density ($N_{\mathrm{H_2}}$) and dust temperature maps are given in Figure B.1 left and right, respectively, which can be compared to the corrected versions displayed in Figures 4.2 and 4.3 in Section 4.2.

While emission in the *Herschel* intensity maps is dominated by the W3 GMC, these maps are still affected by contributions from background and (mainly) foreground material not local to the W3 GMC. To correct for this emission, as done in, e.g., Planck Collaboration et al. (2011b), we need to estimate the contribution $I_{\nu,i}$ at each *Herschel* band from the product $\sigma_{\nu,i} B_\nu(T_i) N_{\mathrm{H},i}$ (including an estimate of β) in Equation 4.1 for two contributing components: dust in foreground/background gas that is traced by H I emission (atomic; subscript a) and CO emission (molecular, subscript m).

We used the H I and CO molecular spectral data cubes from the CGPS to estimate the foreground and background contribution. From visual inspection of the CO cube, the velocity range of the W3 GMC is about -29 to $-60\,\mathrm{km\,s^{-1}}$. The foreground/background gas column was therefore estimated by integrating the respective line emission over velocity, *excluding* this range, giving us $W(\mathrm{H\,I})_a$ and $W(\mathrm{CO})_m$. As seen in Figure B.2, the

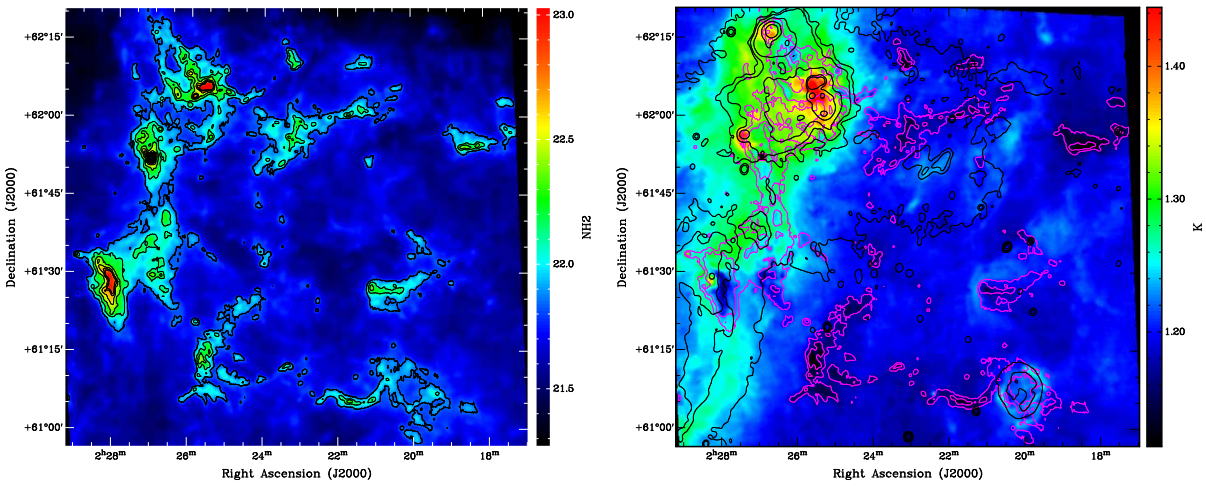

Figure B.1 Left: Column density map of the W3 GMC (log [cm^{-2}]). Figure shows the variety of filaments, pillars and structures that are found throughout the GMC. Contours are $N_{\rm H_2} \approx [7, 10, 20, 35, 50, 65] \times 10^{21}\,{\rm cm}^{-2}$. Right: Dust temperature map of the W3 GMC (log [K]). Magenta contours like the first two contours in left figure as a reference. Black contours of 1420 MHz continuum emission like in Fig. 4.3.

spatial distribution of the foreground/background molecular gas is quite distinct from that of gas associated with the W3 GMC, $W({\rm CO})_{\rm W3}$.

For the atomic component, we determined $N_{{\rm H},a}$ by the standard conversion of $W({\rm H\,I})_a$ (e.g., Lequeux, 2005), ignoring self absorption.[1] For the molecular component, we made a preliminary estimate $N_{{\rm H},m} = 2X_{\rm CO}W({\rm CO})_m$ adopting $X_{\rm CO}$ from Strong et al. (1988). In the final analysis, it is actually the product $\sigma_{\nu,m}X_{\rm CO}$ that is needed, and we calibrate this below. These estimates were put on the same common 9.5″ grid of the preliminary *Herschel*-based $N_{\rm H_2}$ and T maps, which were convolved to the CGPS resolution of $\sim 1'$ for comparison.

[1]The few highly absorbed (negative) regions in this column density map in front of very bright HII regions were replaced by an estimate of the emission using a centered annulus 3′ wide.

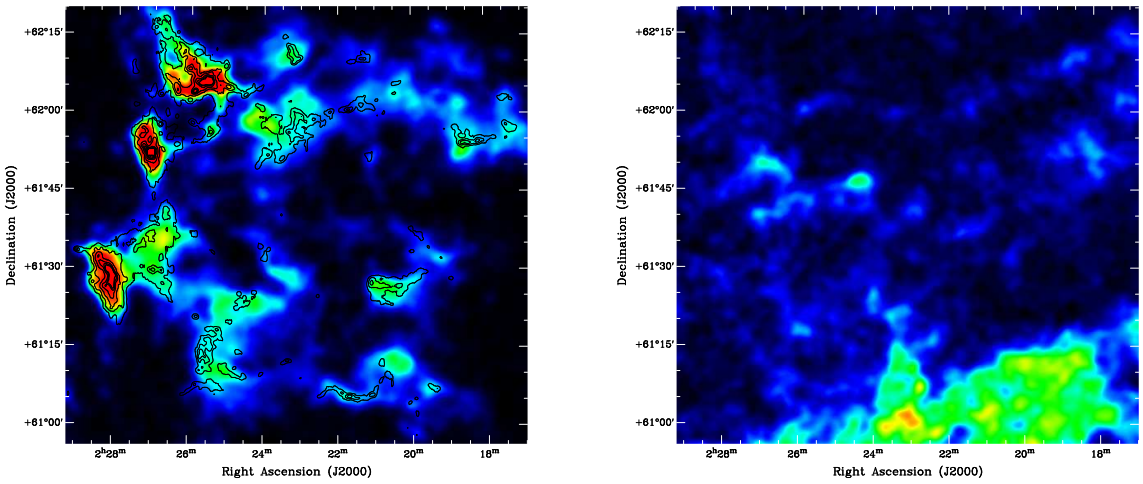

Figure B.2 Left: Map of $W(\mathrm{CO})_{\mathrm{W3}}$, integrated over velocities corresponding to the W3 GMC (linear scale). Contours are of column density $N_{\mathrm{H_2}}$ from the analysis in Section 4.2, the same as in Fig. 4.2: $[7, 10, 20, 35, 50, 65] \times 10^{21}\,\mathrm{cm}^{-2}$. There is a good correspondence but, as expected, because of opacity effects ^{12}CO is not a perfect tracer of column density. Right: Map of the foreground/background $W(\mathrm{CO})_m$, integrated over velocities excluding the range corresponding to the W3 GMC. This has a distinctive morphology and corresponding emission can be seen in the original *Herschel* images, for example below the West Loop.

B.1 Parameters for the Foreground/Background Atomic Component

To determine a temperature representative of the atomic gas, we selected regions with $W(\mathrm{CO}) < 0.5\,\mathrm{K\,km\,s^{-1}}$ and overall low column density in the preliminary Figure B.1, left, with the foreground/background column density greater than the estimated column density in the W3 GMC by at least a factor 5. An example of such a location is the upper left region of the map. From the values in Figure B.1, right, $T_a \sim 16\,\mathrm{K}$, consistent with the lower limit of the temperature range for the atomic material as estimated by Planck Collaboration et al. (2011a,b).

For atomic gas, at our fiducial frequency ν_0, $\sigma_{\nu,a}(1200)$ ranges somewhat about a mean $\sim 1\times10^{-25}$ cm^2 H^{-1}, $\beta = 1.8$, and $T \sim 18$ K (Planck Collaboration et al., 2011a,b). Due to the relatively uniform value of $N_{\rm H,}a$ over the field, we were unable to calibrate $\sigma_{\nu,a}(1200)$ ourselves toward this field and so we adopted this value and $\beta = 1.8$.

With these parameters, we estimated $I_{\nu,a}$ across the entire field, and subtracted them from the observed *Herschel* intensities. As a consistency check, we observed that in the regions dominated by the atomic foreground/background, there is no oversubtraction.

B.2 Parameters for the Foreground/Background Molecular Component

To determine a temperature representative of the molecular gas, we again selected regions of overall low column density and with the foreground/background column density greater than the estimated column density in the W3 GMC by at least a factor 5, but now with $W({\rm CO})_m > 3\,{\rm K\,km\,s^{-1}}$. An example of such location is the region below the West Loop. Then at the positions of these regions in Figure B.1, right, we estimated $T_m \sim 15$ K from the temperature map.

For calibrating the opacity, we further selected regions such that molecular gas is either the dominant foreground/background component by a factor 2.3 or in excess of the W3 column density by a factor 50. By correlating $I_\nu - I_{\nu,a}$ with $W({\rm CO})_m$, we found the slope $\sigma_{\nu,m}X_{\rm CO}B_\nu(T_m)$ frequency by frequency. This provides a consistency check on the adopted T_m and $\beta = 1.8$. The product $\sigma_{\nu,m}(1200)X_{\rm CO}$ was found to be in good agreement for all bands $\geq 160\,\mu$m (those used to create the column density maps), with a mean value $(3.6\pm0.3)\times10^{-5}\,{\rm H^{-1}}\ ({\rm K\,km\,s^{-1}})^{-1}$. We adopted this empirical calibration to estimate $I_{\nu,m}$ across the entire field. Again we checked for oversubtraction.

If $X_{\rm CO} = (2.3\pm0.3)\times10^{20}$ molecules cm^{-2} $({\rm K\,km\,s^{-1}})^{-1}$ from Strong et al. (1988), then $\sigma_{\nu,m} = (1.6\pm0.2)\times10^{-25}\,{\rm cm^2\,H^{-1}}$. Planck Collaboration et al. (2011b) estimated

$\sigma_{\nu,a}(1200)$ to be $2.3\times10^{-25}\,\mathrm{cm^2\,H^{-1}}$ for the molecular phase in the Taurus molecular cloud, within the broad range found in other environments by Martin et al. (2012). If this were the value, then $X_{\rm CO} = (1.6\pm0.2)\times10^{20}\,\mathrm{molecules\,cm^{-2}\,(K\,km\,s^{-1})^{-1}}$. Recent results from *Fermi* (Abdo et al., 2010) in the second quadrant find $X_{\rm CO} = (1.9\pm0.2)\times10^{20}\,\mathrm{molecules\,cm^{-2}\,(K\,km\,s^{-1})^{-1}}$ in the Perseus arm, $(1.59\pm0.17)\times10^{20}\,\mathrm{molecules\,cm^{-2}\,(K\,km\,s^{-1})^{-1}}$ in the Local arm, and $(0.87\pm0.05)\times10^{20}\,\mathrm{molecules\,cm^{-2}\,(K\,km\,s^{-1})^{-1}}$ in more local Gould Belt clouds. For Local arm clouds in the third quadrant, $X_{\rm CO} = (2.08\pm0.11)\times10^{20}\,\mathrm{molecules\,cm^{-2}\,(K\,km\,s^{-1})^{-1}}$ (Ackermann et al., 2011).

B.3 Results

We subtracted the above estimates of $I_{\nu,a}$ and $I_{\nu,m}$ from the *Herschel* intensity maps and then repeated the pixel SED fitting process to find the column densities and dust temperatures characteristic of the W3 GMC itself. For the GMC material, we again adopted the optical depth to column density conversion described in Section 4.2.

On average over the pixels in the map, the foreground/background correction decreases the observed column densities by $\sim 30\pm15\%$, with a greater proportional effect on the lower column density regions and little effect on the high column density peaks and ridges.

The removal of the foreground/background emission clarifies the temperature contrast and gradients in the cloud, like the areas bordering W4 and other warm regions like the Trilobite in the western fields. We note that some "artifacts" are likely to appear in areas in which the foreground/background dominates, because after the subtraction the residual intensity is quite small, whereas the errors remain, so that it is difficult to obtain a reliable fit. The main region suffering from this effect is located south of the West Loop, where the relatively prominent foreground/background CO component was used to calibrate the opacity. Here, the intensity correction has produced a prominent

feature in Figure 4.3 at RA/Dec: $\sim 2^{\rm h}\,22^{\rm m}\,15^{\rm s}$ $+61^\circ\,00'\,00''$, which also produces the spike in T at low column densities seen in Figure 4.4, panel for KR 140. Such regions could be masked for any analysis sensitive to details at low column densities, particularly because these are most prone to other systematic errors; including uncertainties in the *Planck* offsets and the map-making techniques, using the same $\sigma_{\nu,i}$ and T_i for all of the dust in the foreground and background gas components, and optical depth effects in the gas tracers across the field.

Bibliography

Abdo, A. A., Ackermann, M., Ajello, M., et al. 2010, ApJ, 710, 133

Ackermann, M., Ajello, M., Baldini, L., et al. 2011, ApJ, 726, 81

Allen, L., Megeath, S. T., Gutermuth, R., et al. 2007, Protostars and Planets V, 361

Alves, J., Lombardi, M., & Lada, C. J. 2007, A&A, 462, L17

Andre, P., Ward-Thompson, D., & Barsony, M. 2000, Protostars and Planets IV, 59

André, P., Men'shchikov, A., Bontemps, S., et al. 2010, A&A, 518, L102

Argon, A. L., Reid, M. J., & Menten, K. M. 2000, ApJS, 129, 159

Aumann, H. H., Fowler, J. W., & Melnyk, M. 1990, AJ, 99, 1674

Baart, E. E., & Cohen, R. J. 1985, MNRAS, 213, 641

Ballantyne, D. R., Kerton, C. R., & Martin, P. G. 2000, ApJ, 539, 283

Ballesteros-Paredes, J., Vázquez-Semadeni, E., Gazol, A., et al. 2011, MNRAS, 416, 1436

Bastian, N., Ercolano, B., Gieles, M., et al. 2007, MNRAS, 379, 1302

Battinelli, P. 1991, A&A, 244, 69

Benjamin, R. A., Churchwell, E., Babler, B. L., et al. 2003, PASP, 115, 953

Bergin, E. A., & Tafalla, M. 2007, ARA&A, 45, 339

Bernard, J.-P., Paradis, D., Marshall, D. J., et al. 2010, A&A, 518, L88

Bertin, E., & Arnouts, S. 1996, A&AS, 117, 393

Bica, E., Dutra, C. M., & Barbuy, B. 2003, A&A, 397, 177

Bik, A., Henning, T., Stolte, A., et al. 2012, ApJ, 744, 87

Bisbas, T. G., Wunsch, R., Whitworth, A. P., Hubber, D. A., & Walch, S. 2011, ArXiv e-prints

Blum, R. D., & McGregor, P. J. 2008, AJ, 135, 1708

Bohlin, R. C., Savage, B. D., & Drake, J. F. 1978, ApJ, 224, 132

Bonnell, I. A., & Bate, M. R. 2002, MNRAS, 336, 659

—. 2005, MNRAS, 362, 915

Bonnell, I. A., Bate, M. R., Clarke, C. J., & Pringle, J. E. 1997, MNRAS, 285, 201

Bonnell, I. A., Bate, M. R., & Zinnecker, H. 1998, MNRAS, 298, 93

Bressert, E., Bastian, N., Gutermuth, R., et al. 2010, MNRAS, 409, L54

Bronfman, L., Nyman, L., & May, J. 1996, A&AS, 115, 81

Buckle, J. V., Hills, R. E., Smith, H., et al. 2009, MNRAS, 399, 1026

Campbell, M. F., Butner, H. M., Harvey, P. M., et al. 1995, ApJ, 454, 831

Cao, Y., Terebey, S., Prince, T. A., & Beichman, C. A. 1997, ApJS, 111, 387

Carpenter, J. M. 2001, AJ, 121, 2851

Carpenter, J. M., Heyer, M. H., & Snell, R. L. 2000, ApJS, 130, 381

Cesaroni, R., Walmsley, C. M., & Churchwell, E. 1992, A&A, 256, 618

Chan, S. J., Henning, T., & Schreyer, K. 1996, A&AS, 115, 285

Chapin, E. L., Ade, P. A. R., Bock, J. J., et al. 2008, ApJ, 681, 428

Chavarría, L. A., Allen, L. E., Hora, J. L., Brunt, C. M., & Fazio, G. G. 2008, ApJ, 682, 445

Chen, H.-R., Welch, W. J., Wilner, D. J., & Sutton, E. C. 2006, in Astronomical Society of the Pacific Conference Series, Vol. 356, Revealing the Molecular Universe: One Antenna is Never Enough, ed. D. C. Backer, J. M. Moran, & J. L. Turner, 270

Choudhury, R., Mookerjea, B., & Bhatt, H. C. 2010, ApJ, 717, 1067

Churchwell, E., Povich, M. S., Allen, D., et al. 2006, ApJ, 649, 759

Cieza, L. A., Schreiber, M. R., Romero, G. A., et al. 2011, in Bulletin of the American Astronomical Society, Vol. 43, American Astronomical Society Meeting Abstracts #217, 339.09

Clark, P. J., & Evans, F. C. 1954, Ecology, vol. 35, p. 445-453 (1954)., 35, 445

Claussen, M. J., Gaume, R. A., Johnston, K. J., & Wilson, T. L. 1994, ApJ, 424, L41

Clemens, D. P. 1985, ApJ, 295, 422

Codella, C., Palumbo, G. G. C., Pareschi, G., et al. 1995, MNRAS, 276, 57

Csengeri, T., Bontemps, S., Schneider, N., Motte, F., & Dib, S. 2011, A&A, 527, A135

Cyganowski, C. J., Whitney, B. A., Holden, E., et al. 2008, AJ, 136, 2391

Dale, J. E., & Bonnell, I. 2011, MNRAS, 414, 321

De Buizer, J. M., Radomski, J. T., Telesco, C. M., & Piña, R. K. 2005, ApJS, 156, 179

Di Francesco, J., Johnstone, D., Kirk, H., MacKenzie, T., & Ledwosinska, E. 2008, ApJS, 175, 277

Dreher, J. W., & Welch, W. J. 1981, ApJ, 245, 857

Egan, M. P., Price, S. D., & Kraemer, K. E. 2003, in Bulletin of the American Astronomical Society, Vol. 35, American Astronomical Society Meeting Abstracts, 1301

Ellingsen, S. P., Voronkov, M. A., Cragg, D. M., et al. 2007, in IAU Symposium, Vol. 242, IAU Symposium, ed. J. M. Chapman & W. A. Baan, 213–217

Elmegreen, B. 1992, in Star Formation in Stellar Systems, ed. G. Tenorio-Tagle, M. Prieto, & F. Sanchez, 381

Elmegreen, B. G. 2000, ApJ, 530, 277

Elmegreen, B. G., & Lada, C. J. 1977, ApJ, 214, 725

Elmegreen, D. M. 1980, ApJ, 240, 846

Evans, N. J., Shirley, Y. L., Mueller, K. E., & Knez, C. 2002, in Astronomical Society of the Pacific Conference Series, Vol. 267, Hot Star Workshop III: The Earliest Phases of Massive Star Birth, ed. P. Crowther, 17

Evans, N. J., Dunham, M. M., Jørgensen, J. K., et al. 2009, ApJS, 181, 321

Evans, II, N. J. 1999, ARA&A, 37, 311

Fazio, G. G., Hora, J. L., Allen, L. E., et al. 2004, ApJS, 154, 10

Feigelson, E. D., & Townsley, L. K. 2008, ApJ, 673, 354

Feldt, M., Stecklum, B., Henning, T., et al. 1998, A&A, 339, 759

Finkenzeller, U., & Mundt, R. 1984, A&AS, 55, 109

Flaherty, K. M., Pipher, J. L., Megeath, S. T., et al. 2007, ApJ, 663, 1069

Forster, J. R., & Caswell, J. L. 1989, A&A, 213, 339

Froebrich, D., & Rowles, J. 2010, MNRAS, 406, 1350

Garay, G., Rodriguez, L. F., Moran, J. M., & Churchwell, E. 1993, ApJ, 418, 368

Ghosh, S. K., Iyengar, K. V. K., Rengarajan, T. N., et al. 1988, ApJ, 330, 928

Girardi, L., Williams, B. F., Gilbert, K. M., et al. 2010, ApJ, 724, 1030

Gower, J. C., & Ross, G. J. S. 1969, Journal of the Royal Statistical Society. Series C (Applied Statistics), 18, pp. 54

Greaves, J. S., Murray, A. G., & Holland, W. S. 1994, A&A, 284, L19

Green, D. A. 2009, Bulletin of the Astronomical Society of India, 37, 45

Greene, T. P., Wilking, B. A., Andre, P., Young, E. T., & Lada, C. J. 1994, ApJ, 434, 614

Greiner, J. 2001, ArXiv Astrophysics e-prints

Griffin, M., Ade, P., André, P., et al. 2009, in EAS Publications Series, Vol. 34, EAS Publications Series, ed. L. Pagani & M. Gerin, 33–42

Griffin, M. J., Abergel, A., Abreu, A., et al. 2010, A&A, 518, L3+

Gutermuth, R. A., Megeath, S. T., Myers, P. C., et al. 2009, ApJS, 184, 18

Gutermuth, R. A., Myers, P. C., Megeath, S. T., et al. 2008, ApJ, 674, 336

Hachisuka, K., Brunthaler, A., Menten, K. M., et al. 2006, ApJ, 645, 337

Heiderman, A., Evans, II, N. J., Allen, L. E., Huard, T., & Heyer, M. 2010, ApJ, 723, 1019

Heitsch, F., Slyz, A. D., Devriendt, J. E. G., Hartmann, L. W., & Burkert, A. 2006, ApJ, 648, 1052

Hill, T., Motte, F., Didelon, P., et al. 2011, A&A, 533, A94

Hofner, P., & Churchwell, E. 1996, A&AS, 120, 283

Hofner, P., Peterson, S., & Cesaroni, R. 1999, ApJ, 514, 899

Holland, W., MacIntosh, M., Fairley, A., et al. 2006, in Society of Photo-Optical Instrumentation Engineers (SPIE) Conference Series, Vol. 6275, Society of Photo-Optical Instrumentation Engineers (SPIE) Conference Series

Holland, W. S., Robson, E. I., Gear, W. K., et al. 1999, MNRAS, 303, 659

Hughes, V. A., & Viner, M. R. 1982, AJ, 87, 685

Hunter, T. R., Phillips, T. G., & Menten, K. M. 1997, ApJ, 478, 283

Indebetouw, R., Mathis, J. S., Babler, B. L., et al. 2005, ApJ, 619, 931

Jackson, J. M., Rathborne, J. M., Shah, R. Y., et al. 2006, ApJS, 163, 145

Jarrett, T. H., Cohen, M., Masci, F., et al. 2011, ApJ, 735, 112

Jeans, J. H. 1902, Royal Society of London Philosophical Transactions Series A, 199, 1

Kaiser, C. R., Gunn, K. F., Brocksopp, C., & Sokoloski, J. L. 2004, ApJ, 612, 332

Kenyon, S. J., & Hartmann, L. 1995, ApJS, 101, 117

Kerton, C. R., Arvidsson, K., Knee, L. B. G., & Brunt, C. 2008, MNRAS, 385, 995

Kerton, C. R., Ballantyne, D. R., & Martin, P. G. 1999, AJ, 117, 2485

Kerton, C. R., Martin, P. G., Johnstone, D., & Ballantyne, D. R. 2001, ApJ, 552, 601

Klaassen, P. D., & Wilson, C. D. 2007, ApJ, 663, 1092

Klessen, R. S., Ballesteros-Paredes, J., Li, Y., & Mac Low, M.-M. 2004, in Astronomical Society of the Pacific Conference Series, Vol. 322, The Formation and Evolution of Massive Young Star Clusters, ed. H. J. G. L. M. Lamers, L. J. Smith, & A. Nota, 299

Klessen, R. S., Ballesteros-Paredes, J., Vázquez-Semadeni, E., & Durán-Rojas, C. 2005, ApJ, 620, 786

Koenig, X. P., Allen, L. E., Gutermuth, R. A., et al. 2008, ApJ, 688, 1142

Koenig, X. P., Leisawitz, D. T., Benford, D. J., et al. 2012, ApJ, 744, 130

Könyves, V., André, P., Men'shchikov, A., et al. 2010, A&A, 518, L106

Koornneef, J. 1983, A&A, 128, 84

Kraemer, K. E., Jackson, J. M., Kassis, M., et al. 2003, ApJ, 588, 918

Krumholz, M. R., & McKee, C. F. 2008, Nature, 451, 1082

Kurtz, S., Hofner, P., & Álvarez, C. V. 2004, ApJS, 155, 149

Lada, C. J. 1987, in IAU Symposium, Vol. 115, Star Forming Regions, ed. M. Peimbert & J. Jugaku, 1–17

Lada, C. J., & Lada, E. A. 2003, ARA&A, 41, 57

Lequeux, J. 2005, The Interstellar Medium, ed. Lequeux, J.

Little, L. T., White, G. J., & Riley, P. W. 1977, MNRAS, 180, 639

Marigo, P., Girardi, L., Bressan, A., et al. 2008, A&A, 482, 883

Markwardt, C. B. 2009, in Astronomical Society of the Pacific Conference Series, Vol. 411, Astronomical Society of the Pacific Conference Series, ed. D. A. Bohlender, D. Durand, & P. Dowler, 251

Martin, P. G., Roy, A., Bontemps, S., et al. 2012, ArXiv e-prints, ApJ in press

Martins, F., Schaerer, D., & Hillier, D. J. 2005, A&A, 436, 1049

Mathis, J. S. 1990, ARA&A, 28, 37

Matthews, H. E., Goss, W. M., Winnberg, A., & Habing, H. J. 1977, A&A, 61, 261

McKee, C. F., & Ostriker, E. C. 2007, ARA&A, 45, 565

McKee, C. F., & Tan, J. C. 2003, ApJ, 585, 850

Megeath, S. T., Allgaier, E., Young, E., et al. 2009, AJ, 137, 4072

Megeath, S. T., Herter, T., Beichman, C., et al. 1996, A&A, 307, 775

Megeath, S. T., Townsley, L. K., Oey, M. S., & Tieftrunk, A. R. 2008, Low and High Mass Star Formation in the W3, W4, and W5 Regions, ed. Reipurth, B., 264–+

Megeath, S. T., Wilson, T. L., & Corbin, M. R. 2005, ApJ, 622, L141

Megeath, S. T., Allen, L. E., Gutermuth, R. A., et al. 2004, ApJS, 154, 367

Mendigutía, I., Eiroa, C., Montesinos, B., et al. 2011, A&A, 529, A34+

Men'shchikov, A., André, P., Didelon, P., et al. 2012, ArXiv e-prints

Menten, K. 1991, in Astronomical Society of the Pacific Conference Series, Vol. 16, Atoms, Ions and Molecules: New Results in Spectral Line Astrophysics, ed. A. D. Haschick & P. T. P. Ho, 119

Meyer, M. R., Calvet, N., & Hillenbrand, L. A. 1997, AJ, 114, 288

Minier, V., Burton, M. G., Hill, T., et al. 2005, A&A, 429, 945

Minier, V., Peretto, N., Longmore, S. N., et al. 2007, in IAU Symposium, Vol. 237, IAU Symposium, ed. B. G. Elmegreen & J. Palous, 160–164

Minier, V., André, P., Bergman, P., et al. 2009, A&A, 501, L1

Molinari, S., Pezzuto, S., Cesaroni, R., et al. 2008, A&A, 481, 345

Molinari, S., Schisano, E., Faustini, F., et al. 2011, A&A, 530, A133

Molinari, S., Swinyard, B., Bally, J., et al. 2010, PASP, 122, 314

Mooney, T., Sievers, A., Mezger, P. G., et al. 1995, A&A, 299, 869

Moore, T. J. T., Bretherton, D. E., Fujiyoshi, T., et al. 2007, MNRAS, 379, 663

Moore, T. J. T., Shipman, R. F., Plume, R., Hoare, M. G., & Jps International Collaboration. 2005, in Protostars and Planets V, Proceedings of the Conference held October 24-28, 2005, in Hilton Waikoloa Village, Hawai'i. LPI Contribution No. 1286., p.8370, 8370–+

Motte, F., Bontemps, S., Schilke, P., et al. 2007, A&A, 476, 1243

Motte, F., Zavagno, A., Bontemps, S., et al. 2010, A&A, 518, L77

Mottram, J. C., Hoare, M. G., Lumsden, S. L., et al. 2010, A&A, 510, A89

Mottram, J. C., Hoare, M. G., Urquhart, J. S., et al. 2011, A&A, 525, A149

Navarete, F., Figueredo, E., Damineli, A., et al. 2011, ArXiv e-prints

Netterfield, C. B., Ade, P. A. R., Bock, J. J., et al. 2009, ApJ, in press

Neugebauer, G., Habing, H. J., van Duinen, R., et al. 1984, ApJ, 278, L1

Nguyen Luong, Q., Motte, F., Hennemann, M., et al. 2011a, A&A, 535, A76

Nguyen Luong, Q., Motte, F., Schuller, F., et al. 2011b, A&A, 529, A41

Oey, M. S., Watson, A. M., Kern, K., & Walth, G. L. 2005, AJ, 129, 393

Ojha, D. K., Tamura, M., Nakajima, Y., et al. 2009, ApJ, 693, 634

Panagia, N. 1973, AJ, 78, 929

Pandian, J. D., Goldsmith, P. F., & Deshpande, A. A. 2007, ApJ, 656, 255

Pandian, J. D., Menten, K. M., & Goldsmith, P. F. 2009, ArXiv e-prints

Paron, S., Cichowolski, S., & Ortega, M. E. 2009, A&A, 506, 789

Pascale, E., Ade, P. A. R., Bock, J. J., et al. 2008, ApJ, 681, 400

Patanchon, G., Ade, P. A. R., Bock, J. J., et al. 2008, ApJ, 681, 708

Peretto, N., & Fuller, G. A. 2009, VizieR Online Data Catalog, 350, 50405

Peretto, N., Andre, P., Konyves, V., et al. 2012, ArXiv e-prints

Peters, T., Banerjee, R., Klessen, R. S., et al. 2010, ApJ, 711, 1017

Phillips, J. P., White, G. J., Rainey, R., et al. 1988, A&A, 190, 289

Planck Collaboration, Abergel, A., Ade, P. A. R., et al. 2011a, ArXiv e-prints 1101.2036

—. 2011b, A&A, 536, A25

Poglitsch, A., Waelkens, C., Geis, N., et al. 2010, A&A, 518, L2+

Polychroni, D., Moore, T. J. T., & Allsopp, J. 2010, in Astronomical Society of the Pacific Conference Series, Vol. 424, 9th International Conference of the Hellenic Astronomical Society, ed. K. Tsinganos, D. Hatzidimitriou, & T. Matsakos, 165–+

Polychroni, D., Moore, T. J. T., & Allsopp, J. 2012, ArXiv e-prints

Purcell, C. R., Hoare, M. G., & Diamond, P. 2008, in Astronomical Society of the Pacific Conference Series, Vol. 387, Massive Star Formation: Observations Confront Theory, ed. H. Beuther, H. Linz, & T. Henning, 389

Rathborne, J. M., Jackson, J. M., & Simon, R. 2006, ApJ, 641, 389

Rathborne, J. M., Johnson, A. M., Jackson, J. M., Shah, R. Y., & Simon, R. 2009, ApJS, 182, 131

Rathborne, J. M., Shah, Jackson, J. M. R. Y., Bania, T. M., et al. 2004, in Astronomical Society of the Pacific Conference Series, Vol. 317, Milky Way Surveys: The Structure and Evolution of our Galaxy, ed. D. Clemens, R. Shah, & T. Brainerd, 100

Richardson, K. J., White, G. J., Sandell, G., Duncan, W. D., & Krisciunas, K. 1989, A&A, 221, 95

Rieke, G. H., Young, E. T., Engelbracht, C. W., et al. 2004, ApJS, 154, 25

Rivera-Ingraham, A., Martin, P. G., Polychroni, D., & Moore, T. J. T. 2011, ApJ, 743, 39

Rivera-Ingraham, A., Ade, P. A. R., Bock, J. J., et al. 2010, ApJ, 723, 915

Roberts, D. A., Crutcher, R. M., Troland, T. H., & Goss, W. M. 1993, ApJ, 412, 675

Robitaille, T. P., Whitney, B. A., Indebetouw, R., Wood, K., & Denzmore, P. 2006, ApJS, 167, 256

Robitaille, T. P., Meade, M. R., Babler, B. L., et al. 2008, AJ, 136, 2413

Roccatagliata, V., Bouwman, J., Henning, T., et al. 2011, ApJ, 733, 113

Rodón, J. A., Beuther, H., Megeath, S. T., & van der Tak, F. F. S. 2008, A&A, 490, 213

Roman-Duval, J., Jackson, J. M., Heyer, M., et al. 2009, ApJ, 699, 1153

Rosolowsky, E., Dunham, M. K., Ginsburg, A., et al. 2010, ApJS, 188, 123

Roussel, H. 2012, ArXiv e-prints

Rowles, J., & Froebrich, D. 2009, MNRAS, 395, 1640

Roy, A., Ade, P. A. R., Bock, J. J., et al. 2010, ApJ, 708, 1611

—. 2011, ApJ, 727, 114

Ruch, G. T., Jones, T. J., Woodward, C. E., et al. 2007, ApJ, 654, 338

Sakai, T., Oka, T., & Yamamoto, S. 2007, ApJ, 662, 1043

Schneider, N., Csengeri, T., Bontemps, S., et al. 2010, A&A, 520, A49

Schneider, N., Csengeri, T., Hennemann, M., et al. 2012, ArXiv e-prints

Shu, F. H. 1977, ApJ, 214, 488

Simon, R., Jackson, J. M., Clemens, D. P., Bania, T. M., & Heyer, M. H. 2001, ApJ, 551, 747

Simon, R., Jackson, J. M., Rathborne, J. M., & Chambers, E. T. 2006, ApJ, 639, 227

Sousbie, T. 2011, MNRAS, 414, 350

Sridharan, T. K., Beuther, H., Saito, M., Wyrowski, F., & Schilke, P. 2005, ApJ, 634, L57

Stetson, P. B. 1987, PASP, 99, 191

Stil, J. M., Taylor, A. R., Dickey, J. M., et al. 2006, AJ, 132, 1158

Straižys, V., & Kazlauskas, A. 2010, Baltic Astronomy, 19, 1

Strong, A. W., Bloemen, J. B. G. M., Dame, T. M., et al. 1988, A&A, 207, 1

Szymczak, M., Hrynek, G., & Kus, A. J. 2000, A&AS, 143, 269

Takahashi, H., Matsuhara, H., Watarai, H., & Matsumoto, T. 2000, ApJ, 541, 779

Taylor, A. R., Gibson, S. J., Peracaula, M., et al. 2003, AJ, 125, 3145

Testi, L., Felli, M., & Taylor, G. B. 1999, A&AS, 138, 71

The, P. S., de Winter, D., & Perez, M. R. 1994, A&AS, 104, 315

Thompson, M. A., Urquhart, J. S., Moore, T. J. T., & Morgan, L. K. 2012, MNRAS, 421, 408

Thronson, Jr., H. A., Lada, C. J., & Hewagama, T. 1985, ApJ, 297, 662

Tieftrunk, A. R., Gaume, R. A., Claussen, M. J., Wilson, T. L., & Johnston, K. J. 1997, A&A, 318, 931

Tieftrunk, A. R., Gaume, R. A., & Wilson, T. L. 1998a, A&A, 340, 232

Tieftrunk, A. R., Megeath, S. T., Wilson, T. L., & Rayner, J. T. 1998b, A&A, 336, 991

Tieftrunk, A. R., Wilson, T. L., Steppe, H., et al. 1995, A&A, 303, 901

Tothill, N. F. H., White, G. J., Matthews, H. E., et al. 2002, ApJ, 580, 285

Truch, M. D. P., Ade, P. A. R., Bock, J. J., et al. 2008, ApJ, 681, 415

Turner, J. L., & Welch, W. J. 1984, ApJ, 287, L81

Urquhart, J. S., Hoare, M. G., Purcell, C. R., et al. 2009, A&A, 501, 539

van der Tak, F. F. S., Tuthill, P. G., & Danchi, W. C. 2005, A&A, 431, 993

van der Walt, D. J., Gaylard, M. J., & MacLeod, G. C. 1995, A&AS, 110, 81

Vig, S., Ghosh, S. K., Kulkarni, V. K., Ojha, D. K., & Verma, R. P. 2006, ApJ, 637, 400

Voroshilov, V. I., Guseva, N. G., Kalandadze, N. B., et al. 1985, Catalog of BV magnitudes and spectral classes of 6000 stars, ed. Voroshilov, V. I., Guseva, N. G., Kalandadze, N. B., Kolesnik, L. N., Kuznetsov, V. I., Metreveli, M. D., & Shapovalov, A. N.

Wang, P., Li, Z.-Y., Abel, T., & Nakamura, F. 2010, ApJ, 709, 27

Werner, M. W., Roellig, T. L., Low, F. J., et al. 2004, ApJS, 154, 1

White, G. J., Richardson, K. J., Frost, R. F., et al. 1983, MNRAS, 204, 1117

White, G. J., Nelson, R. P., Holland, W. S., et al. 1999, A&A, 342, 233

Williams, J. P., Blitz, L., & McKee, C. F. 2000, Protostars and Planets IV, 97

Wilner, D. J., Ho, P. T. P., & Zhang, Q. 1996, ApJ, 462, 339

Wood, D. O. S., & Churchwell, E. 1989, ApJS, 69, 831

Wright, E. L., Eisenhardt, P. R. M., Mainzer, A. K., et al. 2010, AJ, 140, 1868

Wynn-Williams, C. G., Becklin, E. E., & Neugebauer, G. 1972, MNRAS, 160, 1

Xu, Y., Reid, M. J., Zheng, X. W., & Menten, K. M. 2006, Science, 311, 54

Yorke, H. W. 1993, in Astronomical Society of the Pacific Conference Series, Vol. 35, Massive Stars: Their Lives in the Interstellar Medium, ed. J. P. Cassinelli & E. B. Churchwell, 45–+

Zdziarski, A. A., Gierliński, M., Rao, A. R., Vadawale, S. V., & Mikołajewska, J. 2005, MNRAS, 360, 825

Zhu, Q.-F., Lacy, J. H., Jaffe, D. T., Richter, M. J., & Greathouse, T. K. 2008, ApJS, 177, 584

Zinnecker, H., McCaughrean, M. J., Rayner, J. T., Wilking, B. A., & Moneti, A. 1993, in Reviews in Modern Astronomy, Vol. 6, Reviews in Modern Astronomy, ed. G. Klare, 191–208

Zinnecker, H., & Yorke, H. W. 2007, ARA&A, 45, 481